Nanoscale Magnetic Resonance Spectroscopy with Nitrogen-Vacancy Centers in Diamond

Von der Fakultät 8 Mathematik und Physik der Universität Stuttgart zur Erlangung der Würde eines Doktors der Naturwissenschaften (Dr. rer. nat.) genehmigte Abhandlung

vorgelegt von
Domenico Paone
aus Ludwigsburg

Hauptberichter: Prof. Dr. Jörg Wrachtrup

Mitberichter: Prof. Dr. Klaus Kern

2. Mitberichter: Prof. Dr. Harald Giessen

Tag der mündlichen Prüfung: 05.10.2021

3. Physikalisches Institut der Universität Stuttgart

2021

Summary

The detection of magnetic fields plays an important role in diverse areas ranging from fundamental science to applications in data storage and medicine. Consequently, a variety of magnetic field sensors have been developed including Hall sensors, anisotropic magnetoresistive (AMR) sensors, superconducting quantum interference devices (SQUIDs) and magnetic resonance sensors. However, modern technologies are becoming more inclined towards effects occurring at the nanometer length scale. Examples can be found in the field of biomedical science, where properties of single proteins are investigated which play a crucial role in medicine and pharmaceutics. For a better understanding of such biological compounds, spatial conformations and structures have to be revealed on the single molecule level. Therefore, sensors are required which are able to detect weak magnetic fields with high spatial resolution by implementing nano-magnetic resonance imaging (nano-MRI) techniques. Another example in modern condensed-matter physics comes from superconductivity. Due to the wide range of applications connected to superconductors, including the production of sensitive magnetometers, digital circuits and electromagnets, superconducting systems are catching a huge amount of interest in physics. Indeed, the macroscopic theory of superconductors is able to explain unique phenomena like the Meissner effect. However, microscopic studies on superconductors play an important role in understanding the mechanisms underlying superconductivity. A nanometer scale magnetic sensor could investigate the Meissner state of a superconductor locally, detecting dynamical phenomena such as the formation and motion of single magnetic vortices.

A promising approach for nanoscale magnetic field detection and imaging can be enabled by exploiting quantum effects in the nitrogen-vacancy (NV) defect center in diamond. This point defect shows a spin dependent photoluminescence (PL). The sensing principle relies on microwave excitations which allow coherent manipulation within different spin sublevels in the ground state. These transitions show a Zeemann effect which is dependent to the applied magnetic field and can be read out by recording the corresponding PL of the NV defect. The sensing approach, known as optically detected magnetic resonance (ODMR) spectroscopy, can be used for sensing nuclear and electron spins in a nanometer-sized volume. Applications of NV center based quantum sensing have been shown by electron spin resonance (ESR) of spin labeled molecular chains and nuclear magnetic resonance (NMR) of organic samples. Furthermore, magnetic properties like spin waves, ferromagnetism and superconductivity have been investigated with this approach locally on the μm scale. Therefore, the single spin sensitivity of the NV center is a powerful tool for revealing a deeper understanding in the composition of single molecules and the formation of magnetic domains in solids.

This thesis demonstrates NV center based magnetometry for the detection of single external spins and

the local resolution of collective spin phenomena. All presented experiments have been performed in an ultra-high vacuum (UHV) cryogenic setup operating at a base pressure of $2 \cdot 10^{-10}$ mbar and at a base temperature of 4.7 K.

More specifically, the presented work shows a successful NV center based readout of single optically dark molecules which are usually difficult to address with spectroscopy methods in the optical wavelength region. Two systems have been investigated in this context, namely long-chain spin labeled polyphenols and endofullerene $N@C_{60}$ buckyballs. Thereby, the dipolar coupling between the NV center spin and the corresponding individual target spin has been observed in terms of double electron electron resonance (DEER) spectroscopy. With this technique, the structure of optically dark molecules can be investigated even at the nanometer length scale.

Both external spin systems were identified by the usual NV center sensing protocol which relies on the application of microwave excitation. However, such excitations are often accompanied by local heating effects which could cause undesired changes in the properties of the investigated system. While for molecular spin sensing the local microwave heating has a minor impact on the observed system, the characterization of spin phenomena in solids could be influenced. Prime examples are two-dimensional superconductors which are accompanied by magnetic phases at certain critical temperatures. This problem can be circumvented by utilizing an all-optical, microwave-free measurement scheme.

Therefore, this thesis also introduces the direct fluorescence emitted by an NV ensemble for the detection of the Meissner state in a thin film $La_{2-x}Sr_xCuO_4$ (LSCO) sample. The measured magnetic field profile along the LSCO thin film can be analytically reproduced by Brandt's model, revealing a critical current density j_c of $1.4 \cdot 10^8$ A/cm^2. The good agreement between the measured j_c and the corresponding literature values for LSCO suggests that the all-optical, microwave-free PL rate of the NV center can be utilized as a reliable quantity for the observation of magnetic properties in solids. These measurement schemes can be potentially extended further with optical pump-probe spectroscopy enabling access to dynamical phenomena in nanomagnetic materials with ps time resolution.

Finally, the last part of this thesis highlights experimental attempts for enhancing the spin properties of single shallow NV centers. The spatial resolution of an NV center sensor is defined by the sensor-to-sample distance. Therefore, near-surface NVs are beneficial for sensing purposes. However, shallow NV centers often suffer from spin state instabilities due to charge traps available on the diamond surface. To overcome this limitation, controlled in situ dosing procedures have been implemented. Our results exhibit that surface-modification provides a viable route to enhance the optical properties of shallow NV centers in diamond.

Thus altogether, the results presented in this thesis provide major advances in the field of nanoscale magnetometry.

Zusammenfassung

Die Detektion von magnetischen Feldern spielt in verschiedenen Bereichen eine wichtige Rolle, die von fundamentalen Wissenschaften bis hin zu Anwendungen in der Datenspeicherung und Medizin weit reichen. Folglich wurde eine Vielzahl von magnetischen Sensoren entwickelt, zu denen Hall Sensoren, anisotropische magnetoresistive (AMR) Sensoren, supraleitende Quanteninterferenzeinheiten (SQUIDs) und magnetische Resonanzsensoren gehören. Dennoch fokussieren sich moderne Technologien immer mehr auf Effekte, die auf der Nanometerskala relevant sind. Beispiele können im Bereich der Biomedizin gefunden werden, in welcher Eigenschaften einzelner Proteine untersucht werden, die eine entscheidende Rolle in der Medizin und Pharmazeutik spielen. Um ein besseres Verständnis solcher biologischer Zusammensetzungen zu erhalten, ist es wichtig, die räumliche Orientierung und Struktur auf Ebene einzelner Moleküle zu enthüllen. Daher werden Sensoren benötigt, die in der Lage sind, schwache Magnetfelder mit hoher räumlicher Auflösung in Form der nano-Magnetresonanztomographie (MRT) zu detektieren. Ein weiteres Beispiel kann in der Festkörperforschung im Bereich der Supraleiung gefunden werden. Dank den weitreichenden Anwendungsbereichen von Supraleitern, zu denen die Produktion von sensitiven Magnetometern, digitalen Schaltkreisen und Elektromagneten gehört, haben supraleitende Systeme große Aufmerksamkeit in der Physik erhalten. In der Tat ist die makroskopische Theorie von Supraleitern in der Lage, einzigartige Phänomene, wie den Meissner Effekt, zu erklären. Dennoch spielen mikroskopische Studien eine wichtige Rolle, um die Mechanismen zu verstehen, welche grundlegend für die Supraleitung sind. Ein magnetischer Sensor, der im Nanometerbereich arbeitet, könnte lokal die Meissner Phase eines Supraleiters untersuchen um dynamische Phänomene, wie die Formation und Bewegung magnetischer Wirbelschläuche, zu detektieren.

Ein vielversprechendes Vorgehen für die Detektion von Magnetfeldern auf der Nanometerskala kann durch das Ausnutzen von Quanteneffekten im Stickstoff-Fehlstellen (NV) Defekt Zentrum in Diamanten ermöglicht werden. Dieser Punktdefekt besitzt eine spinabhängige Lumineszenze (PL). Das Sensorenprinzip basiet auf resonanten Mikrowellenanregungen, die kohärente Manipulationen innerhalb des Spin Grundzustandes ermöglichen. Diese Übergänge weisen einen Zeeman Effekt auf, der linear vom angewandten Magnetfeld abhängt und optisch ausgelesen werden kann indem die NV Fluoreszenz aufgenommen wird. Das Detektionsvorgehen, bekannt als optische magnetische Resonanzspektroskopie (ODMR), kann genutzt werden um Kern- und Elektronenspins in Nanometervolumen wahrzunehmen. Anwendungen von Detektionen, die auf dem NV Zentrum basieren, wurden als Elektronenspinresonanz (ESR) in Spin-gekennzeichneten Molekülketten und Kernspinresonanz in organischen Proben aufgezeigt. Zusätzlich wurden magnetische Eigenschaften wie Spin-Wellen, Fer-

romagnetismus und Supraleitung auf μm-Skalen mit dieser Vorgehensweise untersucht. Deshalb ist die Sensitivität des NV Zentrums ein wichtiges Werkzeug um ein tieferes Verständins in der Zusammensetzung einzelner Moleküle und der Formation magnetischer Bereiche zu erhalten.
Diese Doktorarbeit veranschaulicht Magnetometermessungen, die auf dem NV Zentrum basieren, um einzelne externe Moleküle zu detektieren und kollektive Elektronenphänomene aufzulösen. Alle präsentierten Experimente wurden in einem Hochvakuum-Kryostaten durchgeführt, welcher in einem Druckbereich von $2 \cdot 10^{-10}$ mbar und einer Temperatur von 4.7 K arbeitet.
Genauer gesagt zeigt diese Arbeit die erfolgreiche Detektion von optisch dunklen Molekülen, die mit einzelnen NV Zentren charakterisiert wurden und üblicherweise schwer mit Spektroskopiemethoden im optischen Wellenlängenbereich zu adressieren sind. Zwei Systeme wurden dabei untersucht und zwar langkettige Spin-gekennzeichnete Polyphenole und endohedrale $N@C_{60}$ "buckyballs". Dabei wurde die dipolare Koppulng zwischen dem NV Zentrum Spin und dem jeweiligen individuellen Zielspin mithilfe von doppelter Elektronenspinresonanz Spektroskopie (DEER) untersucht. Mit dieser Methode kann die Struktur von optischen dunklen Moleküle, einschließlich ihrer Nanometer Längenskalen, untersucht werden.
Beide Spinsysteme wurden mit den üblichen NV Zentren Detektionsprotokolle untersucht, welche auf den Gebrauch von Mikrowellenanregungen basieren. Solche Anregungen werden oft von lokalen Erhitzungseffekten begleitet, die unerwünschte Änderungen der Eigenschaften des zu untersuchenden Systems induzieren. Während dies auf die Detektion von Molekülen nur geringe Auswirkungen hat, lässt sich die Charakterisierung von Spin Phänomenen in Festkörpern stark davon beeinflussen. Beispiele sind zwei dimensionale Supraleiter, welche einen magnetischen Phasenübergang ab einer bestimmten kritischen Temperatur vollziehen. Dieses Problem kann verhindert werden, indem rein optische, mikrowellen-freie Messungen durchgeführt werden.
Daher leitet diese Arbeit ebenfalls die direkte Fluoreszenz ein, welche von einem NV Zentrum Ensemble emittiert wird, um die Meissner Phase einer dünnen $La_{2-x}Sr_xCuO_4$ (LSCO) Probe zu detektieren. Das Profil des gemessenen magnetischen Feldes kann mit Hilfe des analytischen Brandt Modells rekonstruiert werden um eine kritische Stromdichte $j_c = 1.4 \cdot 10^8$ A/cm^2 der Probe zu erhalten. Da dieser Wert mit den Literaturwerten für LSCO übereinstimmt, kann die rein optische, Mikrowellen freie NV Fluoreszenz als zuverlässliche Messgröße bewertet werden, mit welcher magnetische Eigenschaften in Festkörpern untersucht werden können. Zudem kann die NV Fluoreszenz potentiell mit optischen "pump-probe" Spektroskopie Methoden erweiter werden, um dynamische Prozesse im Pikosekunden Bereich zu untersuchen.
Letztendlich zeigt Kapitel 7 experimentelle Versuche auf, welche die Spineigenschaften sehr oberflächennahen NV Zentren verbessern sollen. Die räumliche Auflösung eines NV Zentrum Sensors ist durch den Abstand zwischen dem Sensor und der Probe definiert. Daher sind NV Zentren, welche nah an der Diamantenoberfläche lokalisiert sind, vorteilhaft für Detektionsanwendungen. Dennoch zeigen oberflächennahe NV Zentren oft Spininstabilitäten auf, die mit Ladungspotentialen auf der Diamantenoberfläche zusammenhängen. Um diese Beschränkung zu bewältigen, wurden

Dosierungsvorgänge, innerhalb des Hochvakuums, auf der Diamantenoberfläche implementiert. Die experimentellen Ergebnisse zeigen, dass Oberflächenmodifikation durchaus in der Lage sind, die optischen Eigenschaften von oberflächennahen NV Zentren zu verbessern.
Die präsentierten Ergebnisse dieser Doktorarbeit erzielen wichtige Fortschritte in Bereichen der Magnetfelmessung auf Nanometerskalen.

Publications

From the presented PhD thesis, two scientific articles have been published and one more publication is in the process of being drafted. Furthermore, two additional articles have been published during this time period from former experiments which were performed within the scope of my Master thesis at the PI4 of the University of Stuttgart.

Publications from my Master Thesis

- T. Teutsch, N. Strohfeldt, F. Sterl, A. Warsewa, E. Herkert, **D. Paone**, H. Giessen and Christina Tarin, *Mathematical Modeling of a Plasmonic Palladium-Based Hydrogen Sensor*, IEEE Sensors Journal **18**, 1946-1959 (2018).

- Q. Ai, L. Gui, **D. Paone**, B. Metzger, M. Mayer, K. Weber, A. Fery and H. Giessen, *Ultranarrow Second-Harmonic Resonances in Hybrid Plasmon-Fiber Cavities*, NanoLett. **18**, 5576-5582 (2018).

Publications from this PhD Thesis

- D. Pinto, **D. Paone**, B. Kern, T. Dierker, R. Wieczorek, A. Singha, D. Dasari, A. Finkler, W. Harneit, J. Wrachtrup and K. Kern, *Readout and Control of an Endofullerne Electronic Spin*, Nature Communications **11**, 6405 (2020).

- **D. Paone**, D. Pinto, G. Kim, L. Feng, M.-J. Kim, R. Stöhr, A. Singha, S. Kaiser, G. Logvenov, B. Keimer, J. Wrachtrup and K. Kern, *All-Optical and Microwave-Free Detection of Meissner Screening using Nitrogen-Vacancy Centers in Diamond*, J. Appl. Phys. **129**, 024306 (2021).

- **D. Paone**, J. Neethirajan, D. Pinto, A. Denisenko, R. Stöhr, A. Singha, J. Wrachtrup and K. Kern, *Charge State Instabilities of Nitrogen-Vacancy Centers in Diamond at Cryogenic Ultra-High-Vacuum Conditions*, in preparation.

Curriculum Vitae

- **09/2011 - 09/2014** Bachelor of Science, thesis at the PI4 of the University of Stuttgart on plasmonic gas sensing
- **2013 - 2017** Trainee at the PI4 of the University of Stuttgart, **research topic**: Plasmonic gas sensing
- **10/2014 - 04/2015** Research internship at CSIRO Sydney Australia, **research topic**: Plasmonic photovoltaic cells
- **04/2015 - 08/2017** Master of Science, thesis at the PI4 of the University of Stuttgart on chemical growth of plasmonic nanostructures
- **09/2017 - 10/2021** Doctor Rerum Naturalium, thesis at the Max Planck Institute for Solid State Research in Stuttgart on magnetic field sensing with NV centers in diamond

Declaration

I, Domenico Paone, hereby declare that this dissertation entitled "Nanoscale Magnetic Resonance Spectroscopy with NV Centers in Diamond" is entirely my own work expect where otherwise indicated. Passages from other sources have been clearly cited within the bibliography. The contents of this thesis have not been submitted to any other examination institution. Furthermore, the printed version fully accords with the submitted portable document format (pdf) version which can be found online.

Stuttgart,

Contents

List of Abbreviations

AO Atomic orbitals

APD Avalanche Photo diode

BDS BeiDous navigation system

CO Carbon monoxide

Co Cobalt

CR Charge reservoir

Cu Copper

CuBe Beryllium Copper

CuO_2 Copper Oxides

CVD Chemical vapour deposition

cw Continious wave

DEER Double electron electron resonance

DMAP Dymethylaminopyridine

DQT Double quantum transition

ENDOR Electron nuclear double resonance

EPR Electron paramagnetic resonance

ESR Electron spin resonance

fcc Face-centered cubic

FFT Fast Fourier transformation

FID Free induction decay

FPGA Field programmable gate array

GLONASS Global'naya Navigatsionnaya Sputnikovaya Sistema

GNSS Global navigation satellite systems

GPS Global positioning system

HF High frequency

H_2O Water

HPHLC High-performance liquid chromatography

HPHT High pressure and high temperature

IR Infrared

ISC Inter-system crossing

JTE Jahn-Teller effect

LBCO Lanthanum barium copper oxide

LCAO Linear combination atomic orbitals

LP Longpass

LSAO Lanthanum strontium aluminum oxide

LSCO Lanthanum strontium copper oxide

MBE Molecular beam epitaxy

MFM Magnetic force microscopy

MO Molecular orbitals

MRFM Magnetic resonance force microscopy

MRI Magnetic resonance imaging

MW Microwave

N Nitrogen

NA Numerical aperture

nanoSQUID Nano superconducting interference device

Nb Niobium

Nb_3Si Niobium silicon

NbTi Niobium titanium

NMR Nuclear magnetic resonance

NO Nitric oxide

N_2O Nitrous oxide

NV Nitrogen-vacancy

NV^- Negatively charged nitrogen-vacancy

NV^+ Positively charged nitrogen-vacancy

NV^0 Neutral nitrogen-vacancy

O Oxygen

ODMR Optically detected magnetic resonance

P Phosphorous

P5C-NR Tetramethylpyrolline carboxylic nitroxide radical

PL Photoluminescence

PMT Photomultiplier tube

Qdyne Quantum heterodyne detection

RF Radio frequency

RHEED Reflection high energy diffraction

SiV Silicon-vacancy

SMP Sub-miniature-P

SQUID Superconducting interference device

STM Scanning tunneling microscopy

TEER Triple electron electron resonance

UHV Ultra high vacuum

UV Ultraviolet

V Vanadium

V_3In Vanadium indium

YBCO Yttrium barium copper oxide

ZPL Zero phonon line

1 Introduction

Magnetic sensors are widely used in a large number of practical and essential applications. Of great importance among these are recording heads for magnetic storage and memory elements of modern devices [1]. Furthermore, magnetometers form the fundamental basis for compass schemes [2] which play a crucial role in Global Navigation Satellite Systems (GNSS), including the Global Positioning System (GPS), the Global'naya Navigatsionnaya Sputnikovaya Sistema (GLONASS), the BeiDou Navigation Satellite System (BDS) and the Galileo positioning system (Galileo). In addition to that, the detection, discrimination and localization of magnetic fields are essential for many security applications [3] as research studies identified several effects on the human health under high magnetic field exposures [4]. These include minor symptoms such as headaches up to serious impacts in increasing the risk of childhood leukemia [5, 6]. As magnetic fields are invisible and penetrate through nearly all materials, a reliable detection plays a crucial role for human safety [3].

The detection of magnetic signals also plays a significant role in magnetic resonance imaging (MRI) which reveals high resolution images of defective tissues in human body [7, 8]. The technique is a consequence of nuclear magnetic resonance (NMR) which is a physical phenomenon of the behavior of nuclei in a strong constant magnetic field [9]. Thereby, the nuclei respond by accumulating an electromagnetic signal with a characteristic frequency. With this, certain compounds within the human tissue can be distinguished for medical diagnosis. Typically, MRI schemes utilize magnetic field gradients of $\approx 70\,\mathrm{mT/m}$ which are able to detect nuclear spin concentrations within a volume of $1\,\mathrm{mm}^3$ [10, 11]. However, a measurable signal requires a contribution of $\approx 10^{15}$ nuclear spins within the investigated compound [12]. A complementary method is formed by electron spin resonance (ESR) (also termed as electron paramagnetic resonance (EPR)), which utilizes electromagnetic signals gathered by excited electron spins instead of atomic nuclear spins [13]. As the gyromagnetic ratio of an electron spin is higher compared to a nuclear spin, lower magnetic field strengths ($\approx 20\,\mathrm{mT}$) are already sufficient for the acquisition of a spin signal. Nevertheless, similar to the case of MRI, also in traditional ESR setups a huge number of spins ($\approx 10^8 - 10^{14}$ [12]) are required to ensure an acceptable signal to noise ratio. Notably, these standard EPR and NMR techniques are not readily available with nanoscale spatial resolution which is often of great interests for investigating the properties and spatial conformations of single cells, proteins or even molecules for gaining more insights into biochemical processes which highly influence the human behavior.

In order to achieve nanoscale spatial resolution, magnetic field sensors have to be down-scaled to the nanometer level. Furthermore, the sensors have to be brought in close proximity to the sample as the magnetic dipole moment and thereby the dominant term in the magnetic dipole-dipole interaction

decreases with $1/r^3$ (where are r defines the sensor-to-sample distance). The detection of magnetic fields at the nanoscale is also crucial for advancements and developments of other modern scientific applications, for instance, in the field of quantum information processing for the realization of quantum computers [14, 15, 16]. As classical computers are entering the quantum realm, quantum properties can be utilized for increasing the computational power as well as the efficiency for specific tasks. The structure of a quantum computing device is based on interacting quantum spin networks [17]. Thereby, single spins take the role of classical bits as so called quantum bits (qubits). While the state of a classical bit can only be 0 or 1, a qubit according to quantum mechanics can take the values $|0\rangle$, $|1\rangle$ and all possible coherent superposition states of these two states. As a result, the break of solely binary states reveals the potential to perform calculations in more efficient manners. However, coherent superposition states of an individual qubit attend to obtain certain instabilities due to environmental magnetic noise or exchange interactions with other qubits within the quantum network [18]. Therefore, the local readout of specific magnetic spins inside the quantum network could reveal information for controlling and stabilizing the coherence of the individual quantum states.

There are several techniques which pave the way towards nanoscale magnetic field sensing. For instance, magnetic resonance force microscopy (MRFM) methods are able to detect single electronic spins [19, 20]. Thereby, the interaction force between a spin specimen and magnetic tip is measured as a shift of the mechanical resonance frequency of the utilized tuning fork. With this, an image of the magnetic distribution of a sample can be reconstructed by scanning the magnetic tip over a certain area. However, the disadvantage of this technique, is the high complexity of the experimental instrument which requires sensitive cantilevers for the detection of forces in the attonewton range. Furthermore, most of the experiments have to be performed at mK temperatures for reducing drifts and instabilities of the magnetic tip.

Other promising attempts include magnetometers based on superconducting quantum interference devices (SQUIDs) which consist of a superconducting loop interrupted by two weak links forming a Josephson junction [21]. By applying an external magnetic field, an electrical current is induced through the superconducting loop and a magnetic flux is generated inside the loop which must be an integer multiple of the magnetic flux quantum $\Phi_0 = 2.07 \cdot 10^{-15}\,\mathrm{Vs}$. A change of the externally applied field leads to a variation of the induced current and magnetic flux within the superconducting ring. As such a slight shift is challenging to detect, the implemented Josephson junction can be utilized for obtaining a measurable signal. In order to achieve this, a current can be applied across the SQUID. As a result, a certain voltage can be measured on the device which mainly depends on the applied current but also on the magnetic field induced current within the superconductor. Observing the variations of the measurable voltage leads to a qualitative detection of external magnetic fields with a sensitivity of $\approx 10\,\mathrm{aT/Hz^{1/2}}$. However, the realization of nanoscale measurements is challenging as the whole superconducting circuit has to be miniaturized to nanometer length scales. Nevertheless, nanoscaled SQUIDs (nanoSQUIDs) have been successfully developed recently with a loop-diameter of $\approx 40\,\mathrm{nm}$ [22]. A more problematic drawback is that SQUIDs are only able to operator at low temperatures due

to the superconducting phenomena which are exploited for the magnetic field measurement. This issue avoids experiments at ambient temperature conditions.
In addition to that, another class of nanoscale magnetic field sensors have emerged over recent years based on single spins in solids including systems as semiconductor quantum dots [23] or phosphorous in silicon [24]. Thereby, the spins originate by certain impurities within a specific material and form stable quantum sensors due to their reliable response to weak external magnetic fields. One of the best studied spin system in solids is the nitrogen-vacancy (NV) defect in diamond [26] which forms the main focus within the scope of this thesis. The impurity consist of a substitutional nitrogen atom and a neighboring carbon vacancy within the diamond crystal. Several experiments demonstrated its ability to detect small magnetic fields at the nanoscale [25]. As a result, the NV center received an increased attention. Measurements can be performed at both cryogenic as well as ambient conditions with a magnetic field sensitivity of $10\,\mathrm{pT/Hz^{1/2}}$ [26]. Furthermore, it can be brought in close proximity to a spin system achieving a spatial resolution in the nm regime. The fundamental sensing principle relies on the spin state dependent photoluminescence (PL) of the NV defect which forms a $S = 1$ ground state [27]. Consequently, three different sublevels ($m_S = 0$, $m_S = -1$ and $m_S = +1$) are involved within the ground state. Thereby, the $m_S = 0$ sublevel exhibits a higher emission compared to the $m_S = -1$ and $m_S = +1$ substates. According to the energy level diagram, microwave (MW) excitations allow coherent manipulations within these spin sublevels. The resulting MW transitions show a Zeeman effect which linearly depends on the applied magnetic field and realizes the performance of optically detected magnetic resonance (ODMR) spectroscopy. Thereby, the resonance lines can be observed as sharp dips within the ODMR spectrum due to the different fluorescence yield of the NV center spin states.
These non-invasive and reliable properties make the NV center to a very promising quantum sensor for discovering physical processes at the nanoscale. Indeed, applications of NV center based sensing schemes have been shown in single molecular spin systems in terms of ESR and NMR spectroscopy revealing molecular distances in the nm region [28]. Additionally, magnetic properties of materials have been investigated including ferromagnetism in permalloys and cobalt (Co) nanowires [29, 30] and superconductivity at the nanoscale [31] giving local insights into magnetic domains. Furthermore, optimizations on the NV center sensing protocols are able to locally detect fast magnetic dynamics in a narrow μs time resolution [32].

This Thesis

The presented thesis describes NV center based measurement schemes for the characterization of molecules and superconductivity in a cryogenic, ultra high vacuum (UHV) environment. The work is separated into 8 chapters.
Chapter 2 describes the fundamental physics of the NV center in diamond and explains measurement schemes which have been implemented to characterize its spin properties. Furthermore, sensing protocols are reviewed which utilize the NV center for performing ESR and NMR spectroscopy on external

spin systems.
Chapter 3 introduces the experimental setup which has been used for performing NV center based measurements at cryogenic (4.7 K) and UHV ($2 \cdot 10^{-10}$ mbar) conditions. The whole assembly of the existing instrument, as well as the upgradations made to the existing setup, are described in this chapter.
In chapter 4 the first experimental results of this thesis are shown. Thereby, single NV centers are utilized for the characterization of nitroxide spin labeled polyphenols and endofullerene $N@C_{60}$ spins. A detection of less than 10 external spins is demonstrated.
Furthermore, chapter 5 describes the readout of a spin bath by an NV center ensemble. The spin bath is formed by P1 defect centers within the diamond lattice. It is demonstrated that a neighboring NV center ensemble is able to control and manipulate the spin state of the dense P1 center spin bath.
In chapter 6 an NV center ensemble is utilized for the characterization of a superconducting $La_{2-x}Sr_xCuO_4$ (LSCO) thin film sample. Thereby, an all-optical, MW-free measurement scheme is presented which relies on the pure fluorescence yield of the NV center ensemble. This circumvents local heating effects which can originate from applying MW fields. The spatial resolution of the thin film Meissner screening is shown.
Afterwards, chapter 7 describes a statistical study for enhancing and stabilizing the spin properties of shallow implanted NV centers. Thereby, autocorrelation measurements, ODMR signals, and emission spectra are obtained for individual NV centers under different diamond surface treatments including nitrogen, carbon monoxide and water dosing. A slight increase of the NV fluorescence yield is reported by utilizing protection layers with strong dipole moments.
In addition to that, chapter 8 presents other alternative defect centers in diamond to the NV center as quantum sensors. Furthermore, the characterization of a novel defect center in diamond is described in terms of an optical study and high frequency (HF) spectroscopy.
Finally, chapter 9 summarizes the demonstrated experiments and presents an outlook on future investigations for revealing interesting magnetic phenomena in nanomagnetic materials.

2 The Nitrogen Vacancy Center in Diamond

As this thesis is focused on NV center based magnetometry it is crucial to introduce the fundamentals of the NV center in this chapter. Therefore, the first section describes the general properties of the NV center in diamond like the crystallographic structure, the electronic structure and the resulting optical properties. The second section of this chapter is dedicated to measurement protocols which use the NV center as magnetic field sensor. These schemes can be utilized for the realization of ESR and NMR experiments at the nanoscale. In the third section, techniques for the fabrication of NV implanted diamond samples are described. Both, the single NV and the NV center ensemble implantation into a diamond matrix are highlighted. Finally, the last section summarizes this theoretical background around the NV center which will be used throughout the whole thesis for the realization and analysis of NV based experiments.

2.1 General Properties of the NV Center

Diamond is a solid form of carbon in which the atoms are arranged in a crystal structure consisted by a repeating tetrahedral pattern of 4 carbon atoms [33]. At standard temperature and pressure, diamond is a stable compound. However, under extreme conditions (1300 C° [34] and 100 GPa [35]) diamond is able to transform to graphite which is another chemically stable form of carbon. The first discovered diamonds were found in India in the 4^{th} century BC., and until the 18^{th} century, India was thought to be the only source of diamond [36]. In 1725, the first deposit of diamond outside India was found in Brazil [36]. In contrary to the Dark Ages, in which diamonds served as talisman and medical aid, today the most uses of diamonds are as gemstones utilized as adornments or in industry as abrasives for cutting hard materials.
From a scientific point of view, diamond induced a whole research field for its ability to host stable atomic defects with interesting physical properties. One of the most explored atomic defect in diamond is the NV center which forms the basis of this thesis. The most important aspects of the NV center will be presented in this section including structural, electronic and optical properties.

2.1.1 Defect Centers in Diamond

The diamond crystal is defined by carbon atoms arranged in a face-centered cubic (fcc) lattice structure [33] with a lattice constant of $a = 3.57\,\text{Å}$ [37]. To form a crystal, the four valence electrons of

the sp^3-hybridized carbon bond to the neighboring atoms. The resulting chemical bonds give rise to the extraordinary hardness and thermal conductivity ($22\,\mathrm{Wcm^{-1}K^{-1}}$ [38]) of diamond. Due to the large band gap of 5.48 eV [39], diamond is regarded as an electrical insulator and optically transparent material up to ultraviolet (UV) wavelengths. Furthermore, the diamond matrix is able to host incorporated atomic defects which are often denoted as impurities. Therefore, diamonds can be classified according to the amount and type of impurities they contain. The four commonly used classes are the Type Ia, Type Ib, Type IIa and Type IIb diamonds [40, 41]. Type Ia diamonds contain a high amount of nitrogen impurities ($< 3000\,\mathrm{ppm}$) in the form of aggregated nitrogen clusters. Type Ib diamonds also contain nitrogen impurities ($< 500\,\mathrm{ppm}$). However, the impurities appear in the form of paramagnetic single nitrogen defects. In contrary, Type IIa diamonds show a low nitrogen concentration $< 1\,\mathrm{ppm}$. In case of a significant boron content, the diamond is classified as Type IIb. Beside nitrogen and boron defects, diamond can also host phosphorous, hydrogen, nickel, cobalt, chromium, silicon, germanium, tin, lead and sulfur atoms. Typically, the defect centers can be detected by optical spectroscopy or EPR methods.

One of the most studied defect in diamond is the NV center which gives an unique combination of optical and spin properties [42]. Fig. 2.1 shows the structure of this defect within the diamond lattice. The NV center is formed by a substitutional nitrogen atom and a carbon vacancy on an adjacent lattice site, possessing a C_{3v}-symmetry [43]. The symmetry axis is given by the vector between the nitrogen atom and the vacancy.

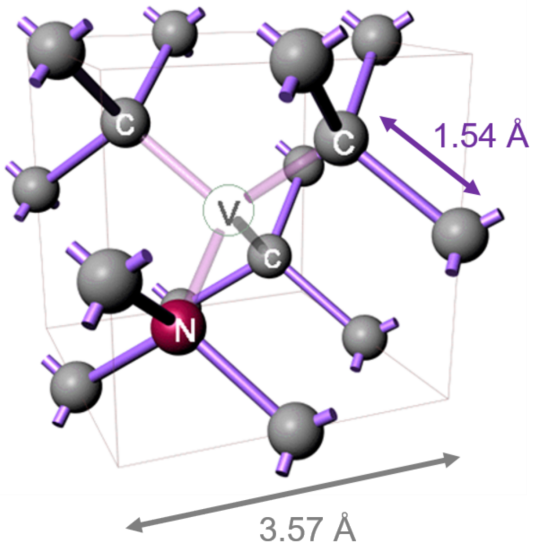

Figure 2.1: Schematic picture of the NV center in the diamond unit cell in which the carbon atoms are represented as gray spheres. The lattice constant of the unit cell is $a = 3.57$ Å and the C-C bond distance is 1.57 Å. A nitrogen atom, depicted as red sphere, substitutes one of the carbon atoms. By removing one of the near-neighbor carbon atoms, a vacancy is created which is depicted in white. The sketch is adapted from [44].

Due to the tetrahedral geometry of the diamond lattice, the NV center can be oriented in four different directions (corresponding to the four equivalent [111] directions of the diamond lattice). The first identification of the NV center was noted in 1965 [45]. Afterwards, several optical and electron spin resonance experiments were performed for understanding its physical properties [42]. These properties will be explained in the following subsections.

2.1.2 The NV Center Hamiltonian

The fundamental for describing physical properties of a quantum system, like a molecule or a localized defect, is the full electronic Hamiltonian. Following the Born-Oppenheimer approximation [46], in which the nuclear motion is fixed and can be separated from the electronic motion, the NV center Hamiltonian can be written as

$$H_{NV}^{full} = \sum_{i} \left(H_{kinetic}^{i} + H_{Coulomb-crystal}^{i} + H_{spin-orbit}^{i} + H_{hyperfine}^{i} \right) + \sum_{i,j} \left(H_{Coulomb-ee}^{i,j} + H_{spin-spin}^{i,j} \right), \tag{2.1}$$

where $H_{kinetic}^{i}$ is the kinetic energy of the i-th electron of the NV electrons, $H_{Coulomb-crystal}^{i}$ describes the Coulomb interaction between the crystal nuclei and the NV electrons, $H_{spin-orbit}^{i}$ is the electronic spin-orbit coupling and $H_{hyperfine}^{i}$ defines the hyperfine interaction between the NV electrons and crystal nuclei [47]. Furthermore, $H_{Coulomb-ee}^{i,j}$ and $H_{spin-spin}^{i,j}$ describe the Coulomb potential and spin-spin potential between the NV electrons [47]. As this Hamiltonian can not be solved exactly, different approaches can be used for partly tackling the equation.

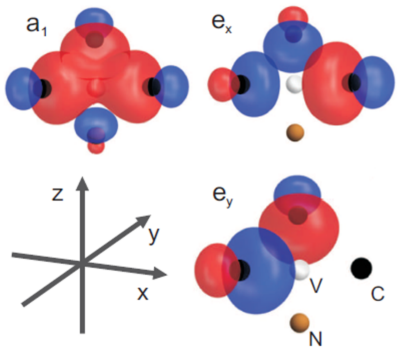

Figure 2.2: Molecular orbitals of the NV center which result from a linear combination of the atomic orbitals of the carbon and nitrogen. The positive parts of the wavefunction are depicted red. Instead, the blue sections show the negative parts of the wavefunction. Especially the a_1 orbital shows the resided electron density close on the vacancy. The figure is adapted from [48].

One method is to use atomic orbitals (AO), which are solutions of the one-electron problem and construct molecular orbitals (MO) as a linear combination of them [43]. These linear combination atomic orbitals (LCAO) are then filled up with electrons. In case of the NV center, the LCAOs are sp^3-hybridized orbitals from the three carbon atoms and one nitrogen atom as depicted in Fig.2.2. The combined orbitals are named corresponding to the representation of the C_{3v} symmetry group a_1, e_x and e_y. Furthermore, group theoretical symmetry approximations, ab initio calculations and experiments can be connected for revealing the full electronic energy spectrum of the NV center [47].
For describing the interaction of the NV center with electromagnetic fields or materials, the Hamiltonian in Eq. 2.1 can even be simplified by the spin Hamiltonian hypothesis [49]. Therefore, only terms containing the electron spin are regarded and thus kinetic and Coulomb interaction terms can be neglected. Furthermore, we can solely focus on the ground state in which the spin-orbit coupling is zero ($L = 0$). Taking these simplifications into account the NV center Hamiltonian from Eq. 2.1 can be written as:

$$H_{NV}^{spin} = H_{ZFS} + H_{HF} + H_{NQ} + H_{EZ} + H_{NZ} + H_{cpl}. \tag{2.2}$$

The zero field splitting (ZFS) due to the spin-spin interaction of the two electrons in the highest occupied molecular orbital is defined by the H_{ZFS} term. The ZFS interaction can be expressed as $\boldsymbol{SDS} = DS_z^2 + E\left(S_x^2 - S_y^2\right)$, where $\boldsymbol{S} = (S_x, S_y, S_z)$ is the electron spin operator and $D = 2.87\,\mathrm{GHz}$ the axial ZFS parameter [42]. The transverse ZFS paramter or strain factor E is, compared to D, very small but highly dependent on lattice distortions. In general, the strain term is negligible and can be considered to $E\left(S_x^2 - S_y^2\right) = 0$.
The second term in Eq. 2.2, H_{HF}, describes the hyperfine interaction with the nitrogen nuclear spin. This can be either an ^{14}N atom with a nuclear spin of $I = 1$ or an ^{15}N isotope with a nuclear spin of $I = 1/2$. The hyperfine term can be expressed as $\boldsymbol{SAI} = A_\parallel S_z I_z + A_\perp\left(S_x I_x + S_y I_y\right)$, in which $\boldsymbol{I} = (I_x, I_y, I_z)$ is the nuclear spin operator and $A_\parallel$ and $A_\perp$ correspond to the hyperfine constants. In case of the ^{14}N atom the hyperfine constants are $A_\parallel = 2.3\,\mathrm{MHz}$ and $A_\perp = 0$ [42]. Instead, for the ^{15}N case, the constants are $A_\parallel = 3.1\,\mathrm{MHz}$ and $A_\perp \approx 2.3 - 3.6\,\mathrm{MHz}$ [42].
Furthermore, H_{NQ} stands for the quadrupole term and is only present for ^{14}N with the nuclear quadrupole interaction of $P = 5.2\,\mathrm{MHz}$ [50]. For the ^{15}N nucleus, this term can be discarded.
The Zeeman interaction of the NV center with an external magnetic field $\boldsymbol{B_0}$ is described with $H_{EZ} = \mu_B \boldsymbol{B_0 g S}/\hbar$. The orbital contributions to the $\boldsymbol{g}$-tensor can be neglected. Therefore, the tensor can be written as $\boldsymbol{g} = g \cdot \mathbb{1}$. Furthermore, if the magnetic field vector $\boldsymbol{B_0}$ is oriented along the NV axis, the Zeeman interaction can be expressed as $H_{EZ} = \gamma B_{NV} S_z$. Thereby, γ is the electron gyromagnetic ratio and can be written as $\gamma = g\mu_B/\hbar$. In general, the Zeeman term is described by the dot product between the magnetic field vector and the spin vector expressed as $H_{EZ} = \gamma|\boldsymbol{B_0}||\boldsymbol{S}|\cos\theta$, including the angle between the two vector orientations θ.
H_{NZ} represents the nuclear Zeeman interaction. In general, this term can be neglected since the nuclear magneton $\mu_N = e\hbar/2m_p$ is orders of magnituded smaller than any other term.

In summary, the NV center spin Hamiltonian can be simplified to [47]:

$$H_{NV}^{spin} = DS_z^2 + A_{\parallel} S_z I_z + \gamma B_{NV} S_z + H_{cpl}. \tag{2.3}$$

Note that the Hamiltonian $H = H'/\hbar$ is written in units of frequency instead of energy. The last term in Eq. 2.3, H_{cpl}, describes the coupling of the NV center spin to magnetic elements in its environment. In this thesis, we focus on the interaction of the NV center with isolated spins which give rise to a dipole-dipole coupling term. This dipole-dipole interaction H_{dip} will be discussed in detail in chapter 4.

2.1.3 Electronic Structure

After we introduced the full NV center Hamiltonian, we can extract its physical properties like the electronic charge or optical behavior. The electronic structure of the NV center can be understood by the electron configuration in the LCAO. Thereby, three different electronic charge states have been theoretically suggested and experimentally verified [43, 51]. The ground states of these are depicted in Fig.2.3.

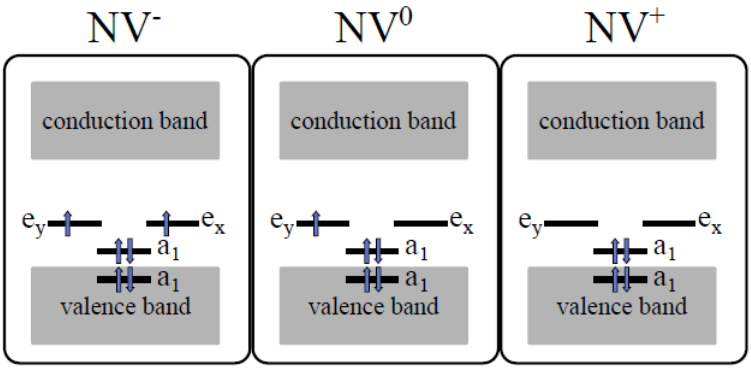

Figure 2.3: NV center charge states and the corresponding energy level diagrams of their ground state. The first a_1 orbital lies within the valence band of diamond. Instead, the other three orbitals lie withing the bandgap. The figure is adapted from [47].

The NV center system consists of three electrons in the dangling sp^3 vacancy orbitals and two additional free electrons in the nitrogen impurity orbitals. This fact gives rise to five electrons that fill up the molecular NV orbitals. The resulting configuration is termed as the neutral NV^0 state and has a total electronic spin quantum number of $S = 1/2$.

Two other electronic states of the NV center are the NV^+ and NV^- states. It is naturally possible for the NV defect to trap or release electrons from or into the energy bands in diamond. Therefore, a positively charged version of the NV center (NV^+) can be realized when the NV defect acts as an electron donor. The total spin quantum number of the NV^+ charge state is $S = 0$.

On the other side, the NV center is able to act as an electron receptor, forming the negatively charged

NV^- state. The additional electron forms an electronic $S = 1$ system. The NV^- center is the most prominent and well-studied defect in diamond, due to its unique spin properties and optical accessibility. All NV center based magnetometry schemes are based on the negatively charged NV center. Also in this thesis, the NV^- forms the nanoscale magnetic field sensor. Therefore, the negative sign will be omitted from now and the general NV expression will stand for the NV^- state.

2.1.4 Optical Properties

For describing the optical properties of the NV center we want to have a closer observation on its ground and excited state. As already discussed in the last subsection, the negatively charged NV center is a $S = 1$ triplet system, formed by the unpaired electrons in the e_x and e_y orbitals. From this $^3A_2$ ground state, one electron can be promoted from the a_1 orbital to the $e_{x,y}$ orbitals, forming the excited ^3E triplet state. Both states are shown in Fig. 2.4(a) for comparison. The resulting energy gap between the NV ground and excited state is 1.945 eV.

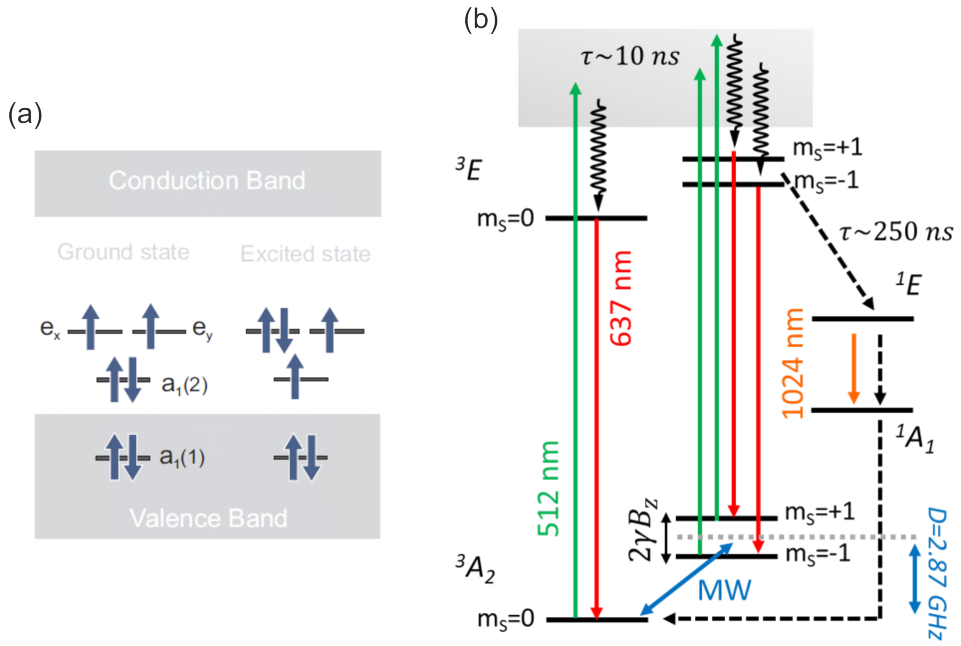

Figure 2.4: Optical Properties of the NV center in diamond. (a) Electronic structure of the NV ground state and the first excited state for comparison. One electron of the $a_1(2)$ orbital can be promoted to one of the $e_{x,y}$ orbitals. The figure is adapted from [37]. (b) Allowed transitions between the ground and excited state which define the optical properties of the NV center. Green laser irradiation promotes the electrons to the excited state. The decay results in a ZPL of 637 nm. Furthermore, a non-radiative decay is possible over metastable singlet states.

A simplified energy level diagram is depicted in Fig. 2.4(b), showing the optical transitions between the $^3A_2$ and ^3E state of the NV center. In general radiative transitions with a zero-phonon line (ZPL)

at 637 nm can be induced [52]. However, only about 4% of the photons are found in the ZPL while the rest stems from relaxation into the phonon sideband [52]. In fact, it has been shown that it is more efficient to excite the NV center off-resonantly with lower wavelengths between 512 nm − 532 nm for increasing its fluorescence counts [53]. Beside these general optical properties, the NV center obtains unique characteristics in its $^3A_2$ ground state. As already discussed, the spin-spin interaction between the two unpaired electrons gives rise to a ZFS of the spin triplets. The resulting splitting between the $m_S = 0$ state and the degenerated $m_S = \pm 1$ states is 2.87 GHz as noted in Fig. 2.4(b). In addition, there is also a non-radiative relaxation channel processed by an inter-system crossing (ISC) [42]. The strong spin state dependence of this ISC leads to the optical spin polarization and optical spin readout of the NV center. For the $m_S = 0$ sublevels the ISC is strongly suppressed. This results in a predominantly radiative decay from the $m_S = 0$ sublevel of the ^3E state into the $m_S = 0$ sublevel of the $^3A_2$ state. Instead, for the $m_S = \pm 1$ states the ISC is comparable to the radiative decay rate. Therefore, the $m_S = \pm 1$ sublevels of the ^3E excited state relax into the singlet system by the ISC. From there, they cross over predominantly to the $m_S = 0$ sublevel of the $^3A_2$ ground state. As the ISC relaxation emits in the wavelength range of 1024 nm, it does not contribute to the 637 nm ZPL emission. Therefore, the fluorescence of the $m_S = 0$ sublevels is higher than for the $m_S = \pm 1$ subsystem. As a result, a fluorescence contrast of up to 30% can be observed [47]. This spin dependent fluorescence mechanism forms the fundamentals of NV center based magnetic resonance spectroscopy which will be discussed in the next section.

2.2 Magnetic Resonance Spectroscopy with NV Centers

After the properties of the NV center have been introduced in the last section, we can now focus on applying the NV center spin system into magnetic resonance spectroscopy methods. The fundamental technique in terms of NV center based magnetomtery are ODMR measurement schemes which combine the NV center fluorescence and the electron spin resonance [54, 55]. Instead of detecting the MW absorption of the NV center, the changes in fluorescence upon spin state manipulations are detected. The spin states are controlled via resonant microwave excitation matching the ZFS of the NV center ground state spin.

2.2.1 ODMR Spectroscopy

The simplest approach for realizing magnetic measurements on NV centers, is the continuous application of microwave and laser radiation for promoting the NV spin into the excited state. Such a measurement scheme is called continuous wave (cw) ODMR spectroscopy and reveals information about the Zeeman interactions on the NV center. As already discussed, the $m_S = 0$ sublevels of the NV center result into a high fluorescence count rate. However, the NV center spin is able to flip from the $m_S = 0$ state to one of the $m_S = \pm 1$ states under resonant microwave excitation. In case of the absence of an external magnetic field, this resonant condition is fulfilled by a microwave frequency

matching the ZFS constant of $D = 2.87\,\text{GHz}$. Thus, sweeping the microwave frequency and matching the resonance condition provide a $m_S = 0 \rightarrow m_S = \pm 1$ transition of the NV spin. As the excited $m_S = \pm 1$ sublevels decay via the non-radiative singlet states, a decrease of the NV fluorescence can be observed. However, cw ODMR spectroscopy methods include several drawbacks due to microwave power broadening and laser frequency fluctuations [47]. Such issues prevent for example the resolution of hyperfine interactions within the NV spin system. Therefore, NV center based spectroscopy methods typically rely on pulsed measurement techniques.

Pulsed ODMR

Pulsed ODMR spectroscopy measurements on NV centers are shown in Fig. 2.5. The basic principle is to polarize the NV spin state via laser radiation and to subsequently manipulate it with microwave excitation. Afterwards, the spin state is read out by an additional laser pulse.

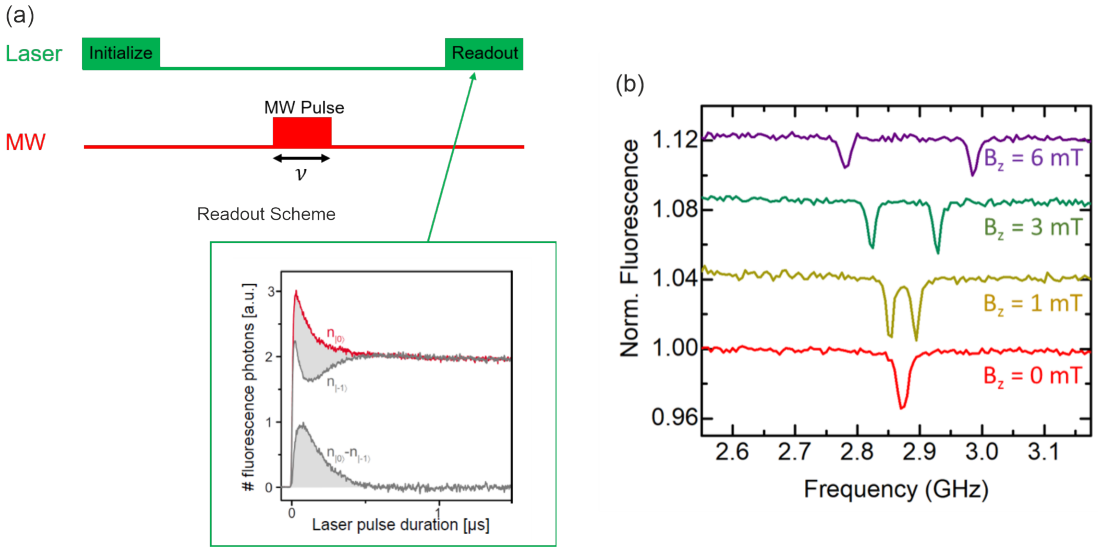

Figure 2.5: ODMR spectroscopy with NV centers in diamond. (a) Pulse scheme for the realization of an ODMR measurement set. The NV defect is initialized with a green laser pulse. After that, a microwave pulse is implemented for exciting the $m_S = 0$ spin substate to one of the $m_S = \pm 1$ sublevels. Therefore, the microwave frequency is swept for matching the ZFS of the ground state spin system. The readout is based on the fluorescence contrast between the $m_S = 0$ state and $m_S = \pm 1$ states. The readout sketch is adapted from [37]. (b) ODMR spectra of an NV center ensemble for different applied magnetic fields. Without magnetic field a resonant line at 2.87 GHz can be observed, indicating the ZFS of the groundstate. By applying a magnetic field, a splitting of the line can be investigated due to the removed degeneracy of the $m_S = \pm 1$ spin sublevels.

As the NV spin is manipulated in absence of the laser illumination, the measurement technique is more robust against laser frequency instabilities. Furthermore, the NV center spin can be coherently manipulated due to the microwave pulses. Such a coherent spin manipulation can be achieved by adjusting

the microwave pulses in a certain length in time. Than, the microwave pulse length corresponds to a certain phase of the quantum spin state. Typically, the resulting fluorescence photons need to be detected in the first $\approx 400\,\text{ns}$ after the onset of the read out laser pulse for evaluating the spin state with high fidelity [37]. This fact is connected with the timescale of the ^3E singlet level lifetime of about $\tau = 250\,\text{ns}$ [56]. Very interesting is the magnetic field dependent behavior of the fluorescence drop in the resulting ODMR spectra which are depicted in Fig. 2.5(b). In presence of an external magnetic field, the $m_S = \pm 1$ degeneracy is removed following a Zeeman splitting. As already described, the Zeeman term can be written as $H_{EZ} = \gamma B_{NV} S_z$ when the magnetic field is aligned parallel to the NV axis. For this case, the full frequency splitting in an NV center ODMR spectrum can be written as

$$\Delta f = 2\gamma B_{NV}, \tag{2.4}$$

in which the gyromagnetic ratio γ is $28\,\text{MHz/mT}$ for the NV center spin [42]. In case of a misaligned field, the frequency splitting depends on the angle between the magnetic orientation and the NV center axis. Also this has already been discussed and can be represented as the dot product in the frequency splitting $\Delta f = 2\gamma B_0 \cos\theta$. By rising the external magnetic field, an increase of the frequency splitting in the ODMR spectrum can be observed. Thus, ODMR spectroscopy is a very fundamental tool for measuring a static magnetic field experienced by the NV center spin system. Therefore, all other measurement schemes which will be discussed in this thesis build up on pulsed ODMR spectroscopy methods.

Rabi Oscillations

Based on the fluorescence drop in the ODMR spectrum, we are able obtain the resonance frequency for the realization of $m_S = 0 \rightarrow m_S = -1$ or $m_S = 0 \rightarrow m_S = +1$ transitions. Instead of applying a microwave frequency sweep, we can now fix the excitation frequency and sweep the duration length of the pulse [57]. Such a measurement scheme is depicted in Fig. 2.6(a) and results in a oscillatory behavior called Rabi oscillation as shown in Fig. 2.6 [58]. The oscillation reveals the coherent manipulation of the NV center spin state between the $m_S = 0$ and $m_S = -1$ sublevels or $m_S = 0$ and $m_S = +1$ sublevels, depending on the fixed frequency of the applied microwave pulse. Typically, the behavior of the spin state within the Rabi oscillation can be depicted by the Bloch sphere representation in which the two Eigenstates $|0\rangle$ and $|1\rangle$ (or $|-1\rangle$) lie at the poles of the sphere. Note that, $|0\rangle$ and $|\pm 1\rangle$ represent the Eigenstates of the $m_S = 0$ and $m_S = \pm 1$ sublevels, respectively. Any superposition of the Eigenstates $|\Psi\rangle = \alpha\,|0\rangle + \beta\,|1\rangle$ can be created and visualized as a vector between the poles of the Bloch sphere. Especially the coherent superposition states

$$|\sigma\rangle = \frac{1}{\sqrt{2}}\left(|0\rangle + e^{i\phi}\,|1\rangle\right), \tag{2.5}$$

which are points on the equator of the Bloch sphere, are of great importance for spin sensing. Here, ϕ is the complex phase and determines the direction along the x and y axis of the Bloch sphere.

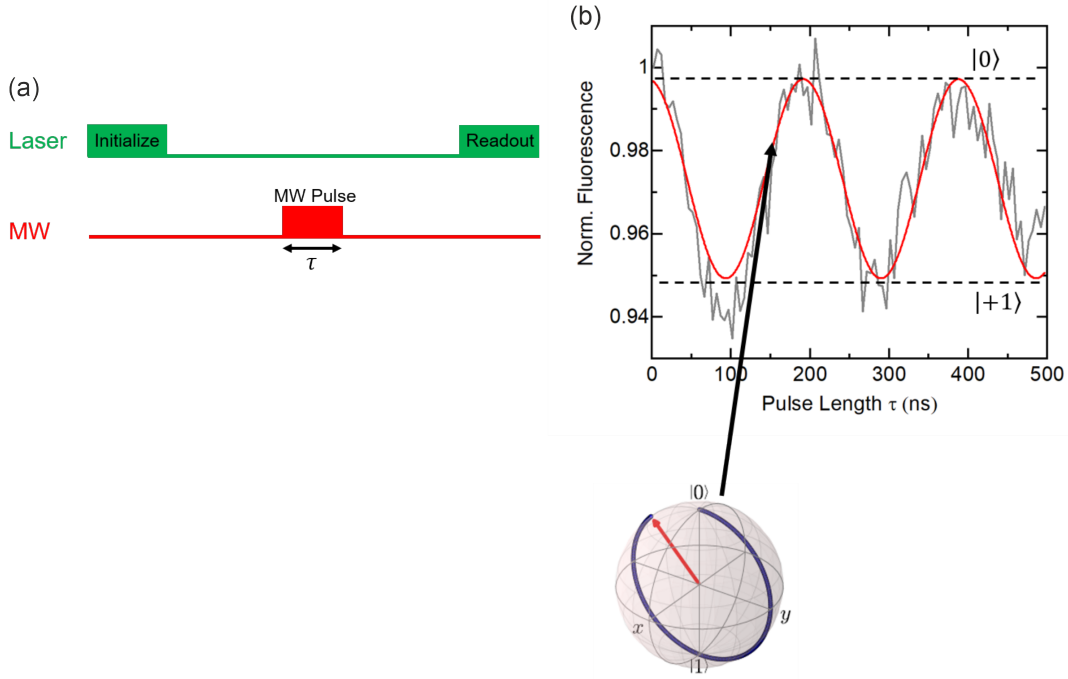

Figure 2.6: Rabi oscillation of the NV center spin. (a) Pulse sequence for driving a Rabi oscillation of the NV center spin. The microwave resonance frequency is fixed at 2.87 GHz and varied in the duration time τ. (b) Resulting Rabi oscillation between the $|0\rangle$ and $|+1\rangle$ states of the NV center ground state spin. The different emitted fluorescence of the spin sublevels makes the detection of the oscillation possible. Each point of the graph can be interpreted as a spin orientation on the Bloch sphere. The Bloch sphere sketch is adapted from [47].

With this, the Rabi oscillation measurement reveals information about the duration length of a microwave pulse for exciting a certain electron spin transition. The two most relevant outcomes are the $\pi/2$ and π pulse parameters. The $\pi/2$ parameter denotes the resonant microwave pulse duration for achieving a transition from the $|0\rangle$ state to the coherent super position state $|\sigma\rangle = \frac{1}{\sqrt{2}}\left(|0\rangle + e^{i\phi}|1\rangle\right)$ [37]. Instead, the π pulse denotes the excitation duration for obtaining a full spin transition $|0\rangle \rightarrow |1\rangle$ [37]. It is worth to mention that the pulse durations depend on the applied MW power. Usually, an increase of the MW power leads to a higher frequency of the Rabi oscillation which can be interpreted as a decrease of the $\pi/2$ and π pulse lengths. The revelation of the resonance frequencies from ODMR spectroscopy and the pulse duration lengths from the Rabi oscillation is the key for advanced measurement protocols which will be discussed in the next subsection.

2.2.2 Lifetime Measurements

So far we focused on the absorption properties of the spin states of the NV center. We have described the microwave excitation within different sublevels and the laser illumination for promoting the ground state to an excited state. However, the temporal spin dynamics involving the lifetime of the NV center spin has not been discussed. As the spin lifetime yields information about the environment of the NV center it is crucial to introduce its behavior. The most important quantities are the longitudinal spin life time (T_1), the transverse relaxation time (T_2^*) and the coherence decay time (T_2).

Longitudinal Spin State Lifetime T_1

The longitudinal spin life time T_1 describes the duration of the preservation of a quantum state before it decays into its thermal equilibrium population due interactions with the environment [59]. In case of the NV center, several processes within the diamond lattice can contribute to such spin decays. Typically, lattice phonons can act as relaxation channels for spin polarization [47]. Furthermore, inelastic scattering processes or dipolar coupling with paramagnetic impurities can provide a random energy for spin flips [47]. Therefore, measuring the T_1 time could give estimates about paramagnetic contributions close to the NV center. A measurement scheme which is able to probe the T_1 relaxation is shown in Fig. 2.7(a) [60].

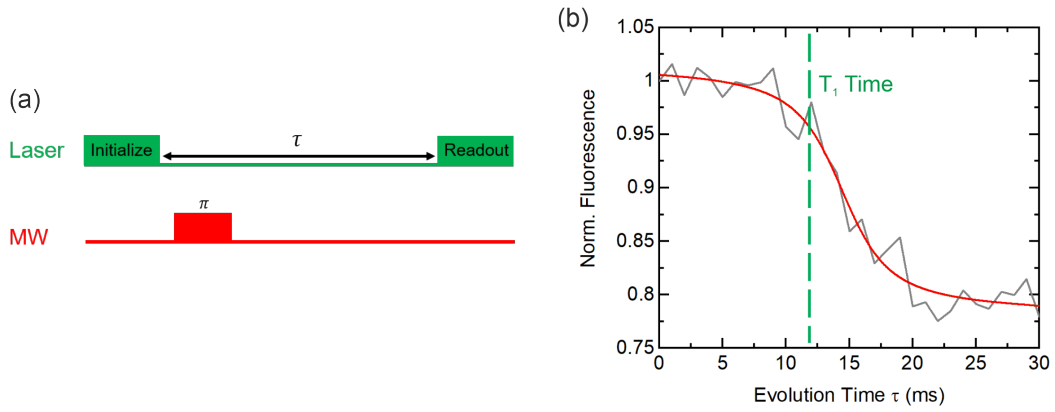

Figure 2.7: Longitudinal spin state lifetime of an individual NV center. (a) Pulse sequence for revealing the T_1 time of the NV center consisting of two laser pulses for initialization and readout. An additional resonant microwave π pulse can be utilized for spin substate control. (b) Resulting fluorescence behavior of the NV center under the described pulse sequence without an additional π pulse (readout of the $m_S = 0$ state) at ambient conditions. The T_1 time of the investigated system can be estimated with an exponential approach to ≈ 12 ms.

The scheme consists of two variably delayed laser pulses. The first laser pulse is used for initialization of the NV center spin. For controlling the spin state, a resonant π pulse can be implemented at the beginning of the waiting time. The fluorescence read out is achieved by the second laser pulse and

measures the remaining population in the corresponding spin state after a time τ. A typical T_1 measurement result is shown in Fig. 2.7(b) and can be described by an exponential fit. In that particular case, the measurement has been performed without a π pulse. Therefore, the $m_S = 0$ has been read out. As a result, the fluorescence level decreases as the $|0\rangle$ state corresponds to the brightest NV center level and the spin decays into an optically darker mixed ground state. Single NV centers are able reach T_1 times in the ms range [60].

Transverse Relaxation Time T_2^*

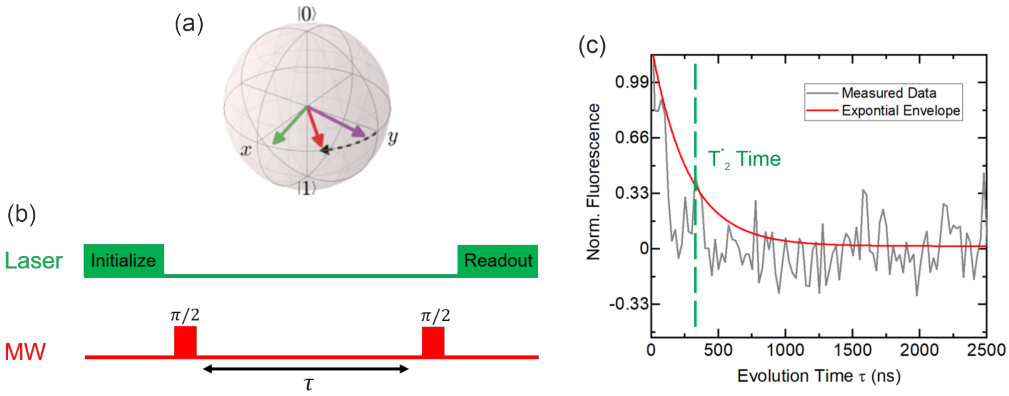

Figure 2.8: Measurement set for estimating the T_2^* time of a single NV center. (a) Phase pick-up of the NV center spin represented in the Block sphere picture. The spin can be excited to the superposition state with a resonant $\pi/2$ pulse. In the coherent state, the spin is able to evolve in the xy-plane of the Bloch sphere due to magnetic noise in the NV environment. The Bloch sphere sketch is adapted from [47]. (b) FID pulse scheme for measuring the T_2 $*$ time. The first $\pi/2$ pulse creates the superposition state. This state is evolved in time. After a certain duration τ, the second $\pi/2$ pulse converts the phase pick-up to a population difference which is read out by a laser pulse. (c) Measurement on a single NV center at ambient conditions. A decrease of the NV fluorescence is observed due to the decoherence of the superposition state. A T_2^* time of $\approx$ 300 ns can be estimated by an exponential envelope function.

Besides investigating the timescale in which the population remains in a certain spin substate of the NV center, there are also other time quantities which are more sensitive towards external magnetic fields. Therefore, we have to evaluate the quantum coherence from Eq. 2.5 in a more detailed manner. Commonly, the phase ϕ is time dependent ($\phi(\tau)$) and is affected by magnetic fields. The resulting magnetic field dependent phase pick-up is

$$\phi(\tau) = \gamma \int_0^\tau b_{eff}(t)\, dt. \tag{2.6}$$

b_{eff} is the sum over all sources of magnetic fields which tune the position of the phase and can be written as

$$b_{eff}(t) = \frac{1}{\gamma} \sum_{i}^{n} \omega_0 - \omega_i(t), \tag{2.7}$$

where ω denotes the specific frequencies of the external magnetic fields. The influence of the magnetic field on the phase pick-up is sketched in Fig.2.8(a). Typical sources for such phase pick-ups are nuclear spins or paramagnetic species close to the NV center which are able to generate a magnetic field oscillating at their characteristic Larmor frequency. The coherent behavior of the NV center can be probed with a free induction decay (FID) measurement sequence (also called Ramsey pulse sequence) as shown in Fig. 2.8(b) [61], [62]. The scheme consist of two resonant $\pi/2$ pulses with a variable time delay of τ. The first $\pi/2$ creates the superposition state $|\sigma\rangle$ of Eq. 2.5. In the beginning, the phase is zero. However, during the variable delay time a phase is picked up due to the multiple magnetic field sources in the NV environment. The second $\pi/2$ converts the phase pick-up to a population difference which is readable by a laser pulse. The phase information is transferred to an actual fluorescence signal of the NV center. A corresponding measurement data set is shown in Fig. 2.8(c) which shows the decay of the fluorescence contrast over time caused by random magnetic field noise including the decoherence of the phase. The resulting decay envelope of the Ramsey measurement has a timescale in the order of few ns for NV centers and is termed as T_2^* time [63]. One of the main sources for decoherence mechanisms in diamond are nuclear spins from ^{13}C carbon atoms [47].

Coherence Time T_2

Typically, the NV center T_2^* timescale of few ns is too short for realizing reasonable sensing protocols [47]. Therefore, it is crucial to extend the coherence of the superposition state $|\sigma\rangle$. A powerful method for achieving this goal is to refocus the spin dephasing mechanism by applying an additional π pulse into the Ramsey measurement scheme. As a result the magnetic interactions are inverted, leading to a sign change of the phase pick-up, and a spin echo will occur when the acquired phase has been canceled. In its simplest form the technique is referred as Hahn echo measurement [64]. The pulse sequence is depicted in Fig. 2.9(a). At the half evolution period, a refocusing π pulse is added which corresponds to a flip of the time evolved spin state by 180° around the x-axis. Mathematically, this can be interpreted as a sign change and the accumulated phase during the second free evolution period can then be written as

$$\phi(\tau) = \gamma \int_0^{\tau/2} b_{eff}(t)\, dt - \gamma \int_{\tau/2}^{\tau} b_{eff}(t)\, dt. \tag{2.8}$$

Consequently, the phase pick-up is canceled if both evolution periods are equal in time length. Thus, the original superposition state $|\sigma\rangle$ will be restored. At the end of the sequence, a final $\pi/2$ pulse converts the remaining phase difference to a population difference. A typical Hahn echo measurement

on a single NV is shown in Fig. 2.9(b). Again, a decay envelope of the decoherence can be observed. However, the resulting coherence decay constant, termed as T_2, is larger than the T_2^* time gained from the Ramsey measurement scheme. For single NV centers the T_2 time can reach up to 100 μs [65]. In practice, the Hahn Echo pulse scheme is slightly modified for removing artifacts from the measured curves. This is achieved, by implementing simultaneously a $3\pi/2$ pulse to the final $\pi/2$ pulse. With this, the coherent state is once flipped to the bright $|0\rangle$ state and on the following pulse sequence to one of the dark $|\pm1\rangle$ states. A contrast curve is created by substracting the two resulting data sets of pure fluorescence. This pulse sequence will be discussed more detailed in chapter 4. Such refocusing pulse schemes build up the fundamental principle of NV center based spin sensing.

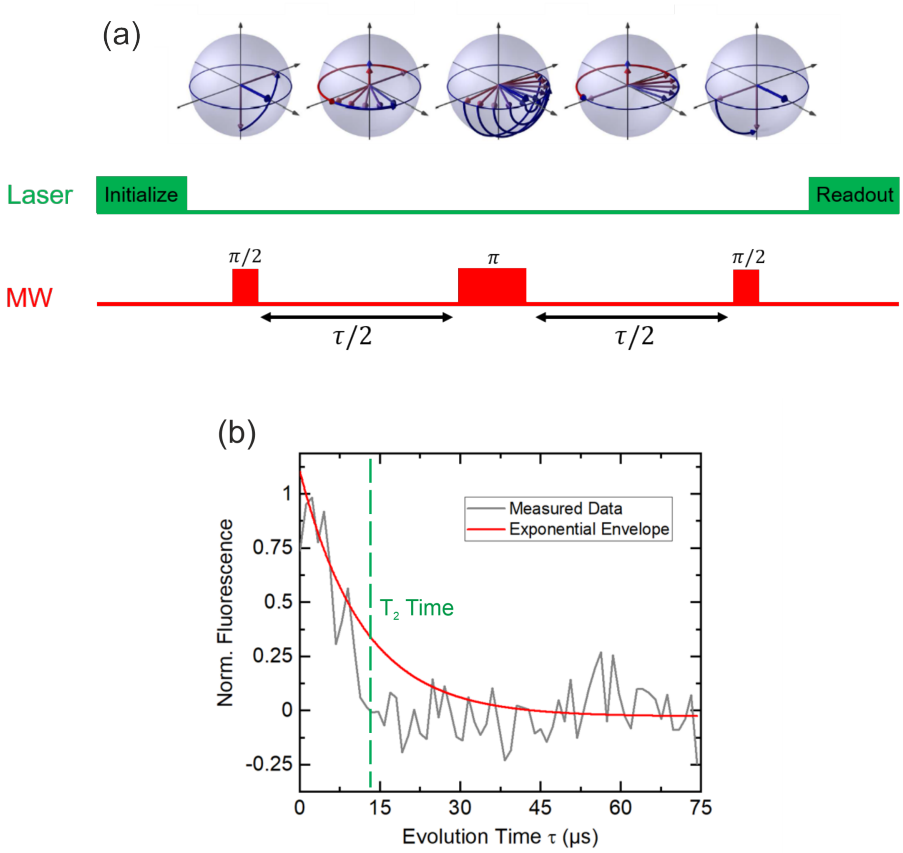

Figure 2.9: Hahn Echo measurement set on an NV center. (a) Pulse sequence and corresponding spin evolution depicted in the Bloch sphere. The first $\pi/2$ pulse creates the superposition state of the NV center spin. After a certain time amount $\tau/2$, the spin evolves and picks up a phase which is dependent on the magnetic noise. A resonant π pulse flips the evolved spin by 180°. After the second free evolution period the phase pick-up is canceled. The final $\pi/2$ pulse converts the remaining phase difference to a population difference. (b) Resulting data from a Hahn Echo Measurement on a single NV center at ambient conditions. Like in the FID measurement scheme, a decrease of the fluorescence can be observed due to the decoherence of the superposition state. However, the exponential envelope yields a higher time constant of 14 μs that is denoted as coherence time T_2.

2.2.3 Spectral Filter Functions

After we described experimental measurement schemes on manipulating the NV center spin state, we want to assign theoretical expressions of how the NV is influenced by the magnetic noise in its environment under these pulse schemes. This issue can be mathematically defined by the spectral filter function $\mathcal{F}(\omega)$ which is a specific formula for each applied sequence. In general, the filter function denotes a selective transmittance of a wavelength specific signal. Together with the spectral density $\delta(\omega)$ of the environmental magnetic noise, the sequence specific filter function $\mathcal{F}(\omega)$ forms the environmental relaxation rate Γ_{env} of the spin system [47]:

$$\Gamma_{env} \propto \int_0^\infty \mathcal{F}(\omega)\delta(\omega)\, dt. \tag{2.9}$$

Therefore, the filter function is an important expression for evaluating the influence of different frequency regimes on the NV center lifetime.

Filter Function for a T_1 Measurement

The spectral filter function for a T_1 measurement pulse sequence can be formed by utilizing Fermi's golden rule which describes the transition rate between different energy Eigenstates in a quantum system [66]. As a result, $\mathcal{F}(\omega)$ consists of two Lorentzians at the frequencies $\omega_\pm = D \pm \gamma B_z$ [47]:

$$\mathcal{F}_{T_1}(\omega) = \frac{\nu}{\pi\nu^2 + (\omega - \omega_+)^2} + \frac{\nu}{\pi\nu^2 + (\omega - \omega_-)^2}. \tag{2.10}$$

The linewidth $\Delta\nu$ of the Lorentzians are dependent on the T_2^* related inhomogeneous broadening $\Delta\nu = 1/T_2^*$. As the ZFS parameter D is in the GHz regime, magnetic noise need to fluctuate at GHz frequencies for having an influence on the T_1 time of the NV center.

Filter Function for an FID Measurement

The filter function for an FID pulse sequence is defined by an oscillation magnetic field with a characteristical frequency ω [47]:

$$\mathcal{F}_{FID}(\omega) = \left(\frac{\sin\frac{\omega\tau}{2}}{\frac{\omega}{2}} \right)^2. \tag{2.11}$$

The sensitivity of the FID sequence is limited by the dephasing T_2^* time of the investigated system.

Filter Function for a Hahn Measurement

In case of a Hahn measurement, the sign of the magnetic field sensitivity is switched by an implemented π pulse within the sequence. Therefore, the sensitivity function alternates between $+1$ and -1 in the

time domain. By applying a Fourier transformation to this alternating square function, the spectral filter function can be derived to [47]

$$\mathcal{F}_{Hahn} = \left(\frac{\sin^2 \frac{\omega\tau}{4}}{\frac{\omega}{4}} \right)^2 . \tag{2.12}$$

As the Han echo pulse sequence decouples the NV center from its environment, the measurement scheme is only sensitive to a narrow frequency range. This spectral regime can be narrowed further by applying multiple decoupling pulses which benefits NV center based NMR measurements and will be discussed in subsection 2.2.5.

2.2.4 ESR Measurement Schemes with NV Centers

One of the most demonstrated applications of NV center sensors is the investigation of single molecular systems with ESR spectroscopy. In general, ESR measurements are widely used in various scientific fields for the detection of free radicals and the identification of paramagnetic complexes revealing their electronic structures [67]. The origin of the ESR signal of a sample can be explained by the Zeeman effect. An unpaired electron in an observable system obtains a spin quantum number of $s = 1/2$ and with this the magnetic components $m_s = \pm 1/2$. In presence of an external magnetic field B_0, a separation of these two magnetic components occurs due to the Zeeman effect with an energy gap of

$$\Delta E = g_e \mu_B B_0, \tag{2.13}$$

in which g_e is the free electron g-factor and μ_B the Bohr magneton. Furthermore, the electron spin can flip by absorbing or emitting photons with an energy value of $\Delta E = h\nu$. Therefore, Eq. 2.13 can be written as

$$h\nu = g_e \mu_B B_0, \tag{2.14}$$

forming the fundamental EPR equation [67]. The mathematical term shows that an external magnetic field is able to induce a precession of the electron magnetic moment (called Larmor precession) which can be investigated in form of absorption measurements. However, the major limitation of such ESR techniques is the huge number of spins ($\approx 10^{12}$ [68]) which are necessary for the measurements, preventing the investigations on nanometer sized samples or single molecules. One way to solve this problem is to implement quantum sensors as the NV center into ESR measurement schemes. In fact, NV center based ESR experiments have been successfully achieved by using double electron electron resonance (DEER) measurement protocols.

DEER Spectroscopy

DEER measurements are able to identify couplings between electronic spins [69]. The resulting coupling strength contains information about the distance between the measured spins and with this the structure of molecules can be studied [70].
NV center based DEER spectroscopy can be realized by implementing an additional π pulse within the NV Hahn echo measurement scheme which we discussed in Fig. 2.9 [71].

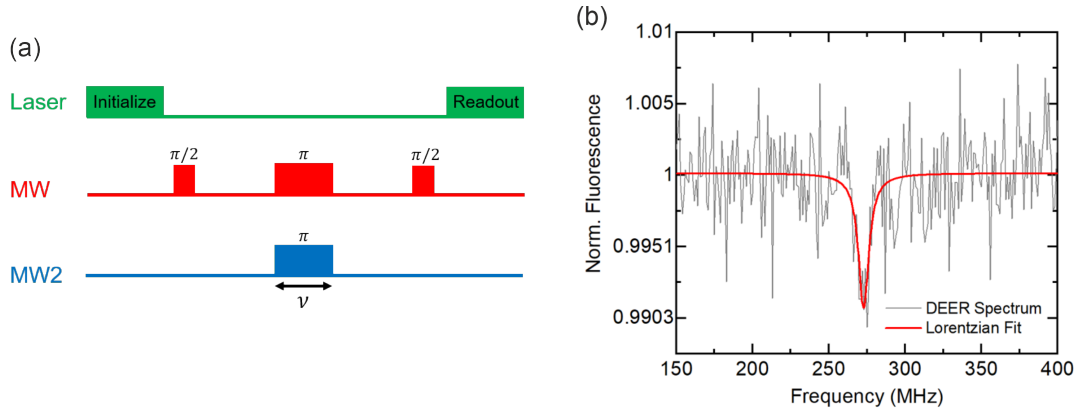

Figure 2.10: DEER measurement set on an NV center realizing ESR spectroscopy. (a) Pulse scheme of the DEER measurement technique consisting of an additional π pulse compared to the Hahn Echo sequence. The additional π pulse is varied in frequency and excites an external spin in the NV environment. Furthermore, it is crucial to time the pulse in the second evolution period of the NV center superposition spin. A resonant excitation of the external spin results into a drop of the recorded NV center fluorescence. (b) DEER spectrum measured by a single NV center at ambient conditions. The sharp fluorescence drop indicates a spin signal of electrons in the NV environment.

The modified pulse sequence is shown in Fig. 2.10(a). The frequency of the additional π pulse is swept in a certain frequency range for matching the resonance condition of the external spin. In resonance, the external spin reverses its S_z component which also inverts the sign of the NV center phase pickup. By timing the additional π pulse right after the NV spin π pulse, the new magnetic field dependent phase pick-up is

$$\phi(\tau) = \gamma \int_0^{\tau/2} b_{eff}(t)\, dt - \gamma \int_{\tau/2}^{\tau} b_{eff,2}(t)\, dt. \tag{2.15}$$

As $b_{eff} = -b_{eff,2}$, the phase pick-up is not canceled to zero like in the scenario of the pure Hahn echo measurement on the NV. Therefore, a change in the NV center fluorescence can be observed by matching the resonance frequency of the investigated spin as shown in Fig. 2.10(b). This phase accumulation is solely permitted for the resonant excitation of the external spins. Depending on the applied magnetic field strength, the resonance frequency of an external electron spin is in the order of

$\approx$ 100 MHz. Based on the DEER pulse sequence, the coupling between the NV center spin and an external spin can be investigated more detailed in form of DEER Double Quantum Transition (DQT), DEER Rabi and DEER Delay measurements. However, these sequences will be discussed in chapter 4, in which we utilize a single NV center for sensing individual molecules.

2.2.5 NMR Measurement Schemes with NV Centers

Besides ESR measurements, also NMR experiments have a great impact in modern science. The magnetic field dependent Larmor precession of the atomic nuclei is extensively used in medicine for magnetic resonance imaging [67]. However, also here the number of nuclear spins has to be huge for gaining a measurable signal. Again, the NV center can be utilized as nanoscale quantum sensor. Nevertheless, more complicated dynamical decoupling schemes have to be implemented by inserting more refocusing π pulses [72]. The reason for this are the different characteristics between electron and nuclear spins. Typically, the electron larmor precession is on the order of $\approx 100\,\text{MHz} - 9000\,\text{MHz}$ [70] leading to a realtively high ΔE which can be measured. Instead, nuclear spin frequencies are on the order of $\approx 200\,\text{kHz} - 1.2\,\text{MHz}$ [72] resulting in a significantly decreased ΔE. Therefore, the NV center as sensor has to be decoupled from its magnetic environment in a more robust manner.

XY8-N Dynamical Decoupling

A frequently used concept, for increasing the robustness of the NV center is the XY8-N pulse scheme, which is depicted in Fig. 2.11(a) [73]. The measurement sequence consists of $N = 8n$ refocusing pulses which are able to cancel out pulse errors in a very efficient way. Furthermore, the symmetrical shape of the sequence decouples the NV against all possible phase noise. Depending on the total number of microwave pulses, the sequence acts as a filter function for a certain frequency ν:

$$\mathcal{F}_{XY8-N} = 2\left(\frac{\sin\frac{\nu\tau}{2}}{\frac{\nu}{2}}\frac{\sin^2\frac{\nu\tau}{4N}}{\cos\frac{\nu\tau}{2N}}\right)^2. \tag{2.16}$$

The sensitivity can be described the width $\Delta\nu$ of the filter function:

$$\Delta\nu = \frac{1}{N\tau}. \tag{2.17}$$

A typical result of this technique is shown in Fig. 2.11(b) which presents the NMR signal of carbon and hydrogen atoms measured with an NV center. However, a drawback of this technique is the limitation of the frequency resolution ($\approx 50 - 100\,\text{kHz}$ [73]) as the measurement protocol is limited by the NV center coherence time [74]. As a consequence, important quantities in the field of NMR can not be observed with the NV center sensor like the chemical shift or the J-coupling which obtain a spectral width on the order of 10 Hz [75].

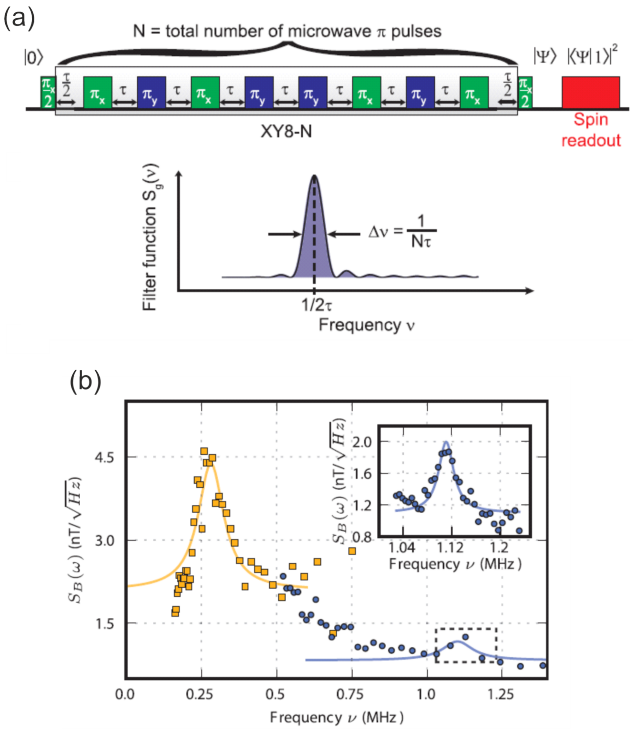

Figure 2.11: NMR spectroscopy with NV centers in diamond. (a) Microwave pulse scheme of the XY8-N sequence. The number and timing of the π pulse train defines the frequency selection and resolution of the measurement technique. (b) Resulting NMR spectrum of the carbon and hydrogen signals recorded by an NV center. The different atomic species of the sample are clearly observable. The resolution of the spectral features is on the order of $50 - 100\,\mathrm{kHz}$.

Quantum Heterodyne Detection Scheme

An ultrahigh resolution sensing scheme based on the NV center can be realized with the Quantum Heterodyne Detection (Qdyne) by combining several XY8 sequences as shown in Fig. 2.12(a) [76]. In this pulse scheme, the NV center fluorescence is measured after each XY8 sequence as a function of time. Each sampling instance consists of an initialization, a phase measurement and a read out of the NV center [76]. The time trace of the measured fluorescence is able to reconstruct the wave form of the magnetic field experienced by the NV center. With a Fast Fourier Transformation (FFT), the time trace can be converted to a frequency scale revealing the Larmor precession of the observed nuclei. Fig. 2.12(b) shows a Qdyne spectrum of a 1 MHz test signal with a resolution of about 5 Hz. The test signal was generated by a cw radio frequency (RF) running through a copper coil which has been positioned close to the NV center diamond sample.
Modifications of the Qdyne measurement scheme have achieved a frequency resolution of even 600 μHz [74].

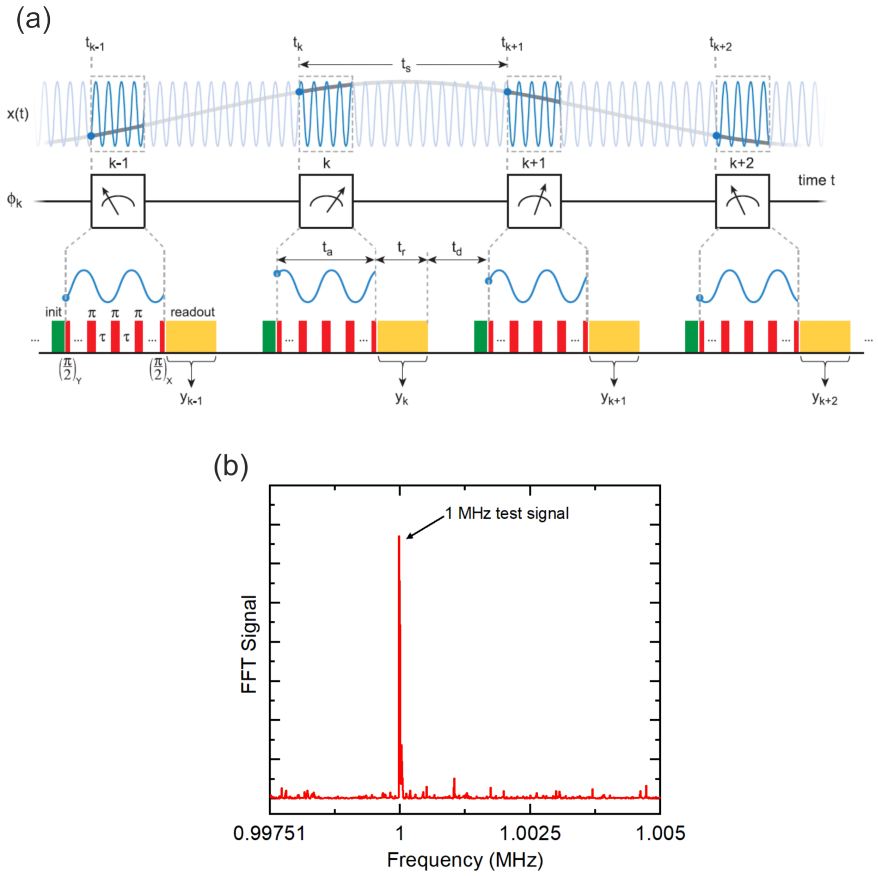

Figure 2.12: NMR spectroscopy using a single NV center based on the Qdyne measurement scheme. (a) Pulse sequence of the Qdyne measurement protocol. A train of XY8-N sequences are attached to each other. After each readout pulse, the fluorescence is measured and recorded as a function of time. The resulting fluorescence time trace can be converted with a FFT into the frequency domain containing spectral information of the magnetic noise in the NV environment. The figure is adapted from [76]. (b) Resulting Qdyne spectrum of a 1 MHZ test signal measured with a single NV center at ambient conditions. The frequency resolution is in the 5 Hz regime.

2.3 NV Center Implantation into Diamond Samples

After we described the theoretical background of the NV center in diamond and its usage in nanoscale magnetometry, we want to briefly introduce fabrication processes which are able to implant NV centers into a diamond sample. However, before we focus on that, the artificial diamond growth is explained.

2.3.1 Artificial Diamonds

Diamonds can nowadays be readily produced artificially in two different approaches. The first fabrication technique relies on the application of high pressure and high temperature (HPHT) to graphite or

another form of carbon for a certain amount of time, forming a diamond sample [77]. An advantage of this technique is the large quantity of diamonds which can be produced. However, the resulting samples contain often a poor quality with many uncontrolled impurities.
Instead, clean diamonds can be created using chemical vapor deposition (CVD) [78]. In this fabrication method, a high quality carbon seed crystal is exposed to a high temperature gas of hydrocarbons which are able to bond to the carbon surface dangling bonds.
NV centers can be created after the diamond fabrication by the implantation of nitrogen ions into the diamond matrix and subsequent annealing by the incorporation of nitrogen during the CVD growth.

2.3.2 Single NV Center Implantation

Typically for single NV membranes, the nitrogen ions are implanted after the diamond sample fabrication. This approach allows the control of the NV center depth which is defined by the kinetic energy of the implanted ions [79]. The vacancies are formed by a subsequent annealing step at temperatures above 650 °C. However, the ion straggling creates a large amount of crystal faults which can influence the NV center spin properties.

2.3.3 NV Center Ensemble Implantation

Also NV ensembles can be fabricated by the direct nitrogen ion implantation. Therefore, the ion beam diameter has to be enlarged for increasing the nitrogen concentration withing the carbon crystal. However, ensembles of NV defects can also be created by the incorporation of nitrogen atoms during the diamond growth process. This fabrication technique is called δ-doping [80]. Afterwards, irradiation with high energy particles or subsequent annealing steps have to be involved for creating vacancies. This approach creates less unwanted crystal defects which influence the NV spin properties. However, a precise location of the incorporated nitrogen atoms is not possible.
Nevertheless both fabrication methods have the ability to create shallow NV centers few nanometers below the diamond surface which is the key for sensing applications.

2.3.4 Diamond Nano-Structuring

The key quantity for NV center based magnetometry is the fluorescence of the defects. Therefore, it is crucial to obtain NV centers with high emission rates. In case of NV center ensembles, a high countrate is achieved by the density of the NV cluster. Regions on the diamond sample with an high NV center density exhibit an intense emission. However, individual NV centers usually obtain a low number of collected photons [81]. For increasing the single NV emission, nanofabrication processes can be performed. An efficient attempt, is the implementation of nanopillars on the diamond surface in which single NV centers are located. The pillar structure acts as an waveguide for the NV emission and increases the collection number of photons [81]. Typically, nanopillars can be fabricated by etching the diamond surface with O_2/O_2+CF_4 plasma [81]. Before of that, the diamond has to be coated with a

plasma resistive mask which defines the pillar geometry. Afterwards, the NV centers can be implanted within the pillars. A corresponding SEM image is shown in Fig. 2.13.

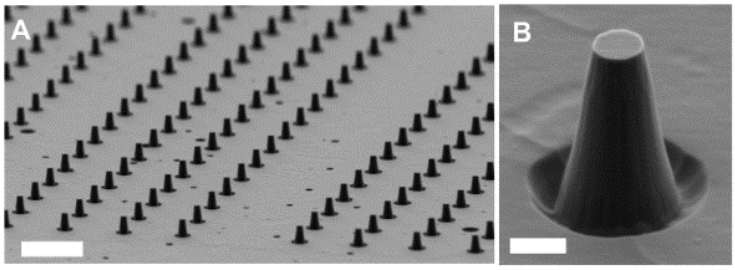

Figure 2.13: SEM image of a nano-structured diamond surface. Due to specific plasma resistive masks, nanopillars can be formed after etching the diamond surface. Afterwards, single NV center can implanted within the pillars. The nanostructure acts as a waveguide for the NV fluorescence and increases the resulting collection photons. The figure is adapted from [81].

2.4 Summary

In this chapter we introduced the NV center in diamond as a nanoscale magnetic field sensor. A detailed overview of the NV properties was given by evaluating its Hamiltonian resulting into the electronic structure and the optical behavior. Most importantly it was shown that resonant microwave pulses can excite different sublevels within the NV center spin ground state. Furthermore, the fluorescence shows a spin dependence which can be used for sensing applications. The simplest measurement scheme can be realized by ODMR spectroscopy revealing static magnetic fields experienced by the NV center. In addition, more sophisticated pulse sequences like DEER schemes can be implemented for the detection of single electrons in the NV environment. NMR spectroscopy can be achieved by modifying the DEER pulse sequences towards dynamical decoupling schemes which is sensitive for nuclei Larmor frequencies. Finally, a short description was given regarding different fabrication processes of NV implanted diamond samples. Artificial diamonds can be created by HPHT or CVD growth methods. Thereby, NV defects can be inserted after the diamond fabrication by nitrogen ion implantation or during the CVD growth process in form of δ-doping. For both techniques, the vacancies are formed via heat exposure or high energy irradiation. The theoretical background of this chapter is crucial for a better understanding of the experimental results of this thesis.

3 Experimental Setup

This chapter presents the experimental setup which was utilized for performing the measurements of this thesis. The first section describes an overview of the setup which consists of a cryostat connected to an UHV chamber. The structure of the cryo-UHV instrument is explained in a more detailed manner in the second section by highlighting the load lock, preparation and main chamber. Furthermore, the measurement head which is positioned within the cryostat is described. The third section is dedicated to the microwave pulse generation which is crucial for realizing spin manipulation measurements on the NV center. In the last section, we focus on the optical elements of the instrument. These are of great importance as the NV center has to be initialized and read out optically. It is also worth to mention that a detailed technical description of the setup can be found in the works [37] and [82] which fully focus on the instrument.

3.1 Overview Scheme of the Setup

The architecture of the experimental setup consists of four different subsystems, namely the confocal microscope, the microwave generation, the vacuum chamber and the cryogenic system. A simplified diagram of the setup is illustrated in Fig. 3.1(a).
For promoting the NV center ground state into its excited level, a pulsed laser with a frequency of 512 nm is used. The NV center emission is collected with avalanche photo diodes (APDs) which are characterized by an efficiency maximum at around 650 nm. These parts, form together with refocusing lenses, a dichroic mirror and a 75 μm pinhole the confocal microscope which is able to image the NV center fluorescence. Apart from the objective which is positioned inside the cryostat, the whole optical setup is assembled outside the vacuum system.
Besides optically exciting the NV center, the spin states have to be manipulated with microwave and RF fields. Therefore, HF sources are coupled into a waveguide on the sample via impedance matched transmission lines within the cryostat. The control of the pulse sequences is achieved by a Field Programmable Gate Array (FPGA) which is able to trigger the switches between the laser and microwave signals [47].

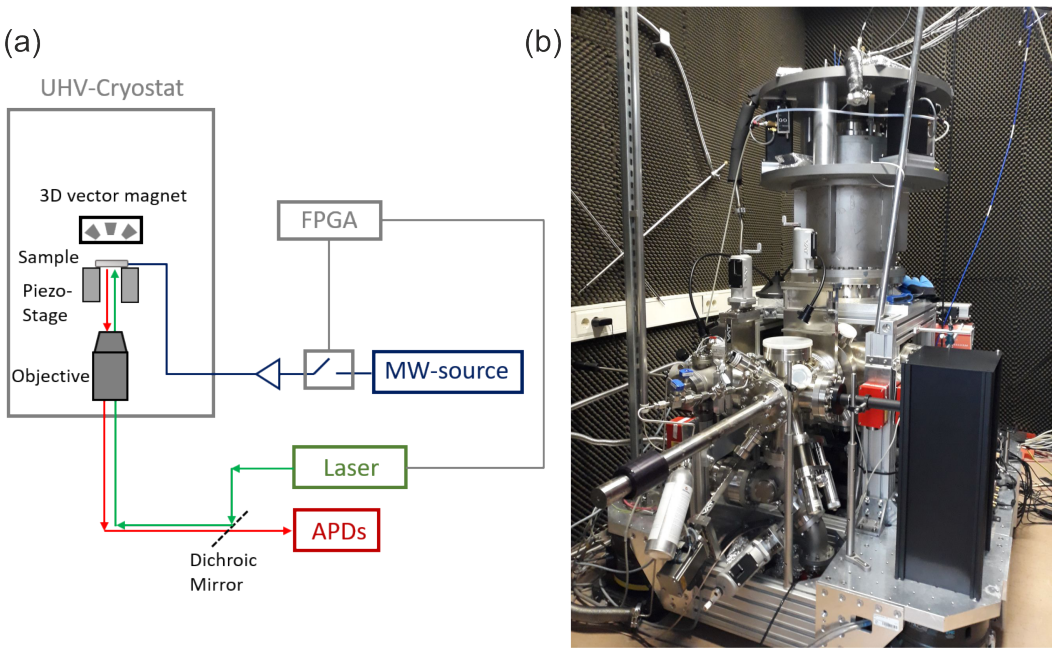

Figure 3.1: Overview of the experimental setup. (a) Simplified sketch of the setup which consists of an UHV-cryostat. The NV-diamond sample is located inside the instrument. Below the UHV chamber, an optical confocal microscope is assembled for exciting and reading out the NV center. Furthermore, a microwave line is implemented for NV center spin manipulation. (b) Photograph of the experimental setup.

For realizing measurements in a cryogenic-UHV environment, a helium bath cryostat is attached to a vacuum chamber. The cryostat is able to reach a base temperature of 4.7 K. Furthermore, different pumps are able to create an UHV environment with a pressure of about $2 \cdot 10^{-10}$ mbar. The vacuum chamber obtains several ports with optically accessible windows in the visible wavelength range for ensuring a transmission of the 512 nm laser light and the 637 nm − 750 nm NV emission. These subsystems will be explained in a more detailed way in the following sections.

3.2 The Cryo-UHV Setup

After giving a general overview of the experimental setup, we want to focus on the cryo-UHV part of the instrument in this section. In the first part, the vacuum setup is described which consists of three separated vacuum chambers named load lock, preparation and main chamber. After that, the cryostat structure and the measurement head are explained.

3.2.1 Load Lock and Preparation Chamber

The first two parts of the UHV setup are the load lock and the preparation chambers. Both are separated from each other by a gate valve. The load lock chamber provides the first step for introducing a sample

from an ambient environment into an UHV system. Typically, a load lock chamber ensures a vacuum of about $2 \cdot 10^{-8}$ mbar.

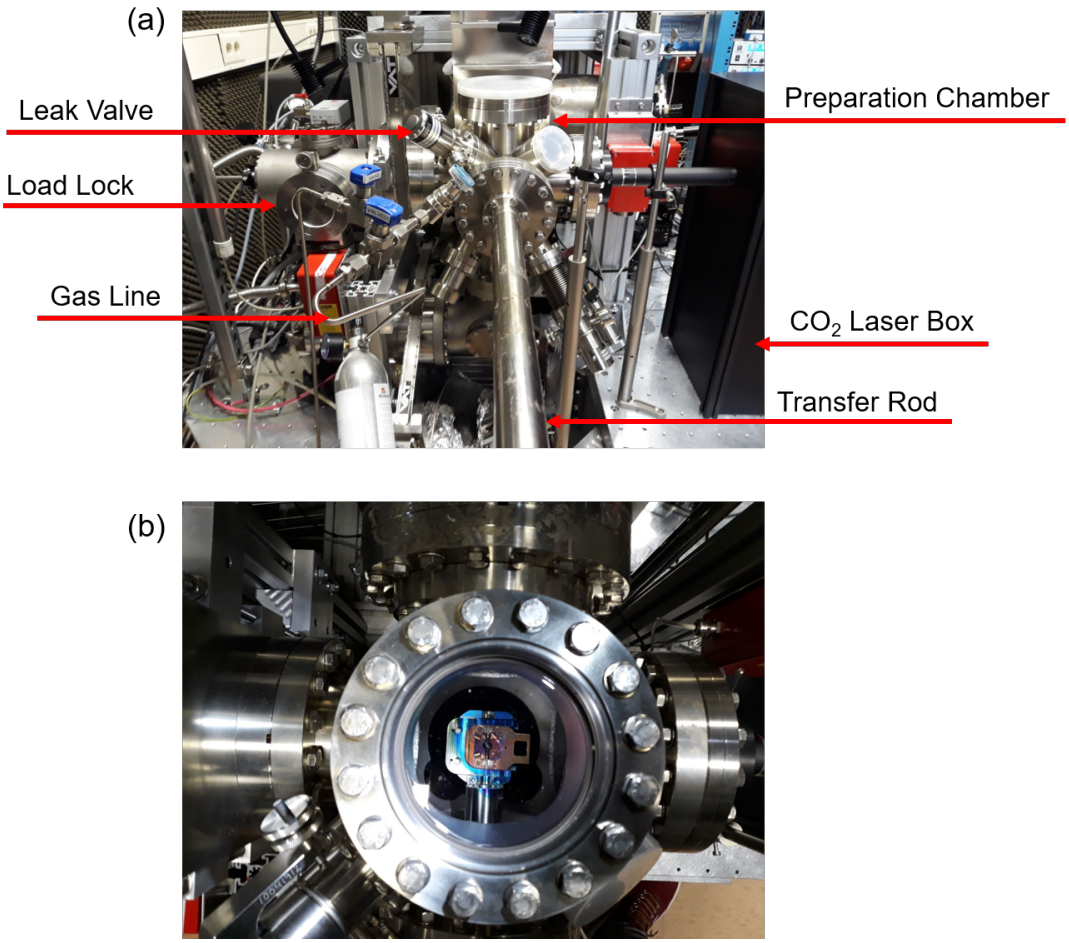

Figure 3.2: Overview of the preparation chamber. (a) Side view photograph of the preparation chamber on which a gas line is connected to it for surface treatments. A leak valve is used for controlling the gas flow. Furthermore, a CO_2 laser is guided to the chamber for cleaning the diamond surface. (b) Top view photograph of the preparation chamber. The sampleholder is stably located into a manufactured mount which is screwed into the magnetic transfer rod.

Before a sample can be introduced into such a chamber, the load lock system has to be vented with pure nitrogen gas. After that, the sample can be mounted on the magnetically coupled linear transfer rod [37]. A membrane pump is used for generating a pre-vacuum state of few mbar. When this is achieved, the system including the sample can be evacuated via turbomolecular pumps down to 10^{-8} mbar [83]. The pressure is read out by cold cathode gauges. The advantage of implementing a load lock chamber into the vacuum system is the in situ sample exchange, as the preparation and main chambers are not vented during the sample transfer.

When the load lock pressure is in the range of 10^{-8} mbar, the sample can be transferred into the

preparation chamber. For this, the gate valve can be opened and the magnetic transfer rod can be introduced into the preparation chamber. Also this system contains a magnetic transfer rod with a stage which is able to hold the introduced sample. In contrary to the load lock, the preparation chamber is equipped with a turbomolecular pump and an ion getter vacuum pump [84]. This pumping combination is able to realize an UHV environment on the order of 10^{-10} mbar. Furthermore, the preparation chamber enables the deposition of different gas molecules upon the diamond surface for modifying the NV center spin properties. Therefore, a leak valve is attached to one port of the chamber. The corresponding gas bottles are connected with steal pipes to the leak valve for ensuring a controllable introduction of the gas. Additionally, a ZnSe vacuum viewport is attached on the preparation chamber which transmits infrared light (IR). A high power 10 μm IR laser beam can be introduced through this port for cleaning the diamond surface. The top and side views of the preparation chamber are shown in Fig. 3.2 highlighting the explained features. After the surface treatment of the diamond, the sample holder can be transferred to the main chamber.

3.2.2 Main Chamber and Cryostat

The main chamber is separated by a gate valve from the preparation chamber and is equipped with a turbomolecular pump and an ion getter vacuum pump. Typically, the readout pressure is at about $2 \cdot 10^{-10}$ mbar confirming the UHV environment in which the sample is located. The central part of the main chamber is the attached cryostat which consist of two stages with distinct base temperatures as shown in Fig. 3.3. The outer part (depicted in green) forms the liquid nitrogen reservoir with a volume of 30 liters and acts as a protection jacket for the 10 liters helium reservoir (inner part depicted in blue) [37]. Due to the extremely low boiling temperatures of the used gases, the nitrogen reservoir reaches a base temperature of 77 K and the helium stage obtains a temperature of 4.7 K [85, 86]. For controlling thermal fluctuations, the cryostat is fabricated from stainless steel which is a poor thermal conductor [37]. In addition, the UHV surrounding decreases thermal conduction from the environment. Therefore, the heat transfer is dominated by thermal radiation and conduction between the electrical wires which are connected to the measurement head. The thermal radiation is suppressed by the implementation of two gold-plated copper shields which are mounted around the measurement head. A shutter mechanism enables the sample transfer and view ports provide optical access. The heat transfer from the electrical connections is minimized by the chosen wire materials. Bronze wires with a thermal conductivity of 1.6 $\frac{\mathrm{W}}{\mathrm{m \cdot K}}$ have been inserted for controlling the piezo motor of the sample stage [37, 87]. Furthermore, the microwave transmission lines are formed by semi-rigid coaxial cables with stainless steel shielding obtaining a thermal conductivity of 2 $\frac{\mu\mathrm{W}}{\mathrm{m \cdot K}}$ [37, 88]. The resulting liquid helium consumption is of about 2.4 liters/day by inserting the described thermal shielding and optimized wiring. However, laser and high frequency applications during extensive measurement sets increase the helium consumption to almost 4 liters/day.

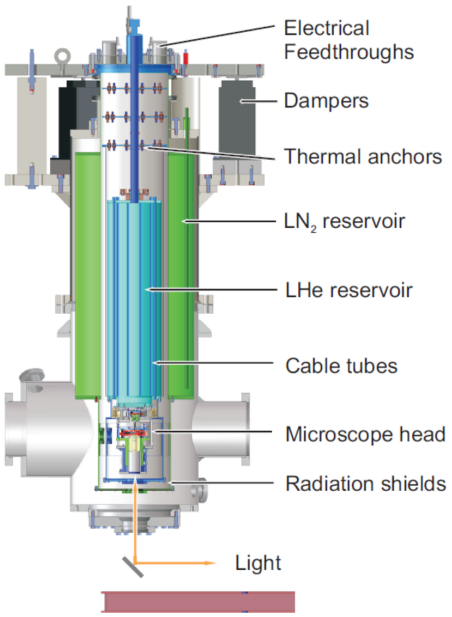

Figure 3.3: Cross-section of the cryostat. The instrument consists of two reservoirs which operate at 77 K (green part) and 4.7 K (blue part). The operation temperature is achieved by filling the reservoirs with liquid nitrogen and helium. The sketch is adapted from [37].

3.2.3 Measurement Head

In the last part of this section, we want to focus on the measurement head as this element combines the key components for the investigation of NV centers, namely the optical and high frequency excitation. Therefore, it is crucial to provide an optical access to the mounted sample with a high collection efficiency. This can be realized by utilizing high numerical aperture (NA) objectives consisting of sophisticated multi-lens systems for correcting chromatic aberration [89]. However, the performance of such lens systems are highly affected by the ultra cold environment as the refractive index and the dispersion of the glasses depends on the temperature [37]. Furthermore, the glass curvature contracts at low temperatures resulting in a change of the lens radius and thickness [37]. Therefore it is crucial to implement a cryogenic compatible high NA objective [90].
Another important part of the measurement head is the home-built sample stage which consists of piezo actuators for three dimensional sample positioning, a mounting fixture for the sample holder and the high frequency transmission lines. The transmission for the MW excitation is crucial for precise NV center spin manipulation. This is achieved by coupling the waveguides of the sample holder with the MW transmission lines of the measurement head by spring-loaded contacts. These connections are assembled by sub-miniature-P (SMP) connectors, a glass-ceramic body and beryllium copper (CuBe) springs on which halfed copper (Cu) spheres are glued. Finally, the spring contacts are interconnected by flexible coaxial cables to the cryostat mount plate from where semi-rigid transmission lines go to the cryostat top plate. A sketch of the measurement head and a corresponding photograph is shown

in Fig. 3.4.

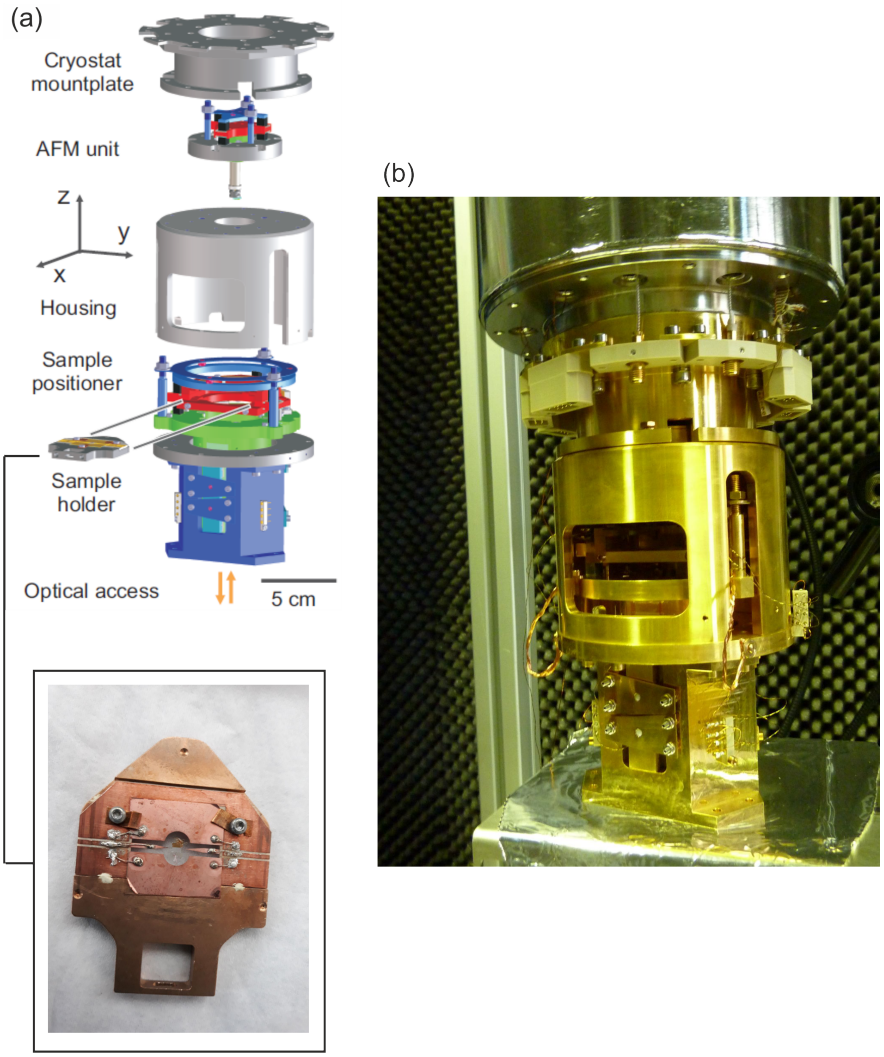

Figure 3.4: Overview of the measurement head. (a) Sketch of the measurement head assembly illustrating the sample mount (in red) and the piezo stage (in blue) adapted from [82]. The inset shows a photograph of the sample holder. The copper waveguides are crucial for the MW transmission. (b) Photograph of the measurement head fixed to the cryostat cold plate.

In addition, an electromagnet is installed inside the measurement head for controlling the orientation and the magnitude of the magnetic field. This is of great importance for performing magnetometry measurements at various field strengths on the NV center. Furthermore, the alignment of the field orientation is crucial as NV centers can be oriented in one of four possible crystal directions (as discussed in chapter 2). A misaligned magnetic field orientation upon the NV axis can quench the NV fluorescence [91]. Therefore a vector magnet design consisting of three mutually perpendicular oriented coils is implemented above the sample holder mount as depicted in Fig. 3.5. Each coils consists of a 5000

loops copper wire shielded by 0.01 mm of a polymer insulation [47]. Additionally, a ferromagnetic core is introduced to the coils for increasing the magnetic field strength. The resulting field amplitude and orientation is controlled by a current source which addresses the coils separately. A magnetic field strength of up to 20 mT can be reached with this configuration [47].

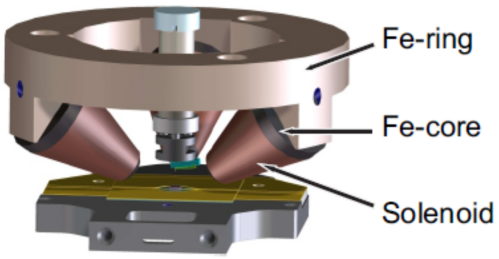

Figure 3.5: 3D sketch of the vectormagnet mounted above the sampleholder position. The magnet consists of three coils oriented perperdicular to each other for the generation of a magnetic field in x, y and z direction. The sketch is adapted from [37].

3.3 Microwave Generation

In the last section we discussed the HF transmission lines within the cryostat which are connected to the sample stage. However, most of the NV spin state manipulation experiments rely on MW pulse sequences and not on cw measurement schemes. Therefore, it is also important to describe the HF setup which creates precise MW pulses. An overview of the HF lines outside the cryo-UHV setup is illustrated in Fig. 3.6.

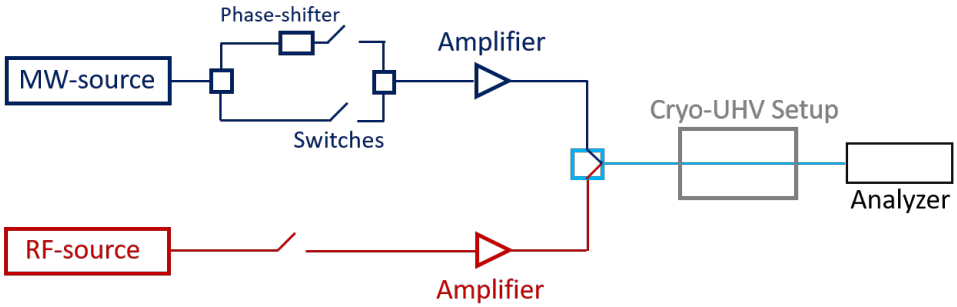

Figure 3.6: Schematic overview of the high frequency setup which is formed by a microwave line for NV center spin manipulation and a radio frequency line for external spin manipulation. For generating pulse schemes, switches are implemented which are controlled by the FPGA. The HF lines go through the measurement head within the cryo-UHV setup and end in a network analyzer device for displaying the transmission.

The first part of the setup consists of two separated signal generators (Vaunix Lab Brick LSG-402 and SMIQ03B) for creating cw high frequency signals. The Vaunix Lab Brick LSG-402 operates in the

frequency range between 1 GHz − 4 GHz and is used for NV center spin manipulation. In contrast, the SMIQ03B generates radio frequencies in the range of 300 kHz − 3.3 GHz and is employed for exciting external electron spins. Both generators have a maximum output power of about +10 dBm. As the signals experience loses through the long cryostat wiring, the output of the generators has to be increased by using two amplifiers which are able to deliver up to +42 dBm. The corresponding pulses are created from the cw signals by fast switches which are coordinated by the FPGA. Additionally, a phase shifter is implemented for requiring microwave pulses with a 90° phase shift relative to each other. This is beneficial for sophisticated pulse schemes to compensate pulse errors. Finally, the signals are coupled into the transmission line of the cryostat with coaxial cables. As already discussed in the last section, the pulses are guided through waveguides on the sample holder. Furthermore, a thin copper wire with a diameter of ≈ 20 μm is bonded across the diamond sample, for guiding the MW signal in close proximity above the NV centers. At the end, the MW transmission can be read out by a network analyzer.

3.4 Optical Setup

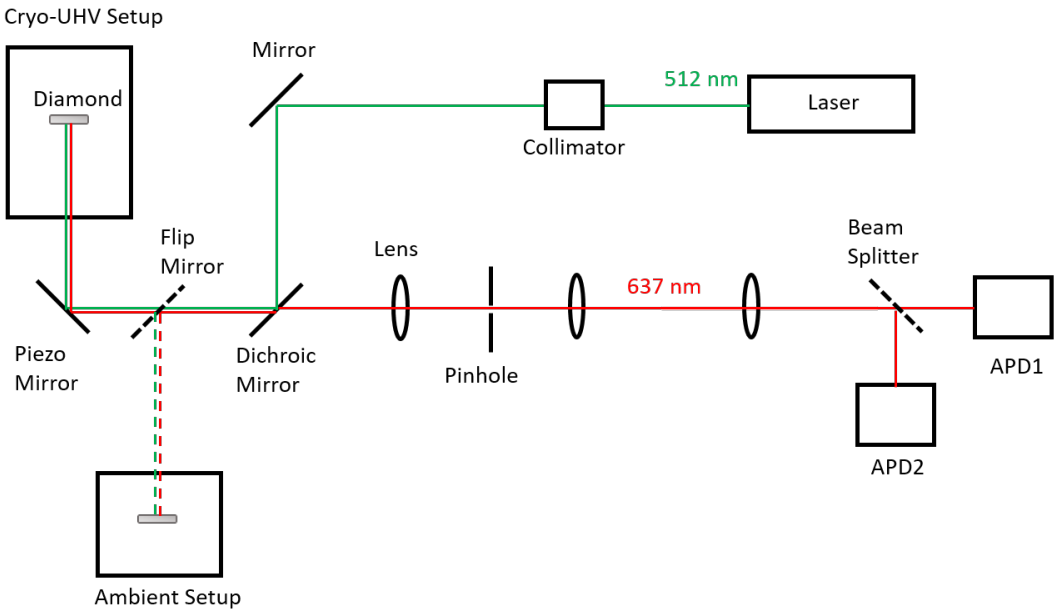

Figure 3.7: Illustration of an NV center specified confocal microscope. A 512 nm pulsed laser is used for optically exciting the NV center. The red NV center emission is collected by two APDs which are mounted in a Hanbury Brown and Twiss geometry. A flip mirror is implemented for performing measurements in the cryo-UHV environment or at an ambient stage.

The following section of this chapter describes the optical setup for imaging NV centers and initializing and reading out their spin state. The optics is assembled in form of a confocal microscopy setup optimized for NV center characterization [92]. Therefore, a pulsed laser (Toptica iBeam-Smart-515)

with a wavelength of about 512 nm is implemented which is used for excitation, initialization and readout of the NV center. The laser light is coupled into a 3 μm single mode optical fiber for ensuring a Gaussian TEM_{00} mode of the beam. At the end of the fiber, the laser light is out coupled and guided into an inversely mounted objective for achieving a collimated beam. Afterwards, the green beam is routed by dielectric silver mirrors to a dichroic beam splitter which is a crucial part of the optical setup. The beam splitter reflects the 512 nm photons of the laser to a 45° tilted piezo-based scanning mirror (PI S-330.8) which guides the beam into the measurement head within the cryo-UHV instrument. The cryogenic compatible objective (attocube LT-APO/VIS/0.82) focuses the excitation light on the diamond surface and collects the red NV emission ranging from 637 nm − 750 nm. The red photons are guided to the dichroic beam splitter which transmits these wavelengths. After that, the light is focused through a 75 μm pinhole which is responsible for the resolution of the resulting image. Finally, the NV fluorescence is recorded by two APDs mounted in a Hanbury Brown and Twiss geometry for performing autocorrelation measurements. As single NV centers acts as single photon sources, autocorrelation measurements are a reliable method for pre-characterizing certain NV centers. The generation of a 2D confocal image is achieved by scanning the laser beam across the diamond surface with the piezo mirror which obtains a scanning range of 60 μm x 60 μm.

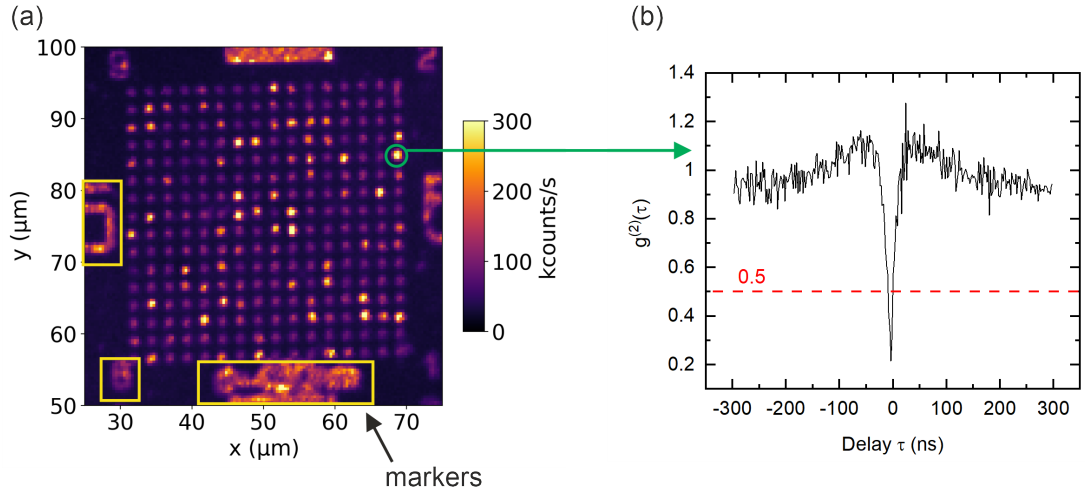

Figure 3.8: Performance of the ambient stage. (a) Confocal image of an NV diamond sample in which the NV centers are implanted in diamond nanopillars. The fluorescence is recorded by scanning the stage in a range of 50 μm x 50 μm. As a result, the defect centers can be observed as bright spots in the image. (b) Autocorrelation measurement of a single NV center. The photon antibunching dip is below 0.5 which is an indicator for the observation of a single photon emitter.

In addition, a flip mirror is implemented between the dichroic beam splitter and the piezo mirror for guiding the green laser beam to an ambient condition stage. This instrument consists of a piezo stage (Piezosystem Jena T-404-01D) with a scan range of 150 μm x 150 μm on which a copy of the sample holder design is mounted. The stage can be used for NV center pre-characterization in an ambient

environment before transferring the diamond sample into the cryo-UHV setup.

Imaging Performance of the Ambient Stage

The imaging performance of the ambient confocal setup is illustrated in Fig. 3.8(a) by presenting an exemplary NV implanted pillar membrane. The fabrication and benefits of such diamond samples are explained in 2.3.4. The piezo stage is scanned in a range of 50 μm x 50 μm. With this, the laser beam is focused on different positions on the diamond sample within the set range. The scanning resolution can be set by the measuring software. The NV centers can be observed as bright round-shaped features. Furthermore, Fig. 3.8(b) shows an autocorrelation measurement of a certain NV center. It can be observed that the photon antibunching point of the correlation curve $g^{(2)}$ is below 0.5 which is a characteristic of a single photon source [93]. This is a reliable method for confirming the investigation of a single NV center which is crucial for realizing ESR spectroscopy on individual molecules.

Imaging Performance of the Cryo-UHV Stage

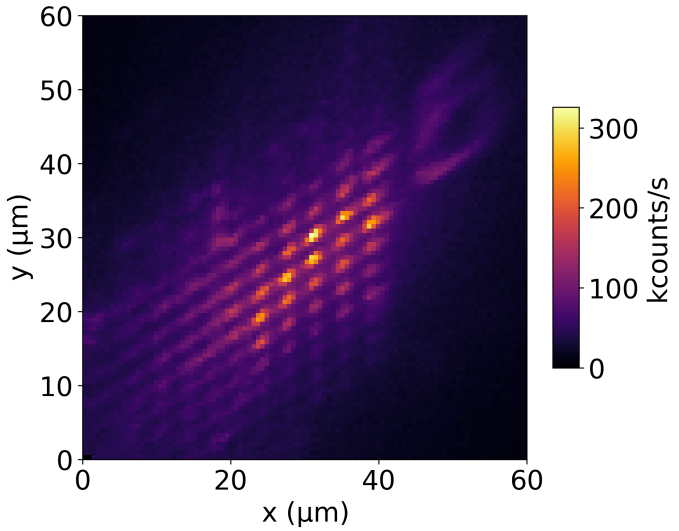

Figure 3.9: Imaging performance within the cryo-UHV environment. The scanning range of the piezo mirror is 60 μm x 60 μm. Also here, the NV centers can be observed as bright spots due to the sample geometry. However, an elliptical shape of the emitters can be investigated. This is explained by the optics within the UHV chamber which does not consist of refocusing lenses.

A full range 60 μm x 60 μm confocal image of the NV fluorescence is shown in Fig. 3.9. Also here the NV centers are shown as bright spots. However, it is evident that the quality of the measured emission varies through the whole image. The most reliable data is recorded in the center of the image in which the laser spot is focused. The reason for the non-uniform laser focus can be explained by the

distance between the piezo mirror and the cryogenic high NA objective which is about 30 cm. Within this distance, no focusing lenses are mounted inside the UHV chamber. Therefore, the divergent laser beam is not refocused before passing through the objective and the confocal images obtain an overall elliptical shape.

3.5 Implemented Improvements in the System Performance

It is evident that the construction of an experimental instrument is a long-term project. For instance, the setup described in this chapter has been developed among three generations of Ph.D. students. Therefore, this section briefly highlights advancements on the experimental setup performed within the scope of this thesis.

Re-Assembly of Microwave Contacts

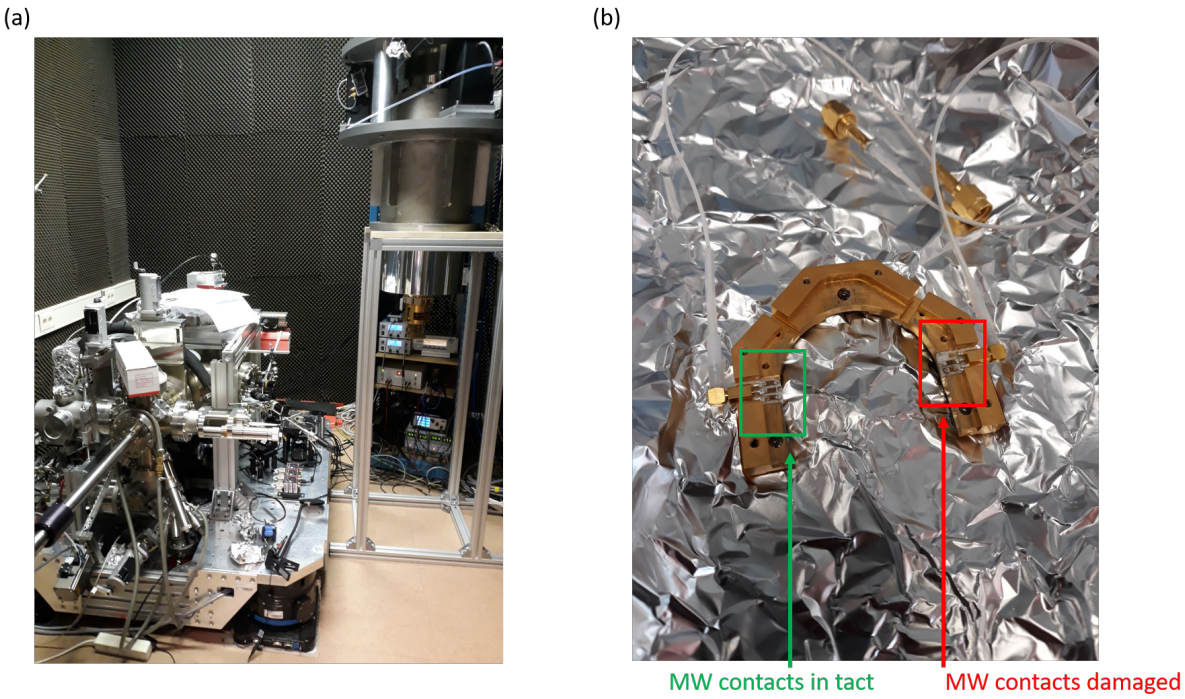

Figure 3.10: Disassembly of the experimental instrument. (a) In order to access the measurement head, the cryostat has to be separated from the UHV main chamber. (b) Microwave connections at the sample stage for ensuring high MW transmissions on the sampleholder waveguides. The green square illustrates the spring contacts on which the Cu spheres are attached. Instead the red square shows the damaged springs on which the Cu spheres have been disassembled.

In 3.2.2 we described the transmission lines within the measurement head. Thereby, the applied MW radiation is coupled to the waveguides of the sample holder through spring-loaded connections on

which halfed Cu spheres are glued for creating the contact. The advantage of such a scheme is the realization of high transmission MW connections. However, sample transfers can potentially damage the attached spheres. In the worst case, the spheres get disassembled from the spring connections. As a result, the MW line is not closed which can be read out on the network analyzer.
Indeed, such a scenario occurred within an experimental set of this thesis. The only way for re-assembling the Cu spheres is to separate the cryostat from the UHV main chamber. The general routine for this procedure is described in this paragraph. In the first step, the whole system has to be heat up to ambient temperatures. As second step, the UHV chamber has to be vented by nitrogen gas. Afterwards, the cryostat can be disassembled from the main chamber with a crane (see Fig. 3.10(a)). By removing the gold-plated radiation shields, the measurement head is accessible and can be removed from the cold plate. Consequently, the samplestage has to be separated from the measurement head. Fig. 3.10(b) shows the location of the Cu spheres. Furthermore, the red square indicates the disassembled spheres. In order to close the MW circuit, new Cu spheres had to be glued on the contacts. This has been achieved by utilizing silver epoxy. Afterwards the cryostat has been re-assembled to the main chamber. The UHV environment was re-created by the attached pump systems described in 3.2.1 and 3.2.2. In the final step, the cryogenic conditions were achieved by implementing liquid nitrogen and helium within the cryostat. As a result, the setup was again functional operating at 4.7 K and $2 \cdot 10^{-10}$ mbar. Furthermore, microwave signals were readable on the network analyzer.

Modifications on the Preparation Chamber

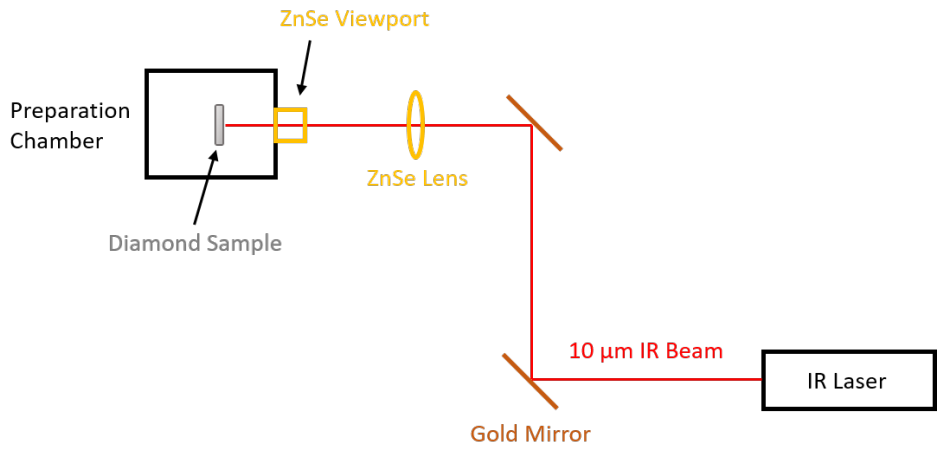

Figure 3.11: Schematic of an optical setup for guiding an IR beam into the preparation chamber.

Another important issue within the scope of this thesis was the modification of the preparation chamber for realizing diamond surface treatments. Therefore, a gas leak valve and an IR beam setup (described in 3.2.1) had to be implemented.
For modifying certain elements within an UHV system, the corresponding vacuum chamber has to be

vented to ambient conditions. Afterwards, changes on the system can be performed. In this particular case, one of the preparation chamber viewports has been exchanged by the gas leak valve. After this procedure, the preparation chamber was pumped down to UHV conditions. Furthermore, a gas line consisting of stainless steel tubes had to be installed directly to the leak valve. With this composition, a certain gas can be introduced to the preparation chamber for depositing on the diamond surface.
In addition to that, it is also crucial to remove clustered impurities from the sample surface. This can be achieved by surface heat treatments. Therefore, an IR laser optical setup has been attached in close proximity to the preparation chamber as shown in Fig. 3.11. Two IR reflective gold mirrors are able to guide the 10 μm laser beam to the viewport of the vacuum chamber. For ensuring a high transmission into the preparation chamber, the viewport is composed of an IR transmitting ZnSe material. Further, a ZnSe lens is mounted in front of this viewport for focusing the beam onto the diamond sample. The readout of the temperature is achieved by an optical pyrometer.

Implementation of a H_2O Dosing Line

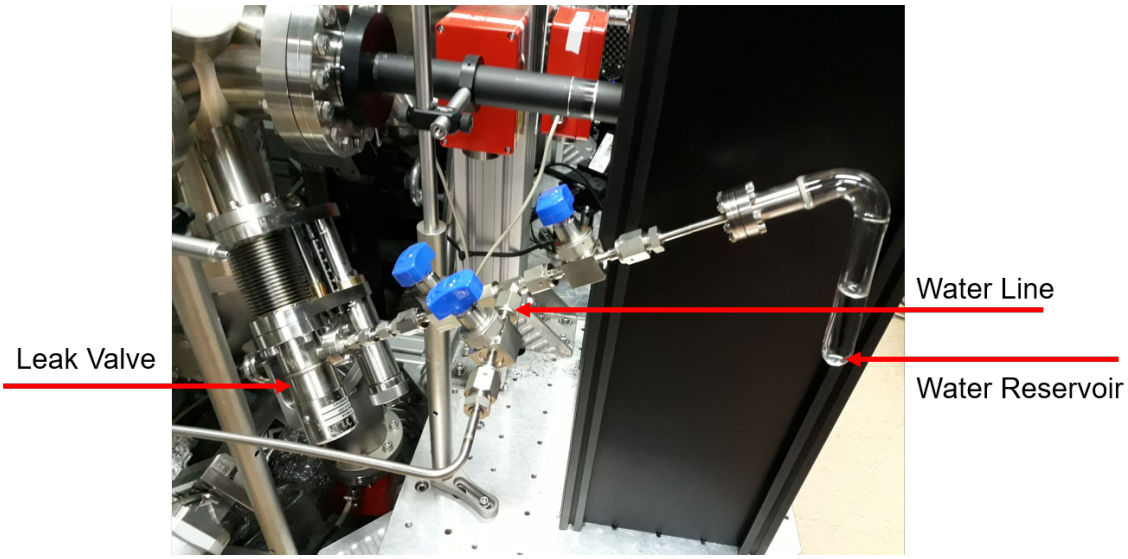

Figure 3.12: Line for performing water dosing experiments. The water is introduced trough a leak valve to the preparation chamber.

Beside of introducing a gas line into the preparation chamber, also a second dosing line was implemented for performing the dosage of more complex compounds. For instance, the deposition of liquids onto the diamond can reveal interesting chemical features or affect the NV center spin properties. Thereby, the formation of thin water layers on the diamond surface is of great interest. Therefore, a water reservoir has been attached to the second dosing line. Similar to the gas path, the water line is connected to a leak valve which ensures the precise introduction of the liquid inside the chamber. The water line architecture is shown in Fig. 3.12. However, before a water dosing procedure can be performed, the liquid has the be purified within the reservoir. In order to achieved this, a freeze-pump-

thaw cycle can be applied. Thereby, the impurities are pumped while the water is freezing. Afterwards, the liquid has to be warmed up and the cycle can be repeated for ensuring highly purified water.

4 Detection of Individual External Spins with Single NV Centers

The investigation of single molecular systems forms the fundamental for a better understanding of biological compounds like peptides and proteins which play a crucial role in medicine and pharmaceutics. Important for the working processes of such bio-molecules are the spatial conformation and structure of individual molecules. Therefore, it is crucial to develop experimental methods which are able to resolve single molecular compounds and the location of individual atoms within these complexes. Several techniques are established for the investigation of molecular structures including NMR, ESR and X-ray crystallography [94]. However, even with advances in these techniques, the major limitation is given by the huge number of molecules ($\approx 10^{12}$ [68]) which are necessary for gathering a reliable measurement signal. As a result, observations on the single molecule level can not be performed and only bulk properties of the system can be studied. Therefore, several super resolution optical microscopy techniques have been developed for enabling access on the single molecule level including photoactivated localization microscopy (PALM) or stimulated emission depletion (STED) microscopy [95, 96]. Another possible approach for tackling this issue is the implementation of single NV centers in ESR. The imaging technique relies on the detection of magnetic signals. Therefore, the NV would not solely image a certain system. It would also reveal physical properties of the system including its magnetic behavior. More specifically, NV center based ESR techniques utilize the dipolar interaction between the NV spin and the external spins of the investigated molecular system [97, 98]. The resulting coupling strength between the spin systems contains information about the spatial arrangement including the length scale of the individual molecule. In fact, such NV center based measurement schemes have been successfully performed in [68] and [97] by the investigation of spin labeled polypeptides. Single NV centers were able to couple to the corresponding spin labels for gaining structural information about the investigated peptides. However, the fast rotational motion of the spin labels prevented the precise and exact estimation of the molecular length. In fact, the length scale was estimated under the assumption of a pure parallel coupling when the spin label orientation is set parallel to the NV axis. Nevertheless, a realistic molecule length of $r = 2.6\,\mathrm{nm}$ was evaluated [97].

For ensuring motion stability and with this a more exact estimation of molecular length scales, we implemented spin labeled polyphenols as observable samples. Chained phenol rings are able to form a compact and stiff molecular structure. As a result, the rotation motion of the attached spin labels is reduced [99]. Indeed, such phenol compounds are named molecular ruler samples in the ESR community due to the high fidelity by accessing their length scale [99]. Nevertheless, no single molecular

measurements of polyphenols have been obtained so far. Most of the studies rely on standard cw ESR techniques measuring a diluted solution of the spin labeled molecules containing $\approx 10^{10}$ spins [100]. Therefore, we present the coupling of a single NV center spin to individual molecular ruler samples as the first detection of a single spin labeled polyphenol in the first section of this chapter. The experiments were performed in the already presented cryo-UHV setup (see chapter 3) at a base temperature of 4.7 K and in an UHV environment of about $2 \cdot 10^{-10}$ mbar. The measurements indicate a dipolar coupling between the NV center spin and the spin labeled polyphenol by a significant NV fluorescence drop in the DEER spectrum. Furthermore, coherent manipulations of the external spin labels were detectable. The limitation of our approach was set by the laser induced instability of the polyphenols compound. A significant reaction between the molecules and the 512 nm laser irradiation led to an instability of the recorded photon counts limiting further experiments for estimating the exact number of detected spins and the molecule length.
Therefore, in the second section we introduce a more photon stable compound, namely the endohedral fullerene N@C_{60} molecule [101]. Even though, the structural conformation of endofullerenes is not highly featured due to their spherical geometry, fullerene compounds are extensively utilized in biomedical applications as MRI and X-ray imaging contrast agents [102]. Furthermore, studies have been performed in which the binding of fullerenes to specific antibiotics has been observed for targeting resistant bacteria [103]. Therefore, studies of endofullerenes at the single molecule level can be interesting for accessing their spin behavior within different coupling mechanisms. Our performed NV center based ESR measurements indicate a successful coupling to less than five external N@C_{60} spins. Also these measurements have been performed at UHV and at 4.7 K cryogenic temperatures. In addition, a coherent manipulation of the N@C_{60} spins was recorded. The results have been published in [71] and [104].

4.1 Molecular Ruler Samples

The first section of this chapter describes the read out of spin labeled polyphenols with a single NV center. As model system, a synthetic rod shaped $C_{42}H_{48}$ phenol compound was chosen. Furthermore, two $C_5H_7NO_3^+$ tetramethylpyrroline carboxylic (P5C) nitroxide radicals, expressed as P5C-NR, were attached to the molecular chain for spin labeling. The resulting $C_{52}H_{62}N_2O_6^{2+}$ compound is illustrated in Fig. 4.1. Typically, the chemical reaction for synthesizing such polyphenols takes place in an iodine solution which is able to dimerize protected monophenols to a rod shaped compound [99]. The spin labeling is achieved through a reaction between the phenols and the P5C-NR molecules in an acidic solution and in presence of dymethylaminopyridine (DMAP) molecules [99]. Based on the spin labels, such structures are often used for checking how precisely angles between molecular frameworks are oriented in nanometer length scales [105]. In general this is achieved by bulk ESR measurements. By using an NV center quantum sensor, this approach can be extended further for the detection of single molecules, revealing their structural conformation.

4.1.1 Bulk ESR Measurements of Spin Labeled Polyphenols

Due to the carbon-nitrogen double bond and the included carboxyl functional group, P5C-NR forms a cyclic imino acid [106, 107]. Its electronic spin of $S = 1/2$ originates from the oxygen radical with a gyromagnetic ratio of $g_{xx} = 2.008, g_{yy} = 2.006$ and $g_{zz} = 2.002$ and the corresponding hyperfine coupling A stems from the near-neighbor ^{14}N nucleus obtaining a nuclear spin of $I_N = 1$ [47, 105]. The resulting hyperfine constants are $A_{xx}, A_{yy} \approx 14\,\text{MHz}$ and $A_{zz} = 103.6\,\text{MHz}$ [47, 108].

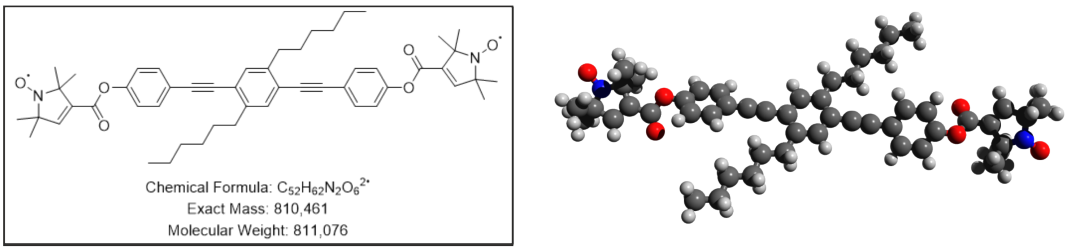

Figure 4.1: Chemical structure of the spin labeled polyphenol $C_{52}H_{62}N_2O_6^{2+}$. In the 3D illustration (right part), the carbon atoms are depicted as gray spheres and the hydrogen atoms as light grey spheres. The oxygen and nitrogen atoms of the P5C-NR spin label radicals are represented as blue and red spheres.

In order to characterize these spin properties, pulsed ESR measurements can be performed on a solution containing the molecules [109]. Fig. 4.2 shows a measurement set in which the spin echo of the molecules was recorded. Similar to the Hahn echo measurement described in chapter 2 [65], the molecules are firstly excited by a $\pi/2$ pulse in their superposition state. Afterwards, a π pulse flips the evolved spin by 180°. Instead of implementing a second and final $\pi/2$ pulse for converting the evolved spin back to its initial state, the spin echo in the xy-plane of the Bloch sphere is read out [64]. The explained pulse sequence is illustrated in Fig. 4.2(a). Typically, the frequency of the pulses is kept constant during the measurement. For the observation of electronic spins, the fixed pulse frequency is on the order of $\approx 9 - 10\,\text{GHz}$ [70]. At the same time, the applied magnetic field is swept. By matching the resonance condition between the fixed frequency and the swept magnetic field, a significant increase of the detectable spin echo can be observed [110]. A resulting pulsed ESR spectrum is shown in Fig. 4.2(b). The $C_{52}H_{62}N_2O_6^{2+}$ molecules were diluted in a ortho-terphenyl solution in a concentration of about 200 μmol/l. The applied magnetic field was swept between 3260 Gs and 3410 Gs. In parallel, the molecules were excited by microwave pulses of 9.5 GHz. The spectrum is characterized by three significant peaks in which the external magnetic field and the applied microwave excitation are in resonance. These peaks, reveal the hyperfine splitting of the spin labels which is composed of all three

directions of the hyperfine and gyromagnetic ratio contributions

$$g_{xx} \cdot A_{xx} \tag{4.1}$$
$$g_{yy} \cdot A_{yy} \tag{4.2}$$
$$g_{zz} \cdot A_{zz}, \tag{4.3}$$

as indicated in the graph. As expected, the A_{zz} contribution forms the largest hyperfine splitting in the spectrum of about $\Delta B \approx 3.6\,\mathrm{mT}$ which can be converted through [111]

$$\Delta\nu = \frac{g_e \mu_B}{h} \Delta B \tag{4.4}$$

to $\Delta\nu \approx 101.3\,\mathrm{MHz}$. This number is in good agreement with the already mentioned value of $A_{zz} = 103.6\,\mathrm{MHz}$ for the nitroxide radical spin label [47]. Also A_{xx} and A_{yy} can be estimated by the presented spectrum using ΔB of about 0.6 mT which leads to $\Delta\nu \approx 16.8\,\mathrm{MHz}$.

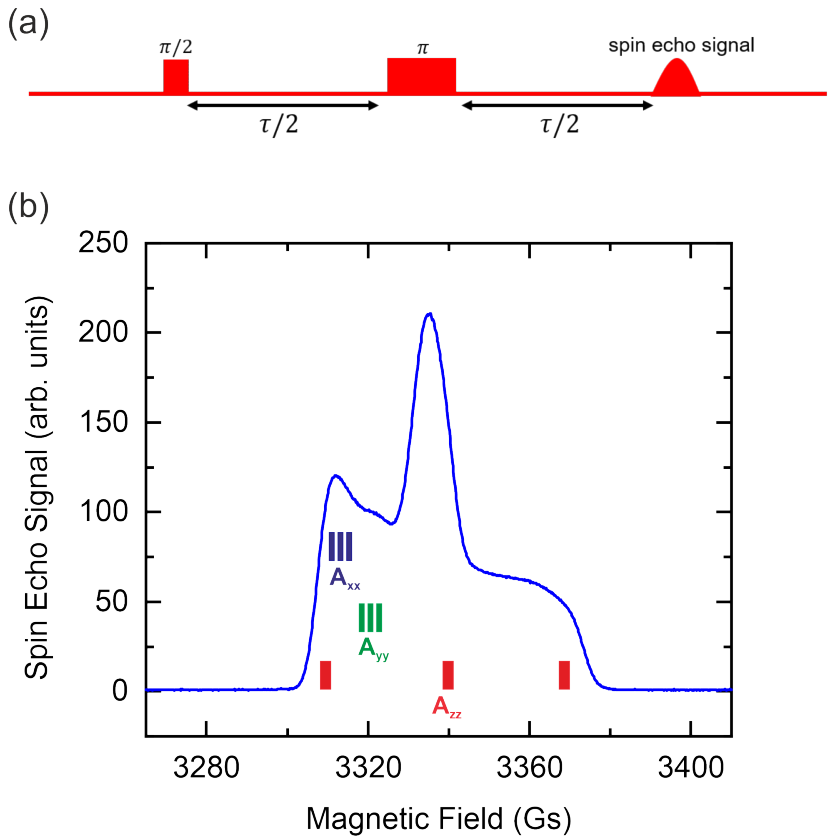

Figure 4.2: Pulsed ESR measurement for the detection of spin echo signals. (a) Pulse sequence characterized by a $\pi/2$ and π spin flips for exciting the spin ensemble into a superposition state. In the end, a spin echo signal is detected. (b) Resulting pulsed ESR spectrum of spin labeled polyphenols measured at 7 K. The measurement has been performed by Gunnar Jeschke, University of Bielefeld.

Potentially, pulsed ESR measurement schemes can be further modified by varying the timing τ between the microwave pulses gaining access on the life time and dynamics of the molecules [112]. Nevertheless, such standard techniques average over $\approx 10^{10}$ molecules within the solution [68]. Therefore, we want to utilize a single NV center as nanoscale magnetic field sensor for detecting the electron resonance of individual spin labels.

4.1.2 Magnetic Dipole-Dipole Interaction

The fundamental principle of NV center based nanoscale ESR experiments is the measurement of the magnetic dipole-dipole interaction between the NV center and the external spins. The spin Hamiltonian for two interacting magnetic dipoles can be written as [113]:

$$H_{dip} = V(r)\left(3(\boldsymbol{S}^k\vec{e}_{kl})(\boldsymbol{S}^l\vec{e}_{kl}) - \boldsymbol{S}^k\boldsymbol{S}^l\right), \tag{4.5}$$

where $\boldsymbol{S}^k$ and $\boldsymbol{S}^l$ are the spin operators of the two involved spins and $\vec{e}_k l$ represents the connecting vector between these. Furthermore $V(r)$ can be expressed as

$$V(r) = -\frac{\mu_0}{4\pi}\frac{\gamma_k\gamma_l\hbar}{r_{kl}^3} \tag{4.6}$$

and contains the distance r_{kl} between the interacting magnetic dipoles. By using the lowering and raising operators $S_- = S_x - iS_y$ and $S_+ = S_x + iS_y$, Eq. 4.5 can be represented as [47, 114]:

$$H_{dip} = \frac{V(r)}{2}(A + B + C + D + E + F). \tag{4.7}$$

The abbreviations A, B, C, D, E, F can be written as:

$$\begin{aligned}
A &= 2(3\cos^2(\Theta_{kl}) - 1)S_z^kS_z^l,\\
B &= (3\cos^2(\Theta_{kl}) - 1)(S_+^kS_-^l + S_-^kS_z^l),\\
C &= 3\cos\left(\Theta_{kl}\right)\sin\left(\Theta_{kl}\right)e^{i\phi}(S_z^kS_+^l + S_-^kS_z^l),\\
D &= C^\dagger,\\
E &= \frac{3}{2}\sin^2(\Theta_{kl})e^{i2\phi}S_+^kS_+^l,\\
F &= E^\dagger.
\end{aligned}$$

The two most important terms are given by A and B. While A describes the generation of a magnetic field at the position of the interacting dipoles, B interprets the energy transfer between the two spins including spin flip-flops. Instead, C, D, E, E represent spin state mixing. As these terms are very small compared to A, B, the spin state mixing can be neglected. Therefore, the dipolar coupling Hamiltonian

can be simplified to [47]:

$$H_{dip} = 2J_{kl}(S_+^k S_-^l + S_-^k S_+^l) + J_{kl} S_z^k S_z^l. \tag{4.8}$$

The introduced quantity J_{kl} is the dipolar coupling strength between the two spins and can be expressed as

$$J_{kl}^{\parallel} = V(r)(3\cos^2(\Theta_{kl}) - 1). \tag{4.9}$$

Of great importance is the angle Θ which represents the spatial orientation between the interacting magnetic dipoles as depicted in Fig. 4.3.

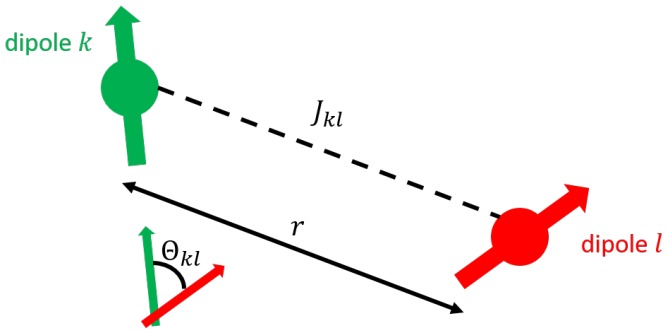

Figure 4.3: Sketch for illustrating the dipole-dipole coupling between to individual spins. Crucial for the coupling strength J_{kl} is the distance r between the two dipoles k, l and the spatial orientation in terms of the angle Θ_{kl}.

4.1.3 Nanoscale ESR Measurements Using a Single NV Center

After the physical components have been described which are involved in the coupling of an NV center spin with an external spin label, the experimental results of the ESR measurements can be presented.

Sample Preparation

As already introduced, the investigated system consists of a single NV center and individual P5C-NR spin labels attached to a rod-shaped polyphenol. For bringing the molecules in close proximity to the NV center, the spin labeled polyphenols have been drop-coated with a pipet to the diamond membrane. Before of that procedure, 0.05 mg of the molecules have been dissolved in 2 ml of chloroform for ensuring the characterization on the single spin level. The diamond membrane on which the molecules have been drop coated is a [100] nanopillar-etched diamond plate (see chapter 2) with a thickness of 30 μm. The NV centers have been implanted with a 5 keV nitrogen ion beam for ensuring a depth < 10 nm of the defect from the diamond surface. After the solution which included the molecules has been drop-coated, the diamond membrane was positioned for 2 h at ambient conditions for evaporating the liquid compounds of the solution from its surface.

DEER Spectroscopy Measurements

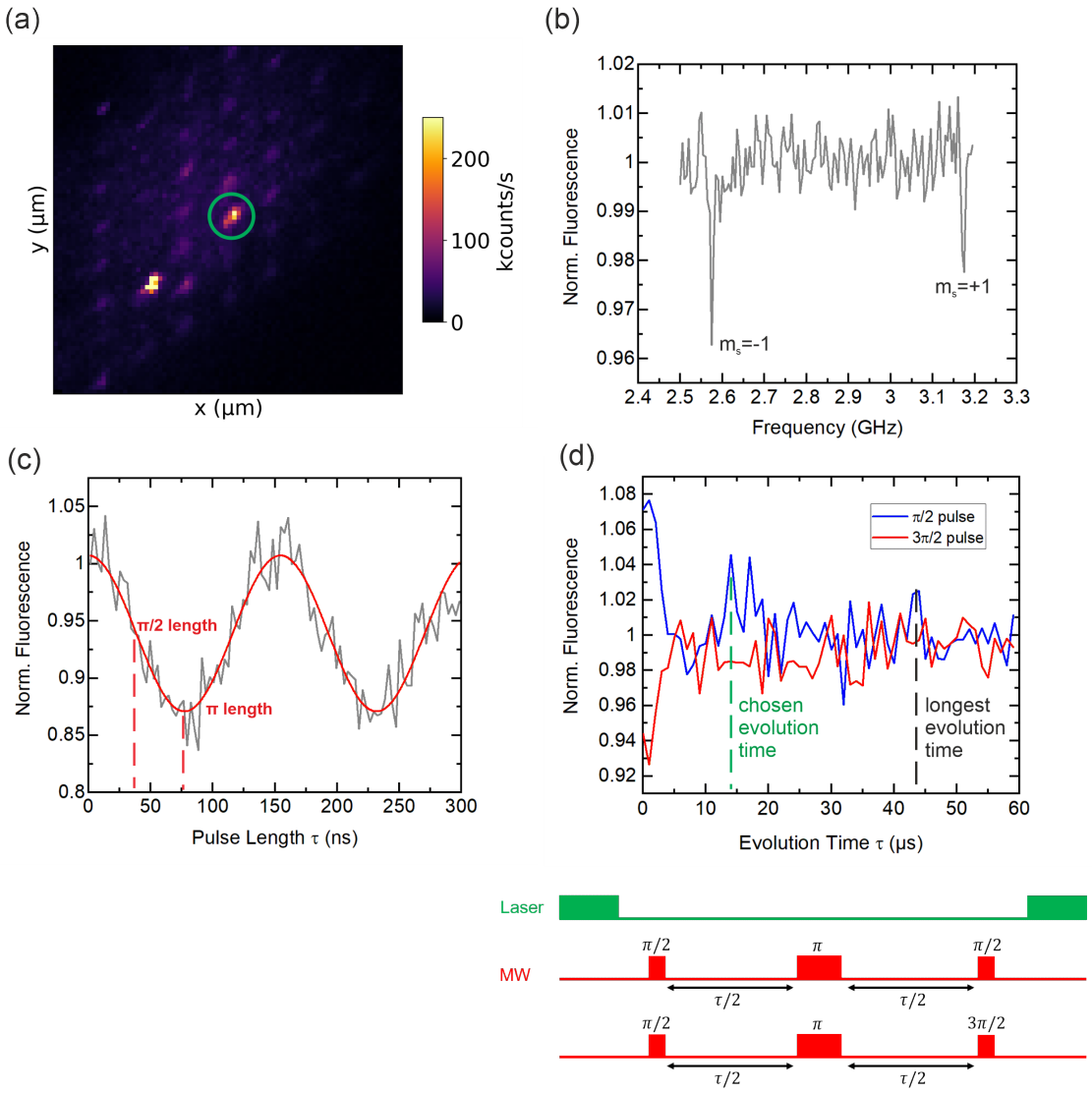

Figure 4.4: NV center pre-characterization inside the cryo-UHV environment (7 K and $9 \cdot 10^{-11}$ mbar). (a) Confocal image highlighting the investigated NV center in the green circle. (b) ODMR spectrum of the chosen NV center under the application of an external magnetic field of 11 mT (estimated by the observed frequency splitting). (c) Resulting Rabi oscillation by fixing the MW frequency at 2580 MHz and sweeping the pulse duration. (d) Hahn measurement on the single NV center by observing the contrast between a $\pi/2$ (flip to $m_S = 0$) and $3\pi/2$ (flip to $m_S = -1$) spin back flip. As reliable evolution time τ of 14 μs has been chosen due to the relatively large obtained spin contrast. Even at an evolution time of 42 μs a spin contrast can be observed. However, the contrast is rather small for reliable quantum sensing measurements.

For performing nanoscale ESR measurements in terms of DEER spectroscopy, the sample was transferred into the cryo-UHV setup. All measurements shown in this section were recorded at 4.7 K and in an UHV environment of $2 \cdot 10^{-10}$ mbar .
Before a DEER measurement can be initialized, several NV specific parameters have to be obtained. Important for this, are the ODMR resonance frequencies between the $m_s = 0$ and $m_s = \pm 1$ substates, the Rabi $\pi/2$ and π lengths and the coherence time T_2, which defines how long a single DEER pulse sequence can be applied. Fig. 4.4 shows a full characterization set of an individual NV center in the cryo-UHV environment under the application of an external magnetic field. The confocal scan (Fig. 4.4(a)) indicates the single NV centers as bright circular spots. For obtaining a suitable signal to noise ratio, the marked NV center has been investigated due to its high fluorescence yield. The corresponding ODMR spectrum is shown in Fig. 4.4(b), indicating a frequency splitting of about 600 MHz between the lower $m_s = 0 \rightarrow m_S = -1$ transition at 2580 MHz and the upper $m_s = 0 \rightarrow m_S = +1$ transition at 3180 MHz. By using the Zeeman term from Eq. 2.4, this frequency splitting corresponds to an applied magnetic field of $\approx$ 11 mT. Based on the transition at 2680 MHz, the microwave pulse duration can be varied for driving a Rabi oscillation. The resulting $\pi/2$ pulse length is at about 40 ns and the π pulse length at 80 ns as illustrated in Fig. 4.4(c). With these parameters, a Hahn measurement can be performed by creating the superposition state of the NV center spin (between the $m_S = 0$ and $m_S = -1$ substates in this particular case) with an initial $\pi/2$ pulse and refocusing the spin dephasing by the π pulse. After that, a final $\pi/2$ pulse highlights the population difference which is correlated to the remaining phase difference. The whole pulse scheme has been explained in a greater detail in chapter 2. In addition to the final $\pi/2$ pulse, a $3\pi/2$ microwave pulse is simultaneously implemented. As a result, the superposition state is once flipped into the bright $m_S = 0$ state and directly in the followed pulse sequence in the $m_S = -1$ state. Instead of recording only one decay curve as depicted in Fig. 2.9(b), two curves are recorded with this measurement scheme as shown in Fig. 4.4(d). The contrast of the two resulting decay curves is more robust against potential artifacts from the measured data [65]. It is evident, that for $\tau = 0$ the fluorescence difference is maximized. In this case the NV center spin is excited into the superposition state and directly flipped in the $m_S = 0$ or $m_S = -1$ without the evolution of a spin dephasing. Nonetheless, a certain pulse sequence duration τ is needed for performing reliable DEER spectroscopy measurements. The longest duration time τ in Fig. 4.4(d) is at about 42 μs which is a reasonable timing quantity. However, the disadvantage at this particular position is the low contrast yield in the resulting population difference. Therefore, it is more beneficial to use a total pulse duration of about 14 μs as a significant fluorescence contrast between the bright and dark sublevels is ensured.
Based on the presented pre-characterization of the single NV center, the DEER spectroscopy measurement was set with resonant microwave pulses at 2680 MHz. The $\pi/2$ and π pulse duration were fixed at 40 ns and 80 ns. The whole pulse sequence time duration τ was set for 14 μs. Defined by the applied magnetic field of 11 mT, the external DEER frequency was swept between 150 MHz and 450 MHz.

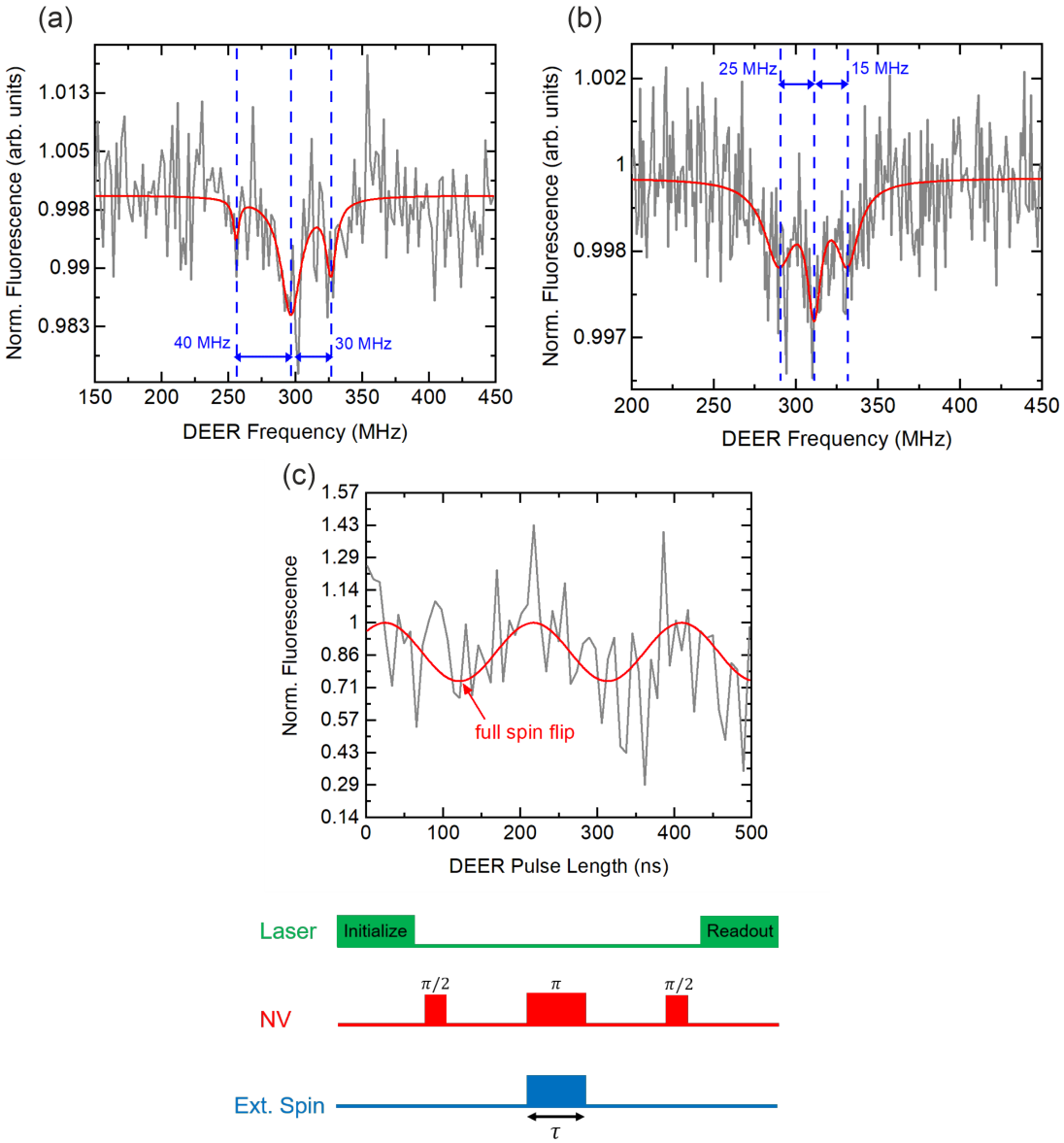

Figure 4.5: DEER spectroscopy utilizing single NV quantum sensors for the observation of spin labeled molecules. The measurements have been recorded at 4.7 K in an UHV environment. (a) Obtained DEER spectrum by the chosen NV center described in Fig. 4.4. Significant drops in the NV fluorescence can be observed indicating the hyperfine interaction of the P5C-NR spin label radical. (b) DEER spectrum obtained by a second NV center as reproducibility measurement. Also here, significant drops of the recorded fluorescence can be observed. However, the hyperfine splitting is shrink compared to the first measurement set. (c) DEER Rabi measurement indicating coherent external spin flip manipulation. The DEER frequency was fixed at 311 MHz and the pulse duration τ was varied up to 500 ns.

The measured DEER spectrum is shown in Fig. 4.1(a) indicating three NV fluorescence dips at about 255 MHz, 295 MHz and 325 MHz. At this frequencies, the external spin label which couples to the

NV center spin is resonantly excited leading to a sign change of its Larmor precession (see Eq. 2.15). Consequently, the magnetic field dependent phase pickup ϕ is not canceled to zero and the NV spin state population at the end of the pulse sequence is not matching exactly the bright $m_S = 0$ substate on the Bloch sphere. As the NV center emission is highly spin state dependent, a drop of the fluorescence is observable. The frequency splitting between the 255 nm−295 nm transitions of 40 MHz and between the 295 nm − 325 nm resonance dips of 30 MHz express the hyperfine interaction of the P5C-NR spin labels attached on the polyphenols. In order to estimate the actual numbers of external spins which are coupling to the NV center, the broadening of the resonance lines within the DEER spectrum can be evaluated [67, 115]. Elasticity measurements on spin labeled organic molecules have shown that nitroxide frameworks can exhibit a T_2^* relaxation lifetime on the order of 10 μs depending on the number of interacting spins [116, 117]. As the spin lifetime is inversely proportional to the width of the measured resonance peaks in the spectrum, we can estimate a relaxation time of the spin labels T_{2sl}^* of [67]

$$T_{2sl}^* = \frac{1}{w_{DEER}}. \tag{4.10}$$

w_{DEER} corresponds to the width of the central DEER peak at 295 MHz and is of about 8.2 MHz. This leads to a T_{2sl}^* of about 0.17 μs indicating that the NV center is coupling to more than a single external spin. Indeed, NV center based DEER measurements on spin labeled peptides have shown a T_{2sl}^* time of about 2 μs in the presence of less than 5 external spins in the NV center detection volume [47, 97]. As our resulting T_{2sl}^* is decreased by a factor of 10, we can roughly assume that the single NV center is already coupling to $\approx$ 50 spins which is, in terms of single spin sensing, a relatively huge number. This fact also explains the asymmetric hyperfine splitting of 40 MHz and 30 MHz. A large number of spins in the detection region of the NV center leads to several individual hyperfine contributions of the involved dipoles due to the random angle distributions relative to the NV center spin axis (see Eq. 4.9). Therefore, several apparent hyperfine splittings between A_{zz}, A_{yy} and A_{xx} can be potentially investigated [47].

Reproducibility measurements can be performed for further supporting the assumption that the individual NV centers are coupling to more than 50 external spins in our investigated system. Therefore, the DEER spectrum was recorded on another NV center pillar. The results of this second DEER spectroscopy measurement set is shown in Fig. 4.5(b). The DEER spectrum was obtained with a $\pi/2$ pulse length of 45 ns and a π pulse length of 90 ns at a fixed microwave frequency of $\approx$ 2620 MHz. Also here, the DEER sequence duration was set at 18 μs. It is evident that the NV properties are very similar compared to the first NV center utilized for gaining spectrum in Fig. 4.5(a). This is beneficial for a direct comparison of the results. The second DEER spectrum obtains a central resonance line at 311 MHz and two side dips at 331 MHz and 289 MHz. Compared to the DEER spectrum in Fig. 4.5(a), the hyperfine splitting seems shrink to 25 MHz and 17 MHz. A slight asymmetry is still observable which again indicates an NV center coupling to a relative large external spin amount. Furthermore, the

reduced hyperfine frequency splitting originates from the specific orientations of the involved nitroxide spins. Nonetheless, external spin manipulation processes can be investigated in the observed sample. This can be achieved by the implementation of a DEER Rabi pulse sequence which is performed at a fixed DEER frequency [71, 104]. Instead of varying the applied radio frequency, the DEER pulse duration is swept. As a result, a collective Rabi oscillation of the external spin labels can be recorded as shown in Fig. 4.5(c). The DEER Rabi measurement was obtained from the firstly investigated NV center which generated the DEER spectrum in Fig. 4.5(a). Therefore, the DEER Rabi pulse frequency was fixed at 295 MHz for exciting the central resonance line of the spin labels. The duration of the pulse was swept up to 500 ns. Consequently, an oscillation with a time period of about 190 ns was measured indicating an external spin flip time of 95 ns.
In fact, more sophisticated pulse sequences can be performed for characterizing the external nitroxide spins in a greater detail. For instance, DEER Hahn pulse schemes are able to reveal the coherence time T_2 of the spin labels [71]. Therefore, an external spin specific Hahn sequence can be implemented within the NV center Hahn branch. Thereby, the excitation frequency of the spin labels gained from the DEER spectrum can be used for the implemented Hahn scheme. Moreover, the exact number of the involved spins can be obtained more accurately than from the observation of the DEER peak linewidth. This is achieved by a so called DEER Delay measurement scheme in which the positioning of the external spin π pulse is varied within the Hahn sequence of the NV [71]. As a result the external spin flip is shifted leading to a coherent oscillation of the NV center electronic spin. Due to the correlation of the NV center spin state and the fluorescence counts outcome, the resulting emission can be written as [71]

$$C_{NV} = \frac{1}{2}\prod_{k}^{N}(1 + cos(J_k\tau)), \tag{4.11}$$

where N denotes the number of coupled spins to the NV center with the coupling strength J_k. The amplitude of the resulting oscillation gives an estimate of the involved spins in the detection range of the NV center. Unfortunately, such sophisticated pulse schemes could not been achieved within the experimental sets of the spin labeled polyphenols. A strong limitation is connected to the photoinstabilities of the molecules even at cryogenic temperatures which will be presented in the following subsection.

4.1.4 Measurement Limitations with the Polyphenols

The photoreaction of an investigated sample with laser irradiation is always a crucial limitation in optical measurement techniques. As the NV center forms an optical defect, it is inescapable to perform NV center based magnetometry with the application of laser light. Especially at room temperature, samples formed by molecular frameworks tend to react with introduced photons in the form of photoreactions or kinetic motions [118]. In both cases, the characteristics of the investigated compounds change during the experimental set leading to undesired features in the final results. A possibility to

circumvent this issue is the performance of measurements in a cryogenic environment which is one of the main motivation highlighted in this thesis for utilizing a cryo-UHV setup. However, we noted even at 4.7 K a significant photoreaction on the utilized polyphenols under the application of the green 512 nm laser which highly limits our potential measurement performance.

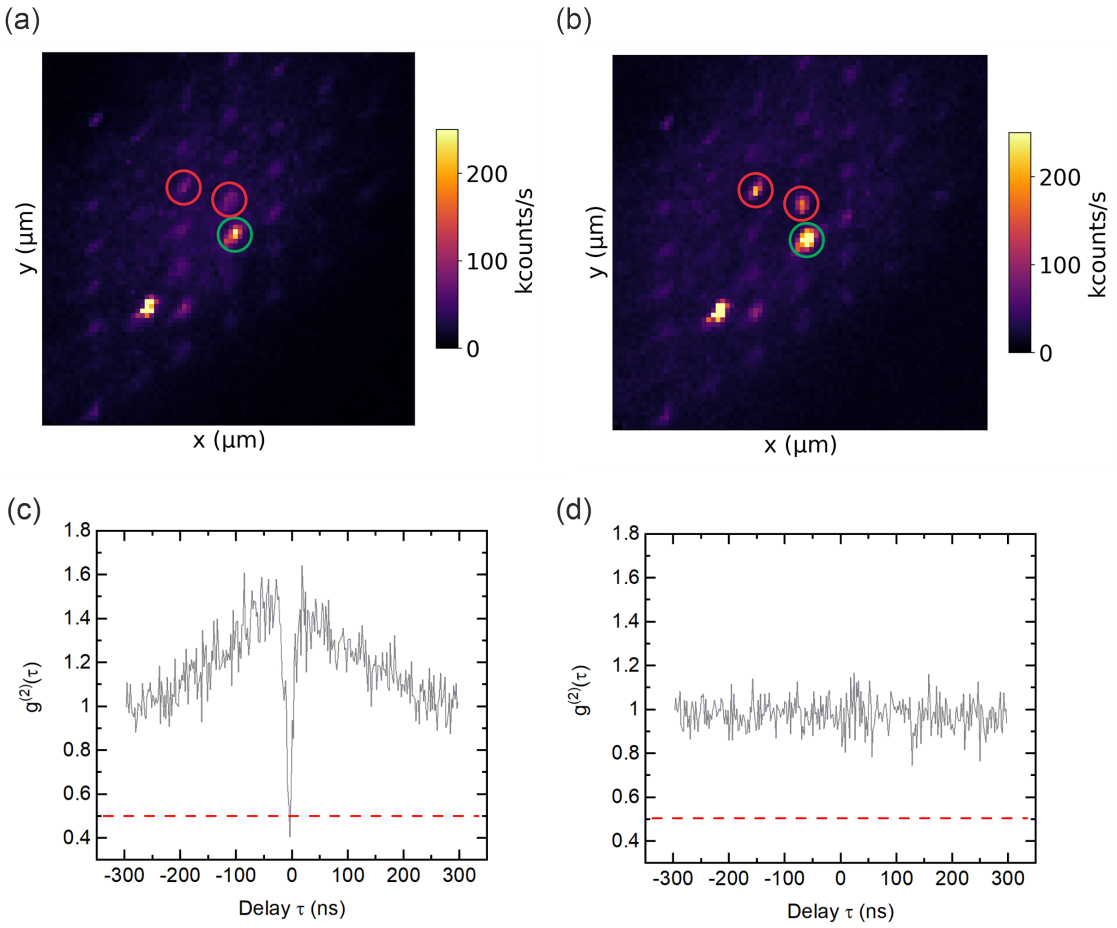

Figure 4.6: Photoinstability of the drop-coated polyphenols onto the diamond surface. (a) Confocal image recorded before the DEER measurement has started. The chosen NV is highlighted by the green circle. The two red circles are showing two NV centers with less emission. (b) Confocal scan after the performed DEER spectroscopy (duration ≈ 13 h). The chosen NV defect (green circle) clearly shows an increased fluorescence count rate. Furthermore, the two other NV centers (red circle) obtain a significantly increased emission compared to (a). (c) Autocorrelation of the single NV center before the DEER measurement, characterized by an antibunching dip below 0.5. This feature is an indicator for the record of the NV emission. (d) Autocorrelation on the same NV after the DEER measurement. No antibunching dip can be observed, indicating that the recorded fluorescence is not stemming from the NV center.

This fact is depicted in Fig. 4.6 showing two confocal scans of the same position on the sample located in the UHV-cryo measurement head. Fig. 4.6(a) presents the initial confocal scan before the DEER

spectroscopy measurement has been started. As usual, the NV implanted pillars are observed as bright spots. The marked NV center exhibits an emission of about 150 kcounts/s. However, after a laser irradiation of about 13 h during the record of the DEER spectrum, a significant fluorescence increase can be noted. Fig. 4.6(b) shows the same position as confocal scan after the DEER measurement indicating an emission increase to about 250 kcounts/s. In both confocal images the laser power was kept constant at about 5 mW. Due to these findings, a photoreaction of the spin labeled molecules can be assumed which increased locally the emitted photons.
For proving this, the autocorrelation of the NV center can be recorded. If the collected photons are contributed by the single NV center within the nanopillar, an antibunching dip below 0.5 should be measurable. Indeed, the autocorrelation of the investigated NV center before the DEER spectroscopy measurement was characterized by an antibunching dip at 0.4, as depicted in Fig. 4.6(c). In contrary, Fig. 4.6(d) shows the autocorrelation measurement of the NV center after the performed DEER spectroscopy. It is evident that no antibunching features can be found in the autocorrelation curve indicating that the collected photons are attributed to an additional emission source. Potentially, such an uncontrolled emitter can be formed by the polyphenols under laser degradation. Diluted spin labeled polyphenols show no light emission in the wavelength range within 650 nm and 700 nm which is the collection region of the confocal microscope implemented in the presented setup (defined by the used longpass filter at 650 nm) [119]. However, laser degradation can potentially change the optical properties of molecules and induce an undesired changed emission. In fact, a photon induced degradation of polyphenols has been reported in literature known as photooxidation [120]. Nonetheless, this has been shown in terms of high-performance liquid chromatography (HPLC) [121] at an ambient temperature of 30 °C [120]. As a result, the molecular polyphenols degraded within 50 min under UV exposure [120]. The increased degradation time of about 13 h noted from the presented molecules can be explained by the cryogenic conditions which stabilize the polyphenols. Unfortunately, NV center based DEER spectroscopy measurements require a high acquisition time beyond several hours due to the rather weak signals generated by the few external spins. Therefore, a long measurement time is unavoidable.
To overcome this limitation for prospective experiments, the sample preparation can be changed by drop coating a thinner layer of spin labeled molecules onto the diamond surface. Furthermore, performing the measurements with lower laser power can elongate or even avoid the degradation of the molecules.

4.2 Endofullerene Spin Qubits

In the second section of this chapter, the readout of individual endohedral N@C_{60} molecules is presented. Compared to the rod-shaped polyphenols, the structural conformation shows no specific characteristics due to the spherical geometry of the C_{60} cage. Nonetheless, medical research applications make fullerene compounds highly attractive. Furthermore, spin quantum computation models based

on endohedral N@C_{60} and P@C_{60} fullerenes have been suggested due to their paramagnetic properties [122]. However, the addressing and readout of single endohedral fullerenes has not been achieved so far which is an important issue in terms of building quantum networks. Studies on N@C_{60} molecules have been performed with ESR techniques in which $\approx 10^6$ spins are usually involved, revealing the hyperfine interaction between the electronic and nuclear spin of the encapsulated nitrogen atom [104, 123]. Again, single NV centers can be utilized for investigating the hyperfine spectrum of individual N@C_{60} molecules which is shown in the following subsections. Similar to the readout of the presented spin labeled polyphenols, the measurements have been performed in terms of DEER spectroscopy observing the dipolar coupling between a single NV center and external N@C_{60} fullerenes.

4.2.1 Endofullerene N@C_{60} Molecules

The endohedral N@C_{60} complex is formed by a single ^{14}N nitrogen atom encapsulated into the center of a C_{60} buckyball cage [124]. As the nitrogen atom is not chemically bonded to the carbon cage, the inserted atom remains isolated at the centrosymmetric (icosahedral) I_h position of the buckyball which is depicted in Fig. 4.7. As a result, the single atom eigenvalues of the ^{14}N remain unchanged and can be adressed by their corresponding transition frequencies [71]. Therefore, single endohedral fullerenes are able to form a controllable qubit [125].

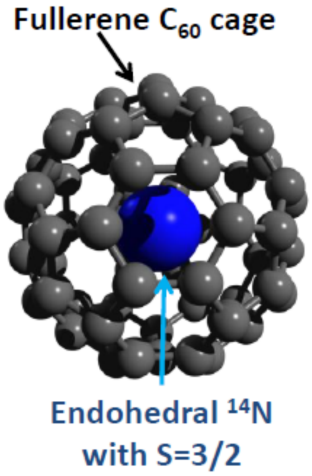

Figure 4.7: 3D illustration of the endohedral N@C_{60} fullerene. An ^{14}N atom is encapsulated inside a C_{60} cage.

The fabrication of such molecular compounds is based on a two step process including the formation of C_{60} cage molecules and the insert of the encapsulated atom. In general, C_{60} buckyballs can be produced by applying a large electric current between two graphite electrodes forming a fullerene rich soot [126]. For extracting the fullerenes from the carbon soot mixture, organic solvents are used. A more accurate separation can also be realized by chromatography. For implementing single atoms into the carbon cages, the C_{60} compounds are sublimated as a thin film on a metallic target [127].

Afterwards, ion bombarding implements the individual atoms [127]. In case of an N@C_{60} fabrication process, the C_{60} thin film is bombarded by an ^{14}N beam source. Typically, a second chromatography step is involved for separating the atomically filled C_{60} complexes from the pure C_{60} cages as the filling factor of such bombarding techniques is on the order of 10^{-4} [127]. The resulting endohedral fullerene solution can than be characterized by x-band cw-ESR spectroscopy [128]. Fig. 4.8(a) shows a typical ESR spectrum of an N@C_{60} solution characterized by three distinct lines. The spectral splitting of $\Delta B = 0.57\,\mathrm{mT}$ corresponds to a frequency splitting og 15.97 MHz which indicates the hyperfine coupling strength between the electronic $S = 3/2$ and nuclear $I = 1$ spin of the encapsulated ^{14}N atoms [124]. For clarification, Fig. 4.8(b) illustrates the energy level scheme and the dipolar transitions of N@C_{60} molecules. Due to the electronic spin of $S = 3/2$, four electronic spin states can be rise as $m_s = \pm 3/2$ and $m_s = \pm 1/2$. In addition, the $I = 1$ nucleus with $m_I = 0, \pm 1$ leads to 12 energy levels. As the transitions are triply degenerated, three lines are observable in the ESR spectrum [123].

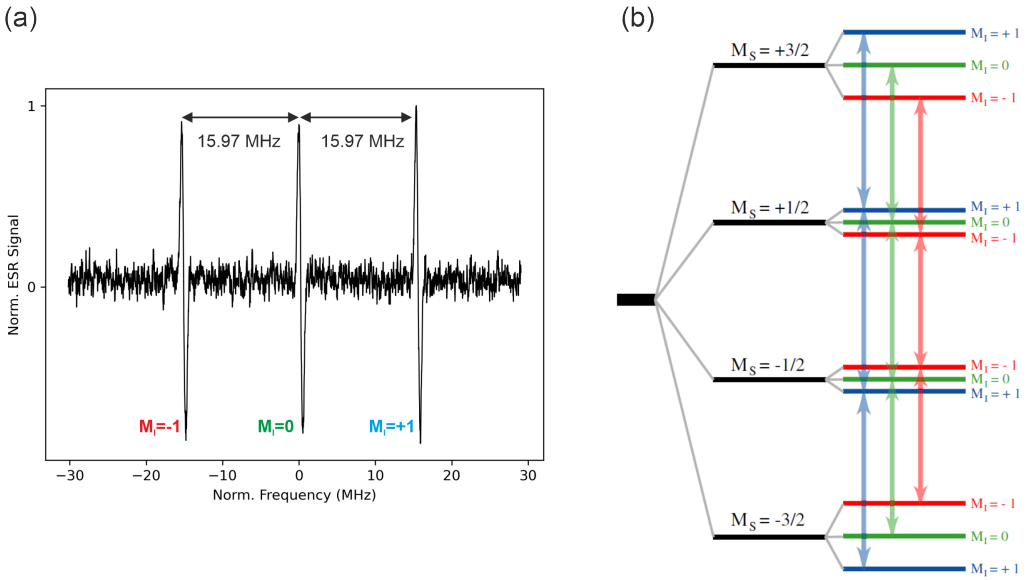

Figure 4.8: ESR study on an N@C_{60} ensemble solution. (a) cw ESR spectrum of an N@C_{60} solution containing $\approx 10^9$ spins. Three resonance line can be observed with a splitting of 15.97 MHz, corresponding the hyperfine interaction between the electronic and nuclear spin. The measurement has been performed by Rene Wieczorek, University of Osnabrück. (b) Energy level diagram of N@C_{60} illustrating the dipolar allowed transitions as colored arrows.

Mathematically, the energy levels of the N@C_{60} spin can be represented by the ground state spin Hamiltonian [71]

$$H^{spin}_{N@C_{60}} = H_{ZFS} + H_{HF} + H_{EZ} + H_{NZ}. \tag{4.12}$$

The zero field interaction term H_{ZFS} can be written as $D(S_z^2 - 5/4)$ and originates from the dipolar interaction between the three unpaired electrons within the $2p_x, 2p_y, 2p_y$ orbitals of the nitrogen atom.

In general, the term is zero due to the centroysymmetric I_h symmetry of the C_{60} buckyball. Nonetheless, asymmetries in the C_{60} cage can potentially rise the H_{ZFS} term [129]. Such asymmetries can appear by putting the molecule on a surface which deforms the perfect centrosymmetry of the C_{60} cage.
H_{HF} describes the already discussed hyperfine interaction in which the nitrogen nucleus is involved. The term can be expressed as $H_{HF} = AS_zI_z$.
The electronic and nuclear Zeeman interactions can be represented as $H_{EZ} = \mu_B g_e B_z S_z$ and $H_{NZ} = \mu_N g_n B_z I_z$. Similar to the spin Hamiltonian of the NV center, H_{NZ} is much smaller compared to H_{EZ} due to the huge difference between the nuclear magneton μ_N and Bohr magneton μ_B on the order of 10^3 J/T [67].
As a result, Eq. 4.12 can be simplified (in units of $\hbar$) to [71]

$$H^{spin}_{N@C_{60}} = AS_zI_z + \mu_B g_e B_z S_z. \tag{4.13}$$

In all expressed terms, S_z and I_z represent the z-component of the electron spin operator $\boldsymbol{S}$ and nuclear spin operator $\boldsymbol{I}$. Furthermore, B_z is the magnetic field across the N@C_{60} spin.

4.2.2 Sensing N@C_{60} Molecules with a Single NV Center

So far, N@C_{60} molecules have been characterized solely by bulk ESR measurements in which typically a large amount of $\approx 10^6$ spins are involved [123]. However, the investigation on the single spin level is of great interest. Especially the interpretation of a single N@C_{60} as a qubit system [122, 125], makes the control of the endohedral spin attractive. Therefore single NV centers can be implemented. In terms of DEER spectroscopy, the dipolar coupling between the NV center and an external N@C_{60} fullerene can be investigated which is shown in this subsection.

Sample Preparation

In order to investigate individual external N@C_{60} spins, the sample preparation has been performed similar as described in 4.1.3 in which the drop coating of the spin labeled polyphenols is explained. An N@C_{60} powder with a filling factor of 10^{-4} (N@C_{60}:C_{60} ratio) was dissolved into toluene forming a 0.1 μmol/L solution. 1 μL of this solution was drop-coated on top of a [100] nanopillar-etched diamond plate. The NV centers are located in less than 10 nm below the diamond surface within the nanopillars which act as cylindrical waveguides. Afterwards, the membrane dried within 2 h at ambient conditions.

DEER Spectroscopy Measurements

The DEER spectroscopy measurements of the prepared system were performed within the cryo-UHV setup in an experimental environment of 4.7 K and $2 \cdot 10^{-10}$ mbar. The investigated NV centers were

chosen regarding their fluorescence yield in the recorded confocal images. A typical confocal scan is shown in Fig. 4.9(a) highlighting the utilized NV center for this study.

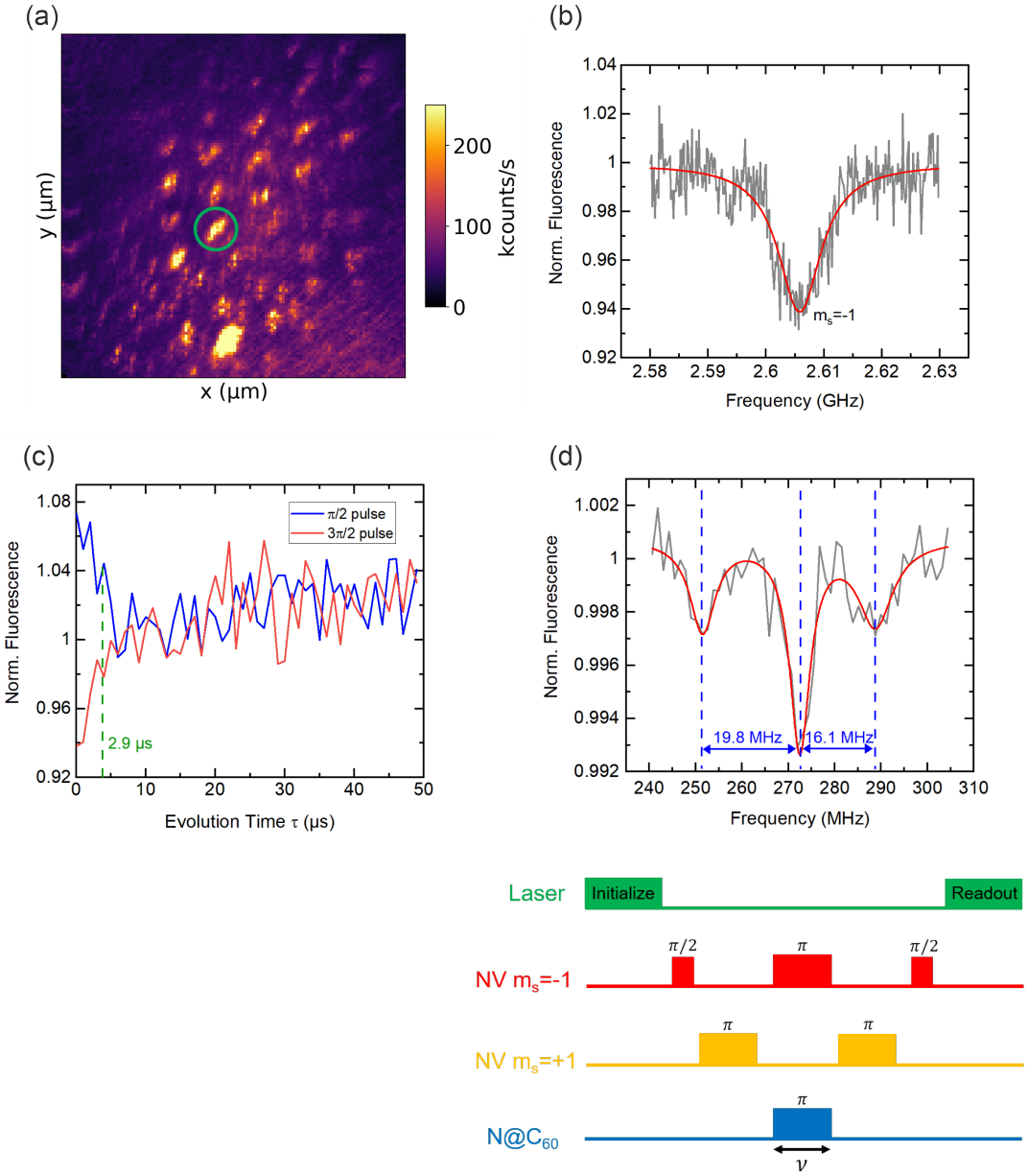

Figure 4.9: Pre-characterization of an individual NV center and detection of N@C_{60} spins at a cryogenic and UHV environment. (a) Confocal image showing the evaluated NV center within the green circle. (b) ODMR line of the $m_S = -1$ transition at ≈ 2605 MHz. According to the linear Zeeman term, this corresponds to an applied magnetic field of 9.4 mT. (c) Hahn measurement with $\pi/2$ and $3\pi/2$ ending pulses. A maximum coherence time of 2.9 μs can be measured. (d) DEER DQT spectrum of an N@C_{60} spin detected by the chosen NV center and simplified DQT pulse sequence. A hyperfine splitting of 19.8 MHz and 16.1 MHz can be observed, indicating deviations of the centrosymmetric C_{60} cage.

As already explained in 4.1.3, the individual NV center has to be characterized in terms of its spin properties, before the DEER spectroscopy measurement set can be started. Usually, this is achieved by the performance of ODMR spectroscopy, the excitation of Rabi oscillations and the measurement of the coherence time as already described in the polyphenol section 4.1. Fig. 4.9(b) depicts the lower ODMR ($m_S = 0 \rightarrow m_S = -1$) transition of the chosen NV center obtaining a resonant frequency excitation at 2605 MHz. This corresponds to an applied magnetic field of ≈ 9.46 mT along the NV center axis. The T_2 of the investigated NV center was measured by a Hahn echo pulse sequence revealing a coherence time of 2.6 μs (presented in Fig. 4.9(c)). With this set of parameters, DEER spectroscopy measurements on the NV-N@C_{60} system can be performed. Nonetheless, the in this section used DEER pulse sequence for the observation of the N@C_{60} spins was slightly modified compared to the standard DEER scheme presented in 4.1 for the investigation of the spin labeled polyphenols.

The hypefine splitting of a single N@C_{60} complex forms a relatively narrow spectrum due to the small frequency splitting of 15.97 MHz. Therefore, it is of great importance to maximize the sensitivity of the NV center quantum sensor for resolving the individual frequency lines of the single external spin. This can be achieved by utilizing a DEER-DQT pulse sequence [130]. In this measurement scheme, the used coherent superposition state $|\sigma\rangle$ is not between the $|0\rangle$ and $|\pm 1\rangle$ states (see Eq. 2.5). Instead, a double quantum superposition $\left|\Psi_{dq}\right\rangle$ between the $|1\rangle$ and $|-1\rangle$ states is utilized. As a result, the NV center spin state is read out as [47]

$$\left|\Psi_{dq}\right\rangle = \frac{1}{\sqrt{2}}\left(e^{-i\phi(t)}\left|-1\right\rangle + e^{i\phi(t)}\left|1\right\rangle\right). \tag{4.14}$$

As both $|-1\rangle$ and $|1\rangle$ substates obtain a phase pickup, the gathered signal is almost doubled which is highly beneficial in terms of single spin sensing. However due to the spin momentum conversion, the double quantum transition $|-1\rangle \rightarrow |1\rangle$ can not be addressed directly. A possible solution is formed by modifying the standard DEER sequence. Additional π pulses on the corresponding other transition are able to create the double quantum superposition state Ψ_{dq}. The pulse scheme is shown in Fig. 4.9(d) starting with a $\pi/2$ pulse for creating the superposition state between the $|0\rangle$ and $|-1\rangle$ state. Afterwards a triple alternating π pulse train is implemented for changing the population between the $|-1\rangle$ and $|1\rangle$ states [47, 130]. The triplet pulse train contains the standard π pulse matching the resonance frequency for the $|-1\rangle$ state and two π pulses applied at the resonance frequency of the $|1\rangle$ state. An additional description of the pulse sequence is noted in the appendix 10. The resulting DEER DQT spectrum is shown in Fig. 4.9(d), indicating three resonance lines with an asymmetric frequency splitting of 19.8 MHz and 16.1 MHz from the central transition at 272 MHz. The values of the observed frequency splittings are in good agreement with the known N@C_{60} hyperfine interaction [123, 124]. Nevertheless, an asymmetry in the ESR spectrum is unusual for endohedral fullerenes due to the I_h cage symmetry. In section 4.1 the asymmetric DEER spectra of the spin labeled polyphenols were explained by the different orientation angles of the attached spins relative to the NV axis. However,

this explanation does not count for the coupling to N@C_{60} fullerenes due to the centrosymmetry of the molecule. Therefore, it has to be assumed that the zero field interaction term H_{ZFS} from Eq. 4.12 is not vanishing for the observed N@C_{60} spin. This is a realistic scenario as the N@C_{60} molecules were drop coated onto the diamond surface [104]. The landing of the fullerenes could cause deviations from the I_h centrosymmetry of the C_{60} cage. As a result, the endohedral nitrogen spins obtain a preferential orientation. Indeed, simulations based on second-order perturbation theory [131] were able to resolve an asymmetric N@C_{60} ESR spectrum with a down-shift of the lower transition by 4 MHz [104]. This has been achieved by assuming an axial zero-field parameter D of 1.52 MHz [104]. Another interesting feature in the DEER spectrum of Fig. 4.9(d) is the increased amplitude of the central hyperfine peak, compared to the outer resonance lines. However, this is a typical feature in NV based DEER spectroscopy which has also been investigated in section 4.1 on the spin labeled polyphenols and indicates the presence of additional (hyperfine-less) parasitic electronic spins in the NV center detection region [71]. For characterizing the observed N@C_{60}, more sophisticated pulse schemes can be applied on the investigated system.

4.2.3 Coherent Control of N@C_{60} Spins

DEER Rabi Measurements

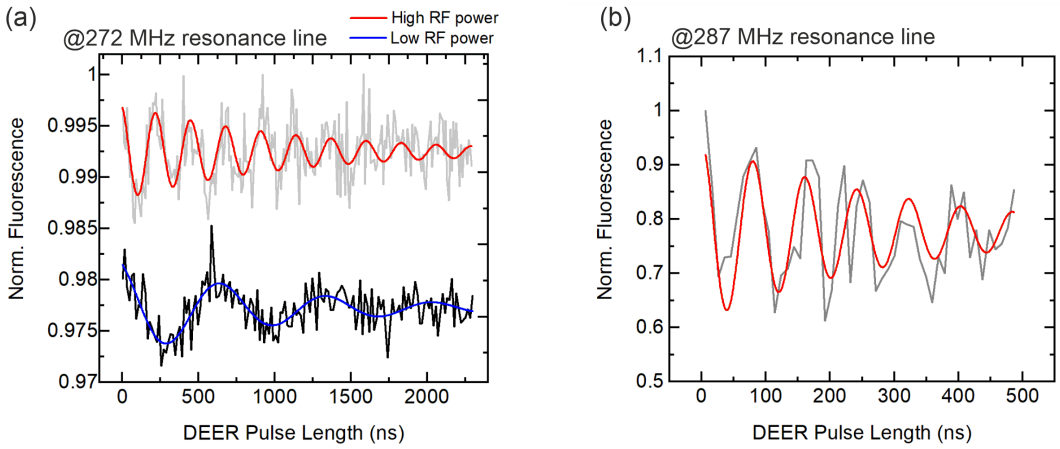

Figure 4.10: DEER Rabi measurements on the external N@C_{60} spin. (a) Rabi oscillations of the endofullerene spin recorded with a fixed DEER frequency at 272 MHz for matching the central resonance line. A coherent manipulation of the external spin can be observed. Furthermore, an expected increase of the Rabi frequency is measured for increasing the applied RF power. (b) Rabi oscillation recorded with a fixed frequency at 287 MHz corresponding to the upper transition in the N@C_{60} DEER spectrum. Also here, spin flips can be investigated proving the actual detection of N@C_{60} spins.

In order to investigate the coupled N@C_{60} spins in a greater detail, spin flip operations can be performed in form of DEER Rabi measurements. Especially, signal oscillations of the outer peaks are

a clear indicator that in fact the electronic spin of the encapsulated ^{14}N atom is observed. Fig. 4.10 presents the DEER Rabi measurements obtained at fixed frequencies at 272 MHz (central transition) and 287 MHz (upper transition). The Rabi oscillation of the central 272 MHz line was recorded for two different RF driving powers (Fig. 4.10(a)). The measurement obtained at an applied pulse power of −20 dBm is denoted as high RF power. In contrast, the low power measurement with −30 dBm is denoted as low RF power. A decrease of the Rabi oscillation frequency from 4.42 MHz to 1.39 MHz can be observed by lowering the applied RF power. This indicates the expected square-root behavior of Rabi oscillations in dependence of the pulse power [104].
As already mentioned, the central peak contains also the signal of additional electronic spins in the NV center environment. Therefore, solely the DEER Rabi oscillation of this frequency line does not fully prove the coupling to an N@C_{60} fullerene. However, the coherent manipulation of the upper transition clearly evidences the existence of an N@C_{60} molecule close by the NV center sensor (Fig. 4.10(b)). By evaluating the exponential decay of the oscillation amplitude, the spin life time T_1 in the rotating frame (as the system is under RF driving) can be revealed which is denoted as $T_{1\rho}$ [132]. For the Rabi driving of the nuclear $m_I = 0$ state (central resonance line), a $T_{1\rho}$ of $\approx 0.9\ \mu$s can be evaluated. Instead, the Rabi oscillation of the nuclear $m_s = +1$ state (upper transition) reveals a $T_{1\rho}$ time of 0.3 μs.

DEER Hahn Measurement

Another important quantity related to single qubits is their coherence time T_2. In terms of NV center based DEER spectroscopy, the coherence time of the external spin can be measured by implementing a Hahn sequence within the DEER pulse scheme. The additional Hahn sequence is performed at the resonance frequency of the external spin. Fig. 4.11 depicts the DEER Hahn measurement on the external N@C_{60} complex which was performed by fixing the external spin frequency at 272 MHz. A significant decay curve can be obtained revealing a T_2 time of $\approx 0.9\ \mu$s. According to literature values, endohedral N@C_{60} fullerenes show T_2 times of about 20 μs [133]. Compared to that, the obtained value from our NV center based technique is relatively small. However, this can be explained by the low NV center T_2 time of 2.9 μs. As the DEER Hahn scheme is implemented in the branch of the NV center Hahn sequence, the resulting coherence time of the external spin is limited by the T_2 time of the utilized quantum sensor. Therefore, the revealed N@C_{60} T_2 time identifies the minimum coherence time of the external spin [71].

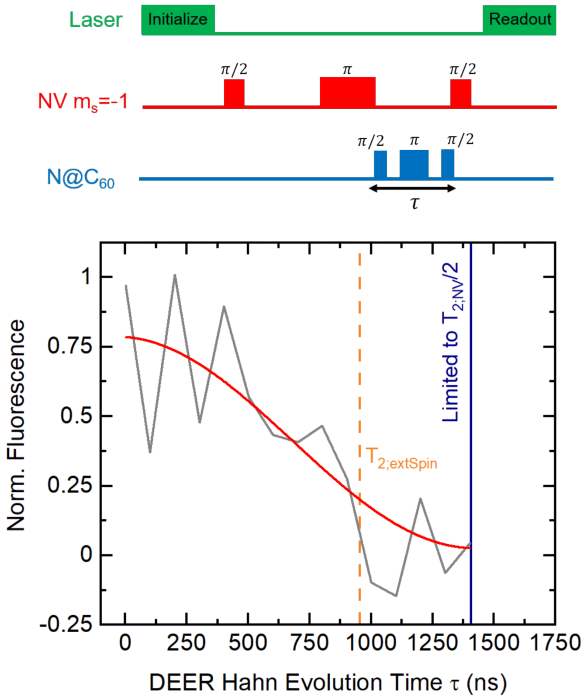

Figure 4.11: DEER Hahn measurement for characterizing the coherence time T_2 of the observed $N@C_{60}$ spin. The pulse scheme consists of an external spin specified Hahn sequence within the NV branch. Therefore, the measurement is $T_{2;NV}$ limited and gives only an estimate for the minimum coherence time of the observed spin.

DEER Delay Measurement

In the last part of this section the performance of a DEER Delay measurement is presented for estimating the actual number of $N@C_{60}$ spins coupled to the NV center quantum sensor. The principle of the pulse sequence has already been explained in 4.1.3. The timing of the external spin pulse can lead to an oscillation behavior of the gather spin signal. According to the obtained amplitude, the number of involved spins N and the corresponding coupling strength J_k can be revealed [47, 71]. Fig. 4.12 shows the resulting DEER Delay curve in which the external spin π pulse was timed within $-1.5\,\mu$s and $1.5\,\mu$s. Also this pulse sequence is limited by the NV center coherence time of $2.9\,\mu$s as the external spin pulse is positioned within the Hahn branch of the NV center. Nonetheless, a decrease of the gathered NV fluorescence can be observed and fitted with Eq. 4.11. The evaluation estimates an NV center coupling to around 3 external spins which can fairly identify the experimental attempt as sensing on the single spin level. Furthermore, the NV center to $N@C_{60}$ coupling strength J_k is estimated to be around 1.22 MHz.

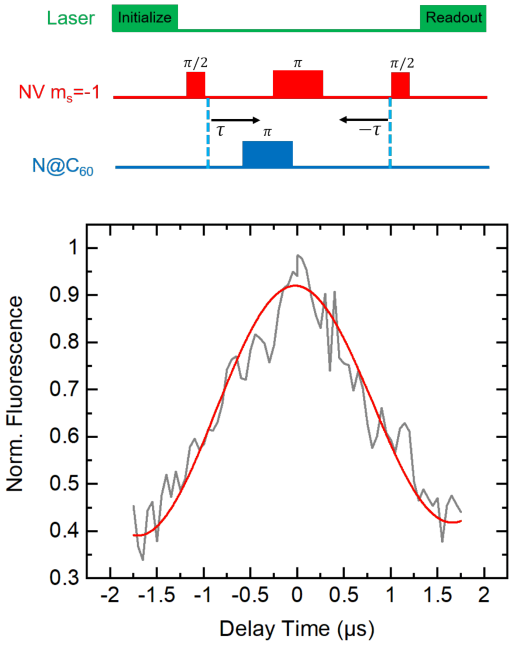

Figure 4.12: DEER Delay measurement on the external $N@C_{60}$ spins for the estimation of the actual number of involved molecules within the NV center detection region. Therefore, the external spin π pulse is varied in its position within the NV center Hahn sequence branch. Evaluation with Eq. 4.11 reveals that 3 $N@C_{60}$ spins are detected by the NV center quantum sensor.

4.3 Summary

In the last section we want to summarize the most relevant results which have been presented in this chapter. This part of the thesis was dedicated to the observation of single spins utilizing the NV center as quantum sensor. Therefore, DEER spectroscopy measurement sets were performed for probing the dipolar coupling between the NV center spin and individual external spins. Two different systems have been investigated.

Spin Labeled Polyphenols

In the first section, P5C-NR spin labeled $C_{48}H_{48}$ polyphenols were observed. The molecules were drop-coated on top of a [100] NV diamond membrane on which nanostructured pillars were etched beforehand. The pillar geometry has been used due to the waveguide mechanism of the structures for enhancing the collection efficiency of the single NV center emission. By performing DEER spectroscopy measurements, a dipolar coupling between the NV center spin and the external P5C-NR spins could be investigated. Furthermore, the hyperfine splitting of a spin labeled polyphenol cluster containing $\approx$ 50 spins was observed. The resulting spectra showed asymmetric hyperfine transitions which could be explained by the different orientations of the spin labels within the molecule clus-

ter. Nonetheless, a coherent manipulation of the external spins was observed in terms DEER Rabi oscillations. Unfortunately, further measurements could not be performed due to photo instabilities of the molecules. A degradation of the molecular compounds was observed in form of a fluorescence increase by performing measurements for 13 h.

Endohedral N@C_{60} Fullerenes

In the second section, the coupling between a single NV center spin and endohedral N@C_{60} fullerenes was investigated. Also here, the molecules were drop-coated on top of a pillar-etched, NV implanted [100] diamond membrane. ESR measurements were performed in terms of DEER DQT spectroscopy revealing the hyperfine interaction of the N@C_{60} spin. Due to the ^{14}N nucleus, the hyperfine spectrum should be presented by three frequency lines with a symmetric splitting of 15.9 MHz. However, our NV center based approach results into an asymmetric frequency splitting of 19.8 MHz and 16.1 MHz. This fact could be explained, by a potential deviation of the centrosymmetric C_{60} cage, leading to a non-vanishing zero field splitting parameter of $D = 1.52$ MHz. As a result the electronic spin of the encapsulated atom shows a preferential orientation. Furthermore, more sophisticated pulse schemes have been performed in order to characterize the N@C_{60} spin. With DEER Rabi measurement schemes, the external spin could be coherently manipulated. In addition, a DEER Hahn sequence revealed a minimum coherence time of 0.9 μs of the observed N@C_{60} spin. Finally, the actual number of involved external spins could be estimated by a DEER Delay pulse sequence. The measurement revealed a number of 3 N@C_{60} spins in the detection region of the NV center.
The presented results of the whole chapter successfully show the coupling of the NV center spin with a few individual external spins. As typical ESR techniques require a huge number of spins on the order of 10^6 to 10^{12}, the NV center as quantum sensor forms an advanced nanoscale magnetometer for the observation of single spin systems. In potential further works, the pulse schemes can be extended to triple electron electron resonance (TEER) spectroscopy measurements which are able to resolve the coupling mechanisms within a quantum network.

5 Measuring Nitrogen Spin Qubits with NV Center Ensembles

Besides applying nanoscale magnetic field sensors in medicine and pharmaceutics, sensitive magnetometers can also be utilized in the field of quantum information processing for detecting the interaction within a qubit network [134]. For this purpose, controlling the quantum dynamics of the network is a crucial task. Especially the qubit spin decoherence limits real-life applications of quantum technologies [135]. Usually, an uncontrolled spin bath (formed by impurities or parasitic electrons) acts as the main source for decoherence processes within the quantum network due to inhomogeneous coupling mechanisms [136]. A possible attempt for solving this issue is the coherent manipulation of the spin bath which potentially suppresses the dephasing of qubits and stabilizes the quantum framework. Although most electronic spin bath impurities are optically dark in the visible wavelength range, their readout can be achieved by ESR or electron nuclear double resonance (ENDOR) spectroscopy methods [137]. In general, this is performed by the application of HF pulses matching the ESR frequency of individual electrons in the $\approx 100\,\mathrm{MHz} - 10000\,\mathrm{MHz}$ regime (depending on the applied magnetic field) [67]. However, typical EPR measurements investigate the spin signal generated by the whole sample. For mitigating decoherence mechanisms, it is crucial to control environmental effects locally. A great approach for this can be realized in terms of scanning tunneling microscopy (STM) [138]. The method is based on vacuum tunneling processes of electrons between a metallic tip and a sample [138]. As a result, the topography of the sample surface can be reconstructed. In connections with high frequency circuits, ESR-STM experiments can be realized which allow the readout and coherent quantum control of surface-supported spin systems [139, 140, 141]. Nonetheless, a huge drawback of STM techniques is the requirement of a well conducting sample. Otherwise, the electron tunneling can not be achieved.

For performing local ESR measurements on environmental spin baths in more general samples, NV centers in diamond can be implemented. As the NV center detection principle relies on the dipolar coupling to external spins, the conductivity of the investigated samples does not play a crucial role. Therefore, this chapter presents the control and readout of an intrinsic spin bath within the diamond lattice utilizing an NV center ensemble. The spin bath is formed by nitrogen impurities termed as P1 centers. The measurements have been performed at UHV and at $4.7\,\mathrm{K}$. Utilizing the NV center ensemble as quantum sensor, the hyperfine spectrum of an P1 center ensemble has been revealed in a detection region of $2\,\mu$m x $2\,\mu$m. Furthermore, DEER Rabi measurements indicated coherent control and manipulation of the P1 center spin bath. Thereby, even the control of dipolar forbidden transitions

was achieved. The results of this chapter have been partially presented in [71].

5.1 The P1 Center in Diamond as Spin Qubit

The P1 center in diamond is, similar to the NV center, a well studied defect within the diamond crystal [142]. It consists of a single nitrogen atom which replaces a carbon atom within the crystal lattice. The defect can be interpreted as a solid state qubit due to its energy level scheme. However, a direct readout of the defect center is not possible. As the P1 center is optically dark, no spectral features can be obtained in the visible wavelength range. Nonetheless by coupling a P1 ensemble to NV centers, the hyperfine spectrum of the nitrogen impurities can be revealed [143]. Usually, this is achieved in terms of DEER spectroscopy which has already been discussed in chapter 2 and 4. However, before the obtained DEER measurements are presented, it is worth to describe the structural properties and the energy level diagram of the P1 defect center.

5.1.1 Structural Properties of the P1 Center

The nitrogen atom of the P1 center forms with the chemically bonded carbon atoms a tetrahedral symmetry which matches the underlying diamond lattice symmetry [71]. A very important feature of the P1 defect is the resulting Jahn-Teller effect (JTE) [144]. This effect describes the geometrical distortion of a molecular bond. The distance of at least one ligand to the central atom is then shifted and the bonding axis of the molecule is elongated. Such spatial distortions occur if different degenerated electron configurations can be occupied within the molecular bond. The elongation turns out to be energetically more favorable for the compound as the occupied molecular orbitals are lowered in energy. At the same time, the non occupied orbitals rise in energy. The splitting of the molecular orbitals removes the energetic degeneracy. For clarification, Fig. 5.1(a) illustrates the JTE on an octahedral compound. The splitting of the degenerated orbitals leads to an elongation along the z-axis in the shown example. In case of the P1 center, the JTE shifts the length along one of the N-C covalent bonds as depicted in Fig. 5.1(b) [71]. In fact, this distortion has an impact on the magnetic P1 center response. An externally applied magnetic field can be aligned along the non distorted bonds or parallel to the Jahn-Teller elongated chemical bond. Therefore, the P1 center experiences an axial and an off-axial magnetic field component.

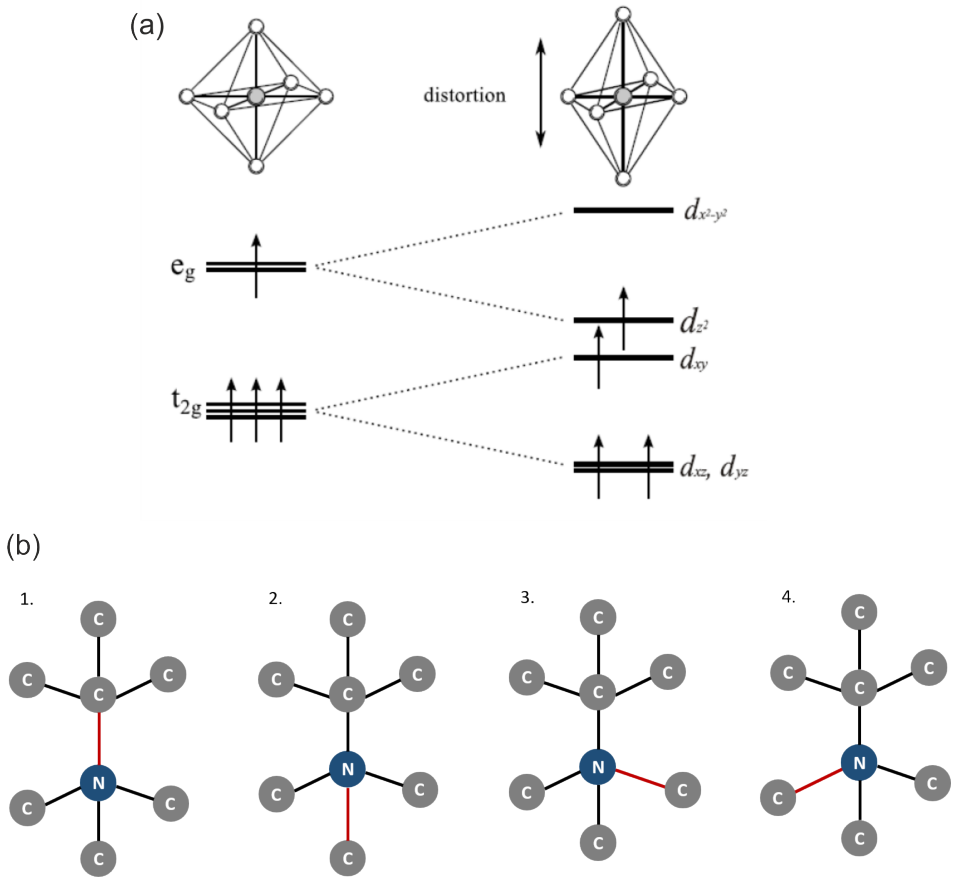

Figure 5.1: Illustration of the Jahn-Teller effect. (a) Distortion of the Mn^{3+} crystal due to the JTE. The rise of the molecular orbitals leads to an elongation of the compound. The sketch is adapted from [145]. (b) JTE on the P1 center in diamond which leads to an elongation of one of the four N-C covalent bonds. The elongated bond is highlighted in red. In a [111] diamond plate, the orientations 2, 3 and 4 are degenerated.

5.1.2 Energy Structure and Selection Rules

Also important to mention is the energy level structure of the P1 defect center. With the energy scheme, the resonance dips within the DEER spectrum can be identified and analyzed. The P1 center forms a $S = 1/2$ electronic spin system which is hyperfine coupled to a $I = 1$ nuclear spin [146]. Therefore, the defect obtains three dipolar allowed transitions ($\Delta m_s = \pm 1, \Delta m_I = 0$) which are highlighted as green arrows in the energy level scheme depicted in Fig. 5.2. Typically, these three lines are clearly observable as resonance dips in measured ESR spectra [143]. However, several publications also reported the investigation of less intense resonance lines which have been identified as the dipolar forbidden transitions ($\Delta m_s = \pm 1, \Delta m_I = \pm 1$) [147, 148, 149]. The intensity ratio between the forbidden transition lines and the dipolar allowed transition signals is about 1:5 [148] and are a typical feature in high density P1 center ensembles [147]. It is assumed that exchange interactions between triads of nitrogen

atoms are responsible for the rise of these dipolar forbidden transitions [147].

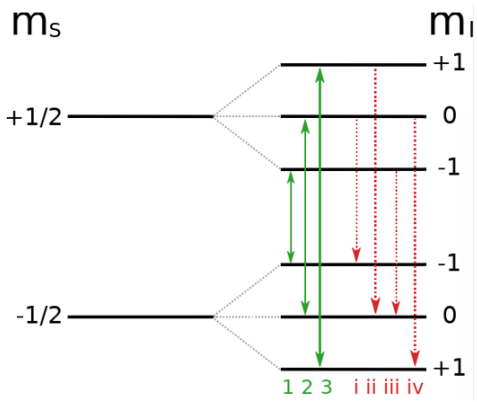

Figure 5.2: Energy level scheme of the P1 center in diamond. The green arrows represent the dipole allowed transitions. Instead, the dotted red arrows indicate dipolar forbidden transitions.

5.1.3 The P1 Center Spin Hamiltonian

In the last part of this section we want to introduce the P1 center Hamiltonian for having the theoretical framework in the evaluation of its spin properties. The P1 center ground state spin Hamiltonian can be written as [71]

$$H_{P1}^{spin} = H_{HF} + H_{EZ} + H_{NZ} + H_{NQ}. \tag{5.1}$$

The term H_{NQ} represents the quadropole interaction. In general, it can be neglected as it is orders of magnitudes smaller compared to the other terms. Also the nuclear Zeeman interaction H_{NZ} can be neglected as it is smaller compared to the electronic Zeeman interaction $H_{EZ} = \mu_B g_e B_z S_z$. Of great importance is the hyperfine interaction term $H_{HF} = A_{\parallel} S_z I_z + A_{\perp}(S_x I_x + S_y I_y)$ as the constants $A_{\parallel}$ and $A_{\perp}$ can be revealed by DEER spectroscopy measurements. For the P1 center, the axial and the off-axial hyperfine components are $A_{\parallel} = 114\,\text{MHz}$ and $A_{\perp} = 86\,\text{MHz}$. With the presented simplifications, the Hamiltonian (in units of $\hbar$) can be written as [71]

$$H_{P1}^{spin} = A_{\parallel} S_z I_z + A_{\perp}(S_x I_x + S_y I_y) + \mu_B g_e B_z S_z. \tag{5.2}$$

Also in this chapter, S_x, S_y, S_x and I_x, I_y, I_z represent the xyz-components of the electron spin operator $\boldsymbol{S}$ and nuclear spin operator $\boldsymbol{I}$. B_z is the applied magnetic field along the P1 center.

5.2 Measuring P1 Centers with an NV Ensemble

After the properties of the P1 defect have been described, the DEER spectroscopy measurements can be presented. The whole experimental set was performed in the cryo-UHV setup. The diamond used for this work is a δ-doped diamond plate (3 mm x 3 mm and thickness of 300 μm) which has been

grown by CVD (see chapter 2). The crystallographic orientation of the diamond plate is along the [111] facet. Due to the δ-doping, the diamond plate contains ensembles of NV centers. Furthermore, P1 center ensembles are embedded in the diamond matrix. It is worth to mention that the P1 centers have not been fabricated on purpose in this work. The huge amount of non-NV center defects could result from the fabrication method [80].

5.2.1 NV Ensemble Properties

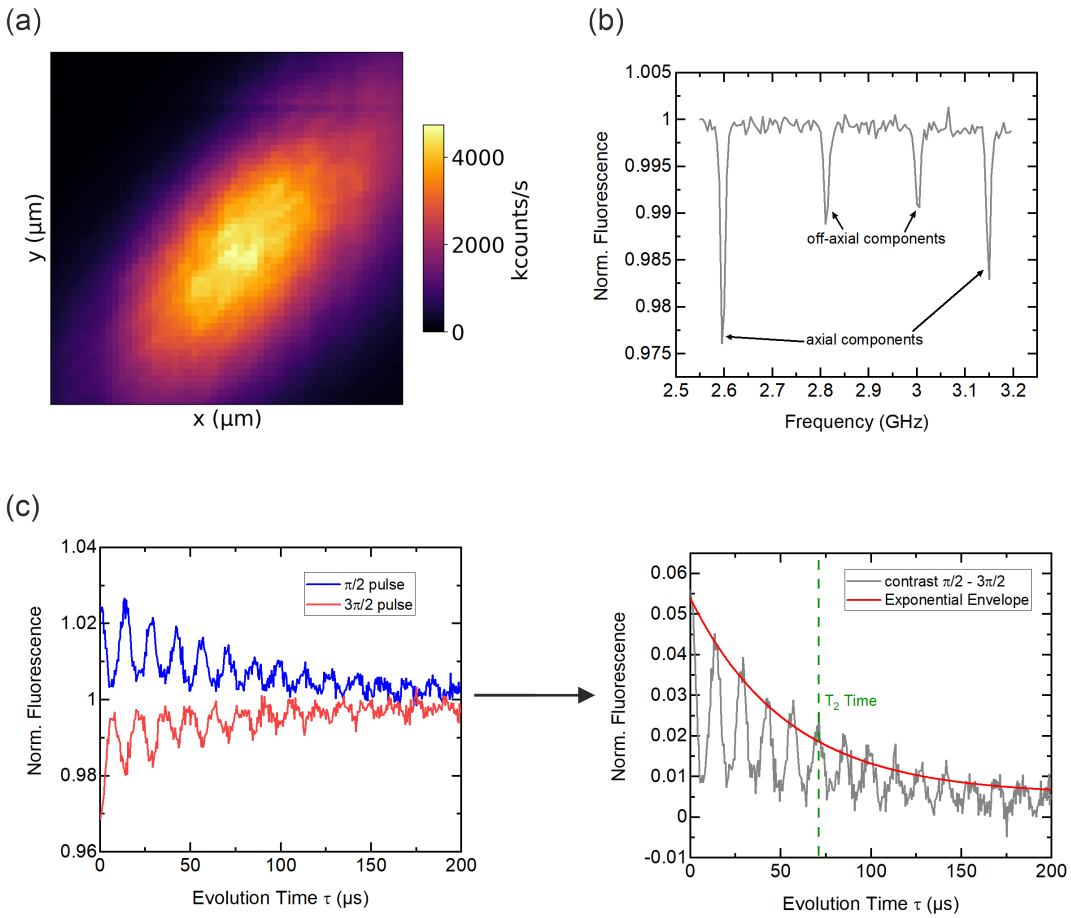

Figure 5.3: Pre-characterization of the NV center ensemble in the cryo-UHV environment. (a) Confocal scan indicating the NV center ensemble as bright cluster with an emission of 4000 kcounts/s. (b) ODMR spectrum obtained under a magnetic field aligned along the z-direction. Four resonance dips can be identified corresponding to NV centers oriented parallel to the magnetic field (outer peaks) and NV centers misaligned to the applied magnetic field (inner peaks). (c) Hahn measurement containing the NV center fluorescence with a $\pi/2$ back flip and $3\pi/2$ back flip. Even at an evolution time of 200 μs, a contrast of the bright and dark NV center spin states can be observed. The contrast plot, obtained by subtracting the $3\pi/2$ (red) curve from the $\pi/2$ (blue) curve, can be fitted with an exponential envelope revealing a T_2 time of 70 μs.

Typically, NV center experiments are performed with [100] oriented diamonds. In such crystallographic matrices, the implanted NV centers have no preferential orientations of their axis [150]. This means, that the NV orientation is distributed equally within the diamond lattice. However, NV centers in [111] oriented diamonds obtain a preferential orientation along the [111] direction [150]. An uniform NV center orientation within the ensemble is beneficial in terms of external magnetic field alignment. As most of the NV centers are pointing towards the [111] direction, the external magnetic field can easily be aligned regarding the majority of the NV centers. In that way, the fluorescence quenching obtained from NV defects which are not oriented as the applied magnetic field is minimized. Consequently, high contrast ODMR spectra can be obtained [151].
Fig. 5.3 shows a measurement set for pre-characterizing an NV center ensemble within the presented [111] diamond plate. The measurements were obtained at 4.7 K and in an $2 \cdot 10^{-10}$ mbar UHV environment. As starting point, Fig. 5.3(a) presents the confocal image of the observed NV ensemble. A fluorescence of $\approx 4000\,\mathrm{kcounts/s}$ can be recorded indicating a relatively high NV center density of $\approx 150\,\mathrm{NVs}/\mu\mathrm{m}^2$. For obtaining the ODMR spectrum of the system, the laser spot is focused at the center of the NV ensemble. The resulting resonance lines are depicted in Fig. 5.3(b). In contrary to the single NV measurements in which only two resonance frequencies are observed, an ODMR spectrum obtained from an [111] oriented NV ensemble shows four resonance lines. Thereby, the outer resonances with a splitting of $\Delta f = 540\,\mathrm{MHz}$ are contributed to the NV centers aligned along the [111] facet. The diamond [111] orientation corresponds to the z-direction. Furthermore, the external magnetic field is also applied along the z-direction. Therefore, the applied magnetic field can be calculated by $B_z = \frac{\Delta f}{2\gamma}$ leading to an estimated magnetic field strength of 9.88 mT. In contrary, the inner resonance lines are contributed by the NV centers which are not oriented in the z-direction. The difference in peak intensity between the inner and outer dips can be explained by the already discussed preferential orientation of the NV centers within a [111] diamond plate. The amount of NVs which are oriented along the z-direction ($\approx 99\%$) is much higher compared to the NV centers aligned in another orientation [150, 151].
An advantage of such a selective NV center alignment is shown in Fig. 5.3(c) in form of a Hahn measurement. In a perfect z-orientated external magnetic field, an efficient decoupling of the NV spins from the environmental noise can be achieved [152]. As a result, the Hahn sequence reveals a relatively huge coherence time of 70 μs compared to the measurements presented in chapter 4 in which the observable T_2 was $< 15\,\mu$s.

5.2.2 Sensing P1 Ensembles

Based on the pre-characterization measurements, DEER spectroscopy can be performed with the NV center ensemble. With this, potential couplings to external spins within the diamond lattice can be investigated. Candidates for external spins can be formed by other impurities like P1 center ensembles. The DEER spectroscopy measurements were obtained by sweeping the external spin pulse frequency from 200 MHz to 600 MHz. The Hahn branch of the NV center ensemble was chosen according to

Fig. 5.3(c) to 70 μs. Fig. 5.4 presents the resulting DEER spectrum in which 8 resonance lines can be observed. The frequency splitting between the central dip at $\approx$ 400 MHz and the most outer peak at $\approx$ 285 MHz is 115 MHz. This is in very good agreement with the axial hyperfine constant $A_{\parallel} = 114$ MHz of the P1 center in diamond. Furthermore, the splitting between the central line and the second outer line at 310 MHz is 90 MHz which would correspond to the off-axial hyperfine constant $A_{\perp} = 86$ MHz of the P1 center. Therefore, a coupling of the NV center ensemble to a P1 ensemble can be assumed. As a consequence, the lines in the DEER spectrum were divided into three categories termed as 1-3, 1′-3′ and i′-ii′, corresponding to the transitions within the level diagram of the P1 center.

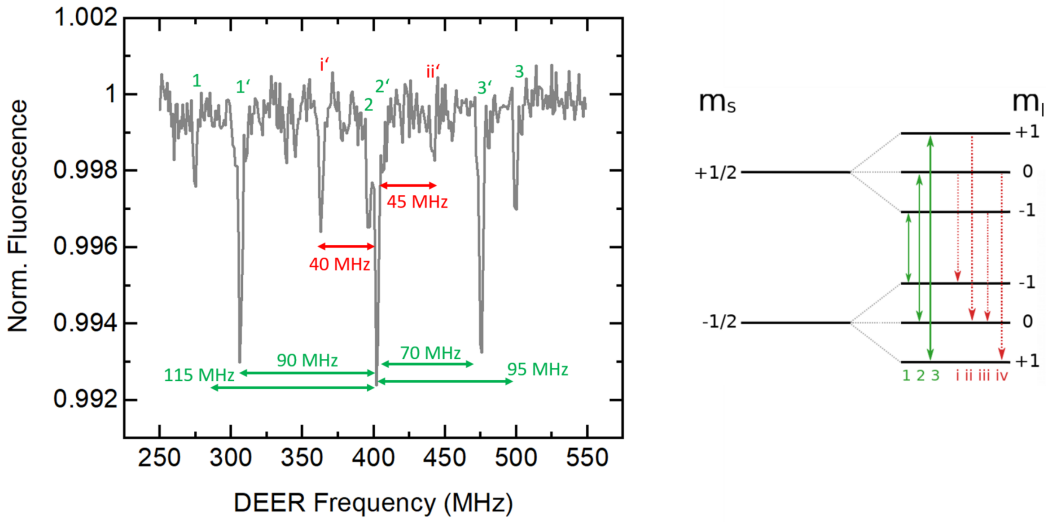

Figure 5.4: DEER spectrum obtained by the investigated NV center ensemble at a temperature of 4.7 K and at an UHV environment of $2 \cdot 10^{10}$ mbar. Due to the frequency splittings, the observation of an P1 center ensemble can be assumed. Therefore, the resonance lines are termed regarding the P1 center energy level scheme illustrated on the right. Dipolar allowed (1-3) and forbidden transitions (i-ii) can be observed.

For clarification, the energy level scheme from Fig. 5.2 is added beside the DEER spectrum. The frequency lines 1-3 indicate the dipolar allowed transitions obtained from the axial oriented P1 centers relative to the applied magnetic field. Instead, the resonance lines from the off-axial P1 centers are termed as 1′-3′. The axial P1 center orientation dependence results from the discussed JTE (see 5.1.1). The third category i′-ii′ corresponds to dipolar forbidden transitions of the off-axial P1 centers. These lines have also been observed in [148]. However, the intensity ratio in [148] was measured to be on the order of 1:5 compared to the dipolar allowed transitions. In contrary, the i′ line (at $\approx$ 360 MHz) in the DEER spectrum of Fig. 5.4 shows an amplitude which is comparable with the allowed axial transitions (1-3). The intensity ratio compared to the strongest line 2′ is almost 1:2.

5.2.3 Detection of P1 Center Forbidden Transitions

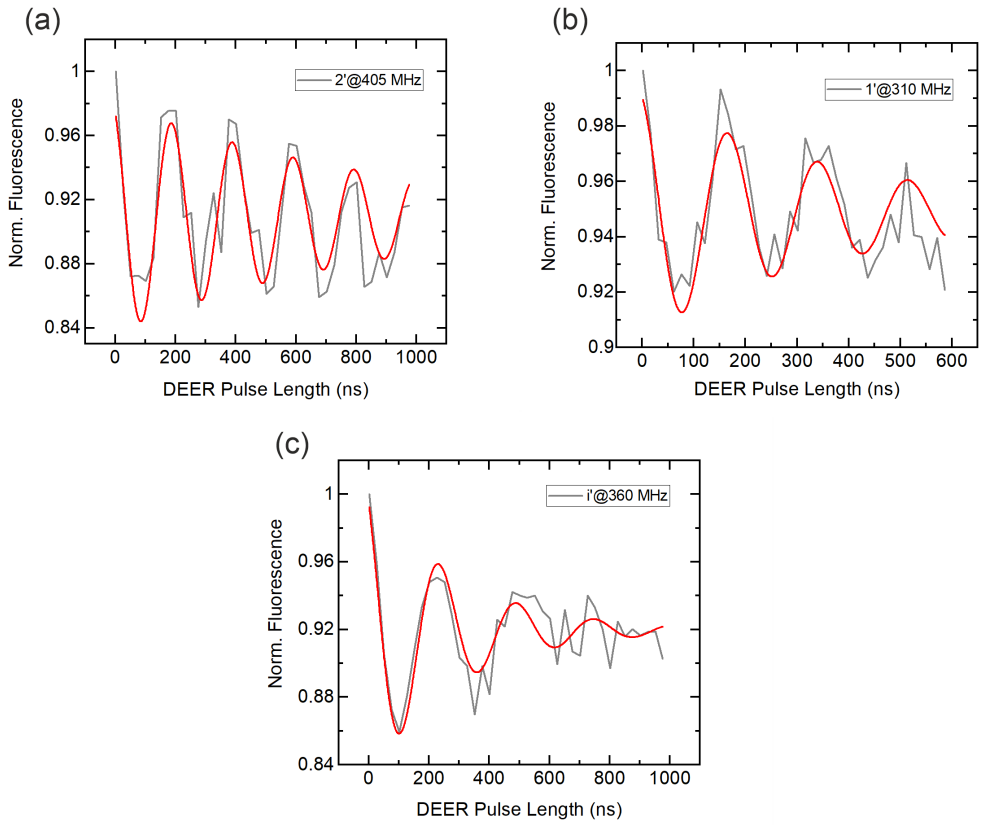

Figure 5.5: DEER Rabi measurements in cryogenic UHV conditions obtained at (a) the central 2′ dipolar allowed transition (405 MHz), (b) the outer 1′ allowed transition (310 MHz) and (c) the forbidden i′ transition (360 MHz). In all three cases, coherent spin manipulation processes can be investigated.

In order to study the dipolar forbidden transitions in greater details, DEER Rabi measurements can be performed. With this, coherent spin flip processes can be investigated for proving the actual existence of external spins within the NV ensemble detection region. Fig. 5.5 shows three DEER Rabi measurements obtained by the central 2′, outer 1′ and forbidden i′ resonances. As expected, the allowed transitions at 405 MHz (Fig. 5.5(a)) and 310 MHz (Fig. 5.5(b)) clearly indicate spin flips of the P1 center ensemble. The spin lifetime in the rotating T_ρ frame of the central line is on the order of $\approx$ 900 ns. Instead for the outer line, the exponential envelope of the oscillation reveals a T_ρ time of about $\approx$ 400 ns. Of greater interest is the measurement on the dipolar forbidden transition at $\approx$ 360 MHz. Only if a DEER frequency line shows DEER Rabi oscillations, it can be surely confirmed that the resonance stems from external spins. In fact, coherent spin manipulations can be observed on the i′ as depicted inf Fig. 5.5(c). By varying the duration of the fixed DEER pulse at 360 MHz from 0 to 1000 ns, 7 spin flips can be observed. Furthermore, a clear exponential decay of the oscillation

amplitude is investigated which estimates a T_ρ time of 288 ns. This findings indicate a relatively stable dipolar forbidden transition within the measured P1 ensemble. A strong anisotropic exchange within the P1 center ensemble can be assumed [147] which can be expressed as [153]

$$R = \frac{1 + 4e^{-3J/2k_BT}}{4 + 2e^{-3J/2k_BT}}. \tag{5.3}$$

In this equation, T is the temperature, k_B the Boltzmann constant and J the exchange energy parameter. In case of a P1 center ensemble, this value has been estimated to $J = 2\,\mathrm{cm}^{-1}$ [147]. According to [147], the P1 center density is estimated to be on the order of 10^{18} spins/cm^3 for observing such strong dipolar forbidden exchange mechanisms.

5.2.4 Measurements at Ambient Conditions

Furthermore, Eq. 5.3 shows a temperature dependence of the anisotropic exchange. Also this has been noted in [147] by comparing P1 center EPR spectra measured at 77 K and 20 K. A decrease of the forbidden transition peak intensity has been recorded by decreasing the temperature.
Therefore, it is reasonable to perform DEER spectroscopy also at ambient conditions. For this, the sample can be placed at the ambient measurement stage which we introduced in chapter 3. The experimental process is the same compared to the measurements within the cryo-UHV setup. Furthermore, nano-fabricated markers enabled to re-find the position of the investigated NV center ensemble for a reliable comparison between the cryo-UHV and ambient condition measurements. Fig. 5.6 shows the recorded DEER spectrum from the ambient measurement setup. An obvious finding is the decreased signal-to-noise ratio of the spectrum compared to the result obtained at 4.7 K. The increased noise level is caused by thermal instabilities in the ambient environment which have an impact on dynamical magnetization processes [154]. As a result, resonance lines are broadened and the resolution of specific transitions is limited. In fact, only three main peaks can be observed with a frequency splitting of about 115 MHz and 90 MHz matching the P1 center hyperfine properties. Therefore, the resonances have been termed according the presented DEER spectrum in Fig. 5.4 to 1(1′), 2(2′) and 3(3′). However, the axial and off-axial components can not be distinguished due to the thermal instabilities at ambient temperatures of $\approx$ 300 K. Nevertheless, the peak widths can lead to the assumption that both orientations contribute within one resonance line. A more important fact is the strong appearance of a resonance dip at 280 MHz which can be identified as the dipolar forbidden transition i′. The intensity ratio compared to the central line at 310 MHz is 1:1.3 which is well above the noted intensity ratio of 1:2 obtained by the measurement at 4.7 K. This is in good agreement with the published results from [147] which indicate decreased intensities of the forbidden resonance lines by lower temperatures. Furthermore, the presented results of this section show that the appearance of dipolar forbidden transitions in the P1 center spectrum mainly depends on the P1 defect concentration within the diamond lattice.

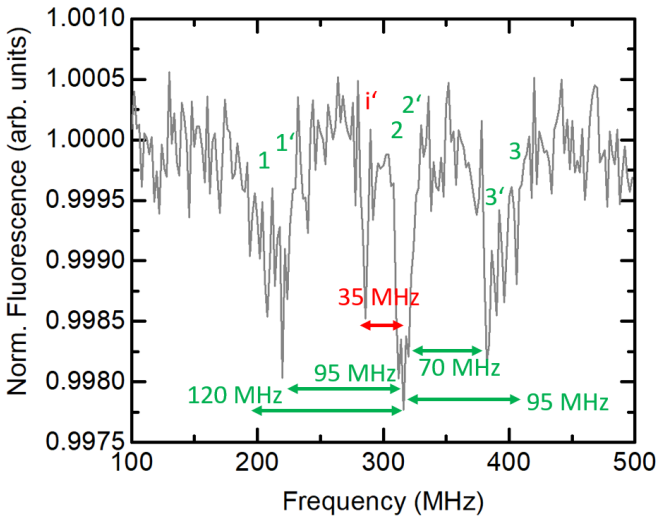

Figure 5.6: DEER spectroscopy measurement at ambient conditions. The P1 center hyperfine spectrum can be reproduced. However, the axial and off-axial components can not be distinguished due to thermal instabilities. Nevertheless, a significant signal of the dipolar forbidden transition i′ can still be observed.

5.3 Summary

In this chapter, the control of an spin bath environment was described. Thereby, an NV center ensemble was used to detect and coherently manipulate an P1 center spin bath within an [111] oriented diamond sample. The measurements were performed in terms of DEER spectroscopy in UHV and at 4.7 K. The resulting ESR spectrum contained frequency splittings being in good agreement with the P1 center hyperfine constants of $A_{\parallel} = 114\,\mathrm{MHz}$ and $A_{\perp} = 86\,\mathrm{MHz}$. Furthermore, the coherent control of the spin bath was presented by DEER Rabi measurements. Interestingly, a strong appearance of dipolar forbidden transitions was observed in the DEER spectrum. The rise of this resonance lines can be attributed to exchange interactions between nitrogen triads in high density P1 center ensembles. Even at these dipolar forbidden transitions, DEER Rabi oscillations could be observed. This is a clear indicator that the recorded forbidden transitions in fact stem from the external spin bath.
In order to study the forbidden transitions more detailed, DEER measurements at ambient conditions have been performed. Also in that scenario, the resulting DEER spectrum showed the appearance of the dipolar forbidden frequency lines. Therefore, a high P1 center density on the order of $10^{18}\,\mathrm{spins/cm^2}$ can be assumed as such strong exchange mechanisms appear only in heavily nitrogen doped diamonds. In parallel, our findings also show that NV center ensembles are able to control spin baths with relatively high spin concentrations which can form suitable applications in the field of quantum information processing.

6 Observation of Superconducting Phase Transitions with NV Centers

Besides utilizing NV centers for the characterization of individual spins, the defects can also be implemented for observing magnetism and collective spin phenomena in solid compounds as superconductors or ferromagnetic materials. Especially studies on superconducting systems are catching the central interest in modern physics due to their wide range of applications. Since the discovery of superconductivity in 1911 [155], advances have been made in understanding the phenomenon. Furthermore, several materials have been investigated which exhibit this effect including different metals, intermetallic compounds and cuprates [156]. Applications of superconductors can be found in the areas of electromagnets, sensors and electronics. In sensing applications, superconductivity plays the central role for SQUIDs which are able to accurately measure magnetic fields and related electromagnetic quantities [156]. Furthermore, magnets based on superconducting materials are largely used in MRI devices for generating the large background magnetic field which is required for NMR scans in biological systems [156].
The main characteristics of a superconductor are the vanishing electrical resistance and the expulsion of external magnetic fields from the corresponding material.

Material	Critical Temperature T_c [K]
Metals	
Nb	9.25
V	5.4
NbTi	9.8
Intermetallics	
V_3In	13.9
Nb_3Si	19
Cuprates	
YBCO	86
LSCO	40
HBGCCO	138

Table 6.1: Examples for superconducting materials and the corresponding critical temperature T_c adapted from [156].

Therefore, the most important physical quantities which characterize a superconducting material are the critical temperature T_c, the critical magnetic field H_c and the critical current J_c. The critical temperature T_c is defined as the temperature point at which the resistance of the material drops abruptly to zero [157]. The process forms phase transition from the normal state to the superconducting state of the material. In this phase the compound acts as an ideal diamagnet and expels external magnetic fields. The phase called Meissner state [158]. Therefore, H_c defines the magnetic field strength at which the expulsion of the field (and with this the Meissner state) is destroyed [158]. Connected to this, the critical current J_c is the maximum value of the current in a superconducting material at which the superconductor passes into its normal state [159]. Examples for superconducting materials can be found in Tab.6.1, illustrating their corresponding critical temperature. Various approaches have already been established for the investigation of superconducting systems and their characteristics including SQUIDs [160], magnetic force microscopy (MFM) [161], STM [162] and the observation of magneto-optical effects [163]. However, each of these techniques suffer from different drawbacks such as limited temperature and magnetic field ranges and most importantly spatial resolution which is a crucial factor for microscopic studies on superconductors. Especially, low dimensional thin film samples of superconducting systems have demonstrated unique magnetic phases like the formation of Abrikosov vortices which are characterized by a circulating supercurrent [164]. The diameter of such a vortex is on the order of few μm [165]. Therefore, magnetic field sensors with a high spatial resolution in the nm range and a high magnetic field sensitivity of $\mu\mathrm{T}/\sqrt{\mathrm{Hz}}$ can be beneficial for such investigations on the single vortex level.
An ideal candidate for these criteria is the NV center in diamond. Therefore, we demonstrate in the present chapter the utilization of NV centers for the characterization of a superconducting $La_{2-x}Sr_xCuO_4$ (LSCO) thin film on a local level. For this, we use the first section for presenting existing work of how NV centers detected superconducting phases by ODMR spectroscopy. After that, we introduce LSCO as type II superconductor by characterizing its T_c and H_c with established experimental methods, namely SQUID and mutual inductance measurements. The main result of this chapter is shown in the third section in which we introduce an all-optical and microwave-free detection method based on an NV ensemble for spatially resolving the Meissner screening of the LSCO thin film sample. The results have been published in [166]. Finally, we report the investigation of single vortices with our all-optical method in the last experimental section of this chapter.

6.1 Measuring the Meissner State with NV Centers

The NV center in diamond forms an ideal candidate for spatial studies of magnetism on superconducting samples due to its high magnetic field sensitivity of $1\ \mu\mathrm{T}/\sqrt{\mathrm{Hz}}$ in the case of single NV centers and $1\ \mathrm{pT}/\sqrt{\mathrm{Hz}}$ in the case of NV ensembles and its spatial resolution of about 100 nm [167]. In fact, NV center ensembles have been used for probing the Meissner state in superconducting samples by recording their ODMR spectra at different temperatures [168, 169]. Due to the magnetic field depen-

dence of the ODMR splitting, the field strength on the NV centers was estimated. For instance, this has been presented in [169] by the investigation of superconducting $LuNi_2B_2C$ and $Ba(Fe_{1-x}Co_x)_x$ samples as depicted in Fig. 6.1.

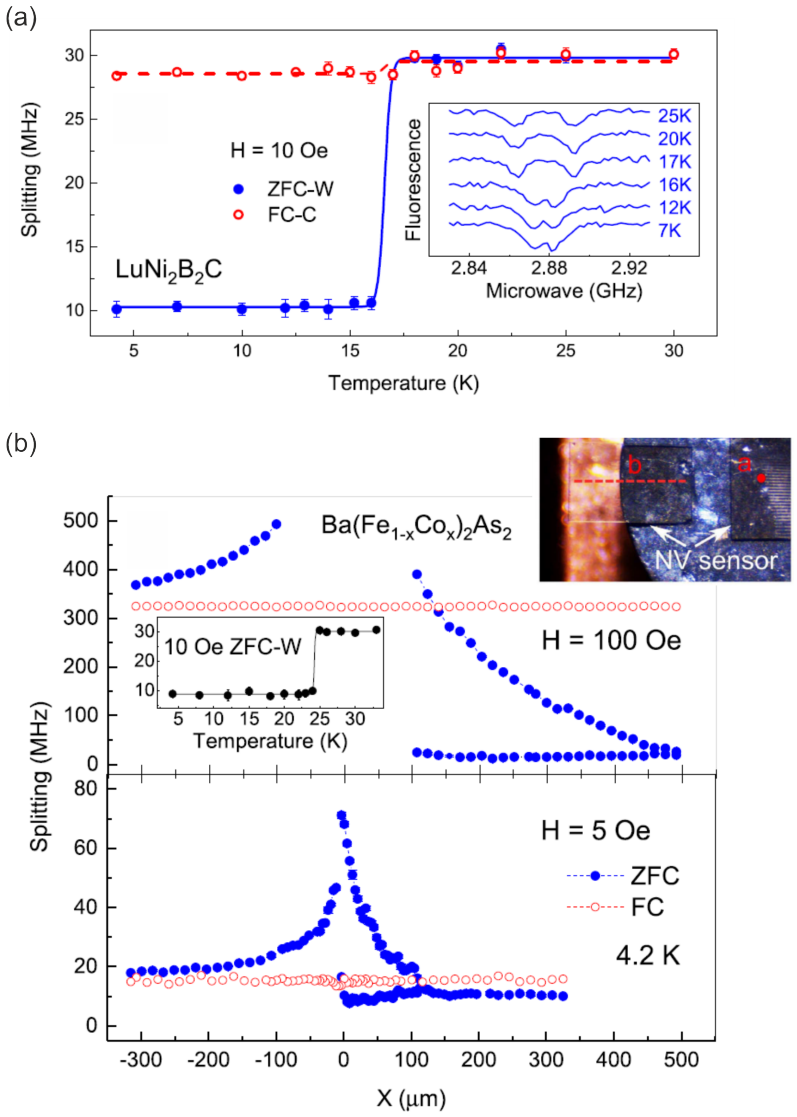

Figure 6.1: Investigation of the Meissner phase by using NV center based ODMR spectroscopy. (a) Frequency splitting of an NV center ODMR spectrum recorded at different temperatures. The NV implanted diamond plate is positioned on top of a superconducting $LuNi_2B_2C$ sample. A significant drop of the frequency splitting at about 16 K can be observed corresponding to the T_c of the investigated compound. (b) Spatial resolution of the Meissner screening in a $Ba(Fe_{1-x}Co_x)_x$ compound by measuring the NV ensemble ODMR spectra across the sample. The inset shows the positioning of the diamond plate at the edge of the sample. An increased ODMR frequency splitting obtained from the NV ensemble outside of the superconductor can be observed compared to the splitting inside of the sample. The figures are adapted from [169].

Thereby, Fig. 6.1(a) shows the ODMR splitting of an NV center ensemble attached to a corresponding $LuNi_2B_2C$ superconductor for different temperatures [169]. An abrupt drop of the frequency splitting was investigated at about 16 K corresponding to the T_c of the sample. As the superconductor went a phase transition from its normal state to its superconducting state (and with this into its Meissner state), the applied magnetic field was expelled from the surface. As a result, the NV centers detected almost no magnetic field in form of a decreased frequency splitting in the ODMR spectra. In addition, the Meissner screening has been spatially resolved by recording NV center ODMR spectra in close proximity to the sample edge. This is illustrated in Fig. 6.1(b) which shows the ODMR frequency splitting at different positions across the edge of a superconducting $Ba(Fe_{1-x}Co_x)_x$ sample [169]. The temperature was kept constant at 4.2 K which is well below the critical temperature of the material of $T_c = 24$ K. The geometry of the investigated system is depicted in the inset of Fig. 6.1(b) showing the NV implanted diamond plate glued at the edge of the superconductor. It was observed that the splitting of the NV centers inside the superconducting sample was lower compared to the splitting of the NV centers outside the superconductor. Also this, was explained by the Meissner state of the material which expels the applied magnetic field.

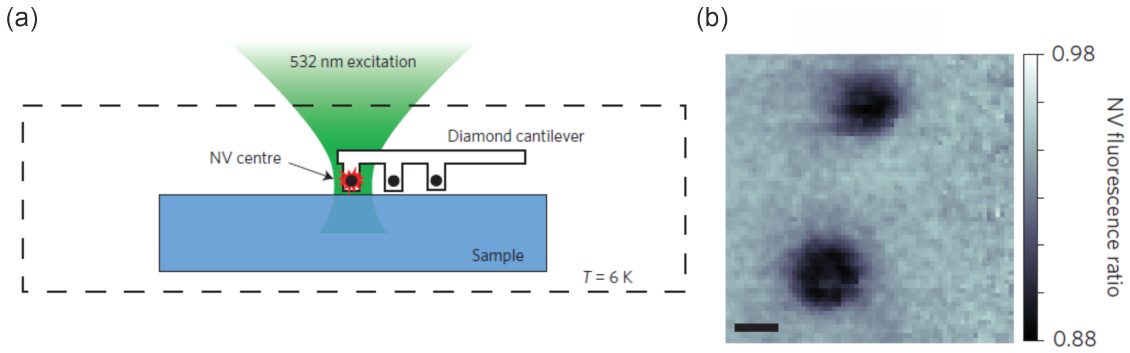

Figure 6.2: Observation of magnetic vortices with single NV centers in a diamond AFM geometry. (a) The AFM tip is made out of diamond. Single NV centers can be implanted at the tip. By scanning the diamond cantilever across a sample, its magnetic characteristics can be investigated locally. (b) Resulting image by scanning an NV implanted diamond tip across the surface of a superconducting $BaFe_2(As_{0.7}P_{0.3})_2$ sample. Single magnetic vortices with a diameter of about 300 nm can be resolved. The scale bar represents 200 nm. Both figures have been adapted from [171].

More sophisticated measurement schemes have been performed by [170] and [171] utilizing single NV centers as scanning probes. The experimental geometry is depicted in Fig. 6.2(a) [171]. For such measurements, a cryogenic atomic force micrscopy (AFM) setup was used in which the AFM probe is made out of a diamond tip [172]. At the apex of the tip, a single NV center was implanted [173]. The probe was scanned over a superconducting sample. Simultaneously, the ODMR spectra of the NV center tip were recorded. By observing the resulting frequency splitting, a magnetization profile of the superconducting surface was reconstructed [170, 171]. With this method, single vortices

with a diameter of about 200 nm have been imaged as shown in Fig. 6.2(b). Based on these imaging techniques, important superconducting quantities could be estimated like the critical field H_c or the London penetration depth λ of the investigated μm-sized samples [174, 175, 176].
Nevertheless, all the presented experiments were based on ODMR spectroscopy which relies on a resonant excitation of the NV center spin sublevels with microwaves. Usually, MW excitations are linked with heating effects which could potentially change properties of the investigated sample [177]. Especially for superconducting systems, the heating above T_c has a crucial impact on the material properties. Therefore, we present in this chapter an all-optical, microwave-free measurement method which solely relies on the direct NV center fluorescence. For demonstrating this, we positioned an NV implanted diamond membrane at the edge of a superconducting LSCO thin film. The properties of LSCO and the characterization of our thin film sample are described in the following section.

6.2 Thin Film LSCO Measurements

LSCO is one of the first discovered and with this one of the most studied high-T_c cuprate superconductors [178]. Cuprates are characterized by layers of copper oxides (CuO_2) alternating with layers of charge reservoirs (CR) [179, 180]. The crystal structure of LSCO illustrating the CuO_2 planes and the involved La and Sr atoms is depicted in Fig. 6.3.

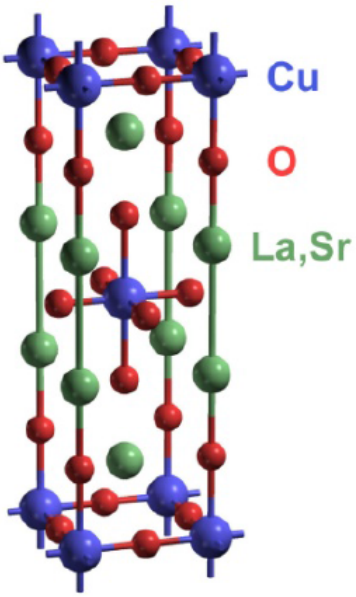

Figure 6.3: Crystal structure of LSCO showing the CuO_2 planes (Cu atoms depicted in blue, O atoms depicted in red) which form the main crystallographic characteristic of the cuprates family. The La and Sr atoms (depicted in green) are positioned within these planes. The sketch is adapted from [180]

Due to their relatively high critical temperature, cuprate based superconductors attracted a huge atten-

tion in condensed-matter physics. While metallic superconductors like niobium (Nb) obtain a T_c of about 9 K, cuprates are characterized by critical temperatures in the range between 35 K (for LBCO) and 138 K (for HGBCCO) [156]. The literature value of T_c for LSCO (the material utilized in this work) is between 35 K and 42 K, depending on the doping level x of the La and Sr atoms [178]. Furthermore, LSCO is, like most of the cuprates, a type II superconductor [181]. This means that the material does not exhibit only one critical magnetic field H_c (like in the case of type I superconductors) [181]. In fact, SQUID measurements are able to show two critical fields in type II superconductors [178, 181]. The first critical field H_{c1} corresponds to the magnetic field strength at which magnetic fluxes start to penetrate through the superconducting surface forming vortices. At the second critical field H_{c2}, the Meissner state of the superconductor is fully destroyed and the material exhibits its normal state. In case of LSCO bulk samples, H_{c1} is about 10^{-2} T whereas the second critical field H_{c2} is about 10^2 T [178]. These quantities depend not only on the doping level of the material but also on the temperature. Due to the wide range of experimental studies on LSCO, the material forms an ideal candidate to benchmark our novel NV magnetometry technique. Furthermore, LSCO has attracted much interest since diamagnetic activities have been measured above T_c of such thin films [182]. Therefore, it also forms an interesting superconducting system which can be investigated in future experiments with our method.

6.2.1 Fabrication and Characterization of the LSCO Sample

The LSCO thin film which has been used in the experiments of this chapter has been grown by ozone-assisted atomic layer by layer molecular beam epitaxy (MBE) on a single crystalline [001] $LaSrAlO_4$ (LSAO) substrate [183]. MBE is characterized by the evaporation of certain elements from metal sources which constitute the desired compound [183]. The evaporated elements are then recombined on the surface of a substrate. For ensuring undesired intermixing of different atoms, the kinetic energy of the incoming atoms has to be kept low. This can be achieved by a low deposition rate and an in situ reflection high energy diffraction (RHEED) control. Furthermore, for growing our LSCO sample the temperature of the LSAO substrate was kept at 630 K and the pressure chamber was maintained at 10^{-5} Torr [166]. The low gas pressure is crucial for ensuring the ballistic path of the evaporated atoms from the metal source to the deposition surface [183]. As a result, we obtain a single crystalline LSCO thin film with a thickness of 20 nm. The doping level of the fabricated sample is at $x = 0.16$. Furthermore, the sample length and width are defined by the substrate size and are both about 1 cm.
In order to characterize our superconducting 20 nm LSCO thin film, we performed mutual inductance measurements and SQUID measurements.

Mutual Inductance Measurement

Measuring the mutual inductance between two coils is a reliable method for estimating the critical temperature of a superconducting sample [184]. The sample has to placed between the two pick-up coils. By applying a weak magnetic field, an electromagnetic interaction between the coils can be

investigated known as mutual inductance. The investigation of the inductance can be recorded under sweeping the temperature. At T_c the superconductor obtains its Meissner phase which disturbs the interaction between the pick-up coils. This can be observed as sharp drop of the mutual inductance. Fig. 6.4 shows the explained measurement set on our LSCO thin film sample The resulting curve reveals a T_c of about 34 K. While the real part of the mutual inductance drops at T_c, the imaginary part shows an observable peak at that temperature.

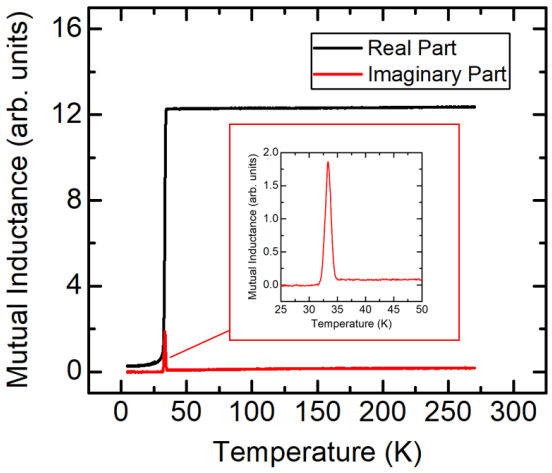

Figure 6.4: Mutual inductance measurement of the utilized LSCO sample. The interaction between two pick-up coils is investigated. Within these, the LSCO sample is positioned. The drop in the real part and the peak in the imaginary part of the mutual inductance identify the T_c of the LSCO sample at about 34 K.

SQUID Measurement

Furthermore, a SQUID measurement can be performed for recording the magnetic moment m of the sample as a function of an externally applied magnetic field. This reveals further information about the magnetic phase diagram of the investigated sample including H_{c1} and H_{c2} [181]. Therefore, the superconductor has been placed in an MPMS3 magnetometer device (from Quantum Design Co.). The resulting magnetic moment curve is depicted in Fig. 6.5 indicating a lower critical field of about $H_{c1} = 2\,\mathrm{mT}$ where magnetic fluxes start to enter the superconducting sample (red box of Fig. 6.5). The Meissner state of the thin film sample is fully destroyed at a magnetic field strength of $H_{c2} = 7\,\mathrm{T}$. In addition, the full star-shape of the hysteresis curve in Fig. 6.5 confirms the diamagnetic behavior of the LSCO sample in its Meissner phase and the absence of ferromagnetic impurities [166].

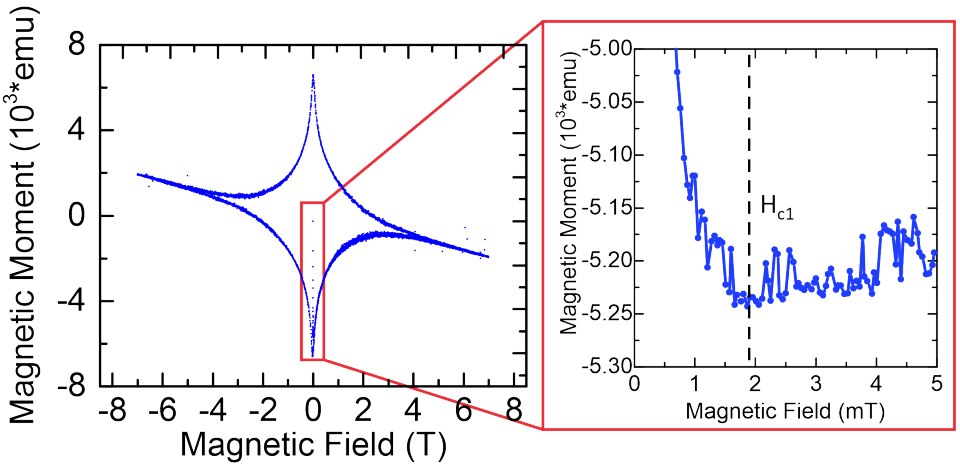

Figure 6.5: SQUID measurement of the utilized LSCO sample within a magnetic field sweep from 7 T to −7 T. The star shaped curve indicates the diamagnetic properties of the sample. The red box illustrates the low magnetic field region of the SQUID measurement showing a first magnetic field penetration at about 2 mT.

6.2.2 Detecting the Meissner State with an NV Ensemble

After we described the characterization of the LSCO sample with conventional magnetometry methods, we want to implement NV centers for locally observing its Meissner state. Therefore, an NV implanted [100] oriented diamond crystal plate (4 mm x 2 mm) was glued at the edge of the LSCO superconductor as illustrated in Fig. 6.6(a). The NV density over the whole diamond plate is about 200 NVs/μm^2. Note that all NV center initialization and readout schemes in this chapter have been performed with a laser wavelength of 512 nm (see chapter 2 and 3). For detecting the Meissner screening of a thin film sample it is crucial to align the external magnetic field perpendicular to the sample surface. In order to achieve this, the magnetic field alignment has been performed by investigating the ODMR spectra of the NV ensemble outside of the superconductor ($y > a$ in Fig. 6.6(a)) [150]. Therefore, not only the frequency splitting Δf is important but also the symmetry of the splitting. Fig. 6.6(c)-(e) show three ODMR spectra of an NV ensemble for different magnetic field orientations. In a [100] diamond membrane, there is no preferential orientation of the NV symmetry axis along one of the four possible crystallographic axes [150]. This fact has already been discussed in chapter 5. As a result, all four NV orientations are obtained almost equally in a dense NV ensemble. Therefore, an NV center ensemble ODMR spectrum shows four frequency lines when the magnetic field is aligned along one of the four axes. Such an example is shown in Fig. 6.6(c). The outer lines correspond to the NV centers which are oriented parallel to the external magnetic field. Instead the inner lines, come up with the NV centers for which the magnetic field is not aligned. Assuming that all four orientations are distributed equally on the investigated ensemble, the ratio between the aligned axes and not-aligned axes is 1:3 [150].

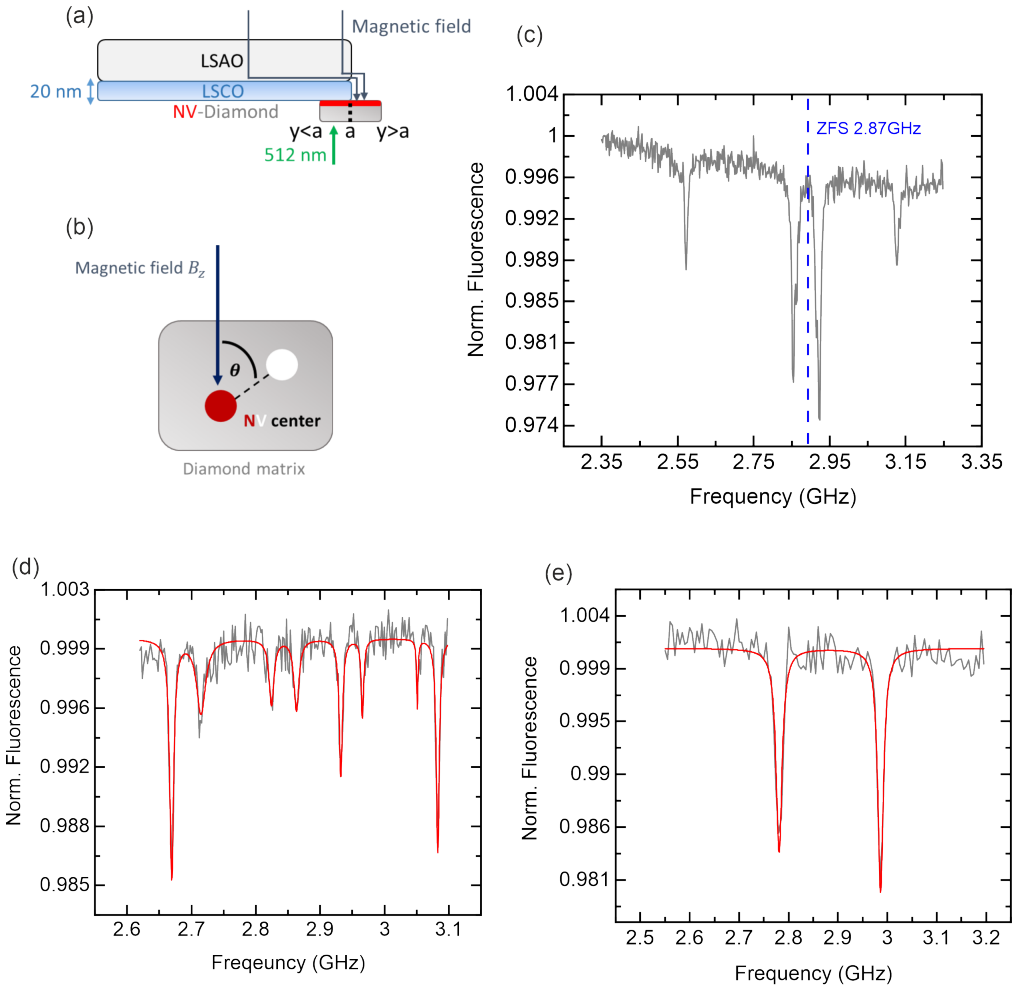

Figure 6.6: Sketch of the sample geometry and magnetic field alignment procedure. (a) The NV ensemble implanted diamond membrane is positioned at the edge of the thin film LSCO sample. This geometry allows the characterization of superconducting effects ($y < a$) and the performance of background measurements ($y > a$). (b) Angular relation between the NV center axis and an applied magnetic field defined by the angle θ. In case of a magnetic field aligned in z-direction, the angle θ is 54.75°. (C) ODMR spectrum of an NV center ensemble in a [100] diamond membrane in which the magnetic field has been aligned along one of the four NV center axis orientation. (d) ODMR spectrum recorded with misaligned magnetic field. (e) resulting ODMR frequency splitting when the magnetic field is oriented in z-direction.

This can be observed by the intensity of the frequency dips in Fig. 6.6(c). The magnetic field can be extracted by the frequency splitting with $\Delta f = 2\gamma B_{NV}$ in case of the outer lines (when NV axis and magnetic field are parallel to each other) or by $\Delta f = 2\gamma B_0 \cos 109.5°$ in case of the inner lines (when the angle θ between magnetic field and NV axis is 109.5°). The angle between the NV axis and the magnetic field is defined by the diamond crystal structure. For a better visualization, Fig. 6.6(b) depicts the angular dependence between the NV center axis and the applied magnetic field direction.

Fig. 6.6(d) presents the ODMR spectrum of an NV ensemble when the external magnetic field is misaligned to all four orientation axes. In that case, eight resonance dips can be observed. Each doublet in the spectrum corresponds to one NV orientation. When the magnetic field is aligned perpendicular to the diamond surface, the ODMR spectrum of an NV center ensemble is characterized by only two symmetric lines as shown in Fig. 6.6(e) (similar to a single NV center spectrum). However, this counts only for [100] oriented diamond samples as in this crystallographic geometry all four possible NV orientations experience the same Zeeman splitting. Again, the resulting frequency splitting depends on the angle θ and can be written as [169]

$$\begin{aligned} \Delta f &= 2\gamma B_z \cos 54.75^\circ \\ &= \frac{2\gamma B_z}{\sqrt{3}}. \end{aligned} \tag{6.1}$$

By investigating the number of frequency dips in the ODMR spectrum of the NV ensemble in $y > a$ and their symmetry, we were able to align the magnetic field in z-direction which is perpendicular to the superconducting sample.

In order to qualitatively detect the Meissner screening, we recorded ODMR spectra inside ($y < a$) and outside ($y > a$) of the superconducting sample. The measurements were performed in the cryo-UHV environment at 4.7 K under the application of an external magnetic field of $B_z = 4.2\,\mathrm{mT}$. As the critical temperature of our LSCO sample is at about 34 K, we can ensure the existence of the Meissner phase of the investigated compound. The resulting ODMR spectra are presented in Fig. 6.7. The red curve (Fig. 6.7(a)) shows the resonance peaks of the NV ensemble inside the superconductor with a frequency splitting of $\Delta f = 60\,\mathrm{MHz}$. According to Eq. 6.1, this corresponds to a z-aligned magnetic field of about 1.8 mT. Instead, the blue curve (Fig. 6.7(b)) depicts the resonance dips of the NV ensemble outside of the superconducting sample. In this case, a frequency splitting of 140 MHz can be observed corresponding to the strength from the applied magnetic field of 4.2 mT. Indeed, the different behavior of the NV ensembles in $y < a$ and $y > a$ can be explained by the manifestation of the Meissner screening in the superconducting sample. The magnetic field is expelled from the surface of the LSCO thin film. As a result, the NV ensemble in $y < a$ experiences less magnetic field compared to the NV ensemble in $y > a$ which is consistent with the already existing work presented in the last section.

The notable non vanishing field in the region of $y < a$ can be attributed to the relatively large NV to superconductor distance which is about 1 μm. This could be verified by a scanning electron microscope (SEM) study which is shown in Fig. 6.8. The tilted SEM images indicate an uniform separation between the diamond and LSCO surface of about 800 nm. Another reason for the non vanishing field inside the superconductor can also be related to the formation of magnetic vortices. As the measurement was performed with a magnetic field strength of 4.2 mT, the lower critical field of $\approx 2\,\mathrm{mT}$ has already been surpassed. As a result, vortices could appear on the LSCO surface generating a weak magnetic field which could be detected by the NV center ensemble. Also this effect has been noted by

spatially resolving the Meissner screening with an NV implanted diamond plate in [169].

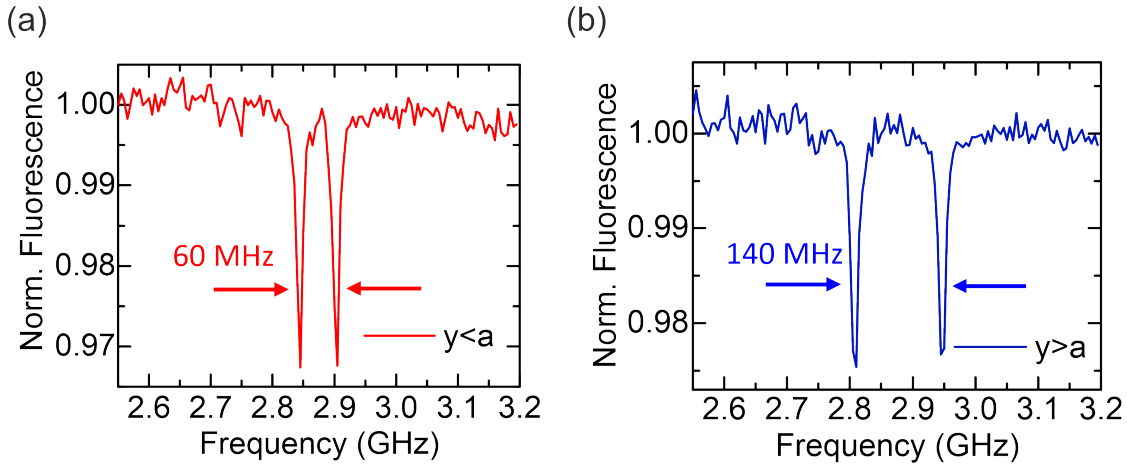

Figure 6.7: Manifestation of the Meissner screening in the 20 nm LSCO thin film observed with NV center ODMR spectra. (a) Resonance frequency splitting for the investigated NV ensemble inside the LSCO sample ($y < a$). A splitting Δf of about 60 MHz can be measured corresponding to a magnetic field strength of about 1.8 mT. (b) ODMR spectrum of an NV ensemble in the region of $y > a$. A frequency splitting of 140 MHz can be observed indicating a magnetic field strength of 4.2 mT. Compared to the spectrum gained in the region $y < a$, the NV centers detect the applied magnetic field. This clearly indicates the Meissner phase of the LSCO sample.

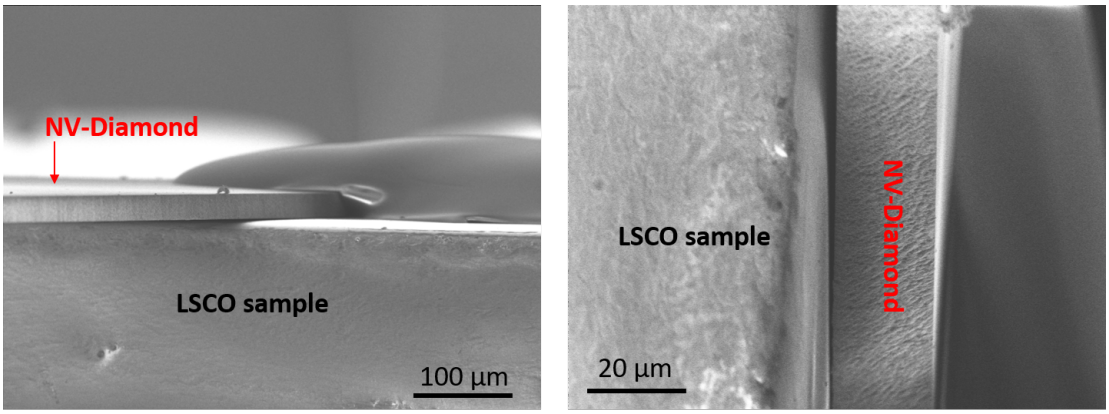

Figure 6.8: SEM images of the system geometry, highlighting the NV diamond membrane positioned at the edge of the LSCO sample. The diamond surface is in close proximity to the LSCO thin film with a distance of about 800 nm. This distance is accurate enough for detecting the Meissner phase of the superconductor, however makes the investigation of local effects (like the formation of vortices) inextricable.

6.3 All-Optical Characterization by Using the NV Fluorescence

In the last section, we reproduced existing findings of how NV centers were able to detect magnetic phases in superconductors. Thereby, the main mechanism relies on microwave resonant ODMR spectroscopy which is linked to heating effects. In fact, it has been shown that local heating effects are able to change the properties of a superconducting sample [177]. Especially the vortex state highly depends on the local temperature which has been demonstrated by simple laser heating effect in [177]. For circumventing this issue, we applied a non-resonant measurement scheme without the utilization of microwave excitation. Therefore, we recorded the direct fluorescence yield of an NV center ensemble which simultaneously decreases by increasing an off-axial magnetic field. The obtained results will be discussed in this section.

6.3.1 The Magnetic Field Dependent Photoluminescence Drop

The direct photodynamics of the NV center fluorescence shows a magnetic field dependence which can be used for qualitatively imaging magnetic processes in an all-optical manner [185]. This can be explained by the NV defect spin dynamics which is altered by high off-axial magnetic fields. In general, the quantization axis is fixed by the NV center orientation. However, under the application of highly misaligned fields, the quantization axis is determined rather by the applied magnetic field [185]. As a result, the spin quantum number m_S is no longer a good quantum number and the eigenstates of the spin Hamiltonian are given by superspositions of the $m_S = 0$ and $m_S = \pm 1$ sublevels. This mixing of the spin subsystem leads to an inefficient spin dependent photoluminescence (PL) rate by enhancing the probability of the non-radiative inter-system crossing to the metastable states ${}^1E$ and ${}^1A_1$. Mathematically, this can be represented in the optical transition rates k_{ij} (depicted in Fig. 6.9(a)) of the NV center energy level scheme which are related to a static magnetic field according to [185]

$$k_{ij}(\boldsymbol{B}) = \sum_{p=1}^{q=1} \sum_{q=1}^{7} |\alpha_{ip}(\boldsymbol{B})|^2 |\alpha_{jq}\boldsymbol{B}|^2 k_{pq}^0. \tag{6.2}$$

The magnetic field dependence is introduced within the coefficients $\alpha_{ij}(\boldsymbol{B})$, which are in general numerically computed using the ground and excited state Hamiltonian of the NV center. The resulting time-resolved fluorescence signal can then be written as [185]

$$\mathcal{R}(t, \boldsymbol{B}) = \eta \sum_{i=4}^{6} \sum_{j=1}^{3} k_{ij} n_i(0) e^{-t/\tau_i}, \tag{6.3}$$

where the pre-factor η represents the collection efficiency in this equation. Fig. 6.9(b) shows the measured behavior of an NV ensemble emission for different magnetic field strengths aligned perpendicular to the diamond surface. The measurement was performed at ambient conditions on an NV center ensemble. A permanent magnet was used for applying a magnetic field through the NV-diamond sample.

By decreasing the distance between the diamond sample and the permanent magnet, the field strength experienced by the NV centers could be increased. A significant decrease of the recorded PL up to 25 % can be noted in the graph of Fig. 6.9(b).

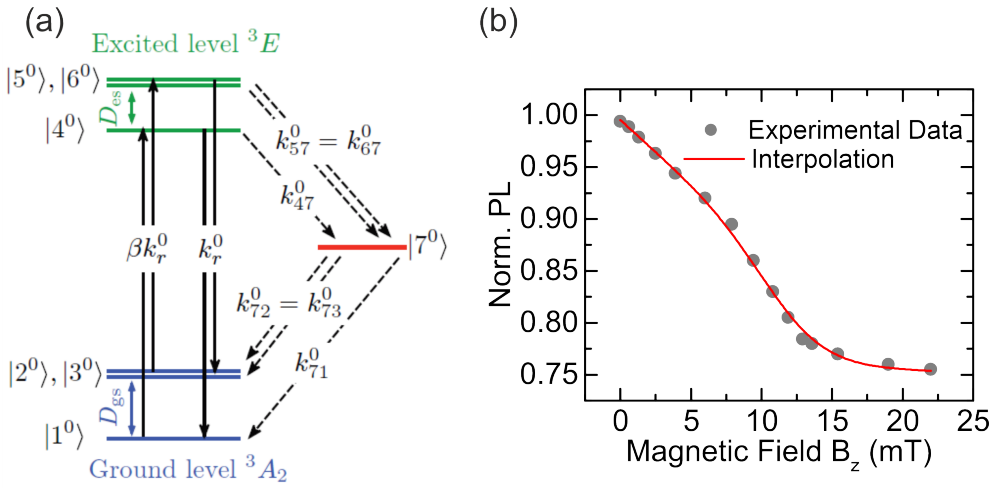

Figure 6.9: Magnetic field dependent photo emission of the NV center. (a) Energy level scheme of the NV center illustrating the transition rates k_{ij} which are crucial for the photodynamics of the defect. The magnetic field dependence within the transitions rates results into a direct response of the NV fluorescence to an applied magnetic field. The sketch is adapted from [185] (b) Measured PL of an NV center ensemble for different magnetic fields oriented in z-direction. A significant drop of the PL can be observed related to the magnetic field strength.

By simultaneously measuring the ODMR spectrum of the NV center ensemble, the experienced magnetic field can be quantitatively estimated. With this, a certain amount of PL drop can be calibrated to a corresponding magnetic field strength. Beside of this calibration measurement, the direct all-optical record of the NV fluorescence forms a microwave-free method. Moreover, measurements of field variations and qualitative observation of magnetic properties do not even rely on estimating an exact field strength. Therefore, the magnetic field dependent fluorescence yield can be used as a sensitive tool for the detection of magnetic phase transitions. In addition, all-optical measurement schemes can be potentially implemented into pump-probe spectroscopy experiments revealing dynamical phenomena on superconducting samples [186]. In the following part we present the all-optical spatial resolution of the Meissner screening caused by the LSCO thin film sample.

6.3.2 Microwave-Free Measurements

The geometry of the investigated system was kept unchanged. The NV implanted diamond membrane was glued across the edge of the 20 nm thin film LSCO sample. Instead of recording the ODMR spectra for an ensemble inside ($y < a$) and outside ($y < a$) of the superconductor, the fluorescence yield was measured in two steps [166]. In the first part of the all-optical measurement scheme, we

detected the pure PL without the application of an external magnetic field. In contrary, the second part measured the fluorescence under the influence of a certain magnetic field strength. After that, the two results were subtracted from each other and normalized for revealing a magnetic field induced PL drop in %. The results of this analysis scheme are presented in Fig. 6.10 showing two normalized confocal images. The optical 2D plot was recorded by scanning the laser spot in a 10 μm x 10 μm with the piezo mirror mounted above the UHV chamber.

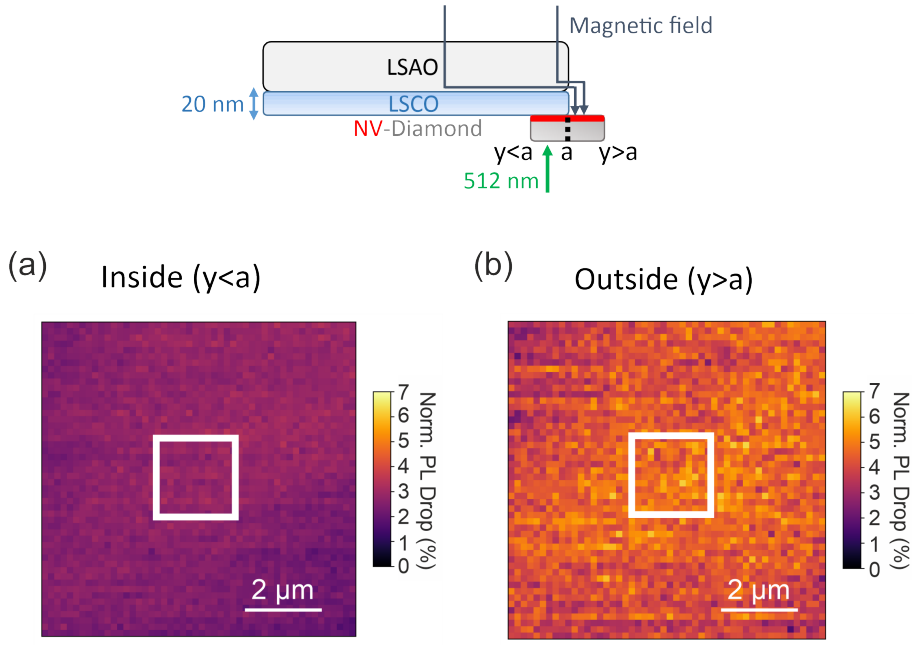

Figure 6.10: All-optical detection of the Meissner screening in LSCO. The system geometry sketch is attached above the two optical images for reminding the significance of the region $y < a$ and $y > a$. (a) Normalized confocal image of the NV fluorescence inside the superconducting area at 4.2 K and under an applied magnetic field of 4.2 mT. The PL counts are averaged within the area of 2 μm x 2 μm (white square). A PL drop of about 2.5 % can be investigated. (b) Normalized confocal scan of an NV center ensemble in the region $y > a$, indicating a count rate drop of about 5.4 %. The difference compared to the NV ensemble in $y < a$ can be explained by the Meissner expulsion of the LSCO superconductor leading to a varied magnetic field strength experienced over the whole diamond membrane.

The resulting NV fluorescence was measured by the implemented APDs of our confocal setup. As already described, the images in Fig. 6.10 were gained by the subtraction of a scan obtained under magnetic field application from a zero-field scan and a subsequent normalization. Also here, the magnetic field was set to 4.2 mT in z-direction within the 4.2 K cold cryostat. It is evident that the zero field normalized confocal scan obtained from the $y > a$ region (Fig. 6.10(b)) is significantly brighter compared to the measurement set in the $y < a$ region (Fig. 6.10(a)) [166]. For obtaining the most reliable results of the PL drop, we chose the central area (depicted as white squares) of the confocal images as the center of the image shows the least optical distortion. This fact has been explained in

chapter 3 and is related to the long optical path of the laser beam. For the NV ensemble inside the superconductor, an averaged PL drop of 2.5 % in the central area of the confocal image was observed. Instead outside of the superconducting sample, the NV ensemble experienced a fluorescence count rate drop of about 5.6 %. The significant difference of 2.9 % in PL drop is a clear indicator for the Meissner state of the LSCO sample. The NV ensemble in the region of $y > a$ experiences the fully z-aligned magnetic field of 4.2 mT. Due to the off-axis component of the magnetic field relative to the NV axes, a certain fluorescence drop can be observed [185]. Also the NV ensemble inside the superconductor experiences a fluorescence drop. However, as presented, the PL drop value is almost halfed compared to the measurements on the NV centers outside of the superconductor which is related to the screening of the magnetic field when the LSCO sample is in its Meissner phase. As a result, a lower magnetic field value was detected by the NV center ensemble and with this a decreased PL drop was recorded. It is also worth to mention, that the presented confocal scans were obtained by a fixed laser power of 0.688 μW which was measured in front of the UHV chamber glass with a powermeter. Such a low laser ensures a minimal local heating which is not sufficient enough for changing the superconducting properties of the LSCO thin film [177].

Spatially Resolved Study of the Meissner Screening

After we investigated the PL drop of a fixed NV ensemble inside and outside of the superconducting sample, we extended the all-optical approach for spatially resolving the Meissner screening of the LSCO thin film. Therefore, the laser focal spot was raster swept over the diamond membrane along the y direction and across the edge of the LSCO sample [166]. Fig. 6.11(a) shows the resulting spatial variation of the PL drop measured at 4.2 K and under an applied field strength of $B_z = 4.2$ mT. As already described, each fluorescence rate is normalized to a zero field measurement for obtaining the relative fluorescence drop. It is evident that two distinct regimes can be characterized in Fig. 6.11(a) by different degrees of the PL drop observed inside ($y < a$) and outside ($y > a$) of the superconductor. For the $y < a$ region, a homogeneous PL drop of about 2 % was measured. Furthermore, a slow increase of the PL drop towards the boundary ($y = a$) can be seen in Fig. 6.11(a). For locations which are far away from the thin film sample ($y > a$), an increased PL drop of about 5.1 % was evaluated. By using the calibration data from Fig. 6.9(b), a conversion from the PL drop to an effective magnetic field was performed. With this, the magnetic field strength in $y < a$ was estimated in a range between 1.8 mT and 2.1 mT. The resulting magnetic field strength curve is depicted in Fig. 6.11(b). Instead, outside of the superconductor, the magnetic field strength is about 4 mT which is in good agreement with the applied magnetic field.

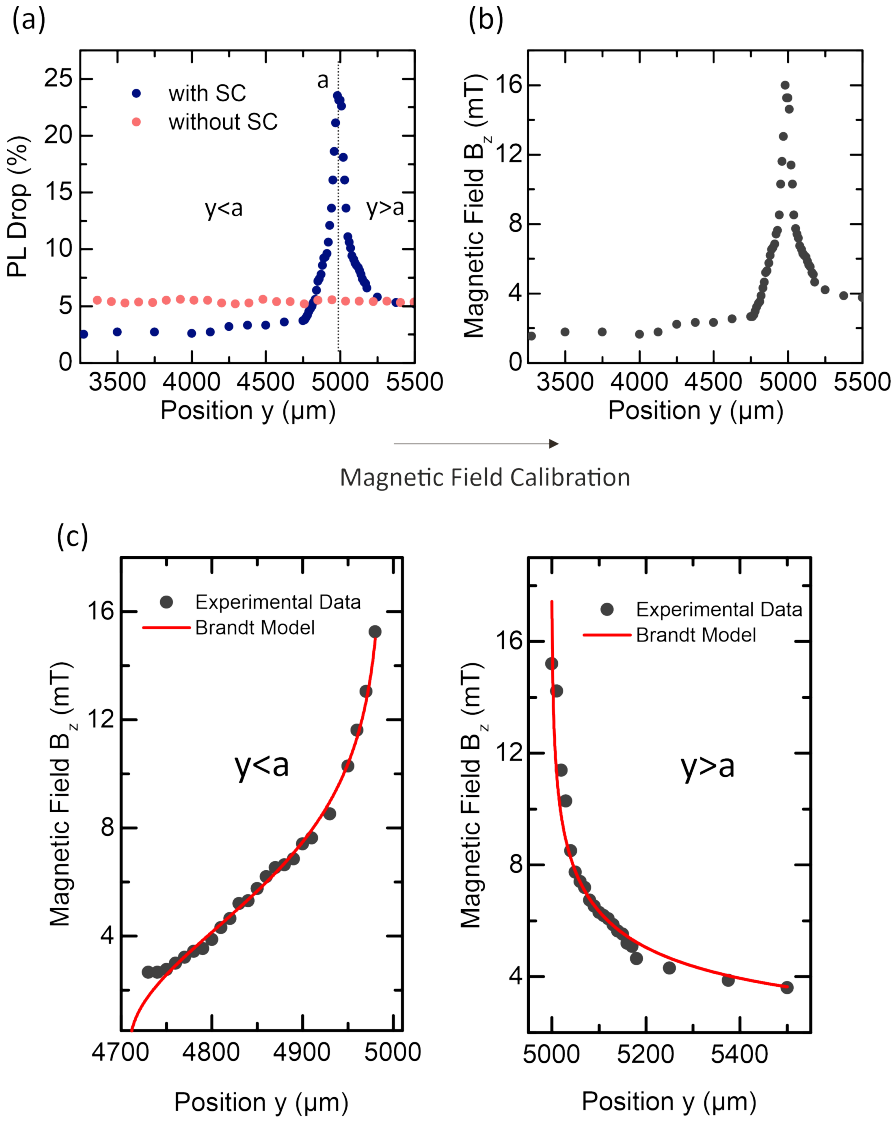

Figure 6.11: Spatially resolved Meissner screening in LSCO using the all-optical NV center based approach. (a) Variation of the PL drop by scanning the laser focal spot over the LSCO sample edge. A clear difference between the regions $y < a$ and $y > a$ can be observed indicating the Meissner phase of the superconducting sample. Furthermore, a sharp increase at the boundary if the LSCO thin film $y = a$ can be observed due to the increased magnetic flux density at the edges of rectangular samples. (b) Converted Pl drop to magnetic field strength curve by using the calibration measurement from Fig. 6.9(b). The inside region obtains a magnetic field strength of about 1.8 mT. Instead, the NV center ensemble of the outside region detects a magnetic field strength of about 4 mT being in good agreement to the applied magnetic field of 4.2 mT. (c) Separated inside ($y < a$) and outside ($y > a$) regions fitted with Brandt's analytical model. Both fitting functions reveal a critical current density j_c of $1.4 \cdot 10^8$ A/cm^2.

The sharp PL drop increase at the boundary of about 23 % was converted to a magnetic field strength of 16 mT. This enhancement depicts a typical feature for rectangular superconducting samples [187].

Due to the diamagnetic character of the superconducting compound in its Meissner phase, the magnetic field flux is screened to the edge of the LSCO sample. This leads, to a significant enhanced magnetic flux density at the boundary of the investigated sample. For fully verifying the impact of the Meissner screening on the measured data, the red dots in Fig. 6.11(a) correspond to a measurement set of the PL drop in absence of the superconducting LSCO. It is clearly visible that a spatial dependence of the PL drop was nit observed in the bare NV membrane.
Furthermore, the magnetic field profile in a superconducting thin film can be analytically evaluated by Brandt's model from 1993 [188]. The model assumes completely flux-free regions on the superconductor leading to a pure Meissner current of [188]

$$J(y) = \begin{cases} \frac{2J_c}{\pi} \operatorname{arctanh} \frac{cy}{(b^2-y^2)^{1/2}} & |y| < b \\ J_c \frac{y}{|y|} & b < |y| < a \end{cases} \tag{6.4}$$

where a corresponds to the already declared notification for the length of the superconducting sample, J_c stands for the critical sheet current in units of A/m and b can be represented in terms of the applied magnetic field H_a as [188]

$$b = a/\cos\frac{\pi H_a}{J_c}. \tag{6.5}$$

From the sheet current $J(y)$, the magnetic field $H(y)$ can be obtained by Ampere's law [188, 189]

$$H(y) = \frac{1}{2\pi}\int_{-a}^{a} \frac{J(u)}{y-u}\,du + H_a. \tag{6.6}$$

With Eq. 6.4, the magnetic field profile of a thin film rectangular superconductor can than be written as [188]

$$H(y) = \begin{cases} \frac{J_c}{\pi} \operatorname{arctanh} \frac{\sqrt{(y^2-b^2)}}{c|y|} & y < a \\ \\ \frac{J_c}{\pi} \operatorname{arctanh} \frac{c|y|}{\sqrt{(y^2-b^2)}} & y > a \end{cases} \tag{6.7}$$

where c corresponds to a constant represented as [188]

$$c = \tanh\frac{\pi H_a}{J_c}. \tag{6.8}$$

The experimental data in Fig. 6.11(b) can be fitted with the presented model in order to quantify the critical current density $j_c = J_c/d$ in which the flux lines start to move under the action of the Lorentz force. By fixing the values $H_a = 4.2\,\mathrm{mT}$ and $a = 5000\,\mu\mathrm{m}$, the fitting parameter result in $b = 4709 \pm 2.2\,\mu\mathrm{m}$, $c = 0.335 \pm 0.0059$ and $J_c = 27997 \pm 2249\,\mathrm{A/m}$. Knowing the critical

sheet current J_c and the sample thickness $d = 20\,\text{nm}$, the critical current density can be calculated to $j_c = 1.4 \cdot 10^8\,\text{A/cm}^2$. This value is comparable with reported j_c values for LSCO nanowires indicating that the NV fluorescence drop is a reliable quantity for the characterization of thin films superconductors [190]. Furthermore, the estimated j_c is in good agreement with a calculation based on the SQUID measurement which has already been presented in Fig 6.5. From Brandt's analytical model, the magnetic moment m in dependence of the critical current can be written as

$$m = J_c a^3 \tanh \frac{\pi H_a}{J_c}. \tag{6.9}$$

By inserting our findings for J_c from the fit to our experimental data, we obtain a magnetic moment of $m \approx 0.012\,\text{emu}$. This value is in a fair agreement to the magnetic moment measured from the SQUID which ranges between 0.0075 emu to 0.0052 emu. The slight mismatch in m can be explained by two factors. First of all, Brandt's model is based on a flux-free system [188]. This is not fully true in our performed measurement, as the applied magnetic field of 4.2 mT surpassed the lower critical field of 2.1 mT of our LSCO sample. Therefore, it is more realistic that the investigated system exhibited a certain number of vortices during the measurement performance. Secondly, the PL drop to magnetic field strength conversion in Fig. 6.9 assumes a field orientation in z-direction. This is a realistic assumption in the regions $y < a$ and $y < a$. However, in proximity of the LSCO edge ($y = a$) the magnetic field is forced to curl around the sample surface leading to a magnetic field which is not only pointing in the z-direction [187]. Therefore, a strong in-plane component of the applied field has to be assumed which potentially explains the overestimation of j_c and m. Nevertheless, the qualitative trend of the Meissner screening can be fully reconstructed with the presented NV based all-optical method and is able to extract important material properties of the investigated compound which are in fair agreement with existing literature values [190].

6.4 Investigation of Superconducting Vortices in LSCO

As last step for the characterization of our 20 nm thin film LSCO sample, we wanted to image the vortex phase in the system. We have seen that the gap between the LSCO surface and diamond membrane is about 800 nm. In fact, this forms a huge limitation in terms of spatial resolution. It has been shown that already an NV probe to superconducting surface distance of 100 nm prohibits the resolution of a single magnetic vortex [170]. Therefore, we modified the system geometry and implemented NV ensemble implanted diamond micro-plates instead of positioning the macroscopic 2 mm x 2 mm diamond plate on the superconductor. As shown in the SEM image of Fig. 6.12, the distance between the two surfaces is more compact and in the range of few nm.

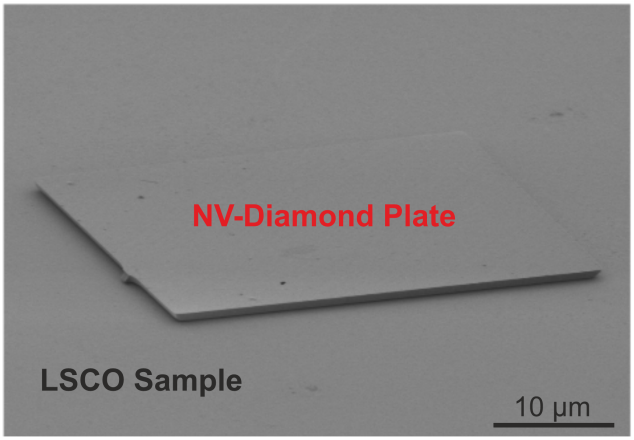

Figure 6.12: SEM image of a diamond micro-plate positioned on top of the LSCO sample. The plate has been implanted with an NV ensemble in a density of $\approx 200\,\mathrm{NVs}/\mu\mathrm{m}^2$. The distance to the LSCO surface is in the nm range with this system geometry.

Nevertheless, the measurement scheme remained the same as in the last section [166]. A confocal scan was recorded by measuring the fluorescence of an NV center ensemble on the diamond micro-plate. After that, the same position was scanned under the application of a z- oriented magnetic field with a strength of about 3 mT. We chose to slightly decrease the applied magnetic field from the initial 4.2 mT as the vortex density increases linearly to the field strength. Again, the two confocal scans were subtracted from each other. The normalization of the data revealed the resulting PL drop in % and is illustrated in Fig. 6.13(a). Averaged over the whole image, a magnetic field induced PL drop of $\approx 3.2\,\%$ was observed. However, compared to the confocal images of subsection 6.3.2, interesting elliptically shaped features were investigated and interpreted as possible magnetic vortices. At the center of these structures, the PL drop amounted to almost 4 %, being in good agreement with the fact that the magnetic field distribution of a single vortex is maximized in its core [191]:

$$B(r) \approx \Phi_0 \sqrt{\frac{\lambda}{r}} \exp\left(-\frac{r}{\lambda}\right). \tag{6.10}$$

Furthermore, the diameters of the elliptical structures are in the range of 2 μm which is in good agreement with existing experimental results [170, 171]. For obtaining a more quantitative impression of the magnetic field within the observed structures, we performed a scanning ODMR spectroscopy measurement. Therefore, we recorded the pixel by pixel ODMR spectra within a range of 10 μm x 10 μm in the upper left part of Fig. 6.13(a). The result is depicted in Fig. 6.13(b), illustrating the frequency splitting within the recorded ODMR spectra. Again, clear elliptical shapes can be observed in the image, supporting the all-optical measurement of Fig. 6.13(a).

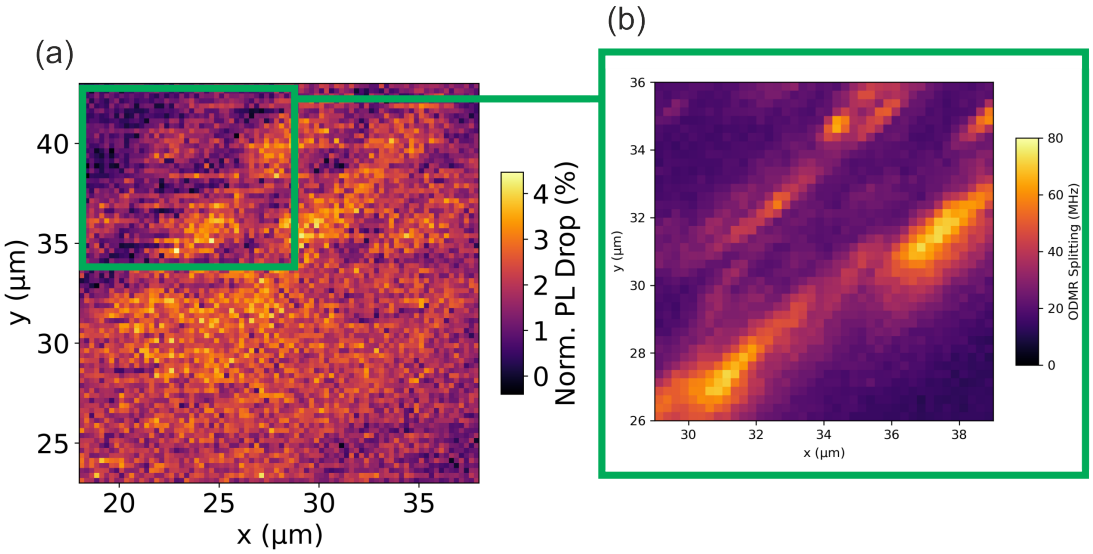

Figure 6.13: Resolution of single vortices detected by an NV center ensemble. (a) All-optical normalized fluorescence drop image of an NV ensemble implanted in the diamond micro-plate. The measurement reveals elliptical structures, indicating the detected magnetic vortices. The vortex diameter is about 2 μm. (b) Pixel by pixel ODMR scan for confirming the magnetic domains in terms of the frequency splitting. A clear similarity of the all-optical image can be evaluated proving the microwave-free measurement method as a reliable approach.

In addition, both figures obtain the same characteristics. The center of the visible structures seems to be the point with the highest magnetic field strength. In case of the all-optical image, this is represented by the highest amount of count rate drop in the core of the assumed vortex. Instead, for the ODMR image, this is indicated by the largest frequency splitting in the core of the magnetic vortex. The measurement set indicates that the presented all-optical scheme is not only able to resolve the Meissner screening of a superconducting compound but also to explore exotic phases like the vortex state in a microwave-free manner.

6.5 Summary

In the last part of this chapter we want to summarize the experimental findings of this project. The motivation was found on already performed work of how NV centers have been used for detecting the Meissner expulsion and the voretx formation in superconducting samples. NV center ensemble were able to resolve the Meissner screening of a superconductor by recording their ODMR spectra. The resulting frequency splitting has been used as an indicator for the amount of magnetic field strength which was experienced by the NV center ensemble. By comparing NV ensembles in close proximity to a superconducting surface with NV centers outside of the corresponding superconductor, clear differences were found in the frequency splitting attributed to the Meissner phase of the investigated

material. Furthermore, single NV centers have been established in diamond-AFM tips for probing the magnetic behavior of a superconducting material. Whenever a vortex was scanned below the NV tip, a significant change of the ODMR spectrum was observed. With this, single vortices with almost 100 nm spatial resolution were investigated and characterized.

Nevertheless, the conventional NV based magnetometry relies on resonant microwave excitation for the record of ODMR spectra. Typically, such measurements schemes are linked to heating effects which potentially change the properties of the investigated sample. For circumventing this issue, we performed all-optical measurement schemes by recording the direct fluorescence yield of an NV center ensemble. The results show that the magnetic field dependent PL drop, which is related to the NV center energy level scheme, is able to qualitatively observe magnetic processes. The investigated system used in this chapter was formed by an NV implanted diamond membrane glued at the edge of a superconducting 20 nm LSCO thin film. By raster scanning the laser focal spot, the PL drop of the NV ensemble was recorded and the magnetic profile of the Meissner screening along the LSCO sample was reconstructed. The whole measurement was performed in an cryogenic UHV environment with a temperature of 4.2 K under the application of a z-aligned magnetic field of 4.2 mT. The results were evaluated with Brandt's analytical model revealing a critical current density of $1.4 \cdot 10^8\,\mathrm{A/cm^2}$. Due to the good agreement with existing literature values, the presented all-optical, microwave-free measurement method can be interpreted as a reliable scheme for the detection of magnetic processes. Furthermore, the ability to detect single vortices with this method has been shown. Elliptical structures were identified in the zero field normalized confocal scans by using NV implanted diamond microplates. The advantage of such μ-meter sized plates is the decreased distance between the NV center ensemble and the investigated superconducting surface. With this, the spatial resolution is high enough for the observation of single vortices.

The magnetic field induced fluorescence drop shown in this chapter can be potentially extended further by a combination with optical pump probe spectroscopy schemes enabling the local detection of time-resolved dynamical magnetic phenomena including the vortex formation and motion in type II superconductors.

7 Towards Stabilizing the Spin Properties of Near-Surface NVs

The whole thesis was focused on the implementation of NV centers into nanoscale magnetic field sensing. Thereby, one of the most utilized techniques is DEER spectroscopy which also has been discussed in the chapters 2, 4 and 5. Of great importance for that, is the NV center coherence time T_2 as the relevant detection pulses are set within the Hahn echo sequence of the NV center. For example, we have seen a strong limitation of the sensing principle in Fig. 4.11. In that experimental section, a single NV center was used for characterizing an external N@C_{60} spin. As the coherence time of that particular NV center was barely $\approx 3\,\mu$s, only the minimum coherence time of the external spin could be revealed.

A possibility for increasing the NV center T_2 time is to implant the defect deep within the diamond lattice ($>$ 30 nnm from the bare diamond surface) [192]. Consequently, the NV defect is protected from environmental magnetic noise which is potentially responsible for the coherence time reduction. However, deep implanted NV centers are challenging to utilize for sensing purpose due to the short detection region ($\approx$ 25 nm) [47]. Therefore, only shallow NV centers can be used as quantum sensors. This fact makes the NV depth tp a critical parameter for sensing applications. In most of the published experiments, the utilized NV centers were positioned about 7 nm from the bare diamond surface [68, 97, 104]. Implanting the defects closer to the surface results into a significant decay of their coherence time limiting their sensitivity. Another important point is the spatial resolution of the NV sensor which also highly depends on the depth of the defect. Nanoscale sensing with atomic resolution can only be realized with sensors positioned in close proximity to the sample [193]. In case of the NV center, the defect should be implanted as close as possible to the diamond surface.

Furthermore, also other important NV characteristics are affected by the implantation depth. A very fundamental property is the fluorescence contrast resulting from the spin state dependent NV emission. The fluorescence difference between the $m_S = 0$ and $m_S = \pm 1$ NV spin states forms the working principle of the NV center as quantum sensor. Only if an emission contrast is detectable, resonance dips can be observed in the DEER spectra. Indeed, it has been shown that the fluorescence contrast varies in dependence of the NV center depth [194, 195, 196]. Usually, shallow NV centers obtain a relatively low spin state contrast compared to deeply implanted defects.

A potential explanation for this behavior can be found in the charge state dynamics of the NV center [195, 196]. In chapter 2, we introduced the three NV center charge states, namely the NV^-, NV^0, and NV^+ states. Especially, charge transitions within the NV^- and NV^0 states seem to give rise to

instabilities of the NV center [196]. These instabilities are enhanced for shallow implanted defects. Therefore, stabilizing the charge distribution close to individual NV centers could potentially increase relevant characteristics like the fluorescence contrast and coherence time. The stabilization can be achieved by dosing protection layers on the diamond surface in a controlled way [197].
This chapter presents attempts for stabilizing the spin properties of near-surface NV centers. In the first section, the characteristics of the NV charge states are explained for giving an understanding of their relevance for sensing purposes. Afterwards, the spin state dependent emission difference of shallow implanted single NVs is introduced in terms of the ODMR contrast. In the first trial, the ODMR contrast was recorded at ambient conditions for several NVs. Afterwards, the same NV centers have been investigated within the cryo-UHV setup for comparing their spin properties. As result, we found a complete loss of the NV^- spin characteristics giving rise to the assumption of a charge state conversion to the NV^0 state. Consequently, surface modification experiments have been performed by dosing nitrogen (N) and carbon monoxide (CO) gas. In addition, liquid water has been dosed onto the diamond sample. . As first result, no significant NV^- charge state stabilization could be obtained by gas dosing. However, introducing water onto the diamond surface revealed hints of a slight NV^- state recovery. The experimental attempts can motivate to study this issue in greater details by dosing more specific gases and liquids.

7.1 Charge State Dynamics of the NV Center

In 2.1.3 we introduced the three charge states of the NV center. As the defect is able to trap or release electrons, the NV center can obtain a negative (NV^-) or a positive (NV^+) charge. Of course, the defect can also exist in its neutral state (NV^0). The different charge states can be distinguished in terms of the electron occupation within the energy bands in diamond which has already been shown in Fig. 2.3. However, this characteristic is challenging to reveal in an experiment. An easier and more reliable way to investigate the charge state of an NV center is to perform spectroscopic measurements while exciting the defect with 532 nm laser pulses [198]. The resulting optical properties of the NV defect significantly vary depending on the charge state. So far, we discussed only the fluorescence characteristics of the NV^- center which is the relevant charge state for quantum sensing applications and exhibits a ZPL at 637 nm. As shown in Fig. 7.1(a), this 637 nm emission can be observed as sharp peak in the NV^- fluorescence spectrum. After the ZPL, the phonon sideband of the NV^- center (starting from $\approx$ 650 nm) can be observed. These two optical characteristics differ when the NV center transits through a charge state conversion. This fact is depicted in Fig. 7.1(b) which compares the fluorescence properties of the three NV charge states. For the NV^0 center, the ZPL is shifted from 637 nm to 575 nm. Also the phonon sideband is shifted to lower wavelengths. Instead, the NV^+ center shows no spectral features. The defect is optically dark. As a result, only the 2nd order Raman line can be observed which is a bulk property of the diamond crystal [199].

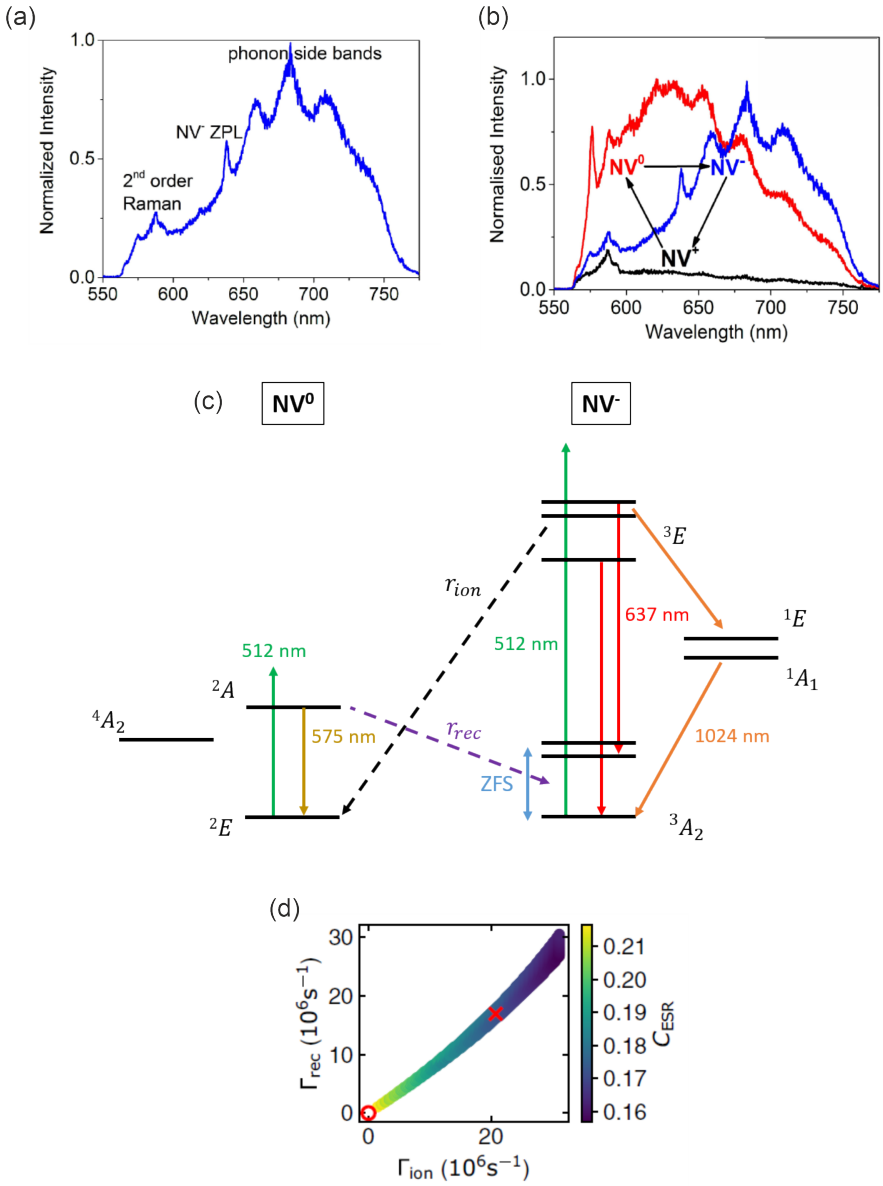

Figure 7.1: Charge state dynamics of the NV center in diamond. (a) Emission spectrum of the NV^- state characterized by a ZPL at 637 nm. (b) Optical comparison of the NV charge states. The NV^+ center is optically dark and does not show characteristic emission features. However, the NV^0 state obtains a notable emission at 575 nm. The spectra are adapted from [200]. (c) Energy level diagrams of the NV^0 and NV^- centers. Due to the ZFS within the NV− ground state, ODMR spectroscopy can be performed on that specific specimen. Instead, when the NV centers obtains its NV^0 state, no ODMR measurements can be performed. Charge transitions within NV^0 and NV^- states are possible and characterized by the rates r_{ion} and r_{rec}. (d) Simulation showing the impact of r_{ion} and r_{rec} on the ODMR contrast. Increasing the transition rates leads to a decrease of the ODMR contrast. The figure is adapted from [196].

Without specific surface treatments (like hydrogen dosing [200]) the NV^+ center forms the most un-

stable state of the three presented charge states. In contrary, the NV^- and NV^0 defects are more manifested and stable in the diamond crystal lattice. Therefore, we will focus only on these two charge states within the scope of this chapter.
A further difference between the NV^- and NV^0 charge states arises from their response under MW excitations. For this, the energy level diagrams are compared in Fig. 7.1(c). As extensively described, the NV^- center obtains a ZFS of 2.87 GHz which allows the performance of ODMR spectroscopy. This property forms a clear fingerprint of the NV^- state as the NV^0 shows no response towards MW applications. Furthermore, the transition dynamics within the NV^- and NV^0 states have been studied extensively in several works [195, 196]. As explanation, Fig. 7.1(c) also shows the ionization and recombination rates r_{ion} and r_{rec} which are depicted as dotted arrows. These quantities play a crucial role for the population rates $\frac{d\rho_{NV^-}}{dt}$ and $\frac{d\rho_{NV^0}}{dt}$ of the corresponding NV center charge states [196]:

$$\frac{d\rho_{NV^-}}{dt} = -r_{ion}\rho_{NV^-} + r_{rec}\rho_{NV^0} \tag{7.1}$$

$$\frac{d\rho_{NV^0}}{dt} = r_{ion}\rho_{NV^-} - r_{rec}\rho_{NV^0}. \tag{7.2}$$

Thereby, ρ_{NV^-} and ρ_{NV^0} represent the NV^- and NV^0 populations. By utilizing these formulae, interesting NV center behaviors can be revealed. For example, the ODMR contrast can be simulated in dependence of the ionization and recombination rates as shown in Fig. 7.1(d). By increasing the transition rates r_{ion} and r_{rec}, a significant drop of the ODMR contrast can be evaluated. Increased transition rates can be interpreted as relatively huge charge state instabilities on the NV center. Therefore, charge state instabilities adversely affect the NV defect quality. These findings, can be even interpreted further in terms of an NV center depth dependence. Near-surface NVs exhibit a low ODMR contrast due to an increased charge state instability [195, 196]. It is worth to mention that this is not only an assumption. In fact spectroscopy measurements revealed the optical properties of NV centers with different depths [195, 196, 198] as shown in Fig. 7.2. Several NV centers of two different samples A and B have been investigated in [196]. Thereby, sample A obtained deeper implanted NV centers. By evaluating the fluorescence spectra in Fig. 7.2, it is evident that sample A showed a clear NV^- feature in form of the ZPL at 637 nm. Instead sample F with shallower NV centers, showed only optical properties matching the NV^0 state.
All these findings lead to the assumption that the key for stabilizing shallow NV centers is the control of their charge state.

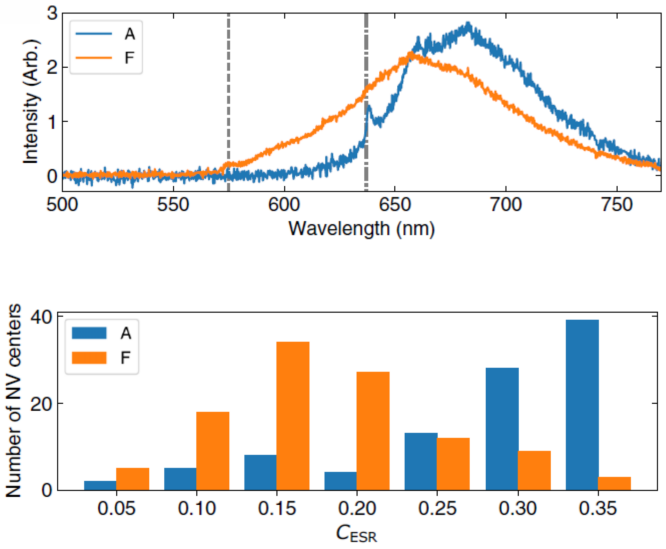

Figure 7.2: Depth dependence of the NV center properties. Two NV implanted diamond membranes are compared in which the NV center depth is varied. Sample A contains deeper implanted defects compared to sample F. Indeed, sample A seems to obtain stronger NV^- characteristics in the emission spectrum. Furthermore, also the ODMR contrast is stronger for sample A compared to the diamond plate F. The results and figures are adapted from [196].

7.2 Near-Surface NVs at Ambient Conditions

In order to understand the depth dependence of the NV center spin properties, we want to reproduce some of the results presented in [196]. Thereby, the focus is on the NV center ODMR contrast as the spin state dependent fluorescence difference clearly indicates the existence of the NV^- charge state. As already explained, ODMR spectroscopy can not be performed on the NV^0 center due to its spin energy level diagram.

The utilized sample for this project was a 4 mm x 4 mm CVD grown diamond plate. After the crystal growth, the membrane was subsequently nitrogen implanted with three different implantation energies of 2.5 keV, 5 keV, and 10 keV (see appendix 10). Finally, the diamond plate was annealed at 650 °C for the formation of adjacent vacancies to the implanted nitrogen atoms. As the implantation energy defines the NV center depth, the resulting diamond membrane consists of three distinct regions in which the defects obtain different depths from the sample surface [201]. Usually, a 10 keV nitrogen-implantation leads to $\approx$ 15 nm deep NV centers [202]. Instead, an implantation energy of 5 keV results into $\approx$ 7 nm deep NV defects [47, 104]. When the kinetic energy of the nitrogen ions is in the range of 2.5 keV, near-surface NV centers can be fabricated with a depth of $<$ 3 nm [195, 202]. With this specific sample geometry, a reliable depth dependence study can be performed. In addition, nanopillars have been etched as the study relies on the investigation of single NV centers. With the waveguide-character of the nanopillars, the single NV emission can be enhanced for performing more reliable

measurements.

The first measurement set was obtained at ambient conditions. In order to prove the observation of a single NV, autocorrelation measurements were recorded (see chapter 3).

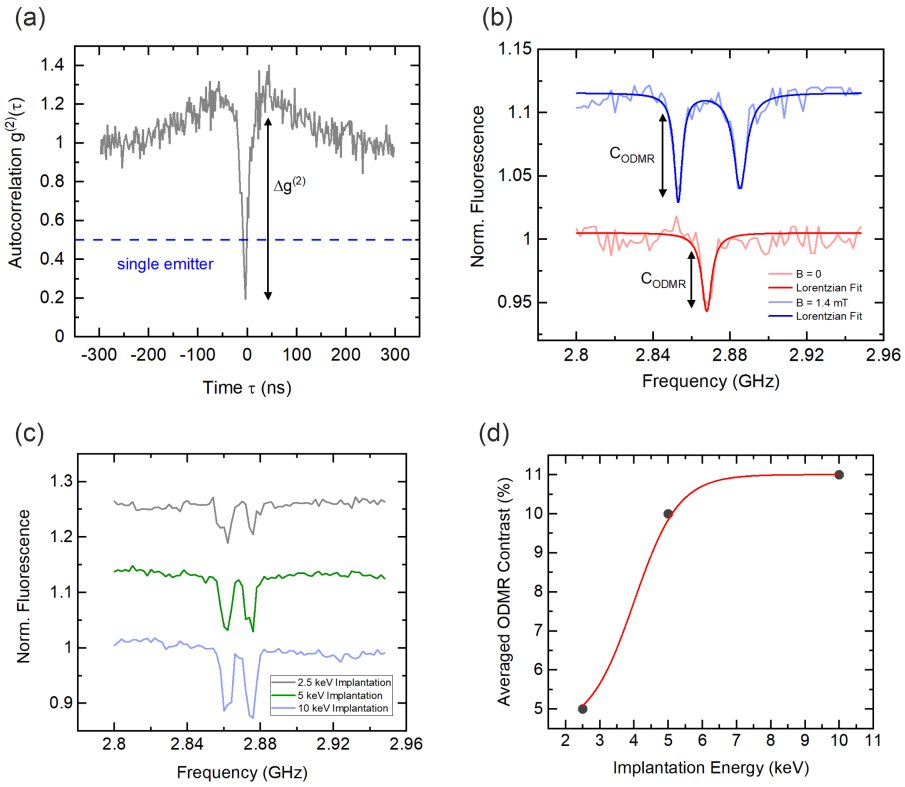

Figure 7.3: NV center characterization at ambient conditions. (a) Autocorrelation measurement of an individual NV center indicating an antibunching dip below 0.5. This is a reliable method for identifying a single photon source. (b) ODMR spectrum of an NV center without the application of a magnetic field (gray curve) and under the observation with a 1.4 mT strong B field in z direction. The Zeeman splitting verifies the investigation of an NV^- defect state. The strength of the signal is termed as ODMR contrast ΔC_{ODMR}. (c) ODMR spectra of three different NV centers which have been implanted by an implantation energy of 2.5 keV, 5 keV and 10 keV. A stronger ODMR contrast can be observed for the NV center inserted by the highest implantation energy. (d) Average ODMR contrast for 25 NV centers observed in the three different implantation energy regions of the diamond membrane. The ODMR contrast increases by increasing the implantation energy. The effect is related to the NV center depth which highly depends on the implantation energy.

Thereby, a typical single NV characteristic is the antibunching dip below 0.5 which is depicted in Fig. 7.3(a). Afterwards, ODMR spectroscopy were performed. Fig. 7.3(b) presents a standard ODMR spectrum of an individual NV center. For clarification, arrows indicate the definition of the ODMR

contrast

$$\Delta C_{ODMR} = (1 - a_{\pm 1}) \cdot 100\% \tag{7.3}$$

in percent. Thereby, $a_{\pm 1}$ is the ODMR dip intensity. This quantity can be compared for several NV centers which have been implanted by different implantation energies. An exemplary result is shown in Fig. 7.3(c) which illustrates three ODMR spectra. Each spectrum corresponds to a single NV center. However, the defects were fabricated by different energies of the nitrogen ion beam. As a result, the NVs obtained diverse depths from the bare diamond surface. As already described, an energetically low implantation beam results into a shallow NV defect. Indeed, a weak ODMR contrast of $\approx$ % was investigated for the NV center implanted with a beam energy of 2.5 keV. Instead, the NV center obtained by an implantation energy of 10 keV showed an ODMR contrast of 11%. In between, the 5 keV implanted defect is characterized by an contrast of 8%. In order to evaluate the results in a more statistical manner, an ODMR spectroscopy study was performed on 25 individual NV centers. The experimental outcome is presented in Fig. 7.3(d) by plotting the average C_{ODMR} of the NV centers for each of the three implantation fields (9 NVs from the 2.5 keV field, 9 NVs from the 5 keV field and 7 NVs from the 10 keV). A clear trend in dependence of the implantation energy and with this of the NV depth was observed. The average NV center ODMR contrast in the field in which the defects were implanted by a 2.5 keV beam is $\approx$ 5%. Instead, the ODMR contrast significantly rises to 10% by observing NV centers in the 5 keV nitrogen-implanted field. Interestingly, only a slight ΔC_{ODMR} increase to 11% is observed by rising the implantation energy to 10 keV. Therefore, the assumption of a specific NV depth threshold is reasonable which defines the stability of the NV center spin.
A potential attempt for explaining this fact is a charge trap model which assumes the existence of electron receptor states on the diamond surface [195]. In general, these potentials are filled with electrons. However, several processes, as laser illumination [203], are able to ionize the charge trap. Consequently, the surface receptor recombines the electron of a nearby NV^- center forcing a charge conversion to the ODMR-free NV^0 state. As the charge traps are only obtained on the diamond surface, solely shallow NV centers are affected by this process. A result of this proposed mechanism could be an unstable NV spin state which is indicated by low ODMR signals [195].

7.3 Measurements at UHV and Cryogenic Conditions

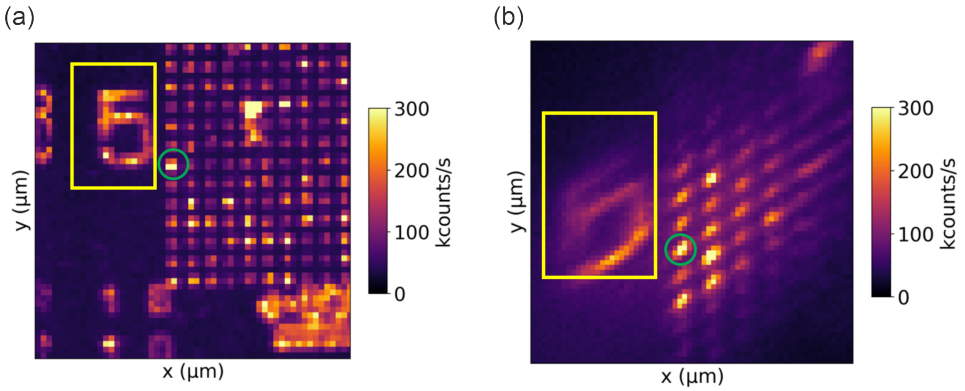

Figure 7.4: Confocal images of the same region obtained at ambient (a) and cryogenic-UHV (b) conditions. Due to the etched markers, individual NV centers can be compared within the two different setups.

In the second step of this project, we want to investigate the properties of shallow implanted NV centers in a cryogenic UHV environment. So far in this thesis, the studied NV center obtained a depth between 7 nm to 20 nm from the diamond surface. Furthermore, the diamond plate was coated with molecules for observing couplings on the single spin level (see chapter 4). The drop-coating can be interpreted as a surface treatment which potentially stabilizes the NV centers. However, in this section we want to study the NV center behavior within a non-coated diamond sample for gaining access to the bare NV center properties. This scenario is of great importance as several magnetic mechanisms like spin waves or skyrmions in solids [204, 205, 206] can be potentially revealed on the nanoscale with NV center sensors in cryogenic UHV environments. The NV characteristics obtained at the cryo-UHV environment are compared to the results gathered at ambient conditions. Therefore, the same NV centers were measured at 4.7 K and $9 \cdot 10^{-11}$ mbar which also were characterized at the ambient stage. This is enabled by lithographically etched markers on the diamond surface.
Fig. 7.4 compares the confocal images obtained at ambient conditions (Fig. 7.4(a)) and in the cryo-UHV setup (Fig. 7.4(b)) of the same region on the sample. A representative NV center is marked by the green circles. The elliptical distortion of Fig. 7.4(b) has already been explained in 3.4 and is related to the optical setup. In order to study the NV characteristics at 4.7 K and $2 \cdot 10^{-10}$ mbar, we decided to compare the obtained autocorrelation and ODMR measurements with results recorded at the ambient stage. Fig. 7.5 presents the impact of a cryogenic UHV environment on the bare NV center properties. Thereby, Fig. 7.5(a) compares the autocorrelation results. The dark gray curve is the $g^{(2)}$-function obtained by the representative NV center at ambient conditions. A clear antibunching dip below 0.5 was observed as indicator for the single photon emitter characteristics of the individual NV center. In contrary, the red curve represents the autocorrelation measurement of the same NV defect in the cryo-UHV setup. It is evident, that no antibunching curve is recognizable. This is a clear indication

for a charge state conversion.

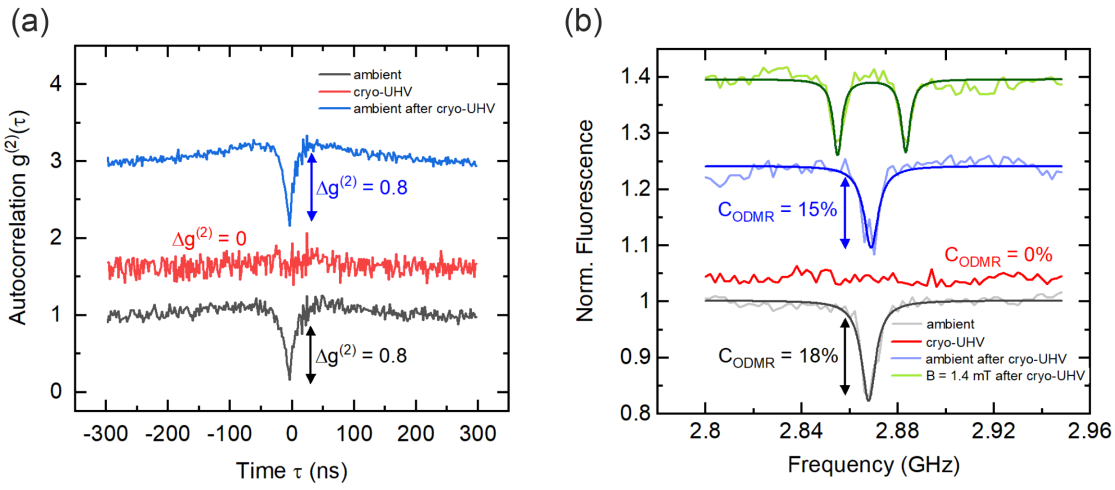

Figure 7.5: Characteristics of a bare NV center in cryogenic 4.7 K conditions and at UHV. (a) Autocorrelation measurements of an individual NV center at ambient (gray curve) and cryo-UHV conditions (red curve). The disappearance of the antibunching dip can be observed. Repeating the measurement after the cryo-UHV round at the ambient stage (blue curve) reveals the antibunching dip in a reproducible manner. (b) A similar behavior can be observed in the ODMR spectra. In addition, a weak magnetic field has been applied on the second ambient stage measurement (green curve) for observing the Zeeman splitting as NV^- center fingerprint.

The optical path of the utilized setup is specified for the investigation of NV^- centers. This is achieved by the implementation of certain optical filters operating at the 637 nm ZPL of the NV^- state. In particular longpass (LP) filters are used which cut off wavelengths below 637 nm. As consequence, the NV^0 center ZPL at 575 nm is not recorded by the photo detectors. Actually, also the NV^0 charge state forms a single quantum emitter. However, the corresponding photons are filtered before reaching the detectors. As a result, the autocorrelation function shows no antibunching dip when the observed NV center obtains its NV^0 charge state. The blue curve in Fig. 7.5(a) depicts the autocorrelation curve of the same NV defect in a second ambient measurement set which was obtained after the characterization in cryo-UHV. In that case, an reappearance of the antibunching dip was observed indicating the recovery of the NV^- charge state.

Similar results were investigated in the recorded ODMR spectra as represented in Fig. 7.5(b). Again, the dark gray curve shows the measurement at ambient conditions, indicating an ODMR signal with $C_{ODMR} = 18\%$. Instead, the red curve depicts the ODMR spectrum measured at 4.7 K and within the UHV environment. A full loss of the ODMR signal was observed. Repeating the experiment on the same NV in a second measurement set at the ambient stage showed the reappearance of the ODMR signal. It is worth to mention that the presented results are reproducible over the majority (65 %) of the 25 characterized NV centers independent from the applied implantation energies within

2.5 keV to 10 keV. An overview table is shown in the appendix 10. Therefore, it is justified to assume an irreversible NV center charge state conversion within the cryogenic UHV environment. Furthermore, solely UHV measurements at ambient 298 K temperatures indicated also there a loss of the NV^- charge population which is shown in the appendix 10. Also this fact, can be potentially explained by the charge trap model proposed in [195]. While the electron charge traps are more stabilized at ambient conditions due to the environmental atmosphere [207], at an UHV environment the receptor states can solely recombine electrons from nearby NV^- centers. As a result, bare NV^- centers can not be observed in the cryo-UHV setup. However, coating the diamond surface with specific molecules can potentially stabilize the NV^- charge state.

7.4 Surface Modifications

Several studies have investigated that surface treatments of the diamond sample can have an impact on the NV properties[208, 209, 210]. For instance, etching the diamond surface with an ion beam [210] leads to covalent surface bonds which obtain a certain electron affinity [211]. Depending on the involved atoms within the bond, the NV^- or the NV^0 states can be stabilized. Thereby, a positive electron affinity enhances the NV^- spin properties. This can be achieved by etching the diamond surface with e.g. a nitrogen ion beam forming carbon-nitrogen bonds with an electron affinity of 3.46 eV [210]. In contrary, a negative electron affinity induces surface charge transfers which are able to force a formation of NV^0 charge states. For example, silicon-carbon bonds on the diamond surface with an electron affinity of -0.86 eV lead to instabilities of the NV^- center [210].
Unfortunately, an ion beam device is not implemented within the utilized experimental setup. Nevertheless, less aggressive surface treatments, as gas dosing, were tried for enhancing the NV^- stabilization. For this, a high-precision leak valve was implemented on the preparation chamber of the setup. The device is able to introduce a small amount of gas into the chamber which deposits than on the sample surface. Even that no chemical bonds are formed, the deposited gas molecules could potentially protect the charge state of shallow NV centers.

7.4.1 Nitrogen Dosing

In the first experimental attempt, we introduced nitrogen gas to the diamond surface. In [210] it has been shown that a nitrogen-carbon bond is able to stabilize the spin properties of the NV^- charge state due to its positive electron affinity. Therefore, it is a justified approach to cover the diamond surface with a nitrogen layer which potentially protect the charge distribution of nearby NV centers. In addition, nitrogen dosing is a straight forward process as the gas is neither aggressive nor toxic [212, 213].
The gas dosage in this experiment is a three step process. First of all, the diamond sample has to be as cold as possible. Otherwise, the introduced gas molecules do not adsorb on the surface. For this, the sample is positioned in the cryogenic measurement head within the main chamber at 4.7 K. After

cooling down, the whole sample holder is transferred to the preparation chamber where the gas dosing is performed. Thereby, a nitrogen gas bottle is connected to the leak valve. By releasing the valve, the nitrogen gas is introduced in the chamber. For estimating the amount of gas, the readout of the pressure sensor is suitable. Typically, the pressure within the preparation chamber is $\approx 3 \cdot 10^{-10}$ mbar. Introducing the nitrogen gas increases the pressure depending on the release volume of the leak valve.

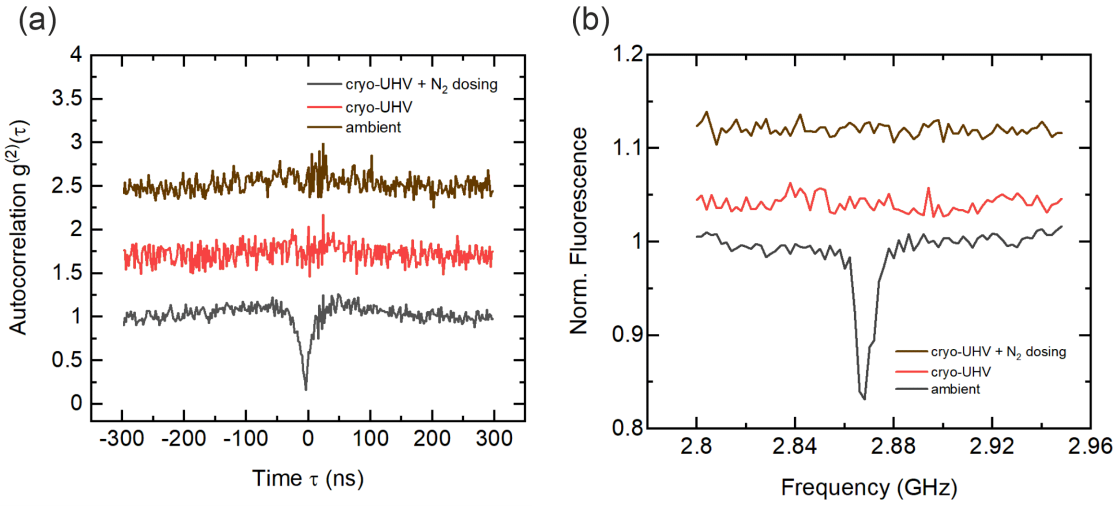

Figure 7.6: Nitrogen dosing on the diamond surface. (a) Autocorrelation curves of an individual NV center.The measurements obtained at ambient (gray curve) and cryo-UHV (red curve) conditions have already been discussed in Fig. 7.5. The brown curve corresponds to the autocorrelation recorded at a cryogenic UHV environment after the dosage of nitrogen gas. Still no antibunching dip can be recovered. (b) Also in terms of ODMR spectroscopy, N_2 gas is not enhancing the NV^- center spin properties. No ODMR signal can be obtained at cryo-UHV conditions.

In this project, the dosing procedure was performed for 60 s at an increased preparation chamber pressure of $5 \cdot 10^{-7}$ mbar. Afterwards, the sample was transferred back to the cryogenic main chamber for NV characterization. Fig. 7.6 shows the resulting NV center properties. The autocorrelation curves (Fig. 7.6(a)) and the ODMR spectra (Fig. 7.6(b)) of an individual NV center are compared for three different scenarios. The first autocorrelation curve (depicted in gray) shows the single emitter characteristic of the observed NV center at ambient conditions by the antibunching dip below 0.5. Furthermore, the red curve indicates the measurement of the same NV center at cryogenic and UHV conditions in which no antibunching feature can be found. For consistency, these data corresponds to the measurements which have already been discussed in 7.3. In addition, the brown curve illustrates the autocorrelation obtained after the nitrogen dosing procedure. Unfortunately, no hint regarding the existence of the NV^- charge state could be found as still no antibunching dip was observed. Similar findings were investigated in the ODMR spectra. At ambient conditions, the NV center showed a clear ODMR signal at 2.8 GHz. However, within the cryo-UHV setup no ODMR feature were measured. Even after nitrogen dosing, the ODMR signal seemed to vanish. Three explanations can be assumed

for this behavior. The first one is a technical speculation by assuming that the nitrogen gas did not deposit on the diamond surface during the dosing procedure. This can be a realistic scenario as the surface temperature of the sample can not be read out within the experimental setup. If the diamond surface exhibits a temperature above the cooling temperature of nitrogen (70 K), the chance of depositing a nitrogen layer is decreased. The second potential explanation assumes a successful deposition of the nitrogen gas. However, it takes the chemical properties of nitrogen into account. The argument of an existing N-C bond with a positive electron affinity proposed in [210] can not be applied on our experimental scenario as no chemical bonds were formed during the gas dosing. To be more precisely, the electronegativity of atomic nitrogen has to be considered. Thereby, nitrogen obtains an electronegativity of 3.07 eV [211]. With such a high electronegativity, nitrogen atoms are able to attract electrons from the diamond matrix. As a result, the NV^- charge state is forced to transform into the NV^0 state. The last and most realistic assumption is the formation of an N_2 molecular layer during the dosing procedure. Nitrogen, similar to oxygen (O), barely occurs as single atom. It is more likely to appear as triple-bonded N_2 molecule due to its electron configuration [211, 213]. As N_2 layer, the deposited compound does not affect the already vanished NV^- charge state.

7.4.2 Formation of an Atmospheric Water Layer

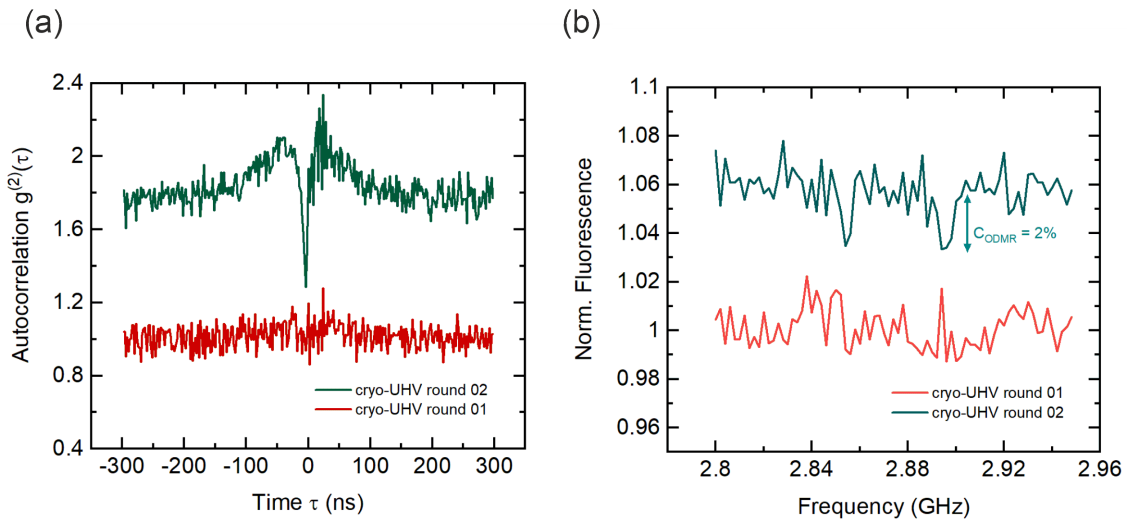

Figure 7.7: Comparison of the same NV center within two different cryo-UHV measurement sets. Before the first cryo-UHV round was obtained, the diamond sample was located for 5 days at the ambient stage. Instead, before beginning a second cryo-UHV experimental set, the diamond plate was positioned for 35 days at ambient conditions. Interestingly, within the second measurement set, NV^- properties were be indicated. A realistic scenario could be the formation of an atmospheric water layer during the elongated characterization measurements at ambient conditions.

In order to ensure a full desorption of the deposited nitrogen layer, we transferred the diamond sample from the cryo-UHV setup to the ambient stage. The standard environmental temperature of 300 K should directly transform the dosed layer to nitrogen gas [212]. For consistency, the 25 characterized NV centers were re-measured obtaining the typical NV^- state features. Afterwards, the sample was positioned within the cryo-UHV setup for continuing the dosing study. However, before the next gas candidate was dosed (namely carbon monoxide) the bare NV centers were measured in an additional experimental set for ensuring the NV^- state disappearance. Surprisingly, hints of an NV^- charge state existence could be found as depicted in Fig. 7.7. Moreover, Fig. 7.7(a) compares the autocorrelation curves obtained from the first (section 7.3) and second (here described) cryo-UHV measurement set. While in the first observation (red curve) no antibunching dip is resolved, in the second measurement (green curve) a clear single emitter feature can be found. In addition, the same trend can be investigated in the ODMR spectra which are presented in Fig. 7.7(b). The ODMR spectrum obtained in the first cryo-UHV measurement round shows no MW transitions. However, a weak ODMR contrast of 2% is observed in the second measurement set.
In order to understand this behavior, it is crucial to know the measurement duration at ambient conditions. Before the first cryo-UHV measurement was performed, the sample was characterized at the ambient stage for 5 days. Instead, the sample was measured for 35 days at ambient conditions before the second cryo-UHV experiment was started. In fact, the exposure of an NV center to an ambient environment can change its spin properties over time due to the natural deposition of magnetic impurities [195]. The formation of such clusters on the diamond surface can act as charge traps and destabilize the NV center. On the other side, the impurities can enhance the spin properties by acting as a protection layer. Typical candidates which are able to self-assemble on surfaces are hydrogen atoms or water vapor [214]. Especially a water layer can be interpreted as an interesting system due to the relatively large dipole moment of the H_20 molecules (≈ 1.85 D) [215, 216, 217]. This polarity can potentially stabilize charge distributions close to the NV centers. Therefore, the results of Fig. 7.7 could be explained by the formation of a water layer when the sample was characterized at ambient conditions. Afterwards, transferring the diamond membrane into the cryo-UHV setup led to a frozen H_2O layer which protected the NV centers.

7.4.3 IR Laser Heating

For ensuring the significant role of this uncontrolled surface modification, surface heating can be performed on the diamond sample. In this work, this was achieved by an IR laser which is mounted outside of the preparation chamber. IR wavelength (10 μm) specific optical components guide the laser beam into the preparation chamber in which the diamond sample is located (see section 3.5). The resulting increase of the surface temperature is read out by an optical pyrometer. In this experimental set, the IR beam was focused for 18 s on the sample. The readout temperature of the pyrometer was ≈ 168 °C. Assuming that the environmental deposited layer is composed of water, the achieved heat treatment should be efficient enough for removing the H_2O molecules.

In order to investigate an impact of the surface heat treatment, Fig. 7.8 compares the autocorrelation curves. Unfortunately, ODMR spectra could not be obtained. Due to the high IR beam power, the microwave wired bonded across the sample got damaged. As a consequence, microwave radiation could not be applied on the diamond. The green curve in Fig. 7.8 presents the measurement before the heat treatment and has already been discussed in section 7.4.2. As already described, an uncontrolled formation of an atmospheric water layer is assumed which is able to protect the NV^- state. This is indicated by the observed antibunching dip. Instead the purple curve illustrates the resulting autocorrelation after the surface heat treatment. In fact, the antibunching dip was observed anymore. The experimental results can be interpreted as a controlled surface treatment by eliminating a certain layer from the diamond sample. Furthermore, it gets more evident, that unprotected bare NV centers contain unstable spin properties in cryogenic UHV environments.

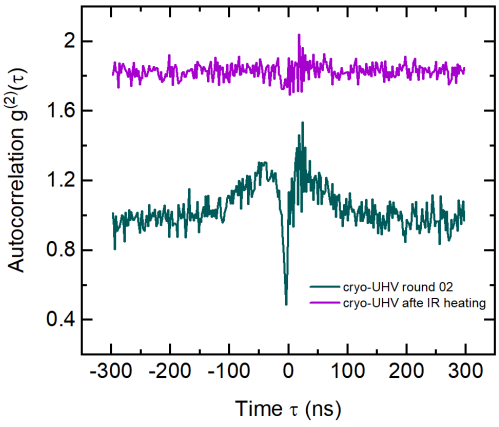

Figure 7.8: Autocorrelations at cryogenic UHV conditions recorded for the same NV center before and after the surface heat treatment. The diamond was exposed to an IR beam for 18 s reaching a surface temperature of 168 °C. The disappearance of the antibunching dip can be observed. This behavior can be interpreted as the removal of a protection layer which stabilized the NV^- charge state.

7.4.4 Carbon Monoxide Dosing

In this experimental section, we want to present a CO dosage of the diamond surface. Assuming that water enhances the NV center spin properties, this effect could be attributed to the dipole moment of H_2O. Therefore, gases which are characterized by certain dipole moments form interesting candidates in order to stabilize the NV center spin state. Thereby, a potential charge stabilizer can be found in carbon monoxide as it obtains a notable dipole moment of 0.11 D [218]. The dosing procedure is similar to the described nitrogen dosage set in 7.4.1. The CO gas was introduced into the preparation chamber for 60 s by observing a pressure increase to $5 \cdot 10^{-7}$ mbar.

The findings in terms of autocorrelation measurements are shown in Fig. 7.9 by comparing the $g^{(2)}$

functions before and after CO dosing. Note that, the curve presented as the non-dosed result corresponds to the heat treated sample. By this, we can ensure a clean diamond surface without the existence of magnetic impurities or protection layers. As already discussed in section 7.4.3, no antibunching dip was observed for the unprotected NV centers within the cryogenic UHV environment. Unfortunately, Fig. 7.9 indicates that a CO dosing procedure is (similar to a nitrogen dosage) not able to recover the NV^- center properties. This assumption is evaluated from the non-investigated antibunching dip. Therefore, the obtained results suggest a strong NV stabilization dependence from the dipole moment of the utilized protection layer. While CO molecules are characterized by a dipole moment of 0.11 D [218], H_2O molecules obtain a dipole moment of 1.85 D [217]. This value is $\approx$ 16 times larger compared to the dipole moment of CO. As a result, a protection layer formed by water molecules has a more efficient control of the charge distribution on the diamond surface. Therefore, studying the NV properties by dosing gases with higher polarities could reveal stabilization mechanisms of the NV charge states.

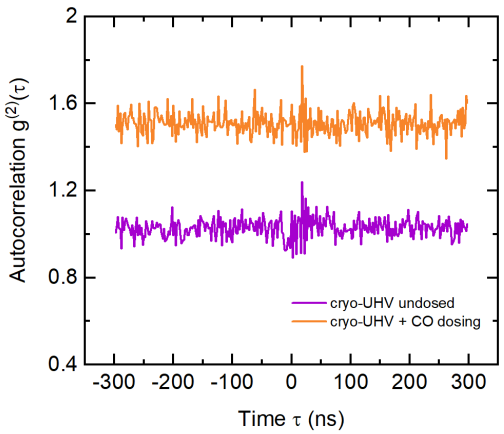

Figure 7.9: CO dosing of the diamond surface. The autocorrelation curves at cryo-UHV conditions of the same NV center are compared before and after the gas dosage. No impact of the CO gas can be observed on the NV center properties.

Also explicit in situ surface treatment with H_2O could be sufficient for stabilizing the NV^- charge state. Motivated by this, we dosed water onto the diamond surface in a controlled manner.

7.4.5 Water Dosing

The water exposure was performed by the implemented dosing line which has already been explained in 3.5. Similar to the gas dosing sets, the amount of introduced water was controlled by a leak valve. Afterwards the NV centers were characterized by their autocorrelation antibunching dip and ODMR spectra contrast. The experimental results are depicted in Fig. 7.10. As usual, the undosed scenario (shown by the red curves) does not reveal any NV^- features. Neither an antibunching dip nor ODMR

resonances were observed by investigating the representative NV center at cryogenic UHV conditions. However, a subsequent water deposition on top of the diamond surface led to a rather interesting NV center behavior (illustrated by the blue curves). The autocorrelation after the H_2O shows a clear antibunching dip. Moreover, even the ODMR spectrum obtains slight features related to MW absorption lines. The gathered results can be evaluated as a minor recovery of the NV^- charge state.

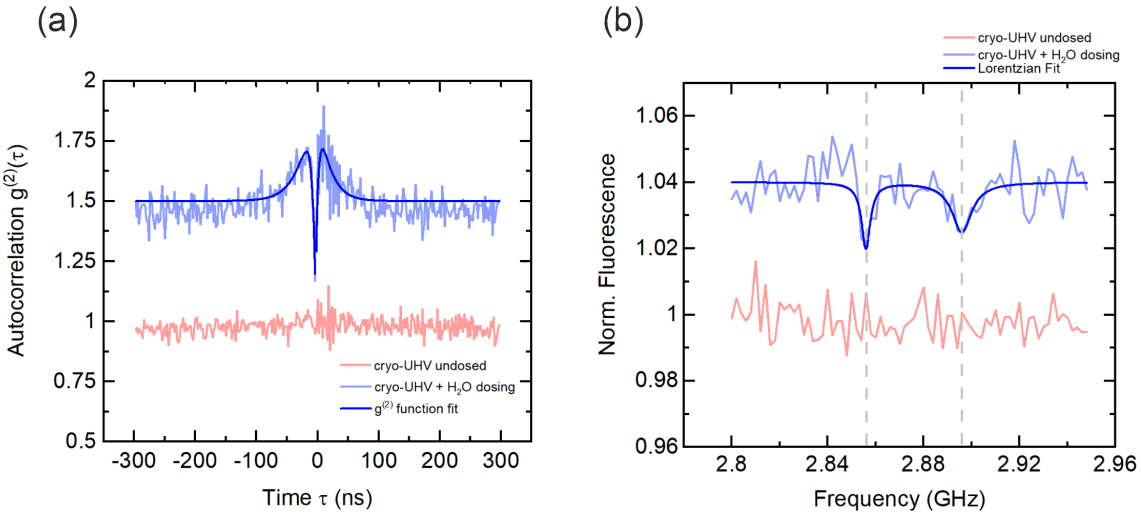

Figure 7.10: Comparison of an NV center in a cryo-UHV environment, measured without surface treatment (red curves) and with H_2O dosing (blue curves). The autocorrelation (a) obtains an antibunching dip by depositing water on the diamond surface. Also the ODMR spectrum (b) indicates a slight appearance of resonance lines when the diamond is exposed to a water dosage.

An explanation can be found by interpreting the deposited water layer as a charge stabilizer. The electric field which is formed by the high dipole moment within the water molecule is capable to stabilize the electron location on the NV defect. As a result, surface charge traps are not able to retract the additional electron from the NV center and the NV^- charge state population is increased. In order to quantify this process, the autocorrelation curve can be fitted with a $g^{(2)}$ function model which is able to reveal information about the transition rates k_{ij}. The function can be expressed as

$$g^{(2)}(\tau) = g^{(2)}_{theo.}(\tau)\rho^2 + 1 - \rho^2. \tag{7.4}$$

Thereby, $\rho = S/(S+B)$ characterizes the signal S to background B ratio. Furthermore, $g^{(2)}_{theo.}$ stands for the theoretical antibunching curve which illustrates the ideal case with a dip dropping to zero. However, due to a certain photon background level this is not achievable in an experiment. The theoretical expression is given by [219]

$$g^{(2)}_{theo.}(\tau) = 1 - \beta e^{-\gamma_1 \tau} + (\beta - 1)e^{-\gamma_2 \tau}. \tag{7.5}$$

In this equation, the parameters γ_1, γ_2 and β are of great importance as they contain information about the transition rate parameters k_{12} and k_{21} for a two level system and k_{23} and k_{31} for a three level system. A detailed expression of these parameters is shown in the appendix 10. Thereby, γ_1 depends solely on k_{12} and k_{21}. Therefore, γ_1 represents a crucial parameter for the NV^0 center as this charge state is characterized by a two level system (described in 7.1). Instead, γ_2 depends on k_{12}, k_{21} and additionally on k_{23} and k_{31}. As consequence, γ_2 plays an important role for the NV^- charge state which is described by a three level system. The outcome of the depicted fit in Fig. 7.10(a) is:

β	γ_1 [ns^{-1}]	γ_2 [ns^{-1}]
1.67	0.166	0.0466

Table 7.1: Fitting parameters of the $g^{(2)}$ function model utilized in Fig. 7.10(a).

According to [219], the magnitude of $\gamma_2 = 0.0466\,ns^{-1}$ is a strong indication for a significant NV^- charge state population. Typically, an NV defect obtaining a more pronounced NV^0 charge state leads to a γ_2 of $< 0.02\,ns^{-1}$ [219]. Therefore, it is reasonable to conclude that a water layer impacts the charge state stability of individual NV centers.
However, at this point it is worth to mention that a full NV^- state stabilization in cryogenic UHV conditions was not achieved by the presented water dosing experiment. Only slight recovery hints as in Fig. 7.10 were observed. Especially the ODMR contrast of the individual NV centers are by far not comparable with ODMR signals obtained at ambient conditions which are on the order of 10%. This supports the indication that H_2O acts more as a charge stabilizer than as an electron donor. The high NV^- stability at ambient conditions is most likely related to compounds formed between H_2O and radicals within the environmental air. Thereby the radicals act as electron donors and the deposited water layer on top of the diamond surface controls the charge distribution. Therefore, dosing water and gas in a simultaneously way could recover NV properties in cryogenic UHV environments which are comparable to characteristics measured at ambient conditions.

7.4.6 Fluorescence Spectroscopy

So far, the NV center characteristics were studied in terms of autocorrelation curves and ODMR spectra. Thereby, the disappearance of features as antibunching dips and resonance lines were assumed to be related to charge state conversions. Quantitatively, $g^{(2)}$ function fits are able to reveal information about the actual energy level scheme of the NV defect for distinguishing the present charge state. In order to additionally proof this argument fluorescence spectroscopy experiments can be performed on the individual NV centers. As discussed in section 7.1, the emission differs in dependence of the NV charge state. While the NV^- center emits a ZPL at 637 nm, the NV^0 state obtains a strong fluorescence line at 575 nm. Therefore, the NV center charge population can be qualitatively estimated by investigating the relative peak intensities of the ZPL within the emission spectrum. Furthermore, the measured spectra can be compared for different experimental conditions.

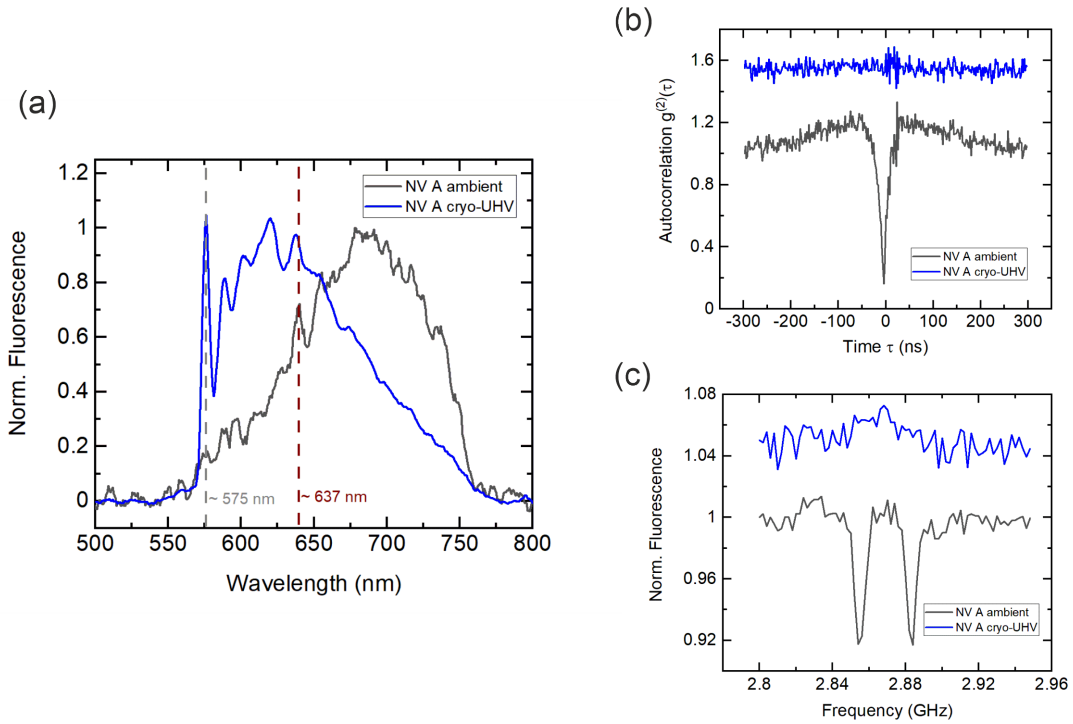

Figure 7.11: Fluorescence spectroscopy on an individual NV center. (a) Comparison of the NV center emission measured at ambient (grey curve) and cryogenic-UHV conditions (blue curve). The significant change of the emitted wavelengths is a strong indicator for a charge state transfer. (b) and (c) Autocorrelation curves and ODMR spectra of the investigated NV center showing the disappearance of NV^- features. Due to the obtained spectra, these issue can be fully related to a forced charge state transfer at cryogenic UHV conditions.

Fig. 7.11(a) shows such a comparison by illustrating the spectra obtained from the same NV center (termed as NV A) at ambient and cryo-UHV conditions. At an ambient environment (grey curve) a significant emission peak at $\approx$ 637 nm was observed. Repeating the measurement when the diamond sample was located into the cryo-UHV setup obtained a spectrum which was characterized by a strong appearance of an emission line at $\approx$ 575 nm. The observed change in the NV fluorescence clearly indicates a charge state transfer. At ambient conditions the NV center stands in the NV^- state and emits light in the wavelength range of 637 nm to 760 nm. However, at cryogenic UHV conditions, the NV center obtains its neutral NV^0 charge state and emits light in a wavelength range of 575 nm to 720 nm. As a result, no antibunching dip and ODMR signals can be obtained within the cryo-UHV which is depicted in Fig. 7.11(b) and (c). In addition to that, the presented fluorescence spectroscopy could also be utilized for observing the impact of a water layer on the NV charge state as shown in Fig. 7.12.

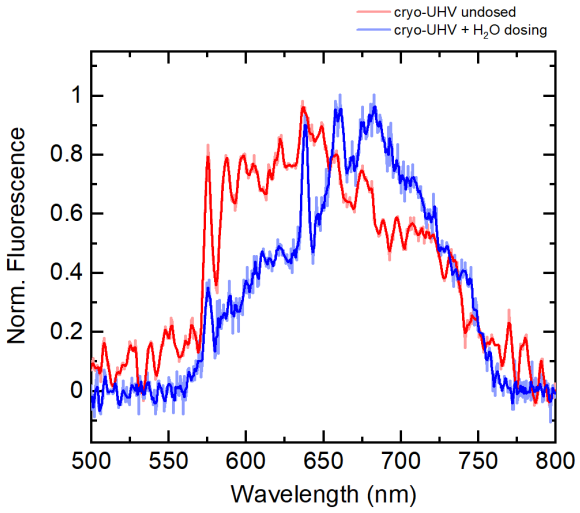

Figure 7.12: Emission spectra of an individual NV center recorded at cryogenic UHV conditions with (blue curve) and without (red curve) water dosing. While in the bare scenario the NV center obtains a high NV^0 population, an appearance of an emission signal at 637 nm suggests a charge state transfer to the NV^- state due to the dosed water layer.

Thereby, the red curve depicts the NV center emission in an undosed scenario. A strong NV^0 contribution can be observed due to the intense fluorescence line at 575 nm. However, recording the emission of the same NV defect after a H_2O dosage (illustrated by the blue curve in Fig. 7.12), reveals a significant drop of the NV^0 contribution. A slight increase of the emission intensity at $\approx$ 637 nm can be observed, which is associated to a charge state transfer towards an NV^- population.

7.5 Summary

In this chapter we presented a fundamental study of the single NV center spin properties. Thereby, we investigated in the first sections the spin characteristics in terms of ODMR spectroscopy for different NV center depths. The depth of the defects within the diamond matrix was defined by the nitrogen ion implantation energy. The first measurements set was performed at ambient conditions. A clear trend of the ODMR contrast in dependence of the NV center depth was observed. Deeper implanted NV defects exhibited a relatively high ODMR contrast of 11 %, compared to shallow NV centers which were characterized by an ODMR contrast of only $\approx$ 5 %. Explanation for this behavior can be found in the charge state dynamics of individual NV centers. Instabilities within the NV^- and NV^0 charge states lead to a decrease of the ODMR signal. Thereby, magnetic impurities form charge traps on the diamond surface which are able to induce charge transfer mechanisms. Near-surface NV centers are highly affected by these processes resulting into the formation of NV^0 states which do not show ODMR signals. As a result, the ODMR contrast of shallow NV centers is decreased relative to the signals obtained from deeper implanted defects.

Afterwards, we observed the NV properties within the cryogenic UHV environment at 4.7 K and $9 \cdot 10^{-11}$ mbar. Thereby, the diamond surface was not coated with specific molecules in order to gain information about the bare NV center characteristics. Surprisingly, we found a complete absence of the NV^- properties in $\approx 65\,\%$ of the investigated NV centers. Neither autocorrelation measurements nor ODMR spectra could be obtained. Therefore, a charge state transition to the NV^0 center is assumed. As the optical setup is specified for detecting the NV^- center emission (ZPL ≈ 637 nm), no NV^0 state photons can be recorded for gathering an antibunching autocorrelation curve. In order to enhance the NV^- signals, we performed several dosing attempts by depositing nitrogen and carbon monoxide protection layers on the diamond surface. Unfortunately, both gases were not able to control the charge distribution on the sample surface for recovering the NV^- state. However, an interesting result was found by maintaining the diamond sample for 35 days at ambient conditions before transferring it into the cryo-UHV setup. In that particular scenario, antibunching dips within the autocorrelation curve and weak ODMR signal of 2 % were observable. A water layer formation within the elongated maintenance of the sample at the ambient stage can be assumed. The high dipole moment of the H_2O molecules (1.85 D) could be a potential reason for controlling the charge state of the NV centers. In fact, controlled water dosing procedures within the preparation chamber indicated a slight recovery of the NV^- charge state.

Therefore, it is reasonable to extend the current work with the implementation of gases obtaining a high polarity compared to CO. Potential candidates are nitrous oxide (N_2O) which obtains a dipole moment of 0.17 D [220] or nitric oxide characterized (NO) by a dipole moment of 0.16 D [221]. Such experiments could reveal a threshold for the minimum dipole moment strength required for an NV^- center recovery. Especially NO is an interesting system as the molecule exhibits an unpaired electron (chemical radical) [222] and can potentially act as an electron donor.

In addition to introducing gases on the diamond surface, also the atomic layer deposition of insulators (as tin oxide or titanium dioxide) or sodium chloride NaCl (dipole moment of ≈ 9 D) could have a huge impact on the NV center spin properties.

The stabilization of shallow NV^- centers can have a great impact on nanoscale magnetic field sensing as the spatial resolution benefits from narrow sensor-to-sample distances.

8 Alternatives to NV Centers as Quantum Sensors

Crystallographic defects in diamond are very common [223, 224]. Already more than 50 known defects are solely attributed to nitrogen impurities [223]. Including other substitutional atoms like boron, phosphorous or hydrogen, the amount of known impurities in diamond reaches more than 500 defect centers [225, 226]. In chapter 2 we mentioned the different categories of defects in diamond. Therefore, it is rather likely that also other incorporated systems within the diamond lattice can be used as quantum sensors similar to the NV center. Of course, the NV defect is the most studied impurity in diamond and due to its unique spin dependent fluorescence properties a highly reliable sensing system. However, we have seen in the last chapter (Ch. 7) that the NV center spin properties crucially depend on corresponding charge states. In presence of magnetic noise, charge transfers are induced which lead to fluctuating NV center properties. Therefore, it would be beneficial to study also other defects in diamond. Having as many types of quantum sensors as possible can only be beneficial in the field of nanoscale magnetometry. By this, disadvantages like instabilities or low coherence times can be compensated depending on the observed magnetic system.
An interesting alternative to the NV center is formed by the group IV colour centers in diamond which include the silicon (Si)-, germanium (Ge)-, tin (Sn)- and lead (Pb)-vacancies [227, 228]. Especially, the SiV defect emerged as a promising competitor to the NV center due to its strong fluorescence with a sharp ZPL at 738 nm [229, 230, 231]. Furthermore, its spin state can be controlled (similar to the NV center) by MW irradiation resulting into an ODMR spectrum with two peaks at 2.7 GHz and 2.76 GHz [231]. The resonance frequencies indicate a linear magnetic field dependence which can be attributed to the Zeeman effect. However, phonon induced mixing between the SiV orbital states causes a strong spin decoherence which result into relatively low T_2 times compared to the NV center coherence [232]. As the T_2 is a crucial parameter for quantum sensing applications, no sensing protocols could be achieved with the SiV center so far. Nonetheless, it is a justified approach to investigate single defects which show photoluminescence due to their interpretation as non-classical light sources. Several applications can be found beyond the field of magnetometry, e.g. in quantum optics, quantum communication and super-resolution optical imaging [233].
Therefore, this chapter presents the study of a novel defect center found in natural diamond. The investigation of bright point defects obtaining an in literature not noted ZPL at $\approx$ 448 nm is described. Furthermore, high frequency measurements have been performed resulting into the investigation of significant ODMR signals at $\approx$ 2263 MHz and $\approx$ 500 MHz. All results have been obtained at ambient

conditions. The work can be extended by the performance of pulsed measurements on the defect for gaining access into its spin dynamics.

8.1 A Novel Defect Center in Diamond

The characterization of the novel defect center is divided into two sections. First of all, the optical properties of the defect are presented by evaluating its emission spectrum. Instead, the second part of the investigation obtains the HF measurements which reveal the ODMR spectrum of the defect center. Both studies are crucial for reconstructing a possible energy level diagram.

8.1.1 Optical Properties

The optical characterization of the novel defect was achieved by the utilization of a confocal microscope setup operating at a wavelength of 405 nm. The experimental setup is shown in Fig. 8.1(a) consisting of a 405 nm laser diode which is guided to the sample stage in which the natural diamond is located. After the sample is excited, the emitted light is passed trough a dichroic mirror which transmits wavelengths > 420 nm. The emission is than recorded by a photomultiplier tube (PMT) detector.
By scanning the sample stage, a confocal image can be reconstructed as shown in Fig. 8.1(b). The defects can be observed as bright features within the image. Furthermore, a flip mirror is implemented in the setup for guiding the emitted light to a high sensitive spectrometer (QEPro). With this, the optical properties of the bright spots can be studied. Fig. 8.1(c) illustrates the resulting emission spectrum showing four spectral lines. The first peak at 405 nm indicates the laser excitation beam which has not been fully reflected from the dichroic mirror. The intense peaks at 432 nm and 455 nm correspond to the first and second order Raman lines [234]. Interesting is the spectral line at 448 nm which has not been noted in literature so far. It can be assumed, that this peak corresponds to a ZPL from an undiscovered defect center. Therefore, we termed the potential impurity as novel defect center.

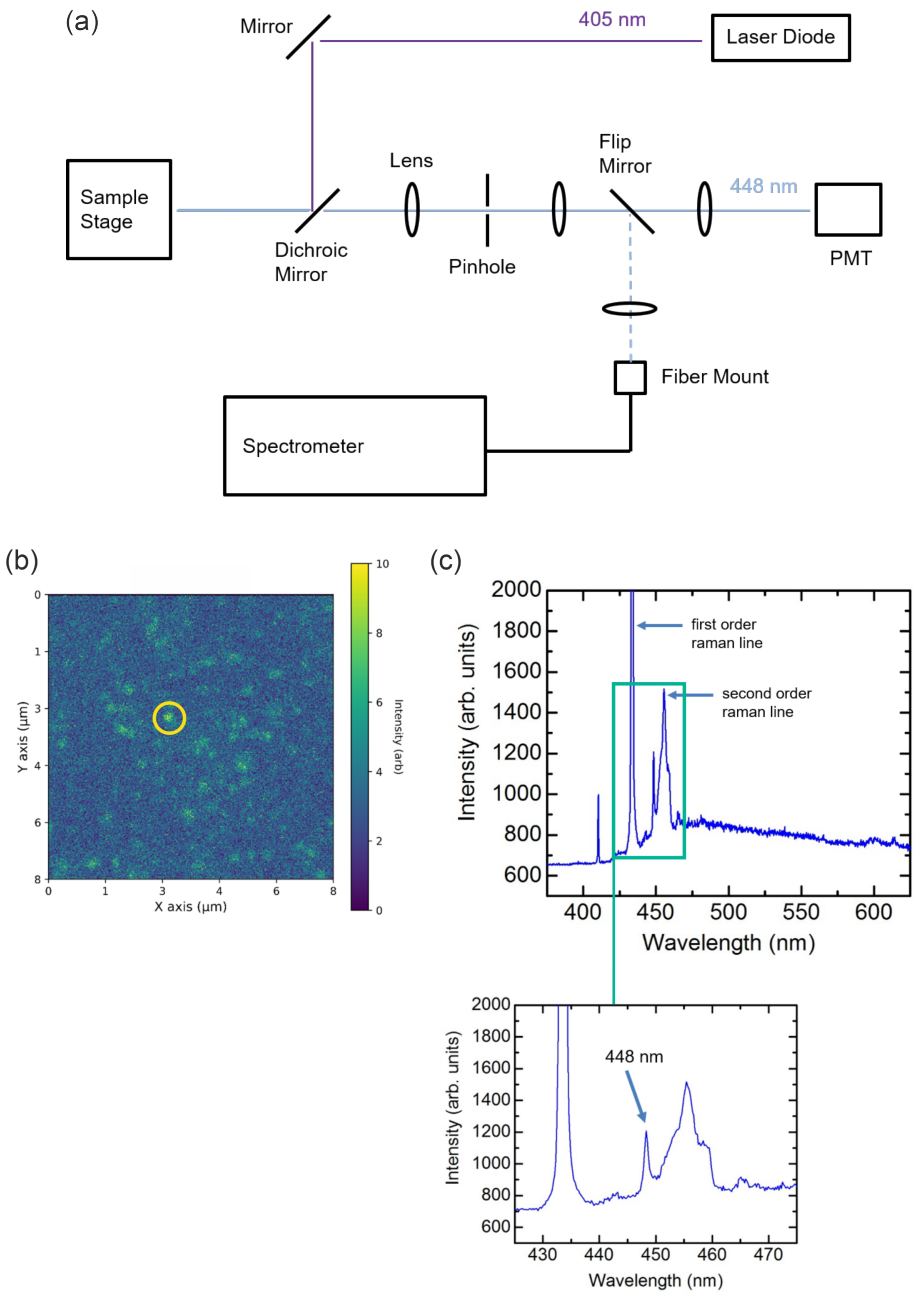

Figure 8.1: Optical characterization of the novel defect center in diamond. (a) Sketch of the confocal microscope setup which is specified for wavelengths between 400 nm and 450 nm. (b) Resulting confocal image indicating the luminescent defects as bright features. The yellow circle highlights the measured emitter. (c) Emission spectrum characterized by a resonance line at 448 nm. This feature is not noted in literature for a ZPL of a defect in diamond.

8.1.2 High Frequency Measurements

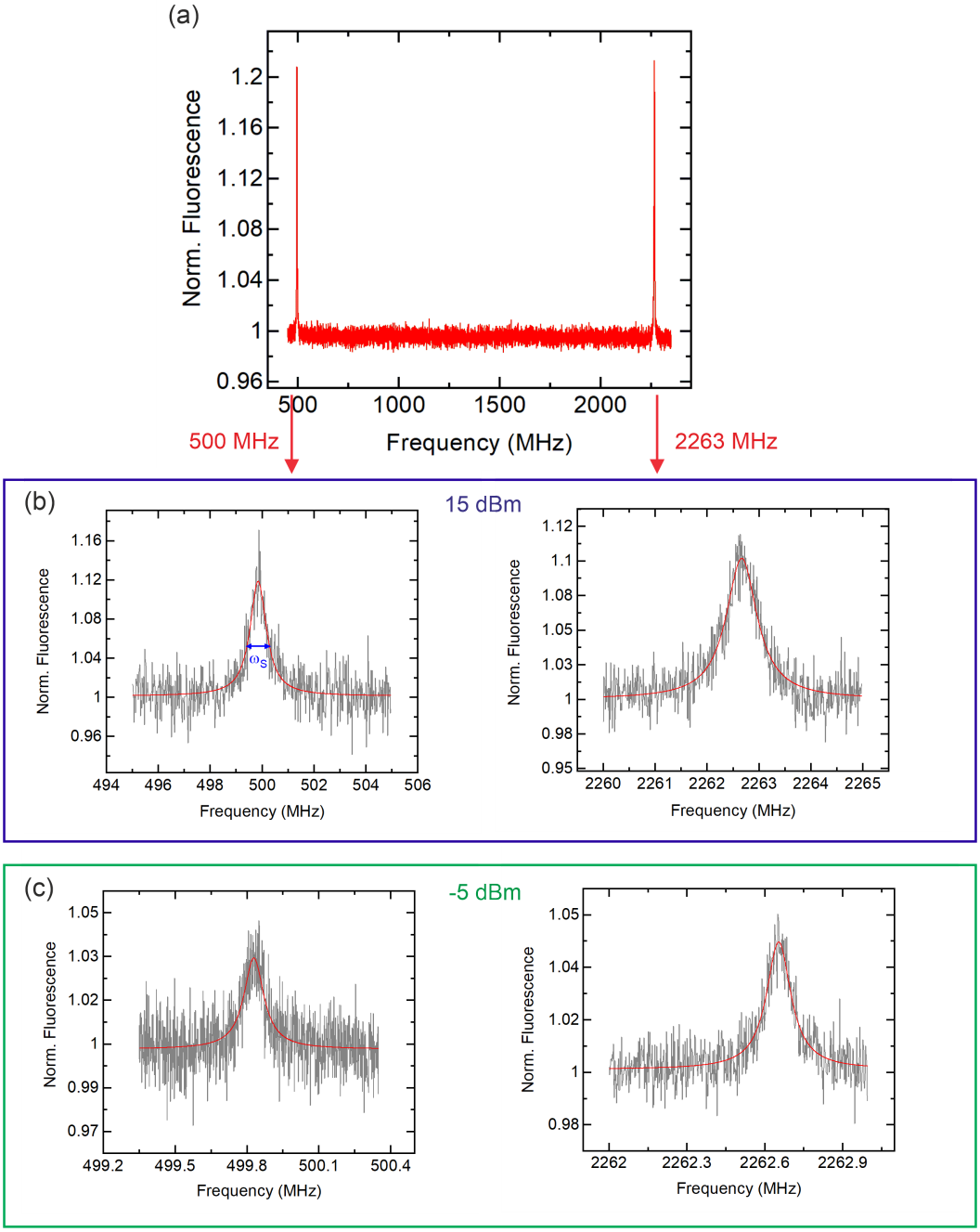

Figure 8.2: ODMR spectroscopy on the novel defect center. All measurements have been obtained at ambient conditions and in the absence of an externally applied magnetic field. (a) The full ODMR spectrum shows two resonance lines at ≈ 500 MHz and 2263 MHz. (b) Power dependence of the signal width ω_S. By deceasing the applied MW power, ω_S is narrowed which enhances the frequency resolution.

In order to study the emitting features more detailed, we performed high frequency measurements on the defect.

cw ODMR Spectroscopy

Thereby, we initiated the experiments with cw ODMR spectroscopy measurements. As no characteristics of the impurity are known, the applied MW frequency was swept within the range from 400 MHz to 2400 MHz. It is also important to mention, that all measurements were performed without the application of an external magnetic field. Indeed, two ODMR signals at 500 MHz and 2263 MHz could be resolved which are depicted in Fig. 8.2(a). The existence of an ODMR signal is a clear indication for the excitation of electronic spin states. In addition, the appearance of two ODMR lines without the application of magnetic fields contains information about the ZFS Hamiltonian

$$H_{ZFS} = D\left(S_z^2 - \frac{1}{3}S(S+1)\right) + E\left(S_x^2 + S_y^2\right) \tag{8.1}$$

of the defect. Thereby, the axial ZFS parameter can be resolved by the mean value of the resonance frequencies

$$D = \frac{2263\,\text{MHz} + 500\,\text{MHz}}{2} = 1381.5\,\text{MHz}. \tag{8.2}$$

The off-axial ZFS parameter E represents the frequency splitting within D and the resonance peaks

$$E = 2263\,\text{MHz} - 1381.5\,\text{MHz} = 881.5\,\text{MHz}. \tag{8.3}$$

Furthermore, the power dependence of the signal width ω_S was investigated (Fig. 8.2(b) and (c)). The application of an MW power of 15 dBm resulted into a width of $\approx$ 2 MHz. Instead, decreasing the power to -5 dBm led to a narrow signal with a width of only ≈ 0.15 MHz. As expected, the decrease of the application power enhances the frequency resolution within the ODMR spectrum.
However, in order to study potential spin dynamics, pulsed measurements have to be involved.

Pulsed HF Measurements

The simplest pulse sequence which can be applied to a spin system is to vary the duration of a resonant excitation pulse. As a result, Rabi oscillations should be observable due to the coherent flips of the spin state. In case of the novel defect center this is shown in Fig. 8.3(a). The measurement was performed at a fixed MW frequency of the lower 500 MHz transition. Furthermore, the duration of the applied excitation pulse was varied between 0 and 700 ns. An oscillating behavior of the emission could be observed indicating a coherent control of the spin state. Under an applied MW power of 10 dBm, a π pulse length of $\approx$ 50 ns could be measured.
For gaining more insights into the spin characteristics, T_1 lifetime measurements have to be performed. Thereby, the measurement is built up by a 405 nm initialization pulse. After a certain delay time, the

defect is read out with an additional 405 nm laser pulse for 3 μs. The first measurement was obtained without the application of a resonant π pulse (Fig. 8.3(b)). Instead, a second measurement set was recorded in presence of a 500 MHz resonant MW pulse (Fig. 8.3(c)). A significant difference of the resulting T_1 times could be observed. The measurement without π pulse indicated a lifetime of 35 μs. In contrary, applying a resonant MW excitation within the lifetime measurement resulted to a T_1 time of 3 μs. This fact can be utilized for explaining the rise in the detected fluorescence when the applied frequency is in resonance. It seems that one of the spin states obtains a relatively small lifetime compared to the other two states. Therefore, the readout of the fluorescence for 3 μs can solely record photons emitted within this time range. As the other states exhibit a lifetime of 35 μs, no photons of these spin levels can be recorded within the 3 μs readout.

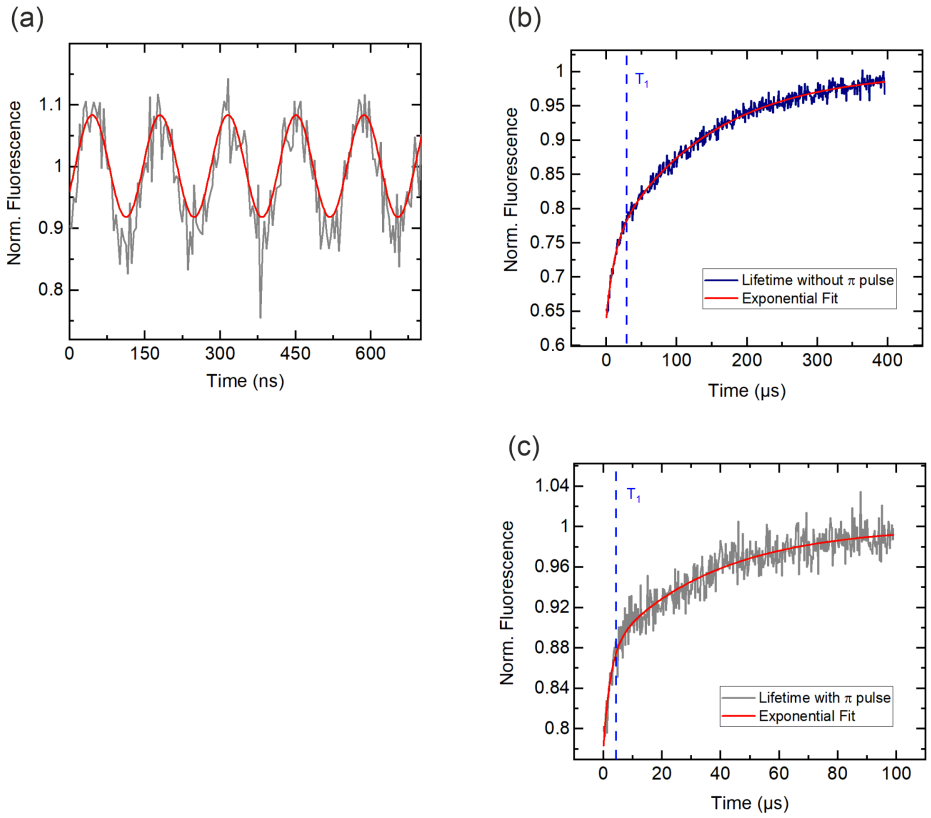

Figure 8.3: Pulsed measurements on the novel defect center. (a) Applying a resonant MW pulse and varying its duration leads to an excitation of Rabi oscillations. This a reliable prove that the spin state of the defect can be coherently manipulated. (b) Lifetime measurement obtained in absence of a resonant π pulse. A T_1 time of $\approx$ 35 μs can be obtained. (c) Instead, implementing a resonant π pulse into the measurement scheme reduces the lifetime to 3 μs.

Reconstruction of an Energy Diagram

With this set of information, a first energy level diagram can be constructed which is illustrated in Fig. 8.4. The ground state of the defect center (termed as $S0$) can be pumped with a 405 nm irradiation to an excited state (termed as $S1$). The direct relaxation path emits a 448 nm radiation which can be identified as the ZPL in the emission spectrum. However, it seems that the excited state $S1$ is coupled to a metastable spin triplet system denoted as 0, 1 and 2. Thereby, the 0 state obtains a lifetime of $T_z = 35\ \mu$s and results in a decay into the $S0$ ground state. Furthermore, resonant HF transitions can be excited with 2263 MHz and 495 MHz irradiation into the 1 and 2 states. These are characterized by a lifetime of $T_{x,y} = 3\ \mu$s.

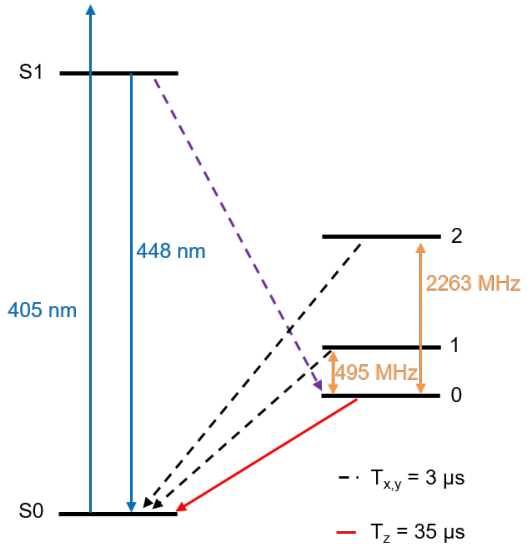

Figure 8.4: Reconstructed energy level diagram of the novel defect center. The scheme is proposed based on the performed measurement sets.

8.1.3 Further Work

Of course, the described energy level scheme is based on assumptions which have been interpreted from the presented results. However, for gathering a more detailed level diagram further measurements have to be performed. For instance, it is crucial to observe the behavior of the ODMR spectrum under the application of a magnetic field. The magnetic field dependent frequency shift of the resonance lines could give estimates for revealing the symmetry axis of the defect. In addition, more sophisticated pulse schemes, like Hahn sequences, can be applied for investigating the coherence time of the defect. This is an important quantity in terms of quantum information processing. With a high T_2 time, the defect could be interpreted as a suitable qubit system. Also pulsed ODMR measurements can be performed for resolving the hyperfine structure within the resonance lines. This is important for revealing the chemical composition of the impurity [235, 236]. Also IR spectroscopy can be utilized

for revealing chemical structures by the appearance of defined optical resonance lines [237]. Especially hydrogen related defects in diamond show significant spectral lines in the IR regime [238]. Only by knowing the atoms which are involved within the defect, the center can be re-fabricated by nanofabrication devices.
Unfortunately, the relatively low fluorescence of the defect center limits the performance of such measurements so far. For instance, applying an external magnetic field directly leads to a quenching of the defect center which dramatically decreases its emission signal. Without an observable fluorescence, the resonance lines can not be recorded. Therefore, it would be beneficial to maximize the emission by implementing waveguides or nanolenses on the diamond surface [239]. Such nanostructures are able to focus the light emitted by the defect center for increasing the fluorescence intensity. With an increased emission, the defect can be investigated to a greater detail.

9 Conclusion

In this last chapter, we want to highlight the most important findings obtained during the course of this thesis. Furthermore, possible future experimental attempts are proposed which could reveal interesting mechanisms in nanoscale magnetism. For instance, the performance of more sophisticated pulse schemes is suggested. With these, single NV centers could observe and control quantum networks containing several individual spins. In addition, the implementation of NV centers into optical pump-probe spectroscopy is outlined. The suggested method would enable accesses to the time domain of magnetic dynamical processes locally at the nanoscale.

9.1 Summary

The presented thesis described the utilization of NV centers as a quantum sensor for the detection of individual molecules, the control of a spin bath ensemble and the spatially resolved detection of the Meissner screening in a thin film superconductor. Furthermore, attempts have been performed for enhancing the spin properties and with this the magnetic field sensitivity of NV centers in terms of diamond surface treatments. The obtained results make significant advances in the field of nanoscale magnetometry using NV centers in diamond and are summarized in the following paragraphs.

The NV Center in Diamond as Quantum Sensor

The NV center is one of the most studied defect in diamond. It consists of a substitutional nitrogen atom and neighboring carbon vacancy within the diamond lattice. Due to its unique optical properties, it can be utilized as nanoscale magnetic field sensor. The working principle relies on the NV center spin dependent fluorescence. The frequently encountered negatively charged NV center forms a $S = 1$ electronic ground state in which the $m_S = \pm 1$ substates are energetically shifted from the $m_S = 0$ state by a zero field splitting of 2.87 GHz. A non fluorescent intersystem crossing from the first excited state to a meta stable singlet state leads to different fluorescence yields depending on the population of the m_S subsystems. Thereby, the NV emission is high in case of a populated $m_S = 0$ substate (bright state) and low when the $m_S = \pm 1$ substates (dark states) are populated. Furthermore, the zero field splitting experiences a Zeeman shift under the application of an external magnetic field. This issue can be measured in terms of ODMR spectroscopy by recording the NV center fluorescence at different MW frequencies. When the MW frequency matches the corresponding resonance splitting, the $m_S = 0 \rightarrow m_S = -1$ and $m_S = 0 \rightarrow m_S = +1$ transitions can be excited. Due to the spin

dependent NV emission, the transition frequencies can be observed as a sharp fluorescence drop in the ODMR spectrum. By evaluating the Zeeman splitting between the $m_S = 0 \rightarrow m_S = -1$ transition and $m_S = 0 \rightarrow m_S = +1$ resonance, the applied magnetic field experienced by the NV center can be estimated.
In addition, several pulse schemes can be implemented which are able to detect the dipolar coupling between NV centers and external spins. By this, the magnetic properties of individual molecules can be investigated. Furthermore, the magnetic behavior of materials can be observed at the nanoscale.

Detection of Individual External Spins with a Single NV Center

In chapter 4, the detection of individual external spins by utilizing a single NV center quantum sensor has been presented. The measurements have been performed at a cryo-UHV setup operating at a temperature of 4.7 K and at a pressure of $2 \cdot 10^{-10}$ mbar. Two different spin bearing molecular systems have been investigated.
In the first experimental set, spin labeled polyphenol chains have been readout by a single NV center. The spin label consisted of a P5C nitroxide radical. In terms of DEER spectroscopy, the coupling between the NV center and the spin labels could be revealed. Thereby, the hyperfine spectrum of the nitroxide radical was recorded indicating a hyperfine splitting between 15 MHz and 40 MHz. The variation of the resulting frequency splittings is attributed to the molecular geometry in which the spin labels obtain different orientations within the polyphenol chain. As the dipolar coupling is dependent on the angular orientation within the interacting spins, different hyperfine contributions have been observed in the measured spectrum. Furthermore, the width of the spectral lines ($\approx$ 8.2 MHz) indicates that the NV center coupled to a molecular cluster containing $\approx$ 50 spin labels. Therefore, the gathered DEER spectra show the averaged hyperfine interactions of the most prominent spin label orientations within the cluster. Unfortunately, further measurements could not been performed due to photoinstabilities of the polyphenol chains. The laser induced photooxidation of the polyphenols lead to a significant increase of the fluorescence emitted by the molecular system. As a consequence, the NV emission could not be recorded after a measurement time of 13 h.
In the second experimental attempt, endohedral N@C_{60} molecules have been studied. Also here, DEER spectroscopy was utilized for observing the dipolar coupling between an individual NV center and an external N@C_{60} spin. In fact, the hyperfine spectrum of the encapsulated ^{14}N atom could be revealed which is usually characterized by a frequency splitting of 15.97 MHz. However, a slight asymmetry of $\approx$ 4 MHz in the DEER spectrum was observed. A potential explanation for this issue is a deviation from the centrosymmetric configuration of the C_{60} cage upon surface adsorption. As a result, the zero field interaction within the N@C_{60} spin system is increased which leads to a preferential orientation of the encapsulated nitrogen spin. Furthermore, more sophisticated pulse sequences have been performed for coherently controlling the external N@C_{60} spins. Thereby, spin flip processes in the form of Rabi oscillations could be observed. In addition, a minimum coherence time of the external spins could be estimated to $\approx 0.99\,\mu$s. By utilizing a DEER Delay pulse scheme, we revealed the ac-

tual number of involved $N@C_{60}$ spins within the NV center sensing region. The evaluation estimates that the NV center coupled to 3 $N@C_{60}$ spins.
The characterization and control of individual spins paves the way for advancing several scientific fields. For instance, structure determination of complex spin bearing biomolecules in NMR or ESR experiments could be achieved at the single molecule level. In parallel, the readout of quantum networks made out of molecular spin qubits can reveal important ingredients which are essential for quantum information processing.

Readout and Control of an Environmental Spin Bath

In the second experimental chapter (Ch. 5), we showed the readout and control of a P1 center spin bath by using an NV center ensemble. Also these measurements were performed at 4.7 K and in an UHV environment. The DEER spectrum obtained by the NV center ensemble indicated the hyperfine characteristics of the P1 defect in diamond. According to the fabrication method of the diamond sample, a high P1 center concentration can be assumed. Furthermore, the appearance of dipolar forbidden transitions within the DEER spectrum enforces the assumption that highly dense P1 center ensembles are implemented within the sample. Nevertheless, the properties of this environmental spin bath could be successfully controlled by utilizing an NV center ensemble. Rabi oscillations of the P1 spin bath were recorded indicating a coherent spin manipulation. In addition, the DEER spectrum has been reproduced at ambient conditions. Also in this measurement set, the dipolar forbidden transitions were intensely observable indicating a high P1 center density within the NV center ensemble detection region.

Spatial Resolution of the Meissner Screening

Not only the detection of individual spins but also collective spin phenomena can be successfully investigated using NV centers. Interesting systems in this context are superconducting materials which are characterized by a perfect diamagnetic behavior in their Meissner phase. In chapter 6 we described the NV center based readout of such a superconducting phase on μm length scales. As investigated superconductor we chose a 20 nm thin film LSCO sample characterized by a critical temperature of $T_c = 34\,\mathrm{K}$. Its response to an externally applied magnetic field was detected by a diamond plate containing an NV ensemble with $\approx 200\,\mathrm{NV}/\mu\mathrm{m}^2$. All measurements have been performed at 4.7 K and at $2 \cdot 10^{-10}$ mbar.
Besides performing the usual MW assisted NV center sensing protocols by measuring ODMR spectra, we also implemented an all-optical measurement scheme for the characterization of the superconducting sample. Experiments based on MW irradiation are often accompanied by local heating effects which can locally change the properties of the sample. By utilizing a MW-free measurement scheme, this issue can be neglected. Therefore, we observed the magnetic field dependent fluorescence yield of the NV center ensemble. An off-axial magnetic field leads to a decrease of the NV center emission. By utilizing this, we were able to resolve the Meissner phase in the LSCO sample. Thereby,

the fluorescence drop was compared between NV centers located outside of the superconductor and NV defects positioned right underneath. In fact, the NV centers below the LSCO sample obtained a lower magnetic field induced fluorescence drop ($\approx 2\%$) than the NV center outside of the superconductor ($\approx 5\%$). The issue can be explained by the manifestation of the LSCO Meissner phase which expels the applied magnetic field. As a result, the NV centers below the superconductor are not able to experience the external magnetic field. Furthermore, a raster scan enabled a spatial resolution of the Meissner screening. The obtained result could be evaluated with Brandt's analytical model revealing a critical current density j_c of $\approx 1.4 \cdot 10^8\,\mathrm{A/cm^2}$ of the LSCO sample. As the obtained value is in good agreement with already known values recorded in literature, the all-optical measurement scheme forms a reliable method for observing magnetism without inducing local heating effects.
In addition to that, the NV center fluorescence can be implemented into optical pump-probe experiments which are able to detect dynamical processes with high temporal resolution.

Enhancing the Spin Properties of Shallow NV Centers by Surface Treatments

Another important issue in the field of NV center magnetometry is the stabilization of NV spin properties. This is (especially for shallow implanted NV centers) a critical task as the spatial resolution and sensitivity of the sensor highly depends on the sensor-to-sample distance. Unfortunately, near-surface NV centers exhibit unstable spin properties due to charge transitions within the NV^- and NV^0 states. As the NV^0 center obtains no spin state dependent fluorescence yield, these neutral NV defects are not suitable for sensing purposes.
Furthermore, shallow implanted NV centers completely lose their NV^- charge state population within a cryogenic-UHV environment. This fact has been shown in chapter 7 of this thesis by measuring autocorrelation curves and ODMR spectra of 25 individual shallow implanted NV centers. As the autocorrelation measurements showed no antibunching dip and the ODMR spectra exhibited no resonance signals, a charge transition to the NV^0 state has been assumed. Therefore, we performed different attempts for stabilizing the NV^- charge state in terms of diamond surface treatments. The dosage of nitrogen and CO gas onto the diamond surface is described. For obtaining an estimate, if the dosed gases are able to recover the NV^- center, we compared autocorrelation measurement and ODMR spectra before and after the dosing procedure. However, both gases were not able to stabilize the NV defect. In contrary, an uncontrolled water layer formation was investigated which indeed partially recovered the NV^- charge state.
Therefore, it can be assumed that the dipole moment of the surface protection layer plays a crucial role for the NV center stabilization. Motivated by this explanation, a controlled H_2O layer formation was finally achieved by dosing water inside the UHV preparation chamber onto the diamond surface. In fact, slight hints for an NV^- charge state recovery was observed following such water dosing. Therefore, gases with higher dipole moments compared to CO like N_2O or NO can be implemented for further studies. Also deposited insulators as tin oxide or titanium dioxide could act as protection layers for the NV^- centers. The stabilization of shallow NV centers paves the way for increasing the sensitivity of

NV center based detection and sensing protocols.

Exploration of a Novel Defect Center in Diamond

Additionally, alternatives to NV centers can be studied for building up a whole platform of nanoscale quantum sensors. For instance, potential candidates are formed by the group IV defect centers in diamond including the well characterized case of SiV center. In chapter 8 the study of a novel defect center in diamond is presented. All measurements have been performed at ambient conditions and in the absence of an externally applied magnetic field.
Thereby, luminescent features within the confocal image of a natural diamond have been investigated by spectroscopy methods exhibiting a ZPL at 448 nm. As such a ZPL is not noted in literature, we termed the bright features as novel defect centers. Furthermore, ODMR signals could be obtained at 500 MHz and 2263 MHz. Rabi oscillations indicated the possibility of coherently manipulating the populated spin states of the defect center. Additionally, T_1 measurements revealed spin state dependent lifetimes of 35 μs and 3 μs. With these information, we were able to reconstruct a first energy level scheme of the defect.
However, further measurements have to be performed in order to study the novel defect center to a greater detail. Of great importance are magnetic field dependent measurements and the resolution of hyperfine splittings within the ODMR signals for identifying the composition of the impurity.

9.2 Outlook

The experiments presented in this thesis show the successful readout of magnetism at the nanoscale. Based on these achievements, further NV center based sensing protocols can be utilized and developed which will enable the investigation of nanoscale magnetic mechanisms in a more detailed fashion.

Readout of Quantum Networks

The characterization of individual external spins is typically achieved by DEER spectroscopy. Thereby, a specified excitation pulse for the external spin is implemented within the Hahn branch of the NV center. As a result, an NV center fluorescence drop can be investigated when the excitation pulse frequency matches the Larmor frequency of the external spin. The obtained DEER spectrum contains information about the spin specific resonance frequencies including the hyperfine interaction within the observed spin and the corresponding nucleus. However, DEER spectroscopy reveals solely the interaction between the NV center sensor and the external spin system. In case of an individual external spin, the NV center reads out the system on the single spin level. Instead, if the observed spin signal originates from a network including several spins, the NV center controls the network as one unit. However, in the field of quantum information processing it is crucial to address each spin qubit in a network individually. Furthermore, it is also important to read out the coupling mechanisms within the spin network. In terms of NV center based magnetic readout, the DEER spectroscopy scheme has

to be modified for controlling the interaction within a whole quantum network. A possible attempt is the implementation of TEER pulse sequences [97, 240]. The measurement scheme is depicted in Fig. 9.1 and contains an NV center Hahn sequence as main branch. Furthermore, a specified Hahn sequence for the first external spin (ext. spin 1), is positioned within the NV Hahn branch. Finally, an additional pulse is implemented which is utilized for exciting a second external spin (ext. spin 2). As a consequent, the NV center reads out frequency transitions which characterize the dipolar coupling between the two observed external spins. By evaluating these, the coupling strength and the distance within the two spin specimens can be estimated. Therefore, TEER sequences can not only be beneficial for reading out a spin network. Also the conformation of a spin labeled molecule has been revealed by utilizing this method [97]. In addition, the pulse scheme can be advanced by implementing more excitation pulses addressing a certain number of spins within the network. This could have a great impact on the concept of time crystals [241, 242]. Only few observations of discrete time crystal signatures have been reported so far [243, 244, 245]. The local readout of such an exotic structure could reveal information for improving concepts in the field of quantum information processing.

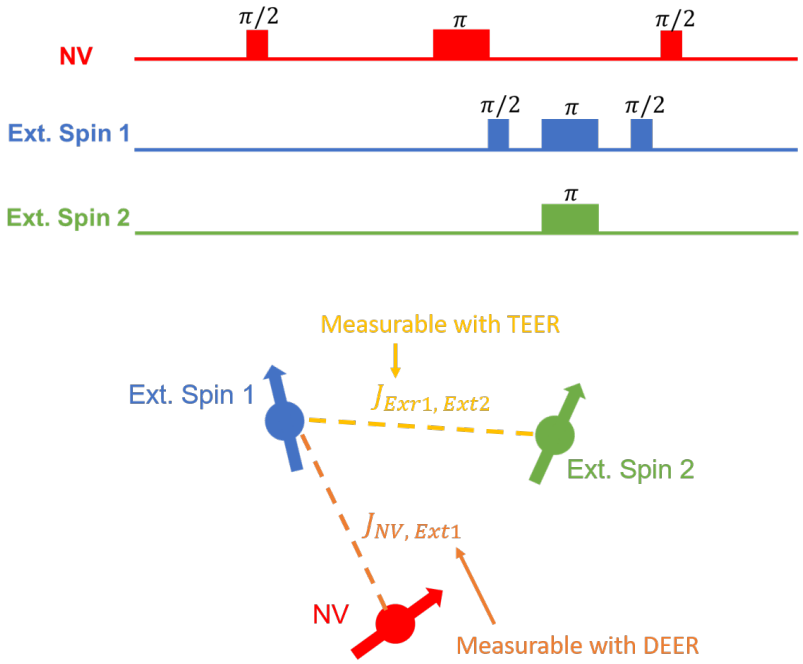

Figure 9.1: TEER measurement sequence for characterizing spin networks. The pulse scheme (on top) consist of a Hahn branch specified for the NV center spin (red). Additionally, a second Hahn branch is implemented for the first external spin (blue). A third pulse branch excites the second external spin (green). For clarification, a sketch of the system is illustrated below the pulse sequence. Instead of measuring the external spin-NV coupling, the TEER scheme utilizes the NV center for observing the coupling within the two external spins.

Pump-Probe Spectroscopy with NV Centers

Beside of measuring magnetic signals from a sample, also the time domain of dynamical magnetic processes is of great importance. Examples are spin lifetimes within the μs and ms regimes which are accessible through pulse-delay measurement schemes. However, some phenomena in magnetism exhibit lifetimes in the ps regime. An interesting mechanism is the light-induced superconductivity observed in high T_c cuprates [246]. Optical pulses at mid-IR and terahertz frequencies are able to tune resonantly specific phonon modes inducing a transient superconducting state above the critical temperature of the corresponding cuprate [246]. Utilizing pump-probe spectroscopy [247], the lifetime of this intriguing magnetic phase can be revealed. For instance, it has been shown that dynamical processes in YBCO obtain a lifetime of $\approx$ 5 ps [248, 249]. Furthermore, ultra short pump fields are able to excite oscillations (Higgs modes) within the superconducting energy gap [250].

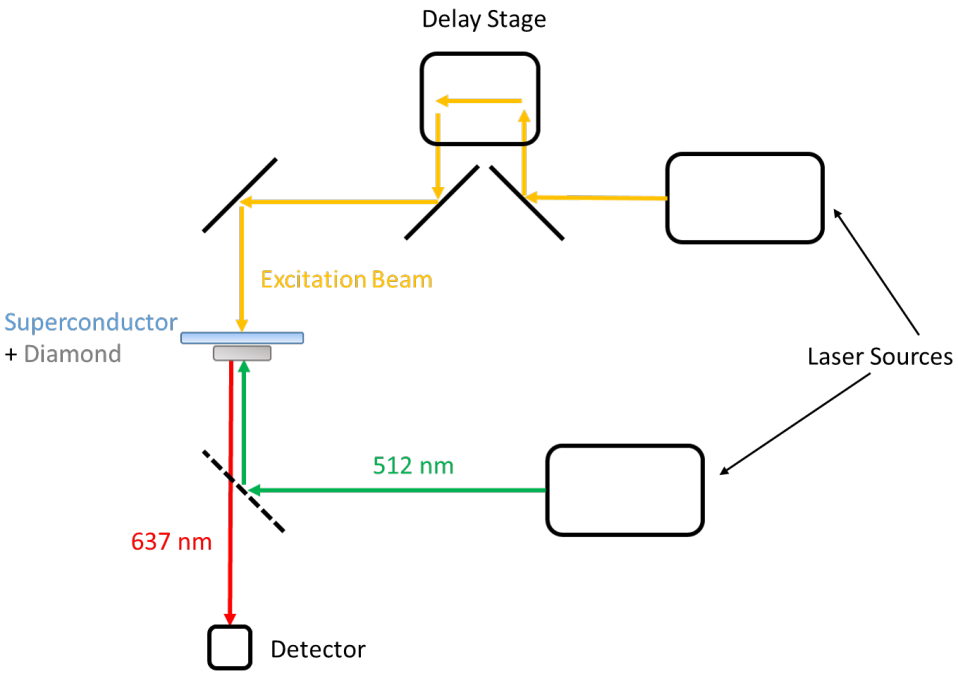

Figure 9.2: NV center implemented pump-probe spectroscopy for revealing the dynamics of magnetic processes at the nanoscale. The NV center implanted diamond is excited with a green laser. The resulting red NV emission is collected by a photon detector device. Simultaneously, an excitation beam changes the properties of the investigated sample (e. g. a superconducting system). The variation in the magnetic behavior can be resolved by changes in the NV center emission. Sweeping the timing of the excitation beam reconstructs the recorded signal in the time domain.

However, the study of the transient Meissner state relies on bulk measurements in which the effect is averaged over the whole superconducting sample. Observing this mechanism with higher spatial resolution could reveal even further information for increasing the critical temperature of certain su-

perconductors. For this, sensitive nanoscale magnetic field sensors would be great candidates. In chapter 6 it has been shown that the magnetic field dependent NV fluorescence can be used for resolving the Meissner phase on μm length scales. This work can be extended further by recording the NV fluorescence within a pump-probe spectroscopy setup. A simplified experimental sketch is shown in Fig. 9.2 in which the sample consists of an NV implanted diamond and a superconducting system. As usual a green laser excites the NV center ground state to its first excited state. Afterwards the red emission is collected from a photon counting device. The process can be repeated under the application of an excitation pulse which changes the properties of the superconducting compound. Comparing the two measurement sets could reveal slight variations in the recorded NV center fluorescence attributed to changes of the superconducting properties. In addition, a delay stage can be implemented which varies the impact time of the excitation pulse. With this, the resolution of magnetic processes can be revealed in the time domain.
As the NV center probes the magnetism locally, also other interesting mechanisms in superconductors can be investigated like the formation and motion of magnetic vortices.

Intrinsic Modifications for Stabilizing NV Center Properties

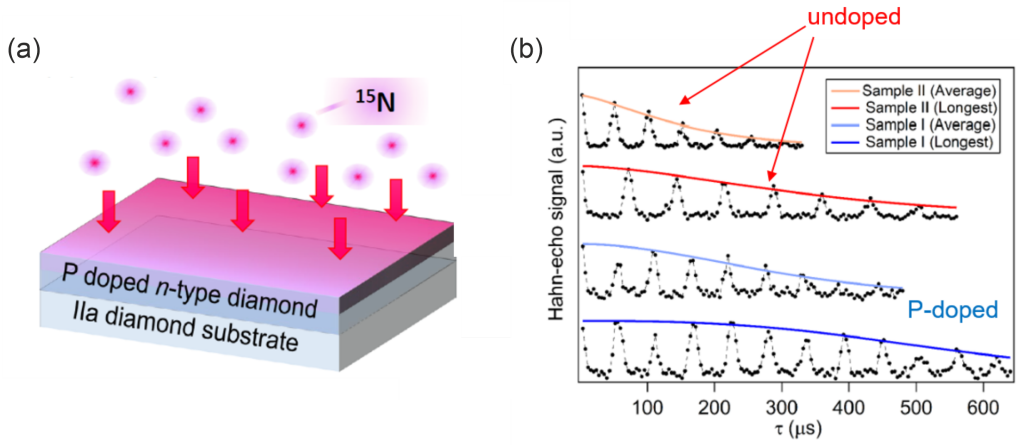

Figure 9.3: Intrinsic modifications for enhancing the spin properties of NV centers. (a) Sketch of a phosphorous doped diamond sample. The n-type layer acts as an electron donor for stabilizing the NV^- charge state. (b) Impact of the n-type P doping. A significant increase of the coherence time can be investigated compared to a diamond sample without doping treatments. The figures are adapted from [251].

In chapter 7, surface functionalization and physisorption methods have been discussed for stabilizing the spin properties of shallow implanted NV centers in a cryogenic UHV environment. Thereby, a slight recovery of the NV^- state was investigated in form of ODMR spectra with a contrast of 2%. However, the utilization of single NV centers as magnetometers requires more stable defects with an ODMR contrast $>$ 10%. So far, surface treatments were not able to achieve this goal for shallow

implanted NV centers. A promising alternative can be formed by intrinsic modifications within the diamond lattice. For instance, diamond samples can be n-type doped with phosphorous (P) atoms which are able to act as electron donors (see Fig. 9.3(a)) [251, 252]. Consequently, the continuous charge donation can stabilize the NV^- state. In fact, first results on P-doped diamonds have been published indicating stable NV^- centers. A significant increase in T_2 times was noted for a doped diamond compared to a non-doped sample as shown in Fig. 9.3(b) [251, 252]. However, the published results corresponds to characterizations at ambient conditions. So far, measurements of doped diamond samples at cryogenic UHV conditions are elusive. The investigation of doped diamond systems within our cryo-UHV setup could potentially reveal new mechanisms for stabilizing NV centers even at such hard conditions. Thereby, similar studies as described in chapter 7 can be performed in order to characterize the NV centers by their autocorrelation curves and ODMR spectra.

10 Appendix

Hyperfine Interaction in the NV Center

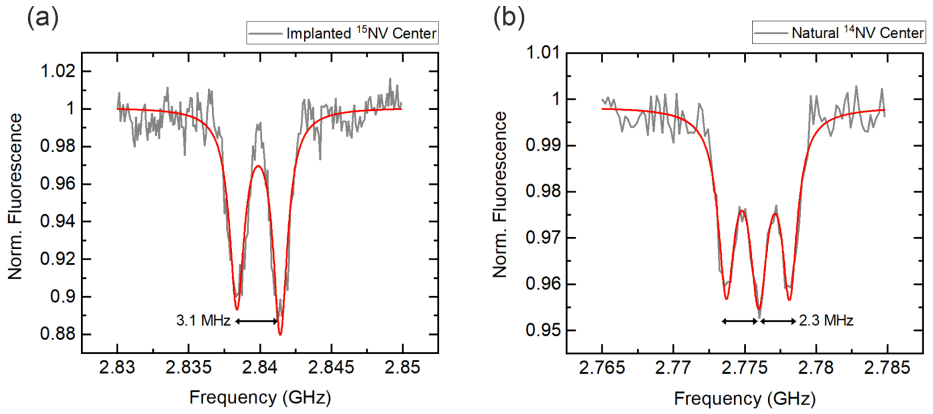

Figure 10.1: ODMR signals of the lower NV center MW transition ($m_S = 0 \rightarrow m_S = -1$) for an implanted ^{15}NV center (a) and a natural ^{14}NV center (b). The hyperfine splitting is 3.1 MHz for the implanted NV defect and 2.3 MHz for the natural impurity.

The implantation of NV defects in diamond samples has been described in chapter 2. However, NV centers can also be implemented within the diamond by natural processes independently from the fabrication method. Usually, natural NV impurities are located relatively deep within the diamond matrix and can not be utilized for sensing purposes. A method which is able to distinguish between natural and implanted NV defects is the resolution of the NV center hyperfine spectrum. Natural NVs incorporate ^{14}N atoms which obtain a hyperfine constant of 2.3 MHz. In contrast, fabricated NV centers are typically implanted with ^{15}N isotopes which are characterized by a hyperfine constant of 3.1 MHz. These constants can be resolved by ODMR spectroscopy as depicted in Fig. 10.1. Furthermore, the hyperfine spectrum of the ^{15}N isotope obtains two dips due to the nuclear spin of $I = 1/2$. Instead, three hyperfine signals are observable for the ^{14}N atom due to the nuclear spin of $I = 1$ in that case.

DEER DQT Pulse Scheme

In 4.2.2 we introduced the DEER DQT pulse sequence for increasing the sensitivity of the NV center spin sensor. Thereby, the superposition state is formed by the $|-1\rangle$ and $|+1\rangle$ states. As the transition

$|-1\rangle \rightarrow |+1\rangle$ can not be directly addressed, the typical DEER pulse sequence has to be modified to a scheme of the form as shown in Fig. 10.2. Tab. 10.1 illustrates the impact of the DEER DQT pulse scheme on the quantum state population. It can be seen that the pulse trains are able to indirectly exchange the populations within the $|-1\rangle$ (b) and $|+1\rangle$ (c) states.

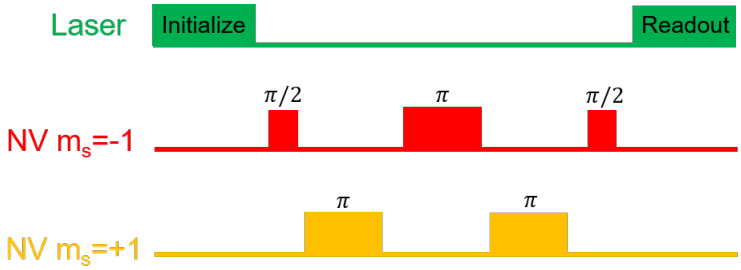

Figure 10.2: DEER DQT pulse sequence for forming the $|\pm 1\rangle$ sensing basis.

Quantum state	Initial population	$\pi(\|0\rangle \rightarrow \|+1\rangle)$	$\pi(\|0\rangle \rightarrow \|-1\rangle)$	$\pi(\|0\rangle \rightarrow \|+1\rangle)$
$\|0\rangle$	a	c	b	a
$\|-1\rangle$	b	b	c	c
$\|+1\rangle$	c	a	a	b

Table 10.1: Impact of the DEER DQT pulse train on the quantum state populations. Even that a transition between the $|-1\rangle$ and $|+1\rangle$ states is forbidden, the pulse scheme is able to exchange the population within these two states. The populations are denoted as a, b and c.

Instabilities in the NV Center PL

In chapter 7 we utilized autocorrelation and ODMR curves for characterizing the NV center spin stability. However, also the recorded PL of the individual NV defect showed interesting features by transferring the diamond sample into the UHV-cryo setup. The behavior is depicted in Fig. 10.3. While the NV fluorescence recorded at ambient conditions (gray curve) obtains a stable count rate, the PL measured in the cryogenic UHV environment (red curve) is characterized by high instabilities. This is identified by the introduced quantities ΔPL_+ and ΔPL_-. Thereby, ΔPL_+ defines the strongest positive fluctuation regarding the baseline. In parallel, ΔPL_- indicates the strongest negative fluctuation regarding the baseline.

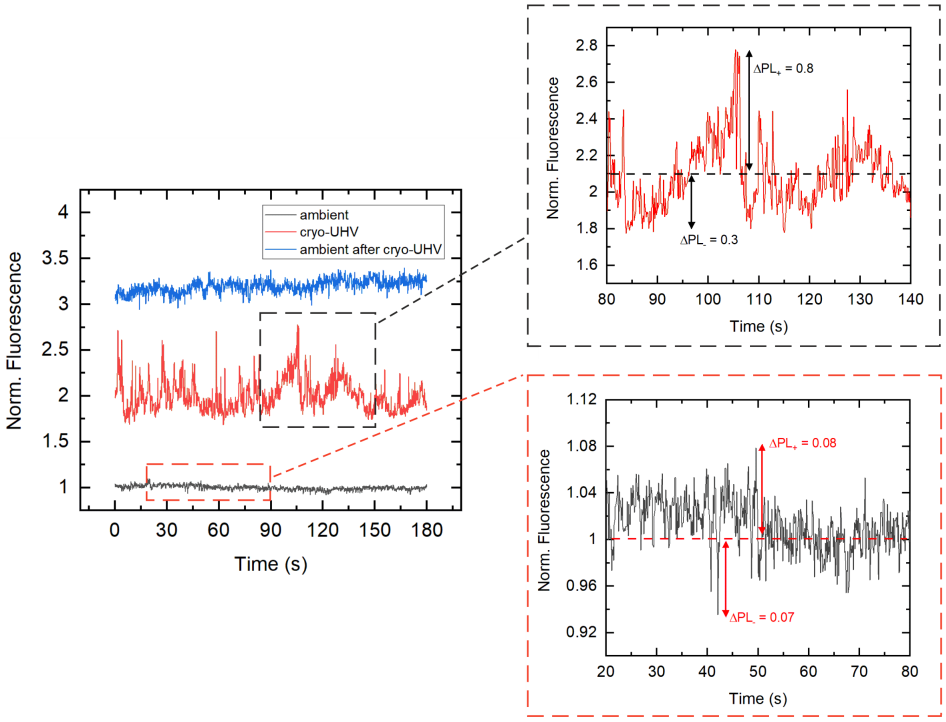

Figure 10.3: Photoluminescence of an individual NV center. At ambient conditions (gray and blue curves) the fluorescence obtains a stable behavior. However, recording the PL at cryogenic conditions and in an UHV environment (red curve) results into an unstable PL time trace.

However, fluctuations within the PL rate can also be attributed to optical instruments of the experimental setup. In general, explicit features as an anti-bunching dip in an autocorrelation curve or absorption peaks in recorded spectra form more reliable quantities for studying the characteristics of an physical system. Nevertheless, the observation in Fig. 10.3 is still an interesting measurement and can potentially be attributed to charge state instabilities within the NV^- and NV^0 states.

Utilized Diamond Membrane for the Dosing Experiments

The experiments in chapter 7 were performed on a [100] oriented diamond nanopillar membrane. Thereby the NV centers were implanted in three distinct regions with three different nitrogen implantation beam energies. With this, the membrane obtained three different NV center depths as the implantation energy defines the resulting depth of the defects. High implantation energies of 10 keV lead to relatively deep NV centers ($\approx$ 12 nm) within the diamond matrix while lower ^{15}N beam energies of 2.5 keV result into shallow NV defects ($<$ 5 nm) [192]. A sketch of the membrane is illustrated in Fig. 10.4(a) which indicates the three regions characterized by different implantation energies (2.5 keV, 5 keV, and 10 keV). Fig. 10.4(b) shows a corresponding light mircoscope image of the membrane.

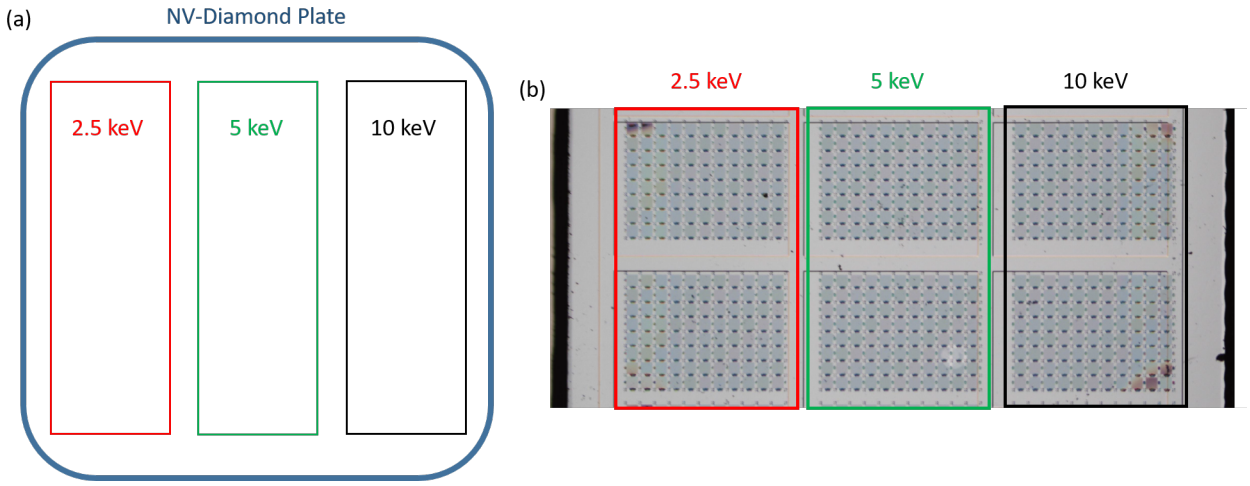

Figure 10.4: Utilized nanopillar diamond membrane for the experiments in Ch. 7.

NV Center Properties at Cryo-UHV Conditions: Statistiscs

Tab. 10.2 illustrates the full statistics of the 25 investigated NV centers in each measurement condition. At ambient conditions, the NV defects obtain stable NV^- charge state properties. By transferring the sample into a cryogenic 4.7 K and $2 \cdot 10^{-10}$ mbar UHV environment, huge instabilities of the NV properties are noted which are related to charge transfer mechanisms to the NV^0 state. It seems that diamond surface modifications with N_2 and CO gas are not playing a crucial role for the NV center charge state dynamics. However, H_2O dosing showed a significant stabilization process for NV centers implanted with a 5 keV nitrogen ion beam.

	2.5 keV	5 keV	10 keV	Condition
stable/total	9/9	9/9	7/7	ambient
stable/total	0/9	5/9	4/7	cryo-UHV 01
stable/total	0/9	5/9	4/7	N_2 dosing
stable/total	0/9	5/9	4/7	CO dosing
stable/total	1/9	7/9	5/7	cryo-UHV 02
stable/total	0/9	4/9	3/7	IR heating
stable/total	1/9	7/9	5/7	H_2O dosing

Table 10.2: Full statistics of the investigated NV centers. The notation "stable" stands for the existence of a stable NV^- charge state population defined by the measured autocorrelation curves, ODMR and emission spectra (see chapter 7).

Autocorrelation Function Fit

In chapter 7, the majority of the experimental results are recorded as autocorrelation curves. Thereby, a strong antibunching dip indicates the investigation of a single photon source. As the experimental setup is specified for the NV^- charge state emission, the existence of a significant NV^0 population is measured as an absence of antibunching features within the autocorrelation curve. However, in general also the NV^0 defect forms a single photon source and can be characterized by an antibunching signal. The great difference between the two charge states is formed by their energy level scheme. While the NV^0 is described by a two level system, the NV^- state is represented by a three level system. Therefore, the photophysics of an NV^0 defect is characterized by only two transition parameters (k_{12} and k_{21}). Instead, the photophysics of an NV^- center is described by four transition parameters (k_{12}, k_{21}, k_{23} and k_{31}). The physical meaning of the parameters is illustrated in Fig. 10.5. As already described in chapter 7, all of these parameters are involved into the theoretical $g^{(2)}$ function [219]

$$g^{(2)}_{theo.}(\tau) = 1 - \beta e^{-\gamma_1 \tau} + (\beta - 1)e^{-\gamma_2 \tau}. \tag{10.1}$$

within the parameters β, γ_1 and γ_2. The explicit expressions for these are [219]

$$\gamma_1 \approx k_{12} + k_{21}, \tag{10.2}$$

$$\gamma_2 \approx k_{31} + \frac{k_{12}k_{23}}{k_{12} + k_{21}}, \tag{10.3}$$

$$\beta \approx 1 + \frac{k_{12}k_{23}}{k_{31}(k_{12} + k_{21})}. \tag{10.4}$$

Thereby, γ_1 solely depends on k_{12} and k_{21} representing the scenario of a two level system. Instead, γ_2 also includes k_{23} and k_{31} for the three level system scenario. Therefore, the magnitudes of the fitting parameters give reliable hints for the investigated charge states.

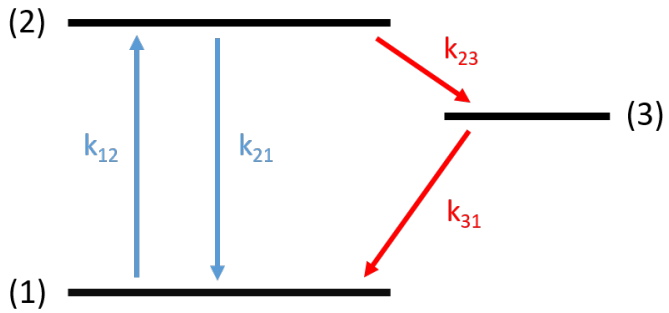

Figure 10.5: General energy level diagram for a three level system characterized by the transition coefficients k_{12}, k_{21}, k_{23} and k_{31}. In case of a two level system, k_{23} and k_{31} disappear and the photphysics is solely described by k_{12} and k_{21}. The sketch is adapted from [219].

Detailed Optical Setup

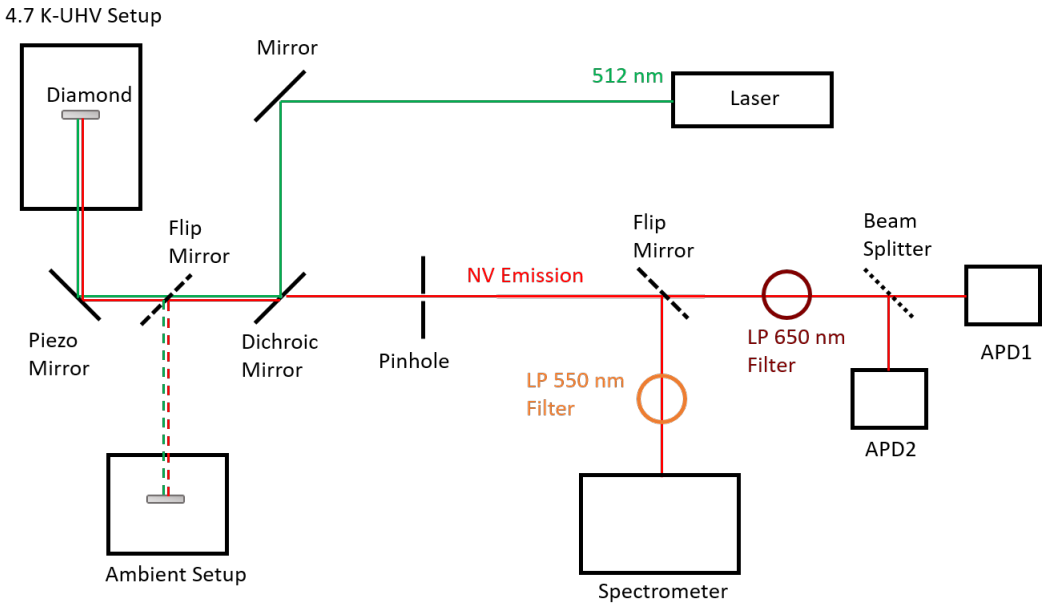

Figure 10.6: Full optical setup which has been utilized within the scope of this thesis.

In 3.4 we discussed the utilized optical setup in its basic principles as confocal microscope. However, as the optical setup has to be specified for the NV emission light, optical filters play a crucial role for the recorded fluorescence count rate. Therefore, Fig. 10.6 illustrates the optical setup with the utilized filters which have not been sketched in 3.4. Furthermore, also the optical spectroscopy path is depicted in Fig. 10.6. Thereby, a longpass (LP) 650 nm filter is implemented in front of the APDs for recording solely the NV^- emission. Instead, in front of the spectrometer a LP 550 nm is mounted for observing also the NV^0 fluorescence. The NV emission can be guided to the spectrometer through an additional flip mirror.

Measurements at Ambient Temperature-UHV Conditions

In order to observe the impact of an UHV environment on the NV center properties, we also performed measurements within the UHV chamber without cooling the cryostat with liquid He. As a consequence, the temperature during this particular measurement was at about 298 K. Fig. 10.7 illustrates the obtained spectra of an representative NV center implanted with a 5 keV nitrogen beam. The gray curve represents the emission of the defect at ambient pressure and temperature conditions. The phonon sideband peaks at $\approx$ 690 nm. Furthermore, a clear ZPL feature can be investigated at 637 nm. These features clearly indicate a stable NV^- charge state population. In contrast, the red curve shows the optical properties of the defect at a temperature of 298 K and a UHV pressure of $2 \cdot 10^{-9}$ mbar. A

significant shift of the phonon sideband maximum to 650 nm can be observed. Furthermore, almost no ZPL emission can be investigated at 637 nm. Therefore, a charge state conversion towards the neutral NV^0 can be estimated. The results indicate that an ultra low pressure environment favors the NV^0 charge state and that a stable NV^- population crucially requires compounds of the ambient air.

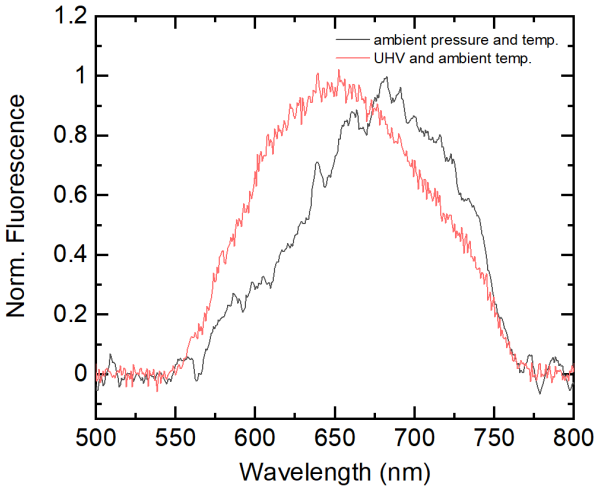

Figure 10.7: Emission spectra of an individual NV center obtained at ambient conditions and UHV 298 K conditions. A significant change of the optical properties can be investigated which are related to the UHV environment. At ambient conditions, the NV^- charge state population is stabilized.

11 Bibliography

[1] J. R. Childress and R. E. Fontana Jr., "Magnetic recording read head sensor technology", C. R. Physique **6**, 997-1020 (2005).

[2] M. J. Caruso, "Applications of magnetic sensors for low cost compass systems", IEEE Xplore Conference, 6656658 (2000).

[3] P. Ripka, "Security applications of magnetic sensor", Journal of Physics: Conference Series **450**, 012001 (2013).

[4] A. K. A. Silva, E. L. Silva, E. S. T. Egito and A. S. Carrico, "Safety concerns related to magnetic field exposure", Radiat. Environ. Biophys. **45**, 245-252 (2006).

[5] S. Greenland, A. R. Sheppard, W. T. Kaune, C. Poole and M. A. Kelsh, "A Pooled Analysis of Magnetic Fields, Wire Codes, and Childhood Leukemia", Epidemiology **11**, 624-634 (2000).

[6] M. L. Mc Bridge et al., "Power-Frequency Electric and MAgnetic Fields and Risk of Childhood Leukemia in Canada", American Journal of Epidemiology **149**, 831-842 (1999).

[7] E. v Reeth, I. W. K. Tham, C. H. Tan and C. L. Poh, "Super-Resolution in Magnetic Resonance Imaging: A Review", Concepts in Magnetic Resonance Part A **40**, 306-325 (2012).

[8] Vijayalaxmi, M. Fatahi and O. Speck, "Magnetic resonance imaging (MRI): A review of genetic damage investigations", Mutation Research **764**, 51-63 (2015).

[9] B. Blümich, "Introduction to compact NMR: A review of methods", Trends in Analytical Chemistry **83**, 2-11 (2016).

[10] S. Winkler et al., "Gradient and shim technologies for ultra high field MRI", NeuroImage. **168**, 59-70 (2016).

[11] M. Fatahi et al., "DNA- double-strand breaks and micronuclei in human blood lymphocytes after repeated whole body exposures to 7 T Magnetic Resonance Imaging", NeuroImage. **133**, 288-293 (2016).

[12] R. Y. Kwong, *Cardiovascular Magnetic Resonance Imaging*, 1st ed. (Humana Press Inc., 2008).

[13] Z. Wang, W. Ma, C. Chen, H. Ji and J. Zhaon, "Probing paramagnetic species in titania-based heterogeneous photocatalysis by electron spin resonance (ESR) spectroscopy-A mini review", Chemical Engineering Journal **170**, 353-362 (2011).

[14] S. Slussarenko and G. J. Pryde, "Photonic quantum information processing: A concise review", Appl. Phys. Rev. **6**, 041303 (2019).

[15] S. S. Biswas, "Quantum Computer: A Reviwe Work", Advances in Computational Sciences and Technology **10**, 1471-1478 (2017).

[16] T. D. Ladd et al., "Quantum computers", nature **464**, 45-53 (2010).

[17] F. Jazaeri, A. Beckers, A. Tajalli and J. M. Sallese, "A Review on Quantum Computing: From Qubits to Front-end Electronics and cryogenic MOSFET Physics", IEEE Xplore conference, 18901084 (2019).

[18] S. Shankar, A. M. Tyryshkin, J. He and S. A. Lyon, "Spin relaxation and coherence times for electrons at the Si/SiO_2 interface", Phys. Rev. B **82**, 195323 (2010).

[19] J. A. Sidles et al., "Magnetic resonance force microscopy", Rev. Mod. Phys. **67**, 249-265 (1995).

[20] D. Rugar, R. Budakian, H. J. Mamin and B. W. Chui, "Single spin detection by magnetic resonance force microscopy", nature **430**, 329-332 (2004).

[21] D. Robbes, "Highly sensitive magnetometers-a review", Sensors and Actuators A **129**, 86-93 (2006).

[22] M. J. M. Perez and D. Koelle, "NanoSQUIDs: Basics & recent advances", Physical Sciences Reviews **3**, 20175001 (2017).

[23] A. J. Ramsey, "A review of the coherent optical control of the exciton and spin states of semiconductor quantum dots", Semicond. Sci. Technol. **25**, 103001 (2010).

[24] A. Morello et al., "Single-shot readout of an electron spin in silicon", Nature **467**, 687-691 (2010).

[25] A. P. Nizovtsev et al., "A Quantum Computer Based on NV Centers in Diamond: Optically Detected Nutations of Single Electron and Nuclear Spin", Optics and Spectroscopy **99**, 233-244 (2005).

[26] J. M. Taylor et al. "High-sensitivity diamond magnetometer with nanoscale resolution", nature physics **4**, 810-816 (2008).

[27] F. M. Hrubesch, "Efficient Electrical Spin Readout of NV^- Centers in Diamond", Phys. Rev. Lett. **118**, 037601 (2017).

[28] R. Schirhagl, K. Chang, M. Loretz and C. L. Degen, "Nitrogen-Vacancy Centers in Diamond: Nanoscale Sensors for Physics and Biology", Annu. Rev. Phys. Chem. **65**, 83-105 (2014).

[29] M. R. Page et al., "Optically detected ferromagnetic resonance in diverse ferromagnets via nitrogen vacancy centers in diamond", J. Appl. Phys. **126**, 124902 (2019).

[30] M. Lee et al., "Magnetic imaging of a single ferromagnetic nanowire using diamond atomic sensors", Nanotechnology **29**, 405502 (2018).

[31] L. S. Bouchard, V. M. Acosta, E. Bauch and D. Budker, "Detection of the Meissner effect with a diamond magnetometer", New J. Phys. **13**, 025017 (2011).

[32] A. Cooper, E. Magesan, H.N. Yum and P. Cappellaro, "Time-resolved magnetic sensing with electronic spins in diamond", Nature Comm. **5**, 4141 (2013).

[33] G. D. Preston, "Structure of Diamond", Nature **155**, 69-70 (1945).

[34] T. Evans and P. F. James, "A study of the transformation of diamond to graphite", Roy. Soc. **277**, 260-269 (1964).

[35] Y. G. Gogotsi, A. Kailer and K. G. Nickel, "Transformation of diamond to graphite", Nature **401**, 662-664 (1999).

[36] S. B. Shirey and J. E. Shigley, "Recent Advances in Understanding the Geology of Diamonds", Gems and Gemology **49**, 188-222 (2013).

[37] E. O. Schäfer-Nolte, *Development of a Diamond-based Scanning Probe Spin Sensor Operating at Low Temperatur in Ultra High Vacuum*, Dissertation in Physics, University of Stuttgart (2014).

[38] J. Che, T. Cagin, W. Deng and W. A. Goddard, "Thermal conductivity of diamond and related materials from molecular dynamics simulations", J. Chem. Phys. **113**, 6888-6900 (2000).

[39] C. D. Clark, P. J. Dean and P. V. Harris, "Intrinsic edge absorption in diamond", Proc. Roy. Soc. **277**, 312-329 (1964).

[40] E. S. de Sa and G. Davies, "Uniaxial stress studies of the 2.498 eV(H4), 2.417 eV and 2.536 eV vibronic bands in diamond", Proc. Roy. Soc. **357**, 231- 251 (1977).

[41] K. Iakoubovskii and G. J. Adriaenssens, "Optical characterization of natural Argyle diamonds", Diamond and Related Materials **11**, 125-131 (2002).

[42] F. Jelezko and J. Wrachtrup, "Single defect centres in diamond: A review", **203**, 3207-3225 (2006).

[43] A. Lenef and S. C. Rand, "Electronic structure of the N-V center in diamond: Theory", Phys. Rev. B **53**, 442-455 (1996).

[44] C. Simon et al., "Quantum Memories", The European Physical Journal D **58**, 1-22 (2010.)

[45] L. D. Preez, *Electron paramagnetic resonance and optical investigations of defect centres in diamond*, Dissertation in Physics, University of the Witwatersand (1965).

[46] M. Born and R. Oppenheimer, "Zur Quantentheorie der Molekülen", Annalen der Physik **389**, 457-484 (1927).

[47] L. Schlipf, *Nanoscale Electron Spin Resonance*, Dissertation in Physics, University of Stuttgart (2017).

[48] M. W. Dohetry, N. B. Manson, P. Delaney and L. C. L. Hollenberg, "The negatively charged nitrogen-vacancy centre in diamond", **13**, 025019 (2011.)

[49] M. H. Levitt, *Spin Dynamics: Basics of Nuclear Magnetic Resonance*, 2nd ed. (John Wiley and Sons, Ltd, 2008).

[50] C. S. Shin et al., "Optically detected nuclear quadrupolar interaction of 14N in nitrogen-vacancy centers in diamond", Phys. Rev. B. **89**, 205202 (2014).

[51] P. Siyueshev et al., "Optically Controlled Switching of the Charge State of a Single Nitrogen-Vacancy Center in Diamond at Cryogenic Temperatures", Phys. Rev. Lett. **110**, 167402 (2013).

[52] C. J. Widmann et al., "Fabrication and characterization of single crystalline diamond nanopillars with NV-centers", Diamond and Related Materials **54**, 2-8 (2015).

[53] N. Aslam, G. Waldherr, P. Neumann, F. Jelezko and J. Wrachtrup, "Photo-induced ionization dynamics of the nitrogen vacancy defect in diamon investigated by single-shot charge state detection", New J. Phys. **15**, 013064 (2013).

[54] P. Delaney, J. C. Greer and J. A. Larsson, "Spin-Polarization Mechanism of the Nitrogen-Vacancy Center in Diamond", Nano Lett. **10**, 610-614 (2010).

[55] I. V. Zhukov, S. V. Anishchik and Y. N. Molin, "ODMR Spectroscopy of NV Centers in Diamond Under High MW Power", Appl. Magn. Reson. **48**, 1461-1469 (2017).

[56] R. Ulbricht and Z-H. Loh, "Excited-state lifetime of the NV infrared transition in diamond", Phys. Rev. B **98**, 094309 (2018).

[57] I. Popa, *Pulsed magnetic resonance on single defect centers in diamond*, Dissertation in Physics, University of Stuttgart (2006).

[58] D, J. Griffiths, *Introduction to Quantum Mechanics*, 2nd ed. (Prentice Hall International, 2004).

[59] H. Ray et al., *MRI: The Basics*, 4th ed. (Lippincott Williams and Wilkins, 2017).

[60] M. Mrozek et al., "Longitudinal spin relaxation in nitrogen-vacancy ensembles in diamond", EPJ Quantum Technology **2**, 2-11 (2015).

[61] I. J. Lowe, "Free Induction Decays of Rotating Solids", Phys. Rev. Lett. **2**, 285 (1959).

[62] K. S. Cujia, J. M. Boos, K. Herb, J. Zopes and C. L. Degen, "Tracking the precession of single nuclear spins by weak measurements", Nature **571**, 230-233 (2019).

[63] J. R. Maze et al., "Free induction decay of single spins in diamond", New J. Phys. **14**, 103041 (2012).

[64] E. L. Hahn, "Spin Echos", Phys. Rev. **80**, 580-594 (1950).

[65] P. L. Stanwix et al., "Coherence of nitrogen-vacancy electronic spin ensemble in diamond", Phys. Rev. B **82**, 201201 (2010).

[66] P. A. M. Dirac, "The Quantum Theory of Emission and Absorption of Radiation", Proceedings of the Roy. Soc. A. **114**, 243-265 (1927).

[67] H. Haken and H. C. Wolf, *Molekülphysik und Quantenchemie*, 5th ed. (Springer, 2002).

[68] F. Shi et al., "Single-protein spin resonance spectroscopy under ambient conditions", Science **347**, 1135-1138 (2015).

[69] W. B. Mims, "Pulsed endor experiments", Proceedings of the Roy. Soc. A **283**, 452-457 (1965).

[70] M. Pannier, S. Veit, A. Godt, G. Jeschke and H. W. Spiess, "Dead-Time Free Measurement of Dipole-Dipole Interactions between Electron Spins", Journal of Magnetic Resonances **142**, 331-340 (2000).

[71] D. Pinto, *Dark Spins as a Qubit Resource: Single and Ensemble Approaches Using a Nanoscale Sensor*, Dissertation in Physics, University of Stuttgart (2018).

[72] T. Staudacher, *Nuclear magnetic resonance spectroscopy on a nanoscopic sample volume*, Dissertation in Physics, University of Stuttgart (2015).

[73] T. Staudacher et al., "Nuclear Magnetic Resonance Spectroscopy on a (5-Nanometer)3 Sample Volume", Science **339**, 561-563 (2013).

[74] S. Schmitt et al., "Submillihertz magnetic spectroscopy performed with a nanoscale quantum sensor", Science **356**, 832-837 (2017).

[75] S. Appelt, F. W. Häsing, H. Kühn and B. Blümich, "Phenomena in J-coupled nuclear magnetic resonance spectroscopy in low magnetic fields", Phys. Rev. A **76**, 023420 (2007).

[76] J. M. Boss, K. S. Cujia, J. Zopes and C. L. Degen, "Quantum sensing with arbitrary frequency resolution", Science **356**, 837-840 (2017).

[77] M. Akaishi, H. Kanda and S. Yamaoka, "High Pressure Synthesis of Diamond in the Systems of Graphite-Sulfate and Graphite-Hydroxide", Jpn. J. Appl. Phys. **29**, L1172 (1990).

[78] J. J. Gracio, Q. H. Fan and J. C. Madaleno, "Diamond growth by chemical vapour deposition", J. Phys. D: Appl. Phys. **43**, 374017 (2010).

[79] C. Santori, P. E. Barclay, K-M. C. Fu and R. G. Beausoleil, "Vertical distribution of nitrogen-vacancy centers in diamond formed by ion impantation and annealing", Phys. Rev. B **79**, 125313 (2009).

[80] K. Ohno et al., "Engineering shallow spins in diamond with nitrogen delta-doping", Appl. Phys. Lett. **101**, 082413 (2012).

[81] S. A. Momenzadeh et al., "Nano-engineered Diamond Waveguide as a Robust Bright Platform for Nanomagnetometry Using Shallow Nitrogen Vacancy Center", Nano Lett. **15**, 165-169 (2014).

[82] E. Schaefer-Nolte, F. Reinhard, M. Ternes, J. Wrachtrup and K. Kern, "A diamond-based scanning probe spin sensor operating at low temperature in ultra-high vacuum", Rev. Sci. Instrum. **85**, 013701 (2014).

[83] Y. K. Hwang and J. S. Heo, "A numerical study of the performance of a turbomolecular pump", KSME International Journal **11**, 77 (1997).

[84] V. V. Anashin, A. A. Krasnov and A. M. Semenov, "A Study of the Gettering Characteristics of Getter Pumps for Different Gases", Instrum. Exp Tech **63**, 893-897 (2020).

[85] D. G. Henshaw, D. G. Hurst and N. K. Pope, "Structure of Liquid Nitrogen, Oxygen, and Argon by Neutron Diffraction", Phys. Rev. **92**, 1229-1234 (1953).

[86] J. Allen and A. Misener, "Flow of Liquid Helium II", Nature **141**, 75 (1938).

[87] J. Tuttle, E. Canavan and M. Di Pirro, "Thermal and Electrical Conductivity Measurements of CDA 510 Phosphor Bronze", AIP Conference Proceeding **1219**, 55 (2010).

[88] A. Kushino and S. Kasai, "Thin semi-rigid cables for cryogenics applications", APS March Meeting 2013 **N36.006**, 18-22 (2013).

[89] C. Robens et al., "High numerical aperture (NA=0.92) objective lens for imaging and addressing of cold atoms", Opt. Lett. **42**, 1043-1046 (2017).

[90] Y. Shibata et al., "Development of a novel cryogenic microscope with numerical aperture of 0.9 and its application to photosynthesis research", BBA-Bioenergetics **1873**, 880-887 (2014).

[91] R. P. Roberts, M. Juan and G. Molina-Terriza, "Quenching dynamics and phot-physics of nitrogen-vacancy centres in nanodiamonds", CLEO/Europe-EQEC **17293597**, 1 (2017).

[92] T. Wilson, *Confocal Microscopy*, 1st ed. (Academic Press Limited, 1990).

[93] M. A. Wayne, J. C. Bienfang and S. V. Polyakov, "Simple autocorrelation method for thoroughly characterizing single-photon detectors", Optics Express **25**, 20352 (2017).

[94] J. C. Kendrew et al., "A Three-Dimensional Model of the Myoglobin Molecule Obtained by X-Ray Analysis", Nature **181**, 662-666 (1958).

[95] E. Betzig et al., "Imaging Intracellular Fluorescent Proteins at Nanometer Resolution", Science **313**, 1642-1645 (2006).

[96] J. Bückers, D. Wildanger, G. Vicidomini, L. Kastrup and S. W. Hell, "Simultaneous multi-lifetime multi-color STED imaging for colocalization analyses", Optics Express **19**, 3131 (2011).

[97] L. Schlipf et al., "A molecular quantum spin network controlled by a single qubit", Sci. Adv. **3**, e1701116 (2017).

[98] E. Schäfer-Nolte et al., "Tracking Temperature-Dependent Relaxation Times of Ferritin Nanomagnets with a Wideband Quantum Spectrometer", PRL **113**, 217204 (2014).

[99] A. Godt et al., "EPR Probes with Well-Defined, Long Distances between Two or Three Unpaired Electrons", J. Org. Chem. **65**, 7575-7582 (2000).

[100] E. Narr, A. Godt and G. Jeschke, "Selective Measurements of a Nitroxide-Nitroxide Separation of 5nm and a Nitroxide-Nitroxide Copper Separation of 2.5nm in a Terpyridine-Based Copper Complex by Pulse EPR Spectroscopy", Angw. Chem. Int. Ed. **20**, 3907-3910 (2002).

[101] A. Weidinger, M. Waiblinger, B. Pietzak and T. A. Murphy, "Atomic nitrogen in C_{60}: N@C_{60}", Appl. Phys. A **66**, 287-292 (1998).

[102] G. Lalwani and B. Sitharaman, "Multifunctional Fullerene- and Metallfullerene-Based Nanobiomaterials", Nano Life **3**, 1342003 (2013).

[103] G. P. Tegos et al., "Cationic Fullerenes are Effective and Selective Antimicrobial Photosensitizers", Chemistry & Biology **12**, 1127-1135 (2005).

[104] D.Pinto et al., "Readout and control of an endofulleren electronic spin", Nature Comm. **11**, 6405 (2020).

[105] G. Jescke, M. Pannier, A. Godt and H. W. Spiess, "Dipolar spectroscopy and spin alignment in electron paramagnetic resonance", Chemical Physics Letters **331**, 243-252 (2000).

[106] A. Lajtha, *Handbook of Neurochemistry*, 2nd ed. (Plenum Press, 1982).

[107] A. D. McNaught and A. Wilkinso, *Compendium of Chemical Terminology*, 2nd ed. (IUPA, 1987).

[108] E. Grell, *Membrane Spectroscopy*, 1st ed. (Springer, 1981).

[109] W. B. Mims, K. Nassau and J. D. Mc Gee, "Spectral Diffusion in Electron Resonance Line", Phys. Rev. **123**, 2059 (1961).

[110] T. Prisner, M. Rohrer and F. MacMillan, "Pulsed EPR Spectroscopy: Biological Applications", Annu. Rev. Phys. Chem. **52**, 279-313 (2001).

[111] H. Haken and H. C: Wolf, *Atom- und Quantenphysik*, 8th ed. (Springer, 2003).

[112] R. J. Blume, "Electron Spin Relaxation Time in Sodium-Ammonia Solutions", Phys. Rev. **109**, 1867-1873 (1958).

[113] A. Abragam, *The Principles of Nuclear Magnetism*, 1st ed. (Oxford University Press, 1983).

[114] F. Rempp, *Decoherence properties of the NV-center in diamond*, Dissertation in Physics, University of Stuttgart (2011).

[115] F. Kong et al., "Kilohertz electron paramagnetic resonance spectroscopy of single nitrogen centers at zero magnetic field", Sci. Adv. **6**, eaaz8244 (2020).

[116] M. M. Haugland, E. A. Anderson and J. E. Lovett, "Tuning the properties of nitroxide spin labels for use in electron paramagnetic resonance spectroscopy thorugh chemical modfication of the nitroxide framework", Electron Paramagnetic Resonance **25**, 1-34 (2016).

[117] M. T. Ruggiero et al., "Measuring the Elasticity of Poly-I-Proline Helices with Terahertz Spectroscopy", Angew. Chem. **55**, 6877-6881 (2016).

[118] H. L. Dai and W. Ho, *Laser Spectroscopy and Photochemistry on Metal Surfaces*, 1st ed. (World Scientific Publishing Co Pte Ltd, 1995).

[119] S. Das, S. Sarmah and A. S. Roy, "Monitoring fluorescence emission behaviors of dietary polyphenols in a serum albumin environment", New J. Chem. **44**, 299-302 (2020).

[120] I. Volf, I. Ignat, M. Neamtu and V. I. Popa, "Thermal stability, antioxidation activity, and photooxidation of natural polyphenols", Chemical Papers **68**, 121-129 (2014).

[121] Y. Xiang, Y. Liu and M. L. Lee, "Ultrahigh pressure liquid chromatography using elevated temperature", J. Chromatogr. A **1104**, 198-202 (2006).

[122] A. A. Popov, *Endohedral Fullerenes: Electron Transfer and Spin*, 1st ed. (Springer, 2017).

[123] C. Knapp, K. P. Dinse, B. Pietzak, M. Waiblinger and A. Weidinger, "Fourier transform EPR study of N@C_{60} in solution", Chemical Physics Letters **272**, 433-437 (1997).

[124] B. Pietzak et al., "Properties of Endohedral N@C_{60}", Carbon **36**, 613-615 (1998).

[125] W. Harneit, M. Waiblinger, C. Meyer, K. Lips and A. Weidinger, "Concept for Quantum Computing with N@C_{60}", Electrochemical Society Proceedings **11**, 358-361 (2001).

[126] H. W. Kroto, J. R. Heath, S. C. O'Brien, R. F. Curl and R. E. Smalley, "C_{60}: Buckminsterfullerene", Nature **318**, 162-163 (1985).

[127] S. Zhou and K. Porfyrakis, *Preparation and Chemistry of N@C_{60}*, 1st ed. (Springer, 2017).

[128] M. Drescher and G. Jeschke, *EPR Spectroscopy: Applications in Chemistry and Biology*, 1st ed. (Springer, 2012).

[129] B. Goedde et al., "Nitrogen dopes C_{60} Dimers (N@C_{60}-C_{60})", Chemical Physics Letters **332**, 12-17 (2001).

[130] H. J. Mamin et al., "Multipulse Double-Quantum Magnetometry with Near-Surface Nitrogen-Vacancy Centers", Phys. Rev. Lett. **113**, 030803 (2014).

[131] F. Schwabl, *Quantenmechanik*, 6th ed. (Springer, 2002).

[132] A. Borthakur et al., "T1rho MRI of ALzheimer's disease", NeuroImage. **41**, 1199-1205 (2008).

[133] J. Twamley, "Quantum-cellular-automata quantum computing with endohedral fullerenes", Phys. Rev. A **67**, 052318 (2003).

[134] L. Childress and R. Hanson, "Diamond NV centers for quantum computing and quantum networks", MRS Bulletin **38**, 134-138 (2013).

[135] B. Nachman, M. Urbanek, W.A. de Jong and C. W. Bauer, "Unfolding quantum computer readout noise", npj Quantum Information **6**, 84 (2020).

[136] J. Jing and L. A. Wu, "Decoherence and control of a qubit in spin baths: an exact master equation study", Scientific Reports **8**, 1471 (2018).

[137] G. Feher, "Observation of Nuclear Magnetic Resonances via the Electron Spin Resonance Line", Phys. Rev. **103**, 834-835 (1956).

[138] G. Binnig and H. Rohrer, "Scanning Tunneling Microscopy", Surface Science **126**, 236-244 (1983).

[139] Y. Manassen, I. Mukhopadhyay and N. R. Rao, "Electron-Spin-resonance STM on iron atoms in silicon", Phys. Rev. B **6**, 16223 (2000).

[140] S. Baumann et al., "Electron paramagnetic resonance of individual atoms on a surface", Science **350**, 6259 (2015).

[141] K. Yang et al., "Coherent spin manipulation of individual atoms on a surface", Science **366**, 509-512 (2019).

[142] R. C. Barklie and J. Guven, "^{13}C hyperfine structure and relaxation time of the P1 centre in diamond", J. Phys. C: Solid State Phys. **14**, 3621-3631 (1981).

[143] G. de Lange et al., "Controlling the quantum dynamics of a mesoscopic spin bath in diamond", Scientific Reports **382**, 10.1038 (2012).

[144] H. A. Jahn and E. Teller, "Stability of polyatomic molecules in degenrate electronic states", Proceedings of the Royal Society of London **161**, 220-235 (1937).

[145] Y. Yahua, *High-Pressure Synthesis, Crystal Structures, and Magnetic Properties of Perovskite-Related Os and Ir Oxides*, Dissertation in Physics, University of Hokkaido (2015).

[146] W. V. Smith, P. P. Sorokin, I. L. Gelles and G. L. Lasher, "Electron-spin resonance of nitrogen donors in diamond", Phys. Rev. **115**, 1546-1552 (1959).

[147] J. Loubser W. van Ryneveld and L. du Preez, "Exchange interaction effects in the e.s.r spectrum of substitutional nitrogen in diamond", Solid State Communications **3**, 307-309 (1965).

[148] E. Bauch et al., "Ultralong Dephasing Times in Solid-State Spin Ensembles via Quantum Control", Phys. Rev. X **18**, 031025 (2018).

[149] J. D. A. Wood et al., "Wide-band magnetic resonance spectroscopy using quantum relaxation of a single spin in diamond", Phys. Rev. B **94**, 155402 (2016).

[150] L. M. Pham et al., "Enhanced metrology using preferential orientation of nitrogen-vacancy centers in diamond", Phys. Rev. B **86**, 121202 (2012).

[151] T. Fukui et al., "Perfect selective alignment of nitrogen-vacancy centers in diamond", Appl. Phys. Express **7**, 055201 (2014).

[152] P. Szankowski, G. Ramon, J. Krzywda, D. Kwiatkowski and L. Cywinski, "Environmental noise spectroscopy with qubits subjected to dynamical decoupling", J. Phys: Conden. Matter **29**, 333001 (2017).

[153] T. Vanngard and R. Aasa, *Paramagnetic Resonance*, 2nd ed. (Academic Press New York, 1973).

[154] M. Barangi and P. Mazumder, "Effect of temperature variations and thermal noise on the static and dynamic behavior of straintronics devices", J. Appl. Phys. **118**, 173902 (2015).

[155] D. Dew-Hughes, "Introduction to Superconducting Materials", Treatise on Materials Science and Technology **14**, 1-46 (1979).

[156] J. W. Bray, "Superconductors in Applications; Some Practical Aspects", IEEE Transactions on Applied Superconductivity **19**, 1051-8223 (2009).

[157] P. F. Dahl, *Superconductivity*, 1st ed. (Springer, 1992)

[158] W. Meissner and R. Ochsenfeld, "Ein neuer Effekt bei Eintritt der Supraleitfähigkeit", Naturwissenschaften **21**, 787-788 (1933).

[159] J. W. Ekin, *Experimental Techniques for Low-Temperature Measurements*, 1st ed. (Oxford University Press, 2006).

[160] L. Ceccarelly at al., "Imaging pinning and expulsion of individual superconducting vortices in amorphous MoSi thin films", Phys. Rev. B. **100**, 104504 (2019).

[161] H. J. Hug et al., "Quantitative magnetic force microscopy on perpendicular magnetized samples", J. Appl. Phys. **83**, 5609-5620 (1998).

[162] P. Kot et al., "Micorwave-assisted tunneling and interference effects in superconducting junctions under fast driving signals", Phys. Rev. B **101**, 134507 (2020).

[163] P. E. Goa et al., "Real time magneto-optical imaging of vortices in superconductors", Supercond. Sci. Technol. **14**, 729-731 (2001).

[164] A. A. Abrikosov, "The magnetic properties of superconducting alloys", J. Phys. Chem. Solids. **2**, 199-208 (1957).

[165] G. Stan, S. B. Field and J. M. Martinis, "Critical Field for Complete Vortex Expulsion from Narrow Superconducting Strips", Phys. Rev. Lett. **92**, 097003 (2004).

[166] D. Paone et al., "All-optical and microwave-free detection of Meissner screening using nitrogen-vacancy centers in diamond", J. Appl. Phys. Phys. **129**, 024306 (2021).

[167] C. L. Degen, F. Reinhard and P. Cappellaro, "Quantum sensing", Rev. Mod. Phys. **89**, 035002 (2017).

[168] V. M. Acosta et al., "Color Centers in Diamond as Novel Probes of Superconductivity", J. Supercond. Nov. Magn. **32**, 85-95 (2019).

[169] N. M. Nusran et al., "Spatially-resolved study of the Meissner effect in superconductors using NV-centers-in-diamond optical magnetometry", New J. Phys. **20**, 043010 (2018).

[170] L. Thiel et al., "Quantitative nanoscale vorex imaging using a cryogenic quantum magnetometer", Nat. Nanotechnol. **11**, 677-681 (2016).

[171] M. Pelliccione et al., "Scanned probe imaging of nanoscale magnetism at cryogenic temperatures with a single-spin quantum sensor", Nat. Nanotechnol. **11**, 700-705 (2016).

[172] T. Shibita, K. Unno, E. Makino, Y. Ito and S. Shimada, "Characterization of sputtered ZnO thin film as sensors and actuator for diamond AFM probe", Sensors and Actuators A: Physical **102**, 106-113 (2002).

[173] W. Smirnov et al., "Diamond-Modified AFM Probes: From Diamond Nanowires to Atomic Force Microscopy-Intergrated Boron-Doped Diamond Electrodes", Anal. Chem. **83**, 4936-4941 (2011).

[174] K. R. Joshi et al., "Measuring the Lower Critical Field of Superconductors Using Nitrogen-Vacancy Centers in Diamond Optical Magnetometry", Phys. Rev. Appl. **11**, 014035 (2019).

[175] Y. Xu et al., "Mapping Dynamical Magnetic Responses of Ultrathin Micron-Size Superconducting Films Using Nitrogen-Vacancy Centers in Diamond", Nano. Lett. **19**, 5697-5702 (2019).

[176] D. Rohner et al., "Real-space probing of the local magnetic response of thin-film superconductors using single spin magnetometry", Sensors **3790**, s18113790 (2018).

[177] S. E. Lillie et al., "Laser Modulation of Superconductivity in a Cryogenic Wide-field Nitrogen-Vacancy Microscope", Nano Lett. **20**, 1855-1861 (2020).

[178] R. Gilardi, S. Streule, N. Momoni, M. Oda and J. Mesot et al., "Doping dependence of the vortex glass and sublimation transitions in the high-Tc superconductor LSCO as determined from macroscopic measurements", Eur. Phys. J. B **47**, 231-237 (2005).

[179] H. Suzuki et al., "Probing the energy gap of high-temperature cuprate superconductors by resonant inelastic x-ray scattering", npj Quantum Materials **3**, 65 (2018).

[180] N. Barisic et al., "Universal sheet resistance and revised phase diagram of the cuprate high-temperature superconductors", PNAS **30**, 12235-12240 (2013).

[181] F. S. Wells, A. V. Pan, X. R. Wang, S. A. Fedoseev and H. Hilgenkamp, "Analysis of low-field isotropic vortex glass containing vortex groups in YBCO thin films visualized by scanning SQUID microscopy", Scientific Reports **5**, 8677 (2015).

[182] I. Iguchi, T. Yamaguchi and A. Sugimot, "Diamagnetic activity above Tc as a precursor to superconductivity in LSCO thin film", Nature **412**, 420-423 (2001).

[183] F. Baiutti, G. Christiani and G. Logvenov, "Towards precise defect control in layered oxide structures by using oxide molecular beam epitaxy", Nanotechnol. **5**, 596-602 (2014).

[184] M. W. Coffey, "Mutual inductance of superconducting thin films", J. Appl. Phys. **89**, 5570 (2001).

[185] J-P Tetienne et al., "Magnetic-field-dependent photdynamics of single NV defects in diamond: an application to qualitative all-optical magnetic imaging", New. J. Phys. **14**, 103033 (2012).

[186] G. L. Carr, R. P. S. M. Lobo, J. LaVeigne, D. H. Reitze and D. B. Tanner, "Exploring the Dynamics of Superconductors by Time-Resolved Far-Infrared Spectroscopy", Phys. Rev. Lett. **85**, 3001 (2000).

[187] E. H. Brandt, "Electric field in superconductors with rectangular cross section", Phys. Rev. B **52**, 15442 (1995).

[188] E. H. Brandt and M. Indenborn, "Type-II-superconductor strip with current in a perpendicular magnetic field", Phys. Rev. B **48**, 893-906 (1993).

[189] J. D. Jackson, *Classical Electrodynamics*, 3rd ed. (Wiley, 1998).

[190] N. E. Litombe, A. T. Bollinger, J. E. Hoffman and I. Brozovic, "LSCO superconductor nanowire devices", Physica C **506**, 169-173 (2014).

[191] V. S. Stolyarov et al., "Expansion of a superconducting vortex core into a diffusive metal", nature communications **9**, 2277 (2018).

[192] S. Ishizu et al., "Spin coherence and depths of single nitrogen-vacancy centers created by ion implantation into diamond via screening masks", J. Appl. Phys. **127**, 244502 (2020).

[193] A. Ariyaratne, D. Bluvstein, B. A. Myers and A. C. B. Jayich, "Nanoscale electrical conductivity imaging using a nitrogen-vacancy center in diamond", Nature Comm. **9**, 2406 (2018).

[194] B. K. Ofori-Okai, "Spin properties of very shallow nitrogen vacancy defects in diamond", Phys. Rev. B **86**, 081406 (2012).

[195] D. Bluvstein, Z. Zhang and A. C. B. Jayich, "Identifying and Mitigating Charge Instabilities in Shallow Diamond Nitrogen-Vacancy Centers", Phys. Rev. Lett. **122**, 076101 (2019).

[196] Z. Yuan, "Charge state dynamics and optically detected electron spin resonance contrast of shallow nitrogen-vacancy centers in diamond", Phys. Rev. Research **2**, 033263 (2020).

[197] F. Brandenburg et al, "Improving the electron spin properties of nitrogen-vacancy centres in nanodiamonds by near-field etching", Nature Scientific Report **8**, 15847 (2018).

[198] S. D. Sudebi et al., "Laser spectroscopy characterization of negatively charged nitrogen-vacancy (NV^-) centers in diamond", OME **9**, 357791 (2019).

[199] S. A. Solin and A. K. Ramdas, "Raman Spectrum of Diamond", Phys. Rev. B **1**, 1687 (1970).

[200] C. Schreyvogel et al., "Active and fast charge-state switching of single NV centers in diamond by in-plane Al-Schottky junctions", Beilstein J. Nanotechnol. **7**, 1727-1735 (2016).

[201] K. Ito et al., "Nitrogen-vacancy centers created by N^+ ion implantation through screening SiO_2 layers on diamond", Appl. Phys. Lett. **110**, 213105 (2017).

[202] R. Fukuda et al., "Lithographically engineered shallow nitrogen-vacancy centers in diamond for external nuclear spin sensing", New J. Phys. **20**, 083029 (2018).

[203] K. Y. Han et al., "Dark state photophysics of nitrogen-vacancy centres in diamond", New J. Phys. **14**, 123002 (2012).

[204] H. Takahashi, K. Takegahara, A. Yanase and T. Kasuya, "Mechanism of low temperature magnetic properties in Ce monopnictides", Journal of Magnetism and Magnetic Materials **31**, 405-406 (1983).

[205] Y. Fujima, N. Abe, Y. Tokunaga and T. Arima, "Thermodynamically stable skyrmion lattice at low temperatures in a bulk crystal of lacunar spine GaV_4Se_8", Phys. Rev. B **95**, 180410 (2017).

[206] S. I. Davis et al., "Spatially modulated susceptibility in thin film $La_{2-x}Ba_xCuO_4$", Phys. Rev. B **98**, 014506 (2018).

[207] E. Meszaros, "Composition and structure of the Earth's atmosphere", Studies in Environmental Science **11**, 11-16 (1981).

[208] M. V. Hauf et al., "Chemical control of the charge state of nitrogen-vacancy centers in diamond", Phys. Reb. B **83**, 081304 (2011).

[209] T. Staudacher et al., "Enhancing the spin properties of shallow implanted nitrogen vacancy centers in diamond by epitaxial overgrowth", Appl. Phys. Lett. **101**, 212401 (2012).

[210] S. Kawai et al., "Nitrogen Terminated Diamond Surface for Nanoscale NMR by Shalloe Nitrogen-Vacancy Centers", J. Phys. Chem. C **123**, 3549-3604 (2019).

[211] C. E. Mortimer and U. Müller, *Chemie: Das Basiswissen der Chemie*, 13th ed. (Thieme, 2019).

[212] D. R. Lide, *CRC Handbook of Physics and Chemistry*, 71st ed. (CRC Press inc., 1990).

[213] C. Harding, *Elements of the p Block*, 1st ed. (Royal Society of Chemistry, 2002).

[214] K. Hosokawa, I. Shimoyama and H. Miura, "Two-dimensional micro-self-assembly using the surface tension of water", Sensors and Actuators **57**, 117-125 (1996).

[215] A. K. Soper, "Water and Ice", Science **297**, 1288-1289 (2002).

[216] C. A. Angel, "Insights into phases of Liquid Water from Study to Its Unusual Glass-Forming Properties", Science **319**, 582-587 (2008).

[217] D. Kang, J. Dai and J. Yuan, "Changes of structue and dipole moment of water with temperature and pressure: A first principle study", J. Chem. Phys. **135**, 024505 (2011).

[218] G. E. Scuseria, "The dipole moment of carbon monoxide", J. Chem. Phys. **94**, 6660 (1991).

[219] M. Berthel et al., "Photophysics of single nitrogen-vacancy centers in diamond nanocrystals", Phys. Rev. B **91**, 035308 (2015).

[220] K. Mogi, T. Komine, K. Hirao, "A theoretical study on the dipole moment of N_2O and the weakly bound complexes formed by N_2O", J. Chem. Phys. **95**, 8999 (1991).

[221] C. P. Smyth and K. B. McAlpine, "The Dipole Moment of Nitric Oxide", J. Chem. Phys. **1**, 60 (1933).

[222] C. Chatgilialoglu and A. Studer, *Encyclopedia of Radicals in Chemistry, Biology ans Materials*, 1st ed. (John Wiley & Sons Ltd., 2012).

[223] Y. V. Babich and B. N. Feigelson, "Distribution of nitrogen-related defects in diamond single crystals grown under non isothermal conditions", Inorganic Materials **42**, 971-975 (2006).

[224] A. T. Collins "The characterisation of point defects in diamond by luminscence spectroscopy", Diamond and Related Materials **1**, 457-469 (1992).

[225] J. E. Shigley, C. M. Breeding and A. H. Shen, "An Updated Chart on the Characteristics of HPHT-Grown Synthetic Diamonds", Gems and Gemology **40**, 303-313 (2004).

[226] J. E. Shigley and C. M. Breeding, "Optical Defects in Diamond: A Quick Reference Chart", Gems and Gemology **49**, 107-111 (2013).

[227] C. Bradac, W. Gao, J. Forneris, M. E. Trusheim and I. Aharonovich, "Quantum nanophotonics with group IV defects in diamond", Nature Com. **10**, 5625 (2019).

[228] T. Iwasaki et al., "Germanium-Vacancy Single Color Centers in Diamond", Scientific Reports **5**, 12882 (2015).

[229] S. V. Bolshedvorskii et al., "Single Silicon Vacancy Centers in 10 nm Diamond for Quantum Information Applications", ACS Appl. Nano Matter. **2**, 4765-4772.

[230] J. N. Becker and E. Neu, "The silicon vacancy center in diamond", Semiconductors and Semimetals **103**, 201-235 (2020).

[231] B. Pingault et al., "Coherent control of the silicon-vacancy spin in diamond", Nature Com. **8**, 15579 (2017).

[232] B. Pingault et al., "All-Optical Formation of Coherent Dark States of Silicon-Vacancy Spins in Diamond", Phys. Rev. Lett. **113**, 263601 (2014).

[233] G. Thiering and A. Gali, "Color centers in diamond for quantum applications", Semiconductors and Semimetals **103**, 1- 36 (2020).

[234] F. Krishnamurti, "The Raman spectrum of diamond", Proc. of the Indian Academy of Sciences-Section A **40**, 211-216 (1954).

[235] R. A. Frosch and H. M. Foley, "Magnetic HYperfine Structure in Diatomic Molecules", Phys. Rev. **88**, 1337 (1952).

[236] K. G. Woodgate, *Elementary Atomic Structure*, 1st ed. (Oxford University Press, 1999).

[237] J. P. Goss, P. R. Briddon, H. Pinto and R. Jones, "Optically active point defects in high quality single crystal diamond", Phys. Status. Solidi A **2017**, 2049-2053 (2010).

[238] E. Fritsch, T. Hainschwang, L. Massi and B. Rondeau, "Hydrogen-Related Optical Center in Natural Diamond: An Update", New Diamond and Frontier Carbon Technology **17**, 63-89 (2007).

[239] T. Duan et al., "A novel fabrication technique for three-dimensional concave nanolens arrays", Journal of Materiomics **6**, 557-562 (2020).

[240] S. Pribitzer, M. Sajid, M. Hülsmann, A. Godt and G. Jeschke, "Pulsed triple electron resonance (TRIER) for dipolar correlation spectroscopy", Journal of Magnetic Resonance **282**, 119-128 (2017).

[241] A. Shapere and F. Wilczek, "Classical Time Crystals", Phys. Rev. Lett. **109**, 160402 (2012).

[242] P. Coleman, "Time crystals", Nature **493**, 166-167 (2013).

[243] J. Zhang et al., "Observation of a discrete time crytsla", Nature **543**, 217-220 (2017).

[244] S. Choi et al., "Observation of discrete time-crystalline order in a disordered dipolar many-body system", Nature **543**, 221-225 (2017).

[245] J. Rovny, R. L. Blum and S. E. Barrett, "Observation of Discrete-Time-Crystal Signatures in an Ordered Dipolar Many-Body System", Phys. Rev. Lett. **120**, 180603 (2018).

[246] S. Kaiser, "Light-induced superconductivity in high-T_c cuprates", Phys. Scr. **92**, 103001.

[247] S. Woutersen, U. Emmerichs and H. J. Bakker, "Femtosecond Mid-IR Pump-Probe Spectroscopy of Liquid Water: Evidence for a Two-Component Structure", Science **278**, 658-660 (1997).

[248] R. D. Averitt et al., "Non equilibrium superconductivity and quasiparticle dynamics in $YBa_2Cu_3O_{7-\delta}$", Phys. Rev. B **63**, 140502 (2001).

[249] C. R. Hunt et al., "Dynamical decoherence of the light induced interlayer coupling in $YBa_2Cu_3O_{6-\delta}$", Phys. Rev. B **94**, 224303 (2016).

[250] A. F. Kemer, M. A. Sentef, B. Moritz, J. K. Freericks and T. P. Devereaux, "Direct observation of Higgs mode oscillations in the pump-probe photoemission spectra of electron-phonon mediated superconductors", Phys. Rev. B **92**, 224517 (2015).

[251] A. Watanabe et al., "Shallow NV centers augmented by exploting n-type diamond", Carbon **178**, 294-300 (2021).

[252] E. D. Herbschleb et al., "Ultra-long coherence times amongst room-temperature solid state spins", nature com. **10**, 3766 (2019).

Acknowledgments

Starting a PhD in physics was maybe one of the most random things which I have ever done in my life so far. When I began my physics studies as young high-school graduate, I have not even known that you can get a Dr. degree in this subject. I just was interested in understanding how nature works. However, I have never thought about how tough physics could be and how hard the pursuit of a Dr. degree will be. Indeed, I never felt more infuriated and disappointed as in the first years of my PhD studies. Nevertheless, I am 100% sure that I have chosen the right path for my life. After each frustrating gathered result, I learned something for improving the experiment. In the end, stuff worked out and I am really satisfied about my achievements. However, there is one thing I want to emphasize in this very last part. Without the help of many people, I still would be the same high-school student as 10 years ago. Therefore, I would like to take the opportunity to thank all these persons which played a crucial role for the existence of this thesis.

First and foremost I am deeply grateful to Prof. Klaus Kern and Prof. Jörg Wrachtrup for giving me the opportunity to work on this interesting project. The application of NV center sensors in a cryogenic-UHV environment is a long-term and of course still not finished joint project between the nanoscale department of Prof. Kern at the Max-Planck Institute (MPI) and the 3rd Physics Institute of Prof. Wrachtrup at the University of Stuttgart. I benefited from their great expertise, continuous support and scientific input in form of fruitful discussions.

In connection to this scientifically great alliance, I also want to thank the whole 3rd Physics Institute of the University of Stuttgart. Especially, I want to mention the scanning-probe group including Dr. Rainer Stöhr, Dr. Andrej Denisenko, Dr. Jianpei Geng, Dr. Margarita Iakovleva, Dr. Qi-Chao Sun, Dr. Rolf Reuter, Dr. Andrea Zappe, Tetyana Shalomayeva, Mariia Gryzlova, Minsik Kwon, Sreehari Jayaram and former members as Dr. Amit Finkler, Dr. Thomas Oeckinghaus, Dr. Dominik Schmid-Lorch, Dr. Andreas Brunner and Philipp Scheiger. Our weekly Tuesday meetings at 9 a.m. were crucial for improving my experiments.

Beside of the 3rd Physics Institute, there were also other important collaborations which had an essential impact on this thesis. Therefore I would like to thank Prof. Adelheid Godt from the University of Bielefeld for the synthesis of spin labeled organic molecules and Prof. Wolfgang Harneit for the composition of N@C_{60} molecules. In addition to that I am also thankful to Gennady Logvenov and Gideok Kim for the fabrication of LSCO samples. I also want to appreciate the great discussions with Prof. Stefan Kaiser and Liwen Feng which initiated the superconductor project of this thesis.

After mentioning the awesome collaborators, I want to deeply thank my closest MPI colleagues which form the Diamond-AFM subgroup of the nanoscale department including Dr. Bastian Kern, Dr. Lukas

Schlipf, Dinesh Pinto, Jeffrey Neethi Neethirajan and Dr. Aparajita Singha. Bastian, as my first supervisor, and Lukas, as my PhD precursor, introduced the whole field of NV center magnetometry to me and supported me through my first year as PhD student. I hope that you guys are doing well in your rather new jobs at Zeiss and Valeo. However, after Bastian left, there was a lack of supervision for the development of my PhD projects which made my life quite hard. Therefore, I want to express my gratitude to Dr. Aparajita Singha who came as the successor of Bastian. She boosted my motivation to another level which enabled me to form an awesome publication into the Journal of Applied Physics (even as featured article). I think we formed an awesome team and I hope that we can proceed with this efficiency for the realization of exciting projects. I also want to mention Jeffrey who is the latest member of the Diamond-AFM subgroup and an awesome Master student. You were the man in the lab of the last few months while I was writing this thesis in my office. I trust in your experiments and the results are great so far. The last person of this group is "The" Dinesh Pinto. We started together this adventure at the MPI and I am impressed from your addiction to science. You were there, whenever I ran into problems for helping me out. There was no question which you could not answer. I think that I am one of the luckiest PhD students at the MPI for having such an awesome office and lab mate. Thanks for all the essential discussions about scientific problems, sport, stocks and crypto currencies.
Remaining on the people which are related to the MPI, I also want to thank the whole nanoscience department of Klaus Kern for great support and fruitful discussions after lunch and on conferences. Moreover, I want to express a big thank you to our highly skilled technicians Wolfgang Stiepany, Peter Andler, Marko Memmler and Isabel Wolf. Seriously, your are the guys which make our instruments running. I am also thankful to Sabine Birtel as the best and most professional secretary of the world.
I also want to thank the persons outside of the MPI including my friends which always believed in my scientific skills. A special "thank you" goes to Jan Schnabel, Marcel Klett, Henri Menke, Michael Schmid, Stefan Käser, Kai Guther and Marc Sartison. We started together our physics studies and now we are all Dr. rer. nat. I am very happy that we are still keeping contact even after 10 years of friendship. Furthermore, I want to acknowledge my parents Antonio and Maddalena Paone and my sister Stefania Paone for their great support. You always believed in my decisions.
Finally, I want to thank my girlfriend Corinna Bossert. I could write several pages about you. However, at some point I have to finish this thesis. Therefore, I will try to make it short. Thank you for your support, thank you for believing in me, thank you for motivating my goals, thank you for accepting me for who I am, thank you for listening to my problems, thank you for finding the right words when I am upset and thank you for staying always on my side. I am pretty sure that you know me better than I do. The time with you is always the best time in my life and I am looking forward to our future.